DOAS measurements of iodine monoxide
from satellite

DOAS Messungen des Spurengases Iodmonoxid vom Satelliten aus

Vom Fachbereich Physik und Elektrotechnik
der Universität Bremen

zur Erlangung des akademischen Grades
Doktor der Naturwissenschaften (Dr.rer.nat)
genehmigte Dissertation

vorgelegt von
Dipl. Phys. Anja Schönhardt

Bremen, 03. September 2009

Dissertation eingereicht am: 03.09.2009

Tag des Promotionskolloquiums: 09.10.2009

1. Gutachter: Prof. Dr. John P. Burrows

2. Gutachter: Prof. Dr. Lars Kaleschke

For my parents
Anne and Rudolf

Abstract

Atmospheric columns of the trace gas iodine monoxide, IO, have been investigated by means of spectroscopic measurements in the visible wavelength range. For this purpose, solar radiation scattered and reflected by the Earth's atmosphere and surface is recorded by satellite instrumentation in nadir viewing geometry. These spectra have been analysed for the absorption signal of the IO vibronic absorption lines. Employing the Sciamachy sensor mounted on the ENVISAT satellite, global observations of IO from space become possible for the first time. The importance of iodine in the atmosphere lies in its high potential for destroying ozone as well as in the formation of new particles which is initiated by condensable iodine oxides and may impact on Earth's radiation budget at least locally.

A major challenge in this work is the smallness of the observed IO optical depths with respect to the instrument's detection limit. The retrieved IO slant columns are therefore averaged over certain time periods of typically several months. Widespread enhanced IO columns have been detected over the Antarctic region with a detailed spatial and temporal distribution. Further regions with positive IO detection are the Eastern Pacific upwelling region and some Northern Hemispheric coast lines. Additional data such as tropospheric BrO distributions, ice concentrations, phytoplankton amounts and diatom abundances have been considered in specific cases for comparison and discussion purposes, addressing the question of sources of atmospheric iodine, which are most probably biogenic.

Successful comparison and validation studies provide confidence in the newly developed satellite IO product, and model calculations have been conducted to investigate the amounts of precursors necessary for the explanation of observed IO abundances. While in some analyses, the limitations of the satellite measurements have been encountered, the presented investigations have advanced the prospects of remote sensing from space for the detection of the minor trace gas IO.

List of publications

1. Articles in peer-reviewed journals

As first author:

- Schönhardt, A., Richter, A., Wittrock, F., Kirk, H., Oetjen, H., Roscoe, H. K., and Burrows, J. P.: Observations of iodine monoxide columns from satellite, Atmos. Chem. Phys., 8, 637-653, 2008.

As co-author:

- Brinksma, E. J., Pinardi, G., Volten, H., Braak, R., Richter, A., Schönhardt, A., van Roozendael, M., Fayt, C., Hermans, C., Dirksen, R. J., Vlemmix, T., Berkhout, A. J. C., Swart, D. P. J., Oetjen, H., Wittrock, F., Wagner, T., Ibrahim, O. W., de Leeuw, G., Moerman, M., Curier, R. L., Celarier, E. A., Cede, A., Knap, W. H., Veefkind, J. P., Eskes, H. J., Allaart, M., Rothe, R., Piters, A. J. M., and Levelt, P. F.: The 2005 and 2006 DANDELIONS NO_2 and aerosol intercomparison campaigns, Journal of Geophysical Research, 113, D16S46, doi:10.1029/2007JD008808, 2008.

- Celarier, E. A., Brinksma, E. J., Gleason, J. F., Veefkind, J. P., Cede, A., Herman, J. R., Ionov, D., Goutail, F., Pommereau, J.-P., Lambert, J.-C., van Roozendael, M., Pinardi, G., Wittrock, F., Schönhardt, A., Richter, A., Ibrahim, O. W., Wagner, T., Bojkov, B., Mount, G., Spinei, E., Chen, C. M., Pongetti, T. J., Sander, S. P., Bucsela, E. J., Wenig, M. O., Swart, D. P. J., Volten, H., Kroon, M., and Levelt, P. F.: Validation of ozone monitoring instrument nitrogen dioxide columns, Journal of Geophysical Research, 113, D15S15, doi:10.1029/2007JD008908, 2008.

- Hains, J., Boersma, F., Kroon, M., Dirksen, R., Volten, H., Swart, D., Richter, A., Wittrock, F., Schoenhardt, A., Wagner, T., Ibrahim, O., van Roozendael, M., Pinardi, G., Gleason, J., Veefkind, P., and Levelt, P.: Testing and improving OMI DOMINO tropospheric NO_2 using observations from the DANDELIONS and INTEX-B validation campaigns, Journal of Geophysical Research, accepted 8 October 2009, doi:10.1029/2009JD012399, in press.

2. Selected oral and poster presentations (only first autor)

Oral presentations at conferences and workshops:

- A. Schönhardt, A. Richter, F. Wittrock, and J. P. Burrows: Observation of IO from Space using SCIAMACHY, Sixth ACCENT-TROPOSAT-2 Workshop on "Observing trace substances from space and integrating the results with models" in Bremen, June 2007.

- A. Schönhardt, A. Richter, F. Wittrock, H. Kirk, H. Oetjen, and J. P. Burrows: Seasonal variations of IO above Antarctica observed in three years of satellite data DPG Frühjahrstagung, Darmstadt, March, 2008.

Presentations at external seminars:

- A. Schönhardt, A. Richter, F. Wittrock, and J. P. Burrows: Iodine monoxide above Antarctica - 4 years of satellite observations, Hamburg, invited talk in the ZMAW Seminar, April 2008.

Poster presentations:

- A. Schönhardt, F. Wittrock, A. Richter, H. Oetjen, J. P. Burrows, M. Van Roozendael, G. Pinardi, H. Bergwerff, S. Berkhout, R. van der Hoff, H. Volten, D. Swart, and E. Brinksma, MAX-DOAS measurements of tropospheric NO_2 from the DANDELIONS-II campaign, DPG Spring meeting, Regensburg, Germany, March 2007.

- A. Schönhardt, A. Richter, F. Wittrock, J. P. Burrows, First observations of atmospheric iodine oxide columns from satellite, EGU General Assembly 2007, Vienna, Austria, April 2007.

- A. Schönhardt, A. Richter, F. Wittrock, H. Kirk, H. Oetjen, and J. P. Burrows: Satellite observations of iodine monoxide and its seasonal cycle above Antarctica, IGAC 10th International Conference 2008, Annecy (France), September 2008.

- A. Schönhardt, F. Wittrock, A. Richter, H. Kirk, H. Schulte i.d.B, and J. P. Burrows: The influence of scattering and absorption processes in sea water on atmospheric radiation - results from ship-borne DOAS measurements, DPG Spring Meeting, Hamburg, März 2009.

Contents

List of Figures

List of Tables

Introduction and Motivation

The atmosphere of planet Earth provides vital prerequisites for many life-forms. Vice versa, the atmospheric composition is significantly determined by the interactions with life. Earth's atmosphere is the only place known in the universe with the present specific mixture of gases, where the amount of oxygen is much higher than would be expected for a system in chemical equilibrium (Wayne, 2000). The Earth system with the different domains - atmosphere, biosphere, oceans and land - is described by the controversial but interesting and thought-provoking Gaia theory (Lovelock, 1990) as a regulatory feedback system sustaining the conditions necessary for the existence of life.

The importance of interdisciplinary research in the context of Earth sciences has been generally recognised. Not only individual aspects need to be studied but also the connections between the different fields and domains. The chemical composition of the atmosphere, for instance, impacts on the Earth's radiation budget causing a temperature response through physical absorption, emission and scattering processes, e.g., by greenhouse gases and aerosol particles. This is accompanied by effects on further conditions such as pressure and wind fields, precipitation and ocean circulations as well as, consequently, by impacts on animal and plant health. Some chemical compounds are stable and hardly undergo interactions, while others are very reactive and may lead to substantial compositional changes. The composition is again influenced by all domains of the Earth system, by emissions of biogenic compounds, by deposition of substances to land and oceans, by chemical and phase transformations and by innumerable other processes, each of which forms only a small part of larger cycles.

Iodine species are relevant in many respects and represent a good example of a multidisciplinary field. Due to many involved domains and pathways, the combination of processes is referred to as the biogeochemical cycling of iodine. In some domains, they play a crucial role in spite of rather low abundances. Although only traces of iodine are needed, it is an essential element for vertebrate life through its involvement in thyroid hormone composition. It has a second biological role by protecting plants from oxidative cell decay. As observed for algae and phytoplankton, for example, gaseous organic iodine compounds are emitted to the atmosphere in these instances. Oceanic salt water supplies the basic iodine atoms for these organisms, and chemical conversions of the concerned species are involved in all steps. Iodine belongs to the chemical family of the halogens and various iodine species are found in sea salt, soils, in plant and animal organisms, and also in the atmosphere.

A few decades ago, halogens and their chemistry have advanced to an important research focus due to their destructive impact on the South Polar ozone. Ozone (O_3) provides a protective layer in the stratosphere absorbing energetic ultraviolet (UV) radiation which is harmful for organisms living on the Earth's surface. Catalytic reaction cycles involving chlorine and bromine from man-made chloroflourocarbons (CFCs) and halons are responsible for the stratospheric ozone destruction as proposed by Molina and Rowland (1974) as well as Stolarski and Cicerone (1974) and observed,

e.g., by Chubachi (1984) and Farman et al. (1985).

In the 1980s, a connection between halogen chemistry and processes in the lower tropospheric layers was discovered. Ozone loss events in the Arctic boundary layer and low ozone concentrations in the tropical troposphere were observed but could not be explained or reproduced by atmospheric chemistry models. Strong ozone depletion events (ODEs) in the Polar boundary layer were found to be accompanied by enhanced amounts of bromine compounds (Barrie et al., 1988). Bromine and iodine chemistry have been identified since as missing links in the understanding of tropospheric ozone levels. Tropospheric ozone influences the atmospheric oxidising capacity and is of essential importance, e.g., through the production of the OH radical, but becomes harmful at too high concentrations (summer smog) and induces additionally direct and indirect radiative forcing. While mankind has already caused serious changes of the atmospheric composition, e.g., in terms of air pollution and increasing greenhouse gases, a healthy environment is a desire affecting everyone on Earth. It has also become a major research objective to better understand the current state of the Earth system, the relevant interactions and the ongoing changes in order to predict future development and possibly restrict further impact as far as possible.

Iodine species have two main implications for atmospheric composition. One of them is the large potential of atomic iodine for catalytic ozone destruction. A second aspect discriminates iodine from the other halogens. Iodine oxides form condensable vapours from which small particles may be generated. These can grow to become cloud condensation nuclei (CCN) and consequently influence the climate state. Similar to sulfate aerosol from DMS (dimethylsulphide) oxidation, particulate iodine contributes to the amount of natural aerosols and CCN, probably mainly in oceanic regions. In both processes, iodine monoxide (IO) plays a central role, as immediate product of ozone depletion by iodine atoms and as the starting point for particle formation via higher iodine oxides. Knowledge on the present IO amounts as well as the identification and quantification of iodine sources in the atmosphere are therefore important. Several inorganic and organic release pathways are currently discussed, but the question has not been fully solved yet.

As IO forms very fast from iodine precursors, it is a good indicator for ongoing iodine chemistry. Although IO abundances observed so far are comparatively low, their impact may be substantial, owing to the fast conversions and catalytic cycles. The first atmospheric measurements of IO have only become possible about 10 years ago (Alicke et al., 1999; Wittrock et al., 2000). Several IO measurements have since then been performed with ground-based instrumentation and balloon-borne devices on a campaign basis. These observations have revealed IO at different locations, mainly at coastal sites and a few Polar research stations.

Several questions on the abundances and sources of IO still remain open. The overall importance of iodine is difficult to assess by local measurements only, as the large scale spatial distribution is not revealed and often the campaign duration restricts the information content on temporal evolution. Satellite observations in general provide a valuable tool for the extension of trace gas measurements to a more global scale, and have improved the knowledge of amounts and source regions for several trace species such as O_3, NO_2, CO_2, HCHO, SO_2 and others. After large and wide spread amounts of bromine oxide (BrO) in the spring time Polar Regions had been observed from satellite some years ago (Richter et al., 1998; Wagner and Platt, 1998), the question was open in how far IO would

reveal a similar distribution.

Prior to this work, IO had not been observed from space before. One of the objectives of the present thesis is the retrieval of IO column densities from the SCIAMACHY satellite sensor. SCIAMACHY is mounted on an Earth orbiting satellite and records solar radiation scattered and reflected by the atmosphere and surface. By spectroscopic means, the amounts of IO are determined from absorption features in the visible spectral region. The applied retrieval technique is the well established Differential Optical Absorption Spectroscopy (DOAS) method. The challenging aspect of this task are the comparably small atmospheric amounts expected for IO, around a few parts per trillion (10^{-12}) in terms of volume mixing ratio and probably confined to the lowest atmospheric layers. The signals of the small spectral IO absorption have to be separated from noise influences. A multitude of quality and consistency checks are necessary to avoid misleading results.

Within the present study, the retrieval of atmospheric IO from SCIAMACHY has been achieved (Schönhardt et al., 2007, 2008). The successful evaluation enables the observation of atmospheric IO columns and their spatial and temporal distribution on a nearly global scale. Observations become possible in locations where no IO measurements have been performed so far. A long term global data set has been analysed, covering more than four years from the beginning of 2004 until mid 2008. These satellite results yield deeper insight into the present IO amounts as well as possible iodine sources. Several geographical regions are investigated, with one main focus being the Antarctic. Connections to simultaneously observed BrO columns, the Antarctic sea ice coverage and the phytoplankton concentrations in oceans are analysed. These comparisons shall help to find links to emission sources. For regions, where the IO amounts stay below the detection limit, the identified upper limits are useful to constrain the potential impact of iodine chemistry in the respective locations. In some investigations, the experimental limitations are reached and the analysed effects remain below the detection capability. Currently, SCIAMACHY is the only satellite for which the retrieval of IO has been made possible. One independent study by Saiz-Lopez et al. (2007a) uses the same instrument and investigates the IO amounts on four days over the South Polar Region.

Within the scope of the present work, several questions connected with satellite and ground-based remote sensing have been addressed. Research activities include the involvement in intercomparison campaigns of ground-based instruments, data analyses and satellite validation activities for trace gases other than IO, the planning of new instrumentation scheduled for aircraft measurements of IO and NO_2 and related optical test measurements. The written doctoral thesis concentrates on the retrieval of IO from SCIAMACHY and directly related research aspects as outlined below.

Outline of this thesis

The first chapter summarises relevant scientific background information. The basic context for the importance of atmospheric iodine research is provided by descriptions of the structure of the atmosphere, the connection of halogens to ozone chemistry and the role of atmospheric O_3. The current state of atmospheric iodine research as well as preceding measurements of iodine oxides are summarised. An introduction into the physical processes involved in the applied measurement method is given, and the utilised instruments are introduced.

Chapter 2 describes the development of the retrieval of IO from Sciamachy data. This includes the data processing steps and details on the DOAS retrieval used for the IO standard fit. Crucial quality and consistency checks for the retrieval results are presented. Calculations of the detection limit for relevant situations are performed, and the uncertainty on the final product is estimated from the precision and accuracy of the satellite IO observations. Additionally tested retrievals not fulfilling the quality and/or consistency criteria are discussed, of which one example is chosen for more detailed analysis as it exhibits similarities to an independent study, discussed in Chapter 4.

Chapter 3 presents global observational results of the IO retrieval from Sciamachy, and the most interesting regions are highlighted. A main focus lies on the Polar Regions, in particular on the Antarctic. Southern Hemispheric maps of the newly established IO retrieval explore the temporal and spatial variations over the sea-ice regions, the ice shelves and the Antarctic continent. Extracted time series show an annually repeated seasonal cycle. Further analyses concentrate on the East Pacific tropical region and on Northern Hemispheric coast lines at high latitudes, for which enhanced IO amounts are identified from the satellite observations.

Chapter 4 reports on validation and case studies of the satellite IO data. Good agreement is demonstrated between the IO observations from the present study and ground-based measurements at an Antarctic Research Station. In contrast, discrepancies between the present study and the only other available independent study of IO from satellite over the Antarctic are discussed. Data from ground-based DOAS measurements are then compared to satellite IO results for an Arctic location. Finally, a careful selection procedure attempts to identify the tidal height dependence of IO levels at two mid-latitudinal sites, which is, however, below the detection possibilities of current satellite observations.

Chapter 5 applies the available CAABA/MECCA chemical box model to compute IO mixing ratios for different scenarios. The question is addressed if present measurements of precursor fluxes are able to explain the accomplished satellite results, and the necessary emission amounts are determined.

Chapter 6 introduces DOAS measurements from a ship campaign through the Atlantic, where the instrument viewed at angles below the horizon recording the water leaving spectral radiance. The objective is to improve satellite measurements over water bodies where problems have been identified in the retrievals of several trace gases. A correction spectrum is extracted and included in some satellite test retrievals.

A summary finally brings together the main results from this work, and an outlook is given which proposes future activities for the assessment of remaining open questions.

1 Scientific background

In this chapter, relevant background information on the subject of this thesis is given. The scientific topic is introduced and an overview over the current state of research is established. The major focus of the present study lies on iodine compounds and especially on the detection of iodine monoxide (IO). Iodine is relevant in many respects, and first of all the importance for the different fields is explained.

The importance of iodine for Earth's atmosphere shall then be set in a broader context, so an overview of the Earth's atmosphere and its special structure and composition is given. Ozone (O_3) is a crucial component in atmospheric composition and importantly, halogens exhibit a strong potential for the destruction of ozone. Therefore, the relevance of O_3 is explained as well as its special role in the different atmospheric layers and the connections to halogen chemistry. Then the main sources of atmospheric halogen species, their chemical pathways and relevant influences are described and the current state of research in atmospheric iodine chemistry.

The present work includes the recording and analysis of measurement data, for which several physical processes play a crucial role. Optical measurements of atmospheric trace gas abundances are performed, where the basic detection principle is the characteristic absorption of light by molecules, and other interactions of light with matter play an additional role. Scattering processes and radiative transfer in the atmosphere needs to be considered in order to understand the measurements. Thereafter, the specific scientific technique is described which the measurements and analyses are based upon and finally, the applied instruments are introduced. The reflections in this chapter also motivate the activities undertaken within this study.

1.1 The relevance of iodine in different fields

Iodine is a natural chemical element and belongs to the family of halogens. It was detected in its elementary state in the beginning of the 19th century in the ashes of sea weed (Schröter et al., 1988). The halogens make up the seventh main group of the periodic table of elements. Iodine carries the chemical symbol I and an atomic number of 127 (53 protons, 74 neutrons). The other halogens are fluorine, chlorine, bromine and astatine with different importance in the various fields of science. Although elements of one family often have similar properties and undergo similar chemical reactions, several characteristics are individual for each element. Especially when considering complex systems such as living organisms, the differences may show considerable impact and each element fulfills a unique role. Iodine is an essential element for vertebrates, hence the supply needs to be assured. This relevance already rises the question for sources and abundances of iodine in the natural environment and causes a connection between atmospheric iodine and, e.g., iodine in the human body.

The appearance of radioactive iodine has added importance to this subject, as the biological uptake of iodine is not isotope specific. Radioactive iodine is being released to the atmosphere in considerable amounts by nuclear power stations and from nuclear weapons tests. Through the food chain and also through the air, it is directly transported into living organisms. It was radioactive iodine and its biological threat which originally promoted measurement techniques for environmental iodine.

1.1.1 Iodine and its relevance for human and animal health

Considering the 96 naturally occurring chemical elements, 25 of these are known to be essential for life. Some of them build up the organic material, of which carbon, hydrogen, oxygen and nitrogen make up 96%, others are crucial constituents of hormones or proteins, and some have certain functionality for the nervous system. Unlike bromine, e.g., for which a relevant function for vertebrates is not known, iodine is a constituent of two crucial thyroid hormones, triiodothyronine (T3) which contains three iodine atoms, and thyroxine (T4) with four iodine atoms per molecule. The thyroid hormones play an important role in controlling the metabolic system and the production of proteins and for other hormone controlling functions.

Due to the importance of iodine for the formation of the thyroid hormones, iodine is an essential element and the daily nutrition needs to contain traces of iodine (about 200μg per day for humans). Iodine insufficiencies can lead to dangerous thyroid hypofunction. This health risk has been identified in the 19th century and iodised salt was proposed to help in eliminating high degrees of iodine deficiencies in affected countries (WHO, 2007, and references therein). The natural and regular uptake of iodine through nutrition also permits radioactive iodine isotopes to enter the organism in case they are available.

1.1.2 Radioactive iodine

Several radioactive isotopes of iodine exist, e.g, iodine-129 and iodine-131. These isotopes are emitted by human activities, mainly from nuclear weapons tests, accidents or leakages in nuclear power stations and from nuclear fuel reprocessing plants. The half-lives vary quite strongly with 15.7 million years for iodine-129 and 8 days for iodine-131. With its comparably short half-life, iodine-131 has additional medical relevance in therapies to specifically cure thyroid hyperfunction (overactive production of T_3 and T_4) but also as a diagnostic tracer.

The availability of radioactive iodine after nuclear accidents poses a threat to animal health, as it is ingested (or inhaled) just in the same way as stable iodine-127 and can accumulate in the thyroids (Robertson and Falconer, 1959). Following the atmospheric nuclear weapons tests in the 1950s and 60s, large amounts of radioactive iodine entered the atmosphere (Chamberlain, 1960). The presence of this encouraged research on the field of iodine chemistry, especially its pathways in the environment (Chamberlain et al., 1960) have to be well known in order to estimate the potential health risk arising from radioactive iodine. Through extensive biological, chemical and geological cycles, these species are of relevance also at further distance from the liberation site. Both species, iodine-131 and iodine-129, can undergo many chemical reactions and enter various domains between the atmosphere and the biosphere before they have transformed to the stable 127-isotope.

1.1.3 The relevance of iodine for the biosphere

Within plants and algae and possibly also for animals, iodine and iodine compounds have been found to protect the living organism from oxidative decay. Reactive oxygen species (ROS), which are partly converted to hydrogen peroxide, cause oxidative damage to organic cells. Iodide ions (I^-) have the ability to scavenge ROS thus preventing cell decay (Küpper et al., 1998). In the reaction of iodide with hydrogen peroxide, iodinated forms of organic substances are produced, which are harmless for the organisms. Especially organisms like brown algae accumulate iodine species in their cells and drive the environmental cycling of iodine through the emission of organic iodine species such as iodomethane. Recently, it has been discovered that the accumulated form in the algae species is actually iodide (Küpper et al., 2008).

Due to the fact that iodine species show such an importance for the biosphere, and uptake from the gaseous, liquid and solid phases as well as the emission of iodine compounds back into the atmosphere or hydrosphere takes place, one refers to the biogeochemical cycling of iodine in this respect. Both directions, the pathways from the atmosphere to the biosphere and vice versa play an important role.

1.1.4 The relevance of iodine in the atmosphere

A detailed overview of the current state of research in the field of atmospheric iodine chemistry is subject of Section 1.5. In short, iodine has an important influence in two aspects:

- Through the reaction with ozone, iodine alters the chemical composition of the atmosphere and its oxidizing capacity.

- Iodine oxides lead to the production of fine particles which may influence the radiation budget.

Most importantly, ozone molecules are destroyed in the reaction with iodine whereby iodine monoxide is formed. Although overall amounts of iodine are rather small, its relevance is enhanced by catalytic ozone destruction cycles (cp. Sec. 1.5.2). After some fundamental properties of the atmosphere are described in the next section, the considerations why ozone is important in the atmosphere are summarised in Sec. 1.3.

1.2 Introduction to Earth's atmosphere

The atmosphere of a planet is the shell around the planet's main body containing a mixture of mainly gaseous substances. While not every known planet exhibits an atmosphere, the atmospheres are unique for the respective planet. The atmosphere of the Earth exhibits an exceptional composition when compared with the atmospheres of other planets in the Solar System. Basic information on the structure and composition of the atmosphere can be found in standard text books, e.g. in Wayne (2000).

Composition of the atmosphere

The special composition of Earth's atmosphere is a consequence of the existence of life on Earth. The current state of the atmosphere in terms of thermodynamics is a steady-state disequilibrium and it is highly reactive. This state is caused by the biological processes, which are responsible for the high amount of oxygen in the atmosphere. Without life, the amount of oxygen would be 10^{13} times smaller than presently observed. Oxygen is a reactive species, so that many possible chemical reactions take place, in which the amount of oxygen is reduced, but the living organisms keep up the high oxygen concentrations continuously. Without life, all possible chemical reactions would take place until achievement of chemical equilibrium. The dry atmosphere consists to 99.9% of the main species nitrogen, oxygen and argon (O_2, N_2 and Ar), while trace species make up only 0.1% of the dry atmosphere. Table 1.1 lists the current composition of Earth's atmosphere (Wayne, 2000). The amounts are given in terms of volume mixing ratio (VMR), i.e. the volume of species considered in relation to the total volume of air. For small amounts, the short notation of parts per million (i.e. 10^{-6}, ppm), parts per billion (i.e. 10^{-9}, ppb) or parts per trillion (i.e. 10^{-12}, ppt) is commonly used.

In addition to the gaseous species, the atmosphere contains liquid or solid substances suspended in air, which are summarised as aerosols. Aerosols may have various composition, size and shape. On their surfaces, certain chemical transformations are induced. Most importantly, they influence the radiation budget, which is a result of their light reflecting and in some cases light absorbing properties. Overall, the current knowledge is that aerosols cause a negative climate forcing, i.e., on average they induce a cooling effect (IPCC, 2007). The fact that aerosols can act as cloud condensation nuclei intensifies their importance for Earth's climate state. The composition and the amount of aerosols is highly variable with time and space and their exact climate impact is yet to be determined.

The greenhouse effect

While the equilibrium temperature of the Earth's surface would be around 255K (-18°C) without the existence of the greenhouse effect, certain gases in the atmosphere such as water vapour cause a natural greenhouse effect of +33K, giving an average global surface temperature of 288 K (+15°C). The greenhouse effect is based on the solar and terrestrial radiation properties. The sun emits a modified black body spectrum with an effective temperature of about 5780 K and a spectral maximum in the visible wavelength range (cp. Sec. 1.6). Earth is an infrared emitter at its effective radiation temperature of 255 K and a spectral maximum at approximately 10 μm. Substances which don't affect the incoming solar radiation much but absorb energy in the terrestrial infrared spectral region contribute to the greenhouse effect. The most important natural greenhouse gases are water vapour, carbon dioxide and methane. Some other greenhouse gases have a much larger warming potential per molecule but are just not as abundant. The reflecting property of the Earth's surface but also of aerosols has an additional influence on the greenhouse effect. As the anthropogenic impact on climate has become apparent over the last decades and processes like global warming are taking place, large research efforts are made to better quantify the different influencing factors and

Gas species	VMR
Main species	
Nitrogen (N_2)	78.08%
Oxygen (O_2)	20.95%
Argon (Ar)	0.93%
Trace species, temporally and spatially constant	
Neon (Ne)	18 ppm
Helium (He)	5.2 ppm
Krypton (Kr)	1.0 ppm
Hydrogen (H_2)	0.5 ppm
Trace species with variable amounts, average values	
Water vapour	0-4%
Carbon dioxide (CO_2)	379 ppm (IPCC, 2007)
Methane (CH_4)	1.7 ppm

Table 1.1: Overview over the composition of Earth's atmosphere. Numbers as reported by Wayne (2000) and IPCC (2007) are given in parts per cent or per million by volume.

their interrelations.

The central species of the present study, iodine compounds, do not act as greenhouse gases themselves. However, the secondary effect of particle formation has a potential influence on the climate state (O'Dowd et al., 2002b).

The layered structure of the atmosphere

The general structure of the atmosphere is relevant for the understanding of the spatial distribution, especially the vertical location, of processes and substances. The vertical structure of the atmosphere can be described by dividing it into subsequent altitude layers, each with individual characteristics.

A typical temperature profile of the mid-latitude atmosphere (U.S. standard atmosphere) is illustrated by Fig. 1.1, showing the different layers which are determined by the temperature structure. In addition, the altitude range of the largest ozone concentration is indicated.

The main part of terrestrial life is concentrated in the lowest layers of the atmosphere. In the troposphere, which reaches from the ground up to the tropopause, the temperature typically decreases with altitude. Strong mixing processes characterise the troposphere as well as direct interactions with the other components of the Earth system (geosphere, hydrosphere, cryosphere and biosphere). This is especially valid for the so-called boundary layer, which is the sublayer closest to the Earth's surface, where friction from the surface has a major influence on the dynamics in contrast to the free troposphere above where friction can be neglected. The boundary layer (BL) therefore stands in direct contact to the surface, the oceans and to plants and animals and its composition is immediately affected by human activities. In terms of chemical composition, the boundary layer often exhibits individual properties. Several recent research studies suggest, that iodine chemistry is mainly located in the boundary layer and has negligible influence in higher altitudes.

The altitude structure varies with latitude, season and other parameters. While the troposphere
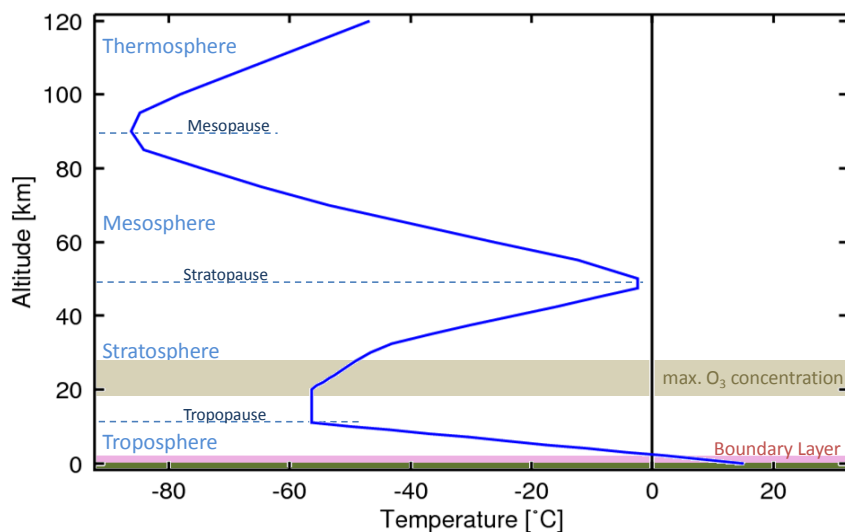
Figure 1.1: Typical temperature profile of the mid-latitude atmosphere (standard U.S. atmosphere), which determines the different layers. The temperature profile is crucially influenced by the ozone layer in the stratosphere.

has a typical height of 10 km in the mid-latitudes, it is lower at the poles (around 8 km) and higher at the equator with up to 15 km, due to large scale dynamics. The height of the boundary layer is also highly variable. In the mid-latitudes values on the order of 1 km, varying between 500 m and 2 km, are common. The structure of the atmosphere in the Antarctic is special in several aspects. Descending motions over the poles compress the layers causing a lower tropopause. Also the boundary layer is shallower with a usual thickness around 200 m.

At the tropopause, the temperature decrease from the troposphere below ceases and is slowly reverted into a temperature increase in the stratosphere above, caused by the strong absorption of solar UV radiation by ozone in the stratosphere. The stratosphere is therefore comparably stable and strong mixing is largely prohibited. Nevertheless, some mixing processes and exchange between the upper troposphere and lower stratosphere (UT/LS region) take place. In the stratosphere, the ozone mixing ratio exhibits its maximum values forming the ozone layer, which is crucial for most living organisms (cp. Sec. 1.3).

The present study mainly focuses on processes located in the troposphere. In some aspects, the higher altitudes become important nevertheless. The chemical family of the halogens (especially chlorine, bromine and iodine) are of relevance in different altitude layers. The importance of halogen species for the chemical composition has been recognized especially in connection with ozone. The most important aspects of atmospheric ozone is addressed by the following sections.

1.3 The importance of ozone

Ozone (O_3) is an important chemical in the atmosphere, especially with regard to life on Earth. The most relevant property of O_3 is its strong absorption of radiation in the ultraviolet (UV) spectral range. For UV radiation below 230 nm, the absorption by oxygen is strong enough to avoid penetration of this part of the solar spectrum down to the Earth's surface. The crucial wavelength region lies between 230 and 290 nm, where biologically important molecules would still experience severe damage and the protection by oxygen is not strong enough. Ozone happens to be the only

chemical in the atmosphere with relevant absorption in this spectral region. O_3 therefore acts as a very important UV shield. Due to its main formation and destruction pathways, O_3 shows a special altitude profile with a distinct maximum in the stratosphere.

Several pieces of information in this and the following section can be found in Wayne (2000) and Brasseur et al. (1999), other sources are cited individually.

Ozone in the stratosphere

The first scheme of O_3 formation and destruction was proposed by Chapman (1930) and was extended later due to some missing O_3 loss mechanisms. The Chapman scheme is mainly given by four reactions, the first one creating odd oxygen (O or O_3), the last one reducing odd oxygen and two with no change in O and O_3. Here and in other following reactions, M is a third body for energy and momentum transfer during collision, typically N_2 or O_2 molecules.

$$
\begin{array}{llll}
O_2 + h\nu & \rightarrow & O + O & \text{(R1)} \\
O + O_2 + M & \rightarrow & O_3 + M & \text{(R2)} \\
O_3 + h\nu & \rightarrow & O + O_2 & \text{(R3)} \\
O + O_3 & \rightarrow & 2\ O_2 & \text{(R4)}
\end{array}
$$
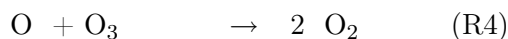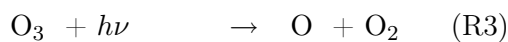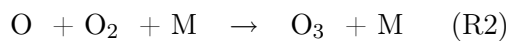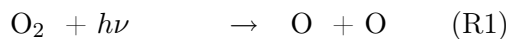
Reaction (R1) represents a photolysis reaction, where $h\nu$ is the energy of the incident photon with Planck's constant $h = 6.626 \cdot 10^{-34}$ Js and frequency ν. The rate with which a photolysis reaction takes place is determined by the concentration of the gas to be photolysed and the photolysis frequency, e.g. J_{R1}, which itself is calculated from the absorption cross section, the quantum yield and the incoming radiation.

As (R4) was found to be too slow to effect the necessary decomposition of ozone in order to balance O_3 production and to achieve agreement with observations, additional mechanisms were proposed. Basically, they follow a simple catalytic cycle, with the species A facilitating O_3 decomposition:

$$
\begin{array}{llll}
A + O_3 & \rightarrow & AO + O_2 & \text{(R5)} \\
AO + O & \rightarrow & O_2 + A & \text{(R6)} \\
\hline
\end{array}
$$

$$
\text{Net: } O_3 + O \rightarrow 2\ O_2
$$
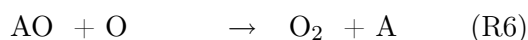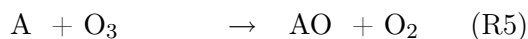
The net reaction gives the same result as (R4), but is mediated by catalyst A. The substance A does not need to be present in large amounts to be effective, because it is not consumed in the cycle and may react again in the same scheme. Species which can act in the above reactions as catalyst A include atomic hydrogen, the hydroxyl radical, nitrogen monoxide, as well as halogen atoms (H, OH, NO as well as Cl, Br and I). Depending on the altitude, these species have different importance for the O_3 loss rate. While chlorine is most influential in the stratosphere and bromine is significant in both, the stratospheric and tropospheric layers, iodine chemistry probably takes place mainly in the lowest parts of the troposphere. The overall chemical scheme for ozone is further complicated due to reactions between the different catalyst families.

While some of the catalysts exist naturally and determine the original amounts of O_3, especially the abundances of halogen species have increased due to human activity. The natural, mainly

oceanic sources of halogens are by far smaller than man made emissions from biomass burning and especially industrial activities. Especially the use of chlorofluorocarbons (CFCs) increased atmospheric burdens of chlorine before the Montreal protocol in 1987 reduced emissions of CFCs. However, large amounts of CFCs have already been emitted to the atmosphere and are eventually transported to the stratosphere. While they are extremely stable in the troposphere, CFCs are e.g. photolytically decomposed in the stratosphere and release reactive chlorine atoms forcing the rapid ozone destruction cycles.

Especially over the Antarctic in spring time, ozone columns (i.e., total ozone amounts integrated from the surface to the top of the atmosphere) nowadays dramatically reduce by typically a factor of three. Original values for Antarctic springtime O_3 columns were in the range of more than 300 Dobson units (1 DU = 2.65×10^{16} molec/cm^2, i.e., a 10 μm high column at standard temperature and pressure), while up to the end of the 20th century, springtime O_3 columns reduced to as low as around 100 DU in some years. The concentration of O_3 even drops to zero in certain altitudes. Situations with column amounts lower than 220 DU are referred to as ozone holes.

The complete mechanism of ozone destruction has been revised many times, as more knowledge on the reaction pathways, concentrations of species and more precise laboratory data became available. Up to today, the exact scheme is not fully clarified. The main reaction cycles destroying ozone in the stratosphere involve Cl atoms, and additionally the species OH and HO_2 (HO_x) as well as NO and NO_2 (NO_x) with combined catalytic reaction cycles. Furthermore, bromine cycles involving Br atoms, e.g. induced by brominated CFCs (halons) mediate ozone destruction. Levels of bromine compounds are by far lower than those of chlorine species, but the potential of ozone depletion by bromine is very large and the presence of Br atoms even enhances the effect of chlorine on ozone destruction by cross reactions.

The strong ozone loss seen in ozone hole situations requires certain surrounding conditions in addition to the presence of ozone depleting atoms and molecules. These conditions are mainly present in Antarctic spring time and include very low temperatures, the formation of polar stratospheric clouds (PSCs) and the stable polar vortex, a nearly enclosed region formed by large scale dynamics which keeps up these conditions for periods of several weeks to months. It is the surfaces of the PSCs, which provide conditions for additional heterogeneous reactions strongly enhancing the ozone loss by converting reservoir species, i.e. fairly stable, non-reactive compounds back into the active catalysts, the Cl atoms (cp. Sec. 1.4.1).

The ozone loss in the stratosphere varies from year to year depending on the meteorological and dynamic conditions. The concentrations of catalytically active species will probably further decrease in the future, but the time scale is rather large due to the long life times of the precursor substances before reaching the high altitudes.

Ozone in the troposphere

In the troposphere, ozone mixing ratios are a lot smaller than in the stratospheric ozone layer. The importance of tropospheric ozone has two aspects. On one hand, ozone poses a severe health risk to humans, animals and plants as it becomes poisonous for living cells above certain limits. On the other hand, however, ozone in the lower atmospheric layers is needed as a main producer of OH

molecules. Below 310 nm, O_3 photolyses to produce excited oxygen atoms, $O^*(^1D)$, which react with water vapour to yield OH:

$$O_3 \ + \ h\nu \quad \rightarrow \quad O_2 \ + \ O^*(^1D) \quad (R7)$$
$$O^*(^1D) \ + \ H_2O \quad \rightarrow \quad OH + OH \quad (R8)$$
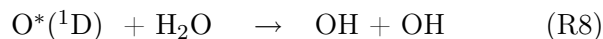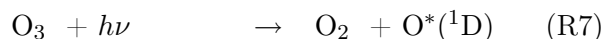
OH is a very influential molecule in atmospheric chemistry. It is extremely reactive and capable of inducing efficient oxidation processes. In this respect, OH is the most efficient agent for decomposing air pollution chemicals as it oxidises most chemicals found in the atmosphere. OH oxidises CO and CH_4, leading to the production of peroxy radicals and subsequently peroxides. Also SO_2 and NO_2 are removed from the atmosphere by reaction with OH, forming sulphuric and nitric acid, which are washed out by wet deposition.

The amount of O_3 in the troposphere is in first place determined by the NO_x ratio due to the following equilibrium reaction cycle:

$$NO_2 \ + \ h\nu \quad \rightarrow \quad NO \ + \ O^*(^1D) \quad (R9)$$
$$O^*(^1D) \ + \ O_2 \ + \ M \quad \rightarrow \quad O_3 \ + \ M \quad (R10)$$
$$O_3 \ + \ NO \quad \rightarrow \quad O_2 \ + \ NO_2 \quad (R11)$$
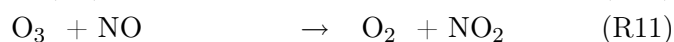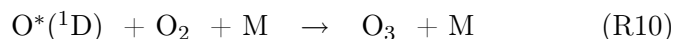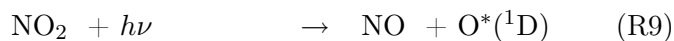
From the NO_x ratio, the photolysis frequency J_{R9} and the reaction rate coefficient k_{R11}, the equilibrium O_3 concentration may be calculated. However, the above equilibrium is disturbed by the presence of additional chemical substances, which lead to either O_3 production or destruction in the troposphere. Bromine chemistry and also iodine chemistry, e.g., reduce tropospheric ozone concentrations (Dickerson et al., 1999; Read et al., 2008). On the other hand, ozone may be effectively produced in the presence of NO_2 and peroxides (RO_2, with e.g. R=H, R=CH_3). The photolysis of NO_2 provides the necessary oxygen atoms as above, while RO_2 reaction schemes convert NO back to NO_2. In polluted regions and with an increased burden of RO_2 from organic precursors, the additional ozone production leads to the phenomenon of summer smog. The O_3 concentration limits in the European Union are 180 $\mu g/m^3$ and 240 $\mu g/m^3$ for information and warning of the population, respectively (European Parliament, 2002).

In conclusion, stratospheric ozone is essential for life on Earth, while in the troposphere its role is more ambiguous.

1.4 Halogens in the atmosphere

From the halogen family, mainly Cl, Br and I play important roles for atmospheric chemistry, while fluorine forms very stable reservoir species (especially HF), and astatine has extremely low abundances. The three relevant halogens show partially similar reactions and influences, but also exhibit some individual properties. Chlorine and bromine were earlier found to have atmospheric relevance than iodine, and some key properties of these two species shall be discussed first. Due to analogies and interactions between the different halogen types also chlorine and bromine are relevant when analysing the role of iodine in the atmosphere. Atmospheric iodine chemistry will be

addressed individually and in detail in the next section.

It was in part the detected influence of halogens on stratospheric chemistry that drove research in tropospheric halogen chemistry. To understand the atmospheric relevance of a substance and to estimate possible future changes, its sources have to be known. From emitted compounds in the troposphere, long-lived species may be transported into the stratosphere.

1.4.1 Halogens in the stratosphere

The main input of halogens to the stratosphere results from transport of long-lived CFCs or halons upwards from the troposphere where they were liberated. Additionally, short-lived compounds (or very short-lived substances, VSLS, several brominated and chlorinated carbons) were identified to contribute to the stratospheric halogen load. The halogen compounds are photolysed in the high altitudes of the stratosphere and release Cl and Br atoms. Alternatively, chemical break-up of CFCs takes place, e.g, in the reaction with the $O(^1D)$ radical (Ravishankara et al., 1993), from which ClO may be released, thereby contributing to the reactive chlorine budget (Brasseur et al., 1999). As soon as the break-up has started, a complex catalytic chemical reaction mechanism is activated. The major effect of this mechanism and hence of halogens in the stratosphere is the destruction of stratospheric ozone:

$$Cl + O_3 \rightarrow ClO + O_2 \quad (R12)$$

Subsequent recovery of the Cl atom (equivalently for Br) via different pathways leads to a catalytic cycle. One important pathway includes reactions on the surfaces of PSC particles, shortly mentioned in Sec. 1.3. PSC particles consist either mainly of HNO_3 (type I) or of H_2O-ice and some HNO_3-hydrates (type II). In both cases, a frozen or liquid aerosol core may be possible. After reaction of ClO with NO_2, chlorine nitrate forms ($ClONO_2$) which can react with HCl (from volcanic eruptions or chemical conversions) on the particle surfaces:

$$ClONO_2 + HCl \rightarrow Cl_2 + HNO_3 \quad (R13)$$
$$Cl_2 + h\nu \rightarrow 2Cl \quad (R14)$$
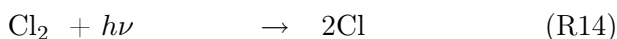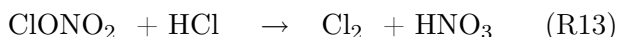
This is an important reaction, as two reservoir species ($ClONO_2$ and HCl) are converted at the same time and two reactive chlorine atoms are released that can enter (R12) again. Additional reactions which occur on PSC surfaces create a complex mechanism which is not yet completely understood. Still some rate coefficients and reaction pathways are debated.

The presence of bromine leads to ozone depletion in two ways. Br atoms directly destroy ozone, and additionally an intensification of the chlorine cycles through reactions of BrO with ClO is effected:

$$BrO + ClO \rightarrow Br + Cl + O_2 \quad (R15)$$
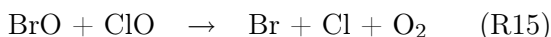
While also different product pathways are possible, this example shows how the cross reaction leads to new release of halogen radicals. When comparing the number of O_3 atoms on average destroyed per halogen atom, bromine is more effective than chlorine approximately by a factor of 50 (Wayne, 2000).

From their maximum abundance in the 1990s (for some compounds much later in the 2000s),

the amounts of several stratospheric halogen species have started to decrease slightly (WMO, 2006). Presently, the amounts of brominated species in the stratosphere lie around 18 to 25 ppt, of which 5 ppt result from brominated VSLS. Amounts of total available chlorine in the stratosphere are 3.5 ppb with the largest amount from the long-lived CFCs and smaller contribution from chlorinated VSLS (around 50 ppt) (WMO, 2006). As discussed later (cp. Sec. 1.5), the relevance of iodine in stratospheric chemistry is most probably small, maybe even negligible, but remains to some extent uncertain.

1.4.2 Halogens in the troposphere

Several sources of halogen species or halogenated compounds are known. After primary release, chemical conversions lead to formation of further substances. Halogens in general are both, of natural and anthropogenic origin.

Natural sources

One original source of natural halogen compounds are the oceans. Sea salt is rich especially in chloride (Cl^-), but also contains bromide and iodide (Br^- and I^-). The number densities are quite different though, as converted from Wayne (2000):

$$\frac{[Cl^-]}{[Br^-]} \approx 660 \ , \quad \frac{[Br^-]}{[I^-]} \approx 15000 \ .$$

Sea salt aerosols contain less bromide and chloride than expected from the respective sodium content, so direct inorganic release of halogen compounds from sea salt particles seems probable. Via photolysis, these molecules yield reactive halogen atoms. Other generally halide rich domains are soils, inland salt water lakes and salt flats.

Coastal areas and the open ocean are sources of several volatile halogenated organic compounds - such as CH_3Cl, CH_3Br and CH_3I, for example. Also polyhalomethanes (e.g., CH_2Br_2, CH_2I_2, CH_2BrI, $CHBr_2Cl$, etc.) are released by biological processes in oceans (Reifenhäuser and Heuman, 1992; Carpenter et al., 1999). While CH_3Cl and CH_3Br have relatively long life times in the troposphere and can be therefore transported to the stratosphere, CH_3I is more easily photolysed with a typical life time of several days and releases I atoms mostly in the troposphere. CH_3Cl is the largest chlorine source gas in general and originates to 10% from the oceans and to 80% from biomass burning. The remaining 10% is produced by industrial activities (Wayne, 2000). Biomass burning may also produce some CH_3I amounts (Andreae et al., 1996). Volcanic eruptions are a variable source of halogenated species. The timing, strength and duration of eruptions and degassing periods are fluctuating, and also the halogen content in the outbursts and degassing processes change and differs between individual volcanos. Emissions from volcanoes contain large amounts of hydrochloric acid, HCl, as well as other chlorine and bromine species (Francis et al., 1998; Bobrowski et al., 2003).

Anthropogenic sources

Apart from the natural sources, there is a substantial anthropogenic influence on atmospheric halogen levels. Methyl chloride from both, natural and anthropogenic sources, is present at an average mixing ratio of 0.5 ppb. The aforementioned CFCs, which are used for industrial purposes, have increased the burden of halogen species dramatically. Industrial applications include the use as refrigerants, solvents or fertilizers. Famous examples of CFCs are $CFCl_3$ and CF_2Cl_2, which carry trade names such as Freon®-11 and Freon®-12. Enormous amounts of CFCs were emitted to the atmosphere before the mid 1990s, and due to their chemical stability in the troposphere (with lifetimes longer than hundred years), the molecules are not altered before they are eventually transported up to the stratosphere and photolytically release Cl atoms.

Considering bromine, an important anthropogenic source are the halons, i.e. brominated CFCs. These compounds have been used as fire extinguishers, with CF_2BrCl and CF_3Br being the most common substances of this family. Their tropospheric mixing ratios amount to several ppt. Atmospheric methyl bromide (CH_3Br) is, apart from its natural sources, produced by human activities, e.g. by use in agriculture and by biomass burning. Current CH_3Br mixing ratios lie around 10 ppt.

Some relevant pathways

Several industrially produced chlorine and bromine species are to a high degree chemically inert in the troposphere so that they do not interfere with tropospheric composition. Others however, are to some extent photolabile also at wavelengths that reach down to the Earth's surface. CH_3Cl and CH_3Br, for example, release Cl and Br atoms also in the troposphere.

Halogens are efficient oxidants. One important example of oxidation pathways is the oxidation of gaseous mercury (Hg) by, bromine atoms, which has been observed in polar regions. The oxidated form of mercury is more easily transferred to snow and other surfaces and can be incorporated by biological organisms. Mercury is poisonous already in very small amounts, which makes this transformation a dangerous process threatening the biosphere in the affected regions.

In addition, halogens react with organic compounds, e.g., hydrogen atoms are replaced by halogens in organic carbons, forming the start of oxidation chains.

Halogen atoms react with O_3 leading to ozone loss also in the troposphere. The importance of ozone for the troposphere has been discussed above, and the destruction of O_3 has a strong influence on the chemical composition. In the mid 1980s, the connection between strong ozone depletion events (ODEs) in Polar Regions and the presence of bromine compounds (in that case of filterable bromine) has been detected at Barrow in the Arctic (Barrie et al., 1988). These events were observed in Polar Spring. In many cases, the ozone mixing ratio shows an anti-correlation with measured bromine amounts. The release and overall process of these events have not been completely resolved yet, but several mechanisms have been proposed. Mostly inorganic release processes from sea ice covered regions are considered, either from sea-ice surfaces directly, or from frost flowers, aerosols or brine (Kaleschke et al., 2004; Sander et al., 2006a; Simpson et al., 2007a; Piot and von Glasow, 2008). Possibly, the low temperatures of the aerosols or surfaces in the respective regions are important for the release mechanism. As the local amounts of bromine compounds often increase

very fast, the following mechanism has been proposed as a possible explanation for the observations.

Bromine explosion and ozone depletion events

The so-called "bromine explosion" is an autocatalytic and multi-phase (m.p.) reaction cycle causing a quick and efficient release of bromine atoms to the atmosphere, more or less directly from the sea salt content (Platt and Hönninger, 2003; Simpson et al., 2007a):

$$
\begin{array}{lll}
HOBr \;+\; Br^- \;+\; H^+ & \xrightarrow{\text{m.p.}} \quad H_2O \;+\; Br_2 & (R16) \\
Br_2 \;+\; h\nu & \rightarrow \quad 2\,Br & (R17) \\
Br \;+\; O_3 & \rightarrow \quad BrO \;+\; O_2 & (R18) \\
BrO \;+\; HO_2 & \rightarrow \quad HOBr \;+\; O_2 & (R19)
\end{array}
$$

$$
\text{Net:} \quad H^+ \;+\; Br^- \;+\; HO_2 \;+\; O_3 \quad \rightarrow \quad Br + H_2O \;+\; 2\,O_2
$$
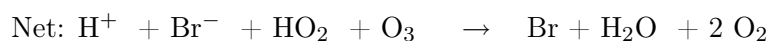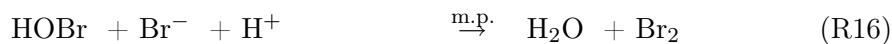
The above reaction scheme then leads to exponential increase in the concentration of BrO, which is often present at levels of several ppt (Simpson et al., 2007a). No biological processes are involved in this proposed mechanism. One important prerequisite for this cycle to happen is some sufficient acidity (involvement of H^+ ions). The crucial reaction in this scheme is the first multi-phase reaction as two inactive bromine species are converted within sea water or sea salt aerosol to Br_2, which enters the atmosphere and potentially yields two highly reactive Br atoms after photolysis. Satellite observations of BrO show that often large areas exhibit enhanced BrO amounts (Wagner and Platt, 1998; Richter et al., 1998), and these areas are connected to regions covered with sea ice (Kaleschke et al., 2004). This process occurs in a similar way on both Hemispheres, in the Arctic and the Antarctic, beginning with Polar Sunrise and lasting for some months.

1.5 Current state of atmospheric iodine research

Although iodine species are typically less abundant than chlorine and bromine species, they have received increasing attention during the last years. This is in part driven by the awareness, that large effects may arise even from small abundances, e.g., through catalytic cycles or by iodine specific pathways. The biological importance of iodine and the presence of radioactive iodine has always added to the need of understanding iodine related processes.

In some occasions, tropospheric iodine compounds have been observed at similar levels as equivalent bromine compounds, which hints at very efficient release mechanisms or even iodine specific pathways. Additionally, through cross reactions between iodine and bromine compounds which may lead to the re-release of reactive bromine atoms, the potential influence of bromine is increased.

In the past years, considerable progress has been made on the field of iodine research and in understanding the relevance of halogens, especially in the troposphere, while many open questions still remain and ask for further research efforts (Platt and von Glasow, 2005). In the following, central aspects of atmospheric iodine chemistry, some identified sources and precursors, as well as the process of particle formation and observations of iodine oxides are summarised.

1.5.1 Sources of reactive iodine compounds in the atmosphere

While iodine is a solid substance at usual atmospheric temperatures, atomic and molecular iodine (I and I_2) exist in gaseous form after release from specific precursors. Atomic iodine and iodine oxides are radicals and consequently reactive gases. One main discussion is concerned with the quantification of organic sources on one hand and inorganic pathways on the other. Although not all questions have been answered yet, large research efforts have led to an increased knowledge and understanding over the past decades.

Already in the 1970s, atmospheric abundances of methyl iodide (CH_3I) were observed by Lovelock et al. (1973) in and over the Atlantic. Measurement activities have since found CH_3I in several other locations, as well as numerous additional organoiodine compounds, e.g., diiodomethane (CH_2I_2), iodochloromethane (CH_2ClI), and propyl iodide (C_3H_7I) (Rasmussen et al., 1982; Reifenhäuser and Heuman, 1992; Schall et al., 1994). These substances are summarised as volatile organic iodine (VOI) or, equivalently, iodinated volatile organic compounds (IVOCs). VOIs are emitted, e.g., by macro-algae (Schall et al., 1994) as well as from phytoplankton (Tokarczyk and Moore, 1994; Hill and Manley, 2009) and bacteria (Amachi et al., 2001). Additionally, molecular iodine (I_2) is emitted from macro-algae (Küpper et al., 1998; Saiz-Lopez and Plane, 2004) after reaction of hydrogen peroxide with iodide. This results in formation of hypoiodous acid (HOI) which is in equilibrium with molecular iodine in sea water (Truesdale et al., 1995).

Many biogenic iodine compounds rapidly photolyse in the daytime atmosphere and release atomic iodine radicals, e.g. (CH_2I_2 + hν → CH_2I + I) or (I_2 + hν → I + I). As soon as atomic iodine is available, reaction with ozone forms iodine monoxide:

$$I \ + \ O_3 \quad \rightarrow \quad IO \ + \ O_2 \qquad \text{(R20)}$$

In several cases, observations support the connection between ground-based measurements of reactive iodine compounds and nearby algae or phytoplankton colonies (Alicke et al., 1999). The release of VOIs and molecular iodine to the atmosphere by macro- and micro-algae then leads to the availability of reactive iodine species. Incubation studies in the laboratory have confirmed the emissions of VOIs from algae to occur, e.g., as result of oxidative stress upon macro-algae (Pedersén et al., 1996). In direct comparisons, polar algae seem to exhibit higher emission rates for iodinated compounds than subtropical algae (Giese and Wiencke, 1999). A similar finding was made for micro-algae, as cold water diatoms were identified to produce iodinated organics at higher rates than temperate species (Tokarczyk and Moore, 1994; Moore et al., 1996).

Highest atmospheric amounts of VOIs were reported for CH_3I for individual occasions, on the East coast of the USA and at the Atlantic coast in France with levels as high as 3800 ppt and 1830 ppt, respectively (Lillian et al., 1975; Peters et al., 2005). For the other VOIs and more frequently also for CH_3I volume mixing ratios on the orders of 0.1-10 ppt were found, e.g. in the Antarctic (Reifenhäuser and Heuman, 1992), at the Irish coast (Carpenter et al., 1999) and at Hudson Bay (Carpenter et al., 2005).

Before 2007, hardly any information was available on the concentrations or even the fluxes of organoiodines in South polar waters. Recent measurements by Carpenter et al. (2007) conducted

in the Antarctic between 70-72°S and 9-11°W in Southern Hemispheric summer (December) then showed the presence of CH_2I_2, CH_2ICl, CH_2IBr in the water column and determined the respective fluxes to the atmosphere. This information is used for model studies in Chapter 5. Amounts are rather small in comparison to measurements in the mid-latitudes (Carpenter et al., 2001), but all examples represent point measurements under specific conditions at restricted times.

While the direct emission of these compounds from algae species constitutes an important organic source of iodine compounds, it has also been suggested that organic compounds may be released by abiotic pathways (Carpenter et al., 2005), following the reaction of HOI with humic material. Although organic material is involved, this release is not an active organic process. Considering polyhalogenated iodocarbons, CH_2I_2 and CH_2ClI have been observed in field measurements (Carpenter et al., 2005), as well as CH_2I_2, CH_2ClI and CHI_3 in laboratory studies (Martino et al., 2009).

1.5.2 Tropospheric iodine chemistry and ozone depletion

From the photolysis of organic or inorganic precursors, atomic iodine is produced. Atomic iodine undergoes a fast reaction with ozone in the atmosphere to form iodine monoxide (IO) and catalytic ozone destruction cycle in areas of iodine release may be initiated (Chameides and Davis, 1980; Solomon et al., 1994) .

Catalytic ozone destruction cycles

Several pathways may regenerate atomic iodine in catalytic cycles, for example through the reaction with other halogen oxides (X = Br or Cl, R21, R22), or alternatively HO_2 (R23) or NO_2 (R27) with subsequent photolysis.

$$
\begin{array}{llll}
I + O_3 & \rightarrow & IO + O_2 & (R20) \\
XO + IO & \rightarrow & I + X + O_2 & (R21) \\
X + O_3 & \rightarrow & XO + O_2 & (R22) \\
\hline
Net: 2\,O_3 & \rightarrow & 3\,O_2 &
\end{array}
$$

$$
\begin{array}{llll}
I + O_3 & \rightarrow & IO + O_2 & (R20) \\
IO + HO_2 & \rightarrow & HOI + O_2 & (R23) \\
 & \rightarrow & OH + I + O_2 & (R24) \\
HOI + h\nu & \rightarrow & OH + I & (R25) \\
OH + O_3 & \rightarrow & HO_2 + O_2 & (R26) \\
\hline
Net: 2\,O_3 & \rightarrow & 3\,O_2 &
\end{array}
$$

$$
\begin{array}{llll}
\text{I} + \text{O}_3 & \rightarrow & \text{IO} + \text{O}_2 & \text{(R20)} \\
\text{IO} + \text{NO}_2 + \text{M} & \rightarrow & \text{IONO}_2 + \text{M} & \text{(R27)} \\
\text{IONO}_2 + \text{h}\nu & \rightarrow & \text{I} + \text{NO}_3 & \text{(R28)} \\
\text{NO}_3 + \text{h}\nu & \rightarrow & \text{NO} + \text{O}_2 & \text{(R29)} \\
\text{NO} + \text{O}_3 & \rightarrow & \text{NO}_2 + \text{O}_2 & \text{(R30)} \\
\hline
\end{array}
$$

$$
\text{Net: } 2\,\text{O}_3 \quad \rightarrow \quad 3\,\text{O}_2
$$
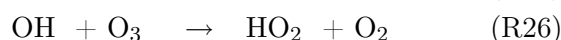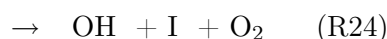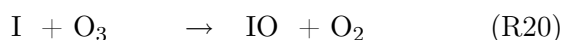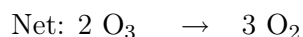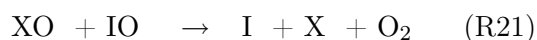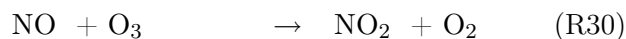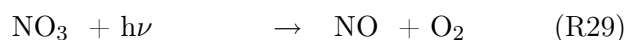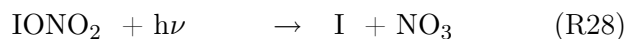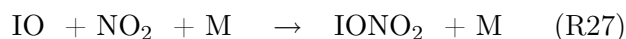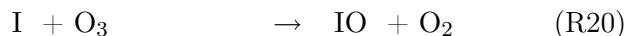
The photolysis reactions (R28) and (R29) in the last cycle may also take different pathways. In those cases, no destruction of ozone takes place as odd oxygen is recovered. This also happens in the following cycle.

Zero ozone loss

In the daytime troposphere, IO is also photolysed quickly, regenerating I atoms but also ozone, which leads to some steady state amount of IO during daytime and to no net loss of O_3:

$$
\begin{array}{llll}
\text{I} + \text{O}_3 & \rightarrow & \text{IO} + \text{O}_2 & \text{(R20)} \\
\text{IO} + \text{h}\nu & \rightarrow & \text{I} + \text{O} & \text{(R31)} \\
\text{O} + \text{O}_2 + \text{M} & \rightarrow & \text{O}_3 + \text{M} & \text{(R32)} \\
\end{array}
$$
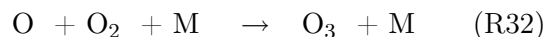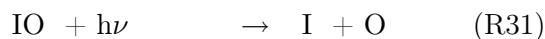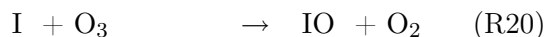
Due to the quick conversion between I and IO, the two compounds are frequently combined to the IO_x family. Although the photolytic life time of IO is small (typically on the order of minutes in the daytime atmosphere), the effective life time of reactive IO_x is much longer.

Influence of iodine on other compounds

Model studies suggest that even small amounts of iodine can play an important role in the release and recycling processes of Br atoms (Vogt et al., 1999). This may further enhance the strength and impact of bromine explosions seen in Polar Regions, and makes the catalytic ozone depletion even more effective. While the reaction of BrO with itself does not proceed at relevant rate, the cross reaction with IO leads the renewed release of atomic Br:

$$
\text{IO} + \text{BrO} \quad \rightarrow \quad \text{OIO} + \text{Br} \quad \text{(R33)}
$$

The presence of iodine in the marine boundary layer can impact on the ratios of $[\text{OH}]/[\text{HO}_2]$ and $[\text{NO}]/[\text{NO}_2]$ (Chameides and Davis, 1980). Mainly through the reaction of IO with HO_2 (R23), the $[\text{OH}]/[\text{HO}_2]$ ratio may be increased. Subsequent photolysis of HOI to OH and I amplifies this tendency even further. The $[\text{NO}]/[\text{NO}_2]$ ratio is usually decreased in the presence of iodine, as the reaction of IO with NO occurs (Chameides and Davis, 1980). Reaction (R27) can shift the effect in the reverse direction, but the overall balance depends on the relative reaction strengths.

1.5.3 Higher iodine oxides and particle formation

In coastal areas, time periods with suddenly large amounts of fine particles and aerosols in the air have been observed (O'Dowd et al., 1999). The source of these events was initially uncertain. Nucleation processes involving H_2SO_4, H_2O and NH_3 have been discussed, but it has been noticed that another formerly unknown species was needed to explain the particle growth to the sizes detected in the measurements (O'Dowd et al., 1999). Marine aerosol had been previously observed to be enriched in iodine with respect to chlorine in comparison to the relation in sea water (Duce et al., 1963). Aerosols therefore might constitute a sink of iodine under certain conditions, but may also act as temporary reservoirs releasing iodine species back to the atmosphere at a later point. Two processes may lead to high iodine amounts in particles. Iodine species are taken up by already present aerosols and additionally, the importance of iodine chemistry as a source of freshly formed particles has been recognised (O'Dowd et al., 2002b; Mäkelä et al., 2002).

In addition to field observations, laboratory studies confirm the condensation of iodine vapours to solid species. In this process higher oxides of iodine play a crucial role. Higher iodine oxides are, e.g., produced in the self-reaction of IO (Cox and Coker, 1983; Bloss et al., 2001; Gómez Martín et al., 2007). Two relevant reaction pathways are:

$$IO + IO \quad\rightarrow\quad OIO + I \qquad (R34)$$
$$IO + IO + M \quad\rightarrow\quad I_2O_2 + M \qquad (R35)$$
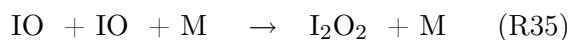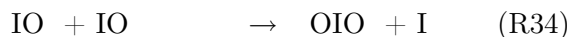
Iodine oxides may also be generated by reaction pathways between IO and other halogen oxides (ClO or BrO) or possibly by minor channels of the reaction of IO with HO_2:

$$IO + BrO \quad\rightarrow\quad OIO + Br \qquad (R33)$$
$$HO_2 + IO \quad\rightarrow\quad OIO + OH \qquad (R36)$$
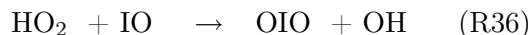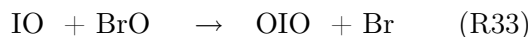
The self reaction of OIO (O'Dowd et al., 1999; Jimenez et al., 2003) is relevant and might lead to polimerisation and chain like growth to iodine oxide clusters in the following form (O'Dowd and Hoffmann, 2005):

$$OIO + OIO \quad\rightarrow\quad I_2O_4 \ \text{(or } [IO]^+[IO_3]^-) \qquad (R37)$$
$$I_2O_4 + nOIO \quad\rightarrow\quad [-I-O-IO_2-]_{1+n/2} \qquad (R38)$$
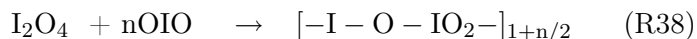
Several aspects are not well known yet, including additional pathways in the reactions above, the rate coefficients and the stability of the produced iodine oxides. In any case, higher oxides (I_xO_y, such as I_2O_4 and I_2O_5) are formed, react further with OIO, and form growing clusters which may subsequently precipitate (O'Dowd et al., 2002b; McFiggans et al., 2004; O'Dowd and Hoffmann, 2005). Some of the higher iodine oxide clusters, being acid anhydrides, are hygroscopic. The exact mechanism, by which aerosols are formed, is not yet established. However, it has been shown that the formation of higher oxides indeed results in the production of fine particles. These may then grow and act as cloud condensation nuclei (O'Dowd and Hoffmann, 2005), which impacts on the aerosol loading and potentially on the Earth's radiation budget. Iodine plays an important role in both, the homogeneous and heterogeneous chemistry of the troposphere at least locally.

One major contributor to the aerosol burden over oceanic regions independently of iodine is sulphate aerosol (Brasseur et al., 1999). The relative importance of particle formation from iodine oxides depends on the ratio of iodine to sulphate particles. Apart from volcanic eruptions and human emissions, sulphur compounds are injected into the atmosphere by marine plankton mainly in the form of dimethyl sulphide (DMS, CH_3SCH_3) as reported by Bates et al. (1992). Via oxidation by OH, DMS forms sulphur dioxide (SO_2) and subsequently sulphuric acid (H_2SO_4). Homogeneous nucleation of H_2SO_4 and H_2O (and NH_3) may lead to a direct formation of particles, while H_2SO_4 also condensates on pre-existing aerosols. DMS as precursor of sulphate aerosol is considered an important source of cloud condensation nuclei (CCN) in maritime regions (Charlson et al., 1987), which affect the global radiation budget. It is an open issue how large the potential impact of iodine particles on atmospheric CCN concentrations is in comparison to the sulphate aerosols. High concentrations of iodine particles have been observed in several occasions, e.g. by O'Dowd et al. (2002a,b), for point locations, giving valuable information on the process of particle formation from iodine oxides. More observations are necessary for the quantification of their overall importance. Observations of IO from SCIAMACHY are helpful in estimating the order of magnitude range for the iodine particle formation, which may serve as a global constraint of its potential importance (cp. Sec. 3.7).

1.5.4 Iodine in the stratosphere

As ozone levels in the lower stratosphere seemed not to be explicable by the chemistry of chlorine and bromine alone, it was thought that iodine species play a role for lower stratospheric chemistry. The influence of iodine on stratospheric ozone destruction was analysed by Solomon et al. (1994) and was found to be potentially large. Due to very efficient ozone destruction, iodine would need to be present only in comparably small amounts as compared to chlorine, for example. Solomon et al. estimated the potential effect of iodine on lower stratospheric ozone loss to be by a factor of 1000 larger as compared to chlorine. However, the overall relevance still depends on the actual iodine levels. While several studies have demonstrated the existence of iodine oxides in the troposphere above the respective detection limits (cp. Sec. 1.5.5), the abundances of iodine species in the stratosphere are not yet well known and have often remained below the detection limits.

The main reasons for iodine compounds to be less abundant in the stratosphere than bromine and chlorine species are the shorter photochemical life times and smaller amounts of iodinated precursor substances. Additionally, iodine is accumulated in aerosols which may reduce the amount of gaseous iodine species at least initially. The WMO therefore states that "it is unlikely that iodine is important for stratospheric ozone loss in the present-day atmosphere" (WMO, 2006).

Measurements of stratospheric IO are relatively sparse. Levels of stratospheric iodine monoxide were measured by balloon based instrumentation (Bösch et al., 2003) in solar occultation using the DOAS method. The observed mixing ratios remained below the detection limit of 0.1 ppt between 12 and 20 km altitude in the probed locations at several latitudes and times and also inside the Arctic polar vortex during winter. At these observed upper limits, the expected ozone destruction is not much larger than without taking iodine chemistry into account.

Recent field studies in the tropics support the findings of low iodine burdens in the upper

troposphere and lower stratosphere region, as upper limits for IO as well as for OIO remain below 0.1 ppt (Butz et al., 2009). Photochemical modelling leads to the estimate that iodine does not influence the ozone levels in these altitudes much.

A similar conclusion, that the significance of iodine for stratospheric ozone loss is most probably negligible was also drawn by Wennberg et al. (1997) after detecting small amounts of IO (<0.5ppt) by Fourier Transform Spectroscopy (FTS) from sunrise observations. Some evidence of stratospheric IO was reported on the basis of ground-based DOAS observations in Arctic regions (Wittrock et al., 2000), identifying possible mixing ratios between 0.65 and 0.8 ppt in the stratosphere.

Due to large uncertainties in the model studies, however, the estimates of the effect of certain iodine amounts on stratospheric chemistry, especially on ozone levels, are to some extent uncertain (Butz et al., 2009). In addition, the potential influence of particulate iodine is usually not taken into account, but iodine may be released from the aerosol phase back into the gas phase. Consequently, the relevance of iodine for stratospheric chemistry remains in part an open issue as it is not clearly supported by observations yet, but cannot be excluded either.

1.5.5 Observations of tropospheric iodine oxides

After the importance of iodine chemistry for tropospheric chemistry had been noticed and estimated in 1980 by Chameides and Davis, the interest in measuring iodine compounds in the atmosphere continuously increased. Especially the potential of iodine for ozone destruction is considered relevant and has been estimated in several studies. Before IO had been really observed in the atmosphere (Alicke et al., 1999), iodine species had been assumed to be present only in smaller amounts (Chameides and Davis, 1980; Solomon et al., 1994; Davis et al., 1996). Several research campaigns have been conducted to complete the picture on iodine oxides. The regions chosen for these studies are far spread and cover locations in the Arctic, the Antarctic, several mid-latitude coastal sites, and some others. An overview over tropospheric measurements of iodine oxides is given in Tab. 1.2.

In 1999, Alicke et al. have detected IO molecules during field measurements. They measured IO amounts in the marine boundary layer (MBL) at Mace Head on the Irish coast by long-path DOAS (LP-DOAS). This is an active DOAS technique using an artificial light source, typically a xenon lamp (Platt and Perner, 1980). The light beam is guided from the light source horizontally through the surface layers over a certain distance of typically several kilometers and is recorded by a spectrometer unit. By using a retro-reflector at a far point, the light emission and light detection units can be placed at the same location. The measured quantity is the volume mixing ratio of the respective trace gas averaged along the horizontal light path. Maximum IO amounts seen by Alicke et al. were in the range of 6 ppt. A connection to the tidal height was identified. IO amounts increase for low tide during solar illumination. Photolabile precursors were released by nearby macroalgae which are exposed to air during low tide. This connection has been observed several times since. The influence of iodine at these concentrations on ozone levels has been estimated by model studies to be substantial (Alicke et al., 1999). Apart from the measurements by Alicke et al., more studies were performed at the Irish coast further analysing and supporting the correlation of IO amounts with low tide, high solar illumination and precursor amounts (Carpenter et al., 1999; Allan et al., 2000; Saiz-Lopez and Plane, 2004; Peters et al., 2005). Additional MBL sites in the mid latitudes

Location	Max. amount	Reference
IO		
Mace Head, Ireland	2.4-7 ppt	Alicke et al. (1999); Carpenter et al. (1999)
		Allan et al. (2000); Saiz-Lopez et al. (2006)
Brittany, Atlantic coast, France	7.7 ppt	Peters et al. (2005)
Roscoff, North coast, France	30 ppt	Whalley et al. (2007)
Dagebüll, North Sea, Germany	1.9 ppt	Peters et al. (2005)
Sylt, North Sea, Germany	2.2 ppt	Oetjen (2009)
Teneriffe, Canary Islands	3.5 ppt	Allan et al. (2000)
Dead Sea	10 ppt	Zingler and Platt (2005)
Cape Verde Islands	1.2 ppt	average amounts, personal communication[+]
Galapagos Islands		R. Volkamer, 2009, amounts not yet published
Maldives	2.8 ppt	Oetjen (2009)
Gulf of Maine, Atlantic	4 ppt	Stutz et al. (2007)
Hudson Bay	<1 ppt	Hönninger et al. (2004)
Ny-Ålesund, Arctic	0.4 ppt	Wittrock et al. (2000); Oetjen (2009)
Cape Grim, Tasmania	2.2 ppt	Allan et al. (2000)
Neumayer Station, Antarctica	10 ppt	Friess et al. (2001)
Halley Station, Antarctica	20 ppt	Saiz-Lopez et al. (2007b)
OIO*		
Mace Head, Ireland	3-9 ppt	Saiz-Lopez et al. (2006); Peters et al. (2005)
Gulf of Maine	30 ppt	Stutz et al. (2007)
Cape Grim, Tasmania	3 ppt	Allan et al. (2001)

Table 1.2: Overview of some important measurements of iodine oxides in the atmosphere. Updated from a previous overview by Peters et al. (2005). *Allan et al. (2001) use the absorption cross section of OIO determined by Cox et al. (1999), which is a factor of 6 larger than the cross sections determined by Bloss et al. (2001) and Spietz et al. (2005), used in the studies from Peters et al. (2005), Saiz-Lopez et al. (2006) and Stutz et al. (2007), with according influence on the derived VMR. [+]unpublished results; http://www.chem.leeds.ac.uk/Atmospheric/Field/fage/iofw.html.

were explored by Allan et al. (2000), Peters et al. (2005) and Oetjen (2009), reporting IO amounts between 2 and 8 ppt. These studies used the LP-DOAS technique or the Multi-AXis-DOAS (MAX-DOAS) method. In the latter, scattered sun-light DOAS is performed with instruments designed to observe radiation at a multitude of different elevation angles, thereby potentially yielding some information on the trace gas profile (Wittrock et al., 2004; Heckel et al., 2005).

The largest amounts of iodine oxides detected so far have also been reported for a MBL location at Roscoff, situated at the French Atlantic coast, by Whalley et al. (2007) and Wada et al. (2007). Whalley et al. applied the Laser induced fluorescence (LIF) method for atmospheric IO measurements. In this in situ method, IO molecules in a restricted volume are excited with a Laser beam, e.g., within the 445 nm absorption band of the IO electronic transition (cp. Sec. 1.6.1). The intensity of the induced fluorescence is observed to determine IO mixing ratios. Largest amounts around 30 ppt were reported for cases when a short integration time of 10 s was used. At the same time and location, the first atmospheric measurements of IO by cavity ring-down spectroscopy (CRDS) have been performed by Wada et al. (2007). The CRDS method determines the damping of a laser pulse with time inside a cavity enclosed by highly reflecting mirrors at both ends. The stronger the absorption is inside the cavity, the shorter the ring-down time becomes. The ring-down times are measured on and off resonance with an IO absorption line, yielding the respective mixing ratio of IO inside the probe volume. Integrating over 30 s and probing a confined air volume, highest IO amounts exceeding 50 ppt were found by Wada et al.. However, the CRDS technique for IO has a detection limit of 10 ppt and higher with according uncertainties on the results.

The studies using LIF and CRDS nicely demonstrate the highly variable character, both with time and space, of IO amounts in the boundary layer. For longer integration times or with techniques averaging over larger spatial areas or distances, the maximum IO amounts are generally smaller. These observations in spatially confined locations have important implications for the formation of fine iodine particles. The generation of higher oxides is non-linear with IO concentration as discussed in Sec. 1.5.3. Consequently, the rate of particle formation increases strongly, if IO amounts are confined to a small region rather than the same amount of molecules being spread over a larger area.

Concerning the Arctic Polar Region, Wittrock et al. (2000) observed IO by ground-based DOAS measurements in Ny-Ålesund, Spitsbergen. Although part of the signal was assigned to small amounts of IO in the stratosphere, the behaviour of the detected absorption signal with respect to the solar zenith angle indicates the presence of some tropospheric IO in Spring time. In the South Polar Region, measurements were conducted at the Neumayer Station using scattered sun-light DOAS (Friess et al., 2001), and later also at Halley Station (Saiz-Lopez et al., 2007b) applying LP-DOAS. Reported IO mixing ratios are on the order of 10 ppt. The observed seasonal cycle is different in the two Antarctic studies. While Friess et al. (2001) find maximum amounts in summer, the IO amounts seen by Saiz-Lopez et al. (2007b) are largest in Spring time (October), where single short-term amounts of IO reach up to 20 ppt. Comparing the two Polar Regions, the IO amounts found in the Antarctic are generally larger than in the Arctic. Ground-based observations in the Canadian Arctic on the Southeast coast of the Hudson Bay (55°N, 75°W), for example, revealed BrO at levels around 30 ppt (Hönninger et al., 2004), while no IO above the detection limit of 1 ppt

was found during the same time period.

In addition to coastal and polar regions, further interesting locations for boundary layer halogen measurements are salt lakes. At the Dead Sea with its high salinity, IO amounts around 10 ppt have been observed by Zingler and Platt (2005).

The OIO molecule has so far been observed only in very few locations, for example at Mace Head with mixing ratios between 3 ppt (Peters et al., 2005) and 9 ppt (Saiz-Lopez et al., 2006) and mostly during the night. Recently, higher amounts of 30 ppt and also during the daytime have been reported by Stutz et al. (2007) for the Atlantic coast at the Gulf of Maine, USA.

There are several advantages to each of the individual measurement techniques. MAX-DOAS instruments do not need an artificial light source and may be left running self-contained also at remote sites for several years. Additionally, they yield some altitude profile information for the analysed trace gas. This passive technique can only measure during day time, while the other techniques are functional also during the night. LP-DOAS measurements observe the atmosphere over a long horizontal distance. Signals at several kilometres distances, e.g., above the ocean, may be picked up. For localised sources however, the signal is averaged over the light path and therefore reduced, so that not the peak concentrations are measured. LIF and CRDS both constitute in situ point measurements at high temporal resolution and may capture peak concentrations at confined locations if they are employed close to sources, but do not yield any information for the surrounding regions. LIF is a very sensitive technique with typically very low detection limits.

In most locations, where field campaigns were conducted, the observed IO and OIO amounts lie in the range between 0 and 10 ppt, while higher amounts are seldom and transitory. The ground-based measurements constitute a valuable basis of iodine oxide observations. They are, however, basically local measurements and cover short temporal periods. Long term global observations by satellite instruments are additionally desired to deepen the insight into amounts, distributions and variations of IO in the atmosphere. From this, the understanding of source regions and of the importance of IO shall be improved.

1.6 Atmospheric effects on radiation

Earth's atmosphere and with it life on Earth is strongly influenced by and dependent on the incoming and outgoing radiation. The solar radiation reaching the atmosphere or even the Earth's surface is a prerequisite for life and responsible for many processes, it drives photosynthesis, initializes many chemical reactions by photolysis and determines the air temperature. The Sun emits radiation which is close to that of a black body at a temperature of 5780 K. The irradiance therefore has a maximum in the visible wavelength region at about 500 nm, which may be calculated from Wien's law:

$$\lambda_{max} = \frac{2900 \frac{\mu m}{K}}{T}$$

Due to absorption and scattering in the Earth's atmosphere, the spectral maximum for the solar irradiance spectrum arriving at the surface is shifted slightly to longer wavelengths. The photon number flux at the top of the atmosphere, however, has its maximum at around 580 nm due to the inversely proportional energy-wavelength dependence. A solar spectrum measured from space

by the SCIAMACHY instrument (cp. Sec. 1.9.1) is shown in Fig. 1.2. The sharp lines in the Solar spectrum are the Fraunhofer lines and are caused by absorbing species in the Sun's photosphere and chromosphere. The strongest lines are typically labeled by Latin letters (Stöcker, 1995) as shown in brown in Fig. 1.2. The Fraunhofer G-band lies within the relevant wavelength range in some cases of the present study.
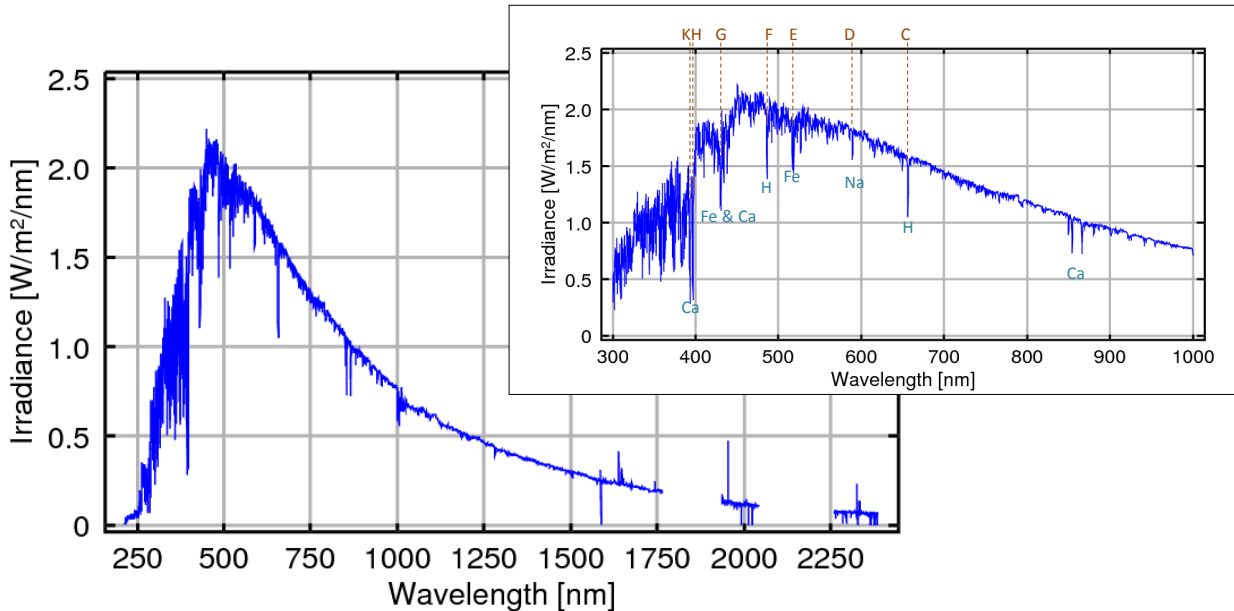
Figure 1.2: A Solar spectrum measured by SCIAMACHY covering all wavelength channels of the instrument. The spectrum has been assembled and calibrated by Jochen Skupin, IUP Bremen. The right figure is a close up of the spectrum between 300 and 1000 nm pointing out some of the Fraunhofer absorption lines with labels (brown) and the responsible atoms (blue).

On its way through the different atmospheric layers, the radiation is affected by processes like scattering at molecules and particles, molecular absorption and reflection. All these factors have to be taken into account in the calculation of radiative transfer.

1.6.1 Molecular absorption

The absorption of radiation in the atmosphere leads to several further effects. For example, a large portion of the UV spectrum is absorbed by ozone before reaching the Earth's surface protecting life from the harmful radiation, and molecules such as H_2O, CO_2, and CH_4 lead to the greenhouse effect by absorbing (and emitting) infrared and microwave radiation.

Each molecule and atom exhibits its unique spectral absorption bands. Therefore, the different species may be identified via spectroscopic measurements of the characteristic absorption structures. The absorption of chemical species in the atmosphere affects electromagnetic radiation passing through regions where the respective species is present. By analysing this radiation, conclusions on the amount of absorber substance along the light path can be drawn. As a crucial prerequisite for the retrieval of a trace gas amount by optical means, the wavelengths of some absorption structures need to be covered by the measurement device.

In general, absorption of light is accompanied by the excitation of the absorbing molecule. From the initial energy state a transition to a higher energy level takes place. Three different types of transitions are distinguished, which are electronic, vibrational and rotational transitions. During an electronic transition, the quantum numbers describing the electronic energy state of the molecule change, i.e., the molecular orbitals of the electrons and the overall wave function will change. The energy of electronic transitions corresponds to radiation in the UV, the visible or the near IR wavelength region depending on the participating levels and the electronic structure of the respective molecule. Vibrational or rotational transitions describe the change of vibrational or rotational states, vibrational transitions have energies corresponding to IR radiation, rotational transitions correspond to wavelengths in the microwave range.

If the photon energy absorbed by a molecule exceeds a certain limit, the dissociation energy, the molecule may break apart into two fractions, i.e., the molecule is photolysed.

Energy structure of a diatomic molecule

The energy states of a molecule are calculated from the Schrödinger equation (Demtröder, 2000) with several modifications in comparison to atomic energy states. The differential Schrödinger equation determines the behaviour and especially the energy states of particle wavefunctions, which describe the particle's properties such as the spatial probability distribution. Solutions of the Schrödinger equation are Eigenfunctions of the Hamilton-Operator, describing the total energy of the system, with Eigenvalues giving the possible energy states.

For a diatomic molecule, a set of quantum numbers Q specifies the energy Eigenvalues $E_Q(r)$, which are not constant as for atoms but additionally depend on the internuclear distance r between the two involved atoms. $E_Q(r)$ is a molecular potential curve in the Born-Oppenheimer approximation, after which the motions of the comparably heavy nuclei can be separated from that of the electrons, and the wave functions of the electrons are calculated for a given internuclear distance r. Vibrations and rotations of a molecule involve the movement of the nuclei. These motions need to be considered in the Schrödinger equation and lead to new quantum numbers in comparison to atomic states. Which quantum numbers are used for the description of the molecular state, depends on the structure of the molecule, i.e., on the strength of the individual momenta. Important quantities in this respect are the electronic orbital momentum (as a sum over all electrons) $\mathbf{L}$, the electronic spin $\mathbf{S}$, the nuclear rotational momentum $\mathbf{R}$ as well as the total angular momentum $\mathbf{J}$. In addition to the principal quantum number n, the magnitudes as well as the projections of the momenta onto the internuclear axis yield relevant quantum numbers. These are, e.g., the projection Λ of $\mathbf{L}$ and the total angular momentum J from $|\mathbf{J}|^2 = \hbar^2 J(J+1)$, with $\hbar = \frac{h}{2\pi}$ the reduced Planck constant. In addition, υ is used to define the vibrational state.

The molecular potential can describe bound states as well as instable molecular states, depending on whether or not the curve exhibits an energy minimum. As soon as the nuclei begin to move considerably, their energy contributes to the overall molecular energy.

Vibrational energy

The wave functions of vibrational states mainly depend on the shape of the molecular potential. If this was a parabola, the vibrations would be that of a harmonic oscillator. However, the shape is not harmonic but distorted with a stronger energy increase for converging nuclei than with growing distance. For $r \to 0$, the energy needs to grow to infinity, while for $r \to \infty$, the energy converges against the value D, which is the sum of the dissociation energy and the zero-point energy. The dependence of the potential energy curve $V(r)$ on the internuclear distance r of a diatomic molecule can mathematically be approximated by the Morse Potential, an empirical formula, where r_0 is the equilibrium bond distance, and a a form factor:

$$V(r) \;=\; D \cdot (1 - \mathrm{e}^{-a(r-r_0)})^2. \tag{1.1}$$

Figure 1.3 shows a schematic of the electronic transitions between different vibrational levels in a diatomic molecule. The potential energy curves were calculated with the Morse Potential formula. The positions of the vibrational levels and the distance between the two Morse potential curves are not exactly to scale, the vibrational levels would lie closer to each other. As the potential is not harmonic, the distance between subsequent vibrational energy levels is not constant but decreases with increasing v. The solutions of the Schrödinger equation for the Morse potential yield the energies of the vibrational states E_{vib} with angular frequency ω:

$$E_{vib} = \hbar\omega \left(v + \frac{1}{2} \right) - \frac{\hbar^2 \omega^2}{4D} \left(v + \frac{1}{2} \right)^2 \tag{1.2}$$

Rotational energy

If the internuclear axis and distance r is kept fixed, rotations around this axis can be considered and the energies E_{rot} are calculated in analogy to classical rotations from the moment of inertia I and the total angular momentum $\mathbf{J}$:

$$E_{rot} = \frac{\mathbf{J}^2}{2I}.$$

Inserting the absolute values for $\mathbf{J}^2 = J(J+1)\hbar^2$, and the constant value $B = \hbar/(4\pi c M r_0^2)$, with the nuclear reduced mass M, the speed of light c and equilibrium distance r_0, the equation reads:

$$E_{rot} = hcB \cdot J(J+1) \tag{1.3}$$

The wavenumbers of rotational emission or absorption lines would increase linearly with J from this equation, and the distances between adjacent lines would be constant. In reality, the internuclear distance slightly increases during rotation, thereby reducing the rotational energy. Therefore, the energies are slightly lower than given by the simple approximation. Energies of rotational excitations are not observed directly in the present study, as spectroscopy in the visible spectral region is performed. Indirectly, rotational energy levels play an important role for the analyses here, as rotational Raman scattering at N_2 and O_2 causes filling-in of Fraunhofer lines in all DOAS mea-
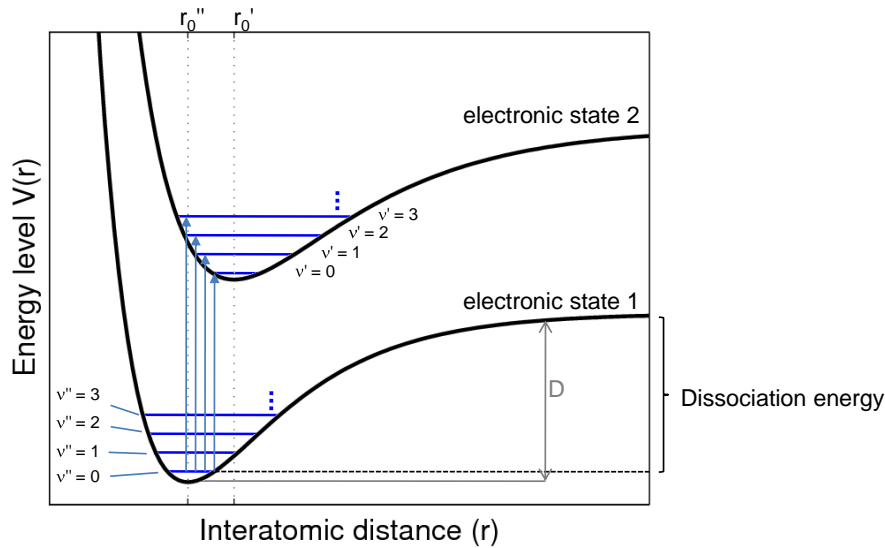
Figure 1.3: Schematic energy band diagram of a diatomic molecule showing two electronic states with several vibrational levels each (distances not exactly to scale). The shape of the energy curves is determined by the Morse-Potential formula, Eq. 1.1. The arrows indicate absorption transitions of the type used for the detection of IO from the lowest vibrational state (v"=0) of the electronic ground level to the different vibrational levels (v'=0,1,2,3...) of the first electronically excited state. The equilibrium bonding distances are denoted with r_0'' and r_0' for the ground and excited states, respectively.

surements of scattered sunlight. The effect of Raman scattering on the measured spectra will be discussed in Sec. 1.6.3.

The absorption spectrum of IO

The specific absorption bands utilised in the measurement and retrieval process belong to the electronic transition from the IO ground state $X_{3/2}^2$ to different vibrational levels of the first electronically excited state $A_{3/2}^2$. The respective absorption cross section for this transition is shown in Fig. 1.4. The shape of the vibronic (vibration-electronic) absorption lines is influenced by the various underlying rotational lines, which are not resolved in this measurement. The invisible substructure causes the lines to broaden. Transition probabilities and also the occupation numbers governed by the Boltzmann distribution determine the magnitude of the bands.

The spectrum was recorded with a FWHM (full width at half maximum) value of 0.07 nm (Spietz et al., 2005; Gómez Martín et al., 2005). The IO absorption cross section reveals an extraordinarily strong differential structure in the wavelength range around 400-460 nm. The presence of several sufficiently narrow peaks in the cross section of IO is crucial for the applicability of the utilised spectroscopy method. For the retrieval of a trace gas amount, broad-band absorption structures are not considered, but only comparably narrow ("differential") features are analysed. The measurement technique will be described in detail below in Sec. 1.8. It is important to note the order of magnitude of the cross section which is 10^{-17} cm^2/molecule, and therefore exceptionally large. In comparison, the differential parts of the cross sections of NO_2 or O_3 obtain an order of magnitude of maximum

10^{-19} cm^2/molecule. If the IO absorption was only that strong (weak), and given the typically observed amounts, it could not be observed from space by the currently available instrumentation.
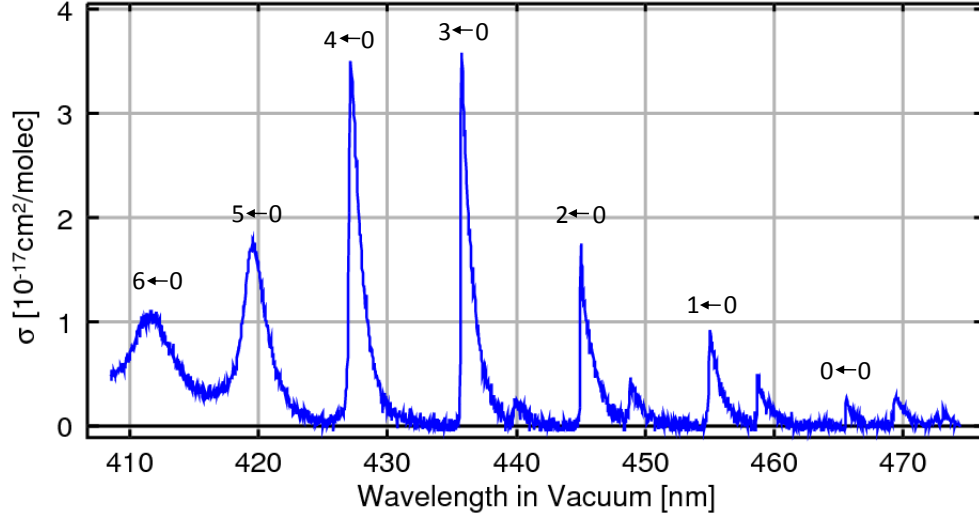
Figure 1.4: Measured spectrum of the absorption cross section σ of IO (Spietz et al., 2005; Gómez Martín et al., 2007) with a resolution of 0.07 nm. Several transition bands from the ground state to the first electronically excited state ($A^2_{3/2} \leftarrow X^2_{3/2}$) and different vibrational states ($v' \leftarrow v''$) can be identified, causing a strong differential structure.

1.6.2 Elastic scattering

Radiation in the atmosphere is scattered at molecules and particles. Scattering processes are divided into two fundamentally different types, i.e., elastic scattering events in which the photon energy remains unchanged, and inelastic processes where the photon gains or loses energy during the interaction.

Depending on the size d ($\sim$diameter) of the scattering object in relation to the wavelength λ of the incoming electromagnetic radiation, the elastic scattering is referred to as Rayleigh scattering ($\lambda \ll d$) or Mie scattering ($\lambda \geq d$). In the Rayleigh approximation, the shape and material of the object does not play a role and is neglected in the calculations. The size relation influences the phase function of the scattering process. The phase function determines the dependency of the scattering probability of the scattering angle (θ), which is measured with respect to the direction of incoming radiation. For Rayleigh scattering in case of an assumed point-like scatterer, the relation is relatively simple:

$$P_{Ray}(\theta) \;=\; \frac{3}{4} \cdot \left(1 + \cos^2(\theta)\right),$$

while for larger and more complicated structures of the scattering objects, the phase functions become stronger structured. Already for Mie scattering, which considers spherical particles, the phase function is no longer symmetric, but forward scattering ($\theta=0°$) is preferred.

The scattering cross section σ_{scat} of a scattering object (atom, molecule, particle) is defined as

the ratio of the power of the scattered radiation per object and the incoming light intensity. The unit therefore is $[\sigma_{scat}] = \mathrm{m}^2$.

The Rayleigh scattering cross section for a scattering atom or molecule for a wavelength $\lambda = 2\pi c/\omega$ is given by:

$$\sigma_{Ray} = \frac{e^4}{6\pi\varepsilon_0^2 c^4 m^2} \cdot \frac{\omega^4}{(\omega_0^2 - \omega^2)^2 + \omega^2\gamma^2},$$

where e, ε_0, c, and m are physical constants denoting the electric charge unit, the dielectric constant, the speed of light and the electron mass, respectively. The parameters γ and ω_0 describe the attenuation coefficient and the resonance frequency, which depend on the individual atom or molecule. For typical scattering molecules in the atmosphere (N_2, O_2 etc.), the resonance frequencies lie in the far UV spectral range, so that for visible (and near UV) radiation the approximations $\omega \ll \omega_0$ is well fulfilled. Therefore, all terms in the denominator except for the constant term ω_0^4 can be neglected and the wavelength dependency of σ_{Ray} becomes:

$$\sigma_{Ray} = \frac{e^4}{6\pi\varepsilon_0^2 c^4 m^2 \omega_0^4} \cdot \omega^4 \propto \lambda^{-4}.$$

This wavelength dependency becomes relevant in several considerations of atmospheric radiation transport. The scattering cross section of larger and possibly structured particles exhibits a less prominent wavelength dependency.

1.6.3 Raman scattering

In contrast to the elastic scattering processes described in the previous section, Raman scattering at atoms and molecules causes a wavelength shift of the scattered photon and the process is inelastic. More precisely, a photon is absorbed by an atom or molecule, which passes over to a virtual (or real) level for a short time. The state of the molecule then relaxes back into a vibrationally or rotationally excited level of the electronic ground level. During this relaxation, a new photon is emitted. The energy difference between the incident and emitted photon, consequently, is the difference between the ground level energy and the rotationally or vibrationally excited level (see also Fig. 1.5). The spectrum of the outgoing photons consists of several peaks resulting from the different discrete excitation levels. These spikes are called the Stokes lines. If the atom or molecule initially was in a vibrationally or rotationally excited level, and the relaxation leads back to the ground level, the emitted photon has a higher energy than the incident one. The resulting spectrum consists of the so-called Antistokes lines. The line structure of the Raman scattering cross sections for scattering at N_2 and O_2 molecules is demonstrated in Fig. 1.6. The positions and intensities are determined by the energy levels (Eq. 1.3) and the individual transition probabilities.

This inelastic process has important effects on the spectrum of scattered sun light as compared to direct sunlight. Basically, scattering of a photon of a certain wavelength occurs with a probability proportional to the intensity present at the respective wavelength. Due to the presence of strong and narrow absorption features like the Fraunhofer lines, rotational Raman scattering (RRS) at air molecules strongly changes the spectrum of scattered sun light. In these wavelength regions, the scattering at the spectral sides of Fraunhofer lines, where the intensity is relatively high, is
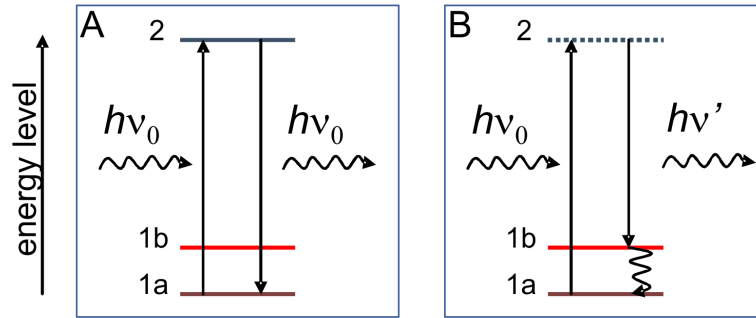
Figure 1.5: The difference between elastic scattering (A), where the outgoing photon has the same energy as the incident, and the inelastic Raman scattering, where the emitted photon has longer or shorter wavelength than the absorbed photon (B). In the Stokes case, the atom or molecule is left over in an excited vibrational or rotational state (1b). The initial level (1a) is energetically lower. In the Raman process the excited level (2) can be a virtual level.
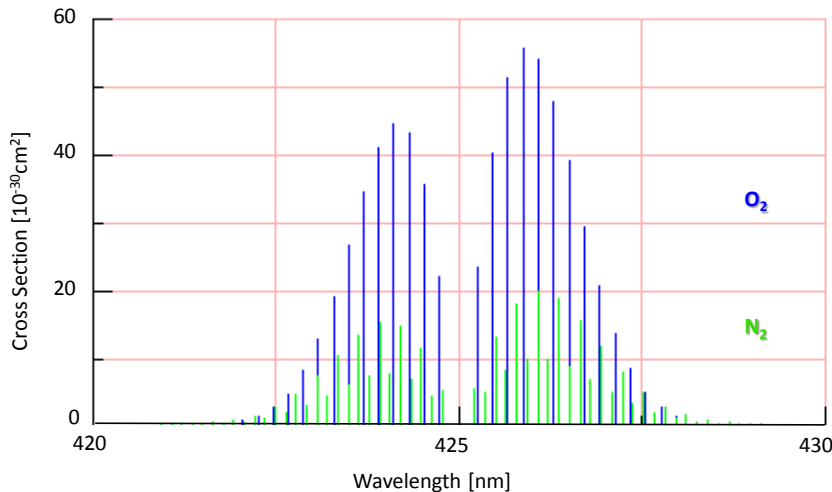
Figure 1.6: Raman spectrum for N_2 (green) and O_2 (blue) for an incident wavelength of 425 nm showing the Stokes ($\lambda > 425$ nm) and Antistokes ($\lambda < 425$ nm) lines. The spectrum was calculated using a programme by Marco Vountas available at http://www.iup.uni-bremen.de/~vountas/ Ring/AIR.html, see also Vountas et al. (1998).

more probable than for wavelengths within the Fraunhofer lines. Therefore, a certain number of photons scatters from the sides of the Fraunhofer lines into the wavelength region within the lines, and far less photons from within the lines scatter to longer or shorter wavelengths. As a result, the Fraunhofer lines appear less deep and strong in the scattered sunlight as compared to direct sun light. Calculations for this effect are presented in connection with the DOAS retrieval method in Sec. 1.8.

The process of filling-in of the Fraunhofer lines has been discovered by Shefov (1959), Grainger and Ring (1962). It was then termed the *Ring effect* and was explained only later as resulting mainly from inelastic Raman scattering (Brinkmann, 1968). This filling-in of absorption lines can be observed not only for the Fraunhofer structures but also for strong absorptions in the Earth's atmosphere, such as from ozone. After considerable absorption has taken place, e.g. within the ozone layer, and the pronounced absorption bands appear, inelastic Raman scattering causes a noticeable filling-in of these structures. The exact shape of the resulting spectrum depends on many parameters, such as the main scattering molecules and their energy level structures.

The rotational Raman scattering on air molecules leads to wavelength shifts on the order of a few nanometers. Additionally, vibrational Raman scattering (VRS) at liquid water molecules, e.g., in oceans takes place. In locations over water bodies, sun light enters the water, travels a certain distance and may be scattered back towards the satellite instrument. On the way through the ocean water, vibrational Raman scattering leads to infilling of absorption lines due to the same principle as in the atmosphere and may influence atmospheric absorption measurements (Vountas et al., 2003). The difference between RRS and VRS effects lies in the resulting spectral structure, as the typical distance between vibrational energy levels leads to wavelength shifts on the order of several tens of nanometers.

1.7 Radiative transfer in the atmosphere

1.7.1 Description of radiative transfer

Radiative transfer equations (RTE) calculate how light travels through the atmosphere, considering in principle all processes of absorption, scattering, reflection, refraction and emission. All radiation input and losses at a certain altitude and direction need to be calculated considering both, direct and diffuse parts of the light. Losses are caused by absorption and scattering of the direct and diffuse radiation, the source of radiation is the scattering into the respective altitude and angle as well as the reflection at the Earth's surface. Emission processes are negligible in the UV and visible wavelength regions and therefore not relevant for this study. These processes result in the change of the intensity of diffuse radiation I with altitude z:

$$\mu\frac{dI(\lambda)}{dz} = -I(\lambda, z) \cdot \varepsilon(\lambda, z) + Q(I, \lambda, z) + R(I, \lambda, z) \tag{1.4}$$

$$\mu\frac{dI(\lambda)}{dz} = -I(\lambda, z) \cdot \left(\sum_i \sigma_i(\lambda, z) \cdot \rho(\lambda, z) + \sigma_{Ray}\rho_{Ray}(z) + \sigma_{Mie}\rho_{Mie}(z) \right)$$
$$+ Q(I, \lambda, z) + R(I, \lambda, z) \tag{1.5}$$

where the sum runs over all chemical species i, and the other variables have the following meanings:

$I(\lambda, z)$	-	radiation intensity at a certain wavelength λ and altitude z
ε	-	extinction coefficient combining absorption and scattering effects
$\sigma_i, \sigma_{Ray}, \sigma_{Mie}$	-	cross sections of molecular absorption, Rayleigh and Mie scattering
$\rho_i, \rho_{Ray}, \rho_{Mie}$	-	densities of absorbing molecules, Rayleigh and Mie scatterers
μ	-	the cosine of the zenith angle θ
Q	-	integral source term describing radiation gain from elastic scattering
R	-	integral source function for radiation from Raman scattering

The source term Q contains three terms which describe the single scattering of the direct radiation from above, the single scattering of the direct radiation which has been reflected at the Earth's surface, and a term for multiple scattering, i.e., scattering of the diffuse radiation I_k. For the reflection at the ground in the second term, a Lambertian surface is assumed with a spectral

reflectance $\alpha(\lambda)$ (albedo). The solar zenith angle θ_0 is taken into account by $\mu_0 = 1/\cos(\theta_0)$. For simplicity, the wavelength dependence is denoted by a subscript for the wavenumber k.

$$
\begin{aligned}
Q_k(z, \mu, \phi) \;=\;& \frac{b_k(z)}{4\pi} F_k \exp\left(-\frac{\tau_k(z)}{\mu_0}\right) P(\gamma_0, z, \gamma) \\
& + \frac{b_k(z)}{4\pi} \alpha_k \mu_0 F_k \exp\left(-\frac{\tau_k(0)}{\mu_0}\right) \int_\Omega d\gamma' P(\gamma', z, \gamma) \exp\left(-\frac{\tau_k(0) - \tau_k(z)}{\mu'}\right) \\
& + \frac{b_k(z)}{4\pi} \int_\Omega d\gamma' P(\gamma', z, \gamma) I_k(z, \gamma')
\end{aligned}
$$

The two direct terms contain the solar flux F_k at the top of the atmosphere (z_0) and the optical depth $\tau_k(z)$ of the atmosphere between z_0 and z: $\int_{z_0}^{z} \varepsilon_k(z')dz'$. The integrals run over the solid angle Ω and integrate over the contributions of direct and diffuse radiation scattered according to the phase function P from zenith and azimuth angles $(\mu', \phi') = \gamma'$ into angles $(\mu, \phi) = \gamma$. All source terms are proportional to the altitude dependent scattering coefficient $b_k(z)$.

The Raman scattering term R contains the contributions (energy redistributions) from Raman scattered photons. The terms making up R are equivalent to the terms in Q with some modifications:

1. The elastic scattering coefficients b_k need to be replaced by rotational Raman scattering coefficients $b_{j,i}^{RRS}$ for a scattering process involving a wavelength shift $\lambda_i \leftarrow \lambda_j$.

2. For the calculation of I_k at λ_i, the direct and diffuse radiation at all neighboring wavelengths λ_j need to be considered, and an integration (practically a summation) over the respective spectral region is performed.

3. The phase function P is replaced by the phase function of Raman scattering P^{RRS}.

Due to the dependence of Q (and R) on the diffuse radiation $I(z, \gamma)$ in the last part of multiple scattering, the RTE becomes a differential-integral-equation, for which numerical solution methods are necessary. The radiative transfer programming code applied within the scope of this work is the Sciatran model (Rozanov et al., 1997, 2005b), which has been developed at the University of Bremen.

1.7.2 The SCIATRAN radiative transfer code

Sciatran is a radiative transfer code, in which numerical integration of the RTE (Eq. 1.4) is implemented. The calculation can be done in different degrees of complexity, for example considering the amount of involved scattering events. In the applied model runs in this study, multiple scattering is taken into account. Concerning the curvature of the Earth's atmosphere, different approximations are possible. In the full spherical mode, refraction in the atmosphere is taken into account, while this is neglected in the simple plane-parallel approximation. The pseudo-spherical mode considers refraction only for the direct radiation, but not for the diffuse parts, and also takes into account the altitude dependence of the radiation zenith angle.

Different versions of Sciatran are available with individual advantages. Some versions contain improvements above former ones. However, in the latest versions, inelastic Raman scattering is not yet implemented as an additional effect on the transported radiation (neglect of the terms

contained in R). Intensity spectra including the effect of Raman scattering need to be calculated with SCIATRAN Version 1.2.

The solution of the RTE uses the following approach. In a first step, a variable separation is performed for the azimuthal dependence of the intensities and phase functions. For this, the scattering phase functions need to be developed into a sum of Legendre polynomials and the intensities are rewritten as Fourier series. Furthermore, the approach of finite differences is applied which transforms the integrals into sums. Gradients of quantities $\frac{dX}{dz}$ will be turned into finite differences $\frac{\Delta X}{\Delta z}$ between two altitude levels. In addition to the altitude, also the angles are discretised. Within a given discrete step of these variables the depending functions are taken to be constant. The chosen altitude grid will influence the accuracy but also the time consumption of the computations.

Before a model run can be started, the atmospheric state and the geometry of interest needs to be defined. This includes, e.g., the viewing geometry (from a satellite or ground-based point of view), the viewing angles and the underlying surface albedo. Aerosol properties (models, amounts, profiles) can be defined and altitude profiles of trace gases as well as temperature and pressure profiles are needed. Absorption cross sections of considered trace gases and a high resolution solar input spectrum need to be provided. For the latter, the Fraunhofer atlas by Kurucz et al. (1984) is used.

Within the present study, the SCIATRAN code has been used for several calculations:

- The computation of the Ring effect (cp. Sec. 1.6.3) was performed using SCIATRAN Version 1.2. A reference spectrum describing this effect is needed for the DOAS retrieval routine and will be explained in detail in Sec. 1.8.2. To determine the spectral structure of the Ring effect, the intensity at the position of the satellite is calculated twice by SCIATRAN, once including Raman scattering and once without.

- Calculations of total as well as altitude dependent light path enhancements (air mass factors) through certain trace gas layers in the atmosphere are performed using SCIATRAN Version 2.0. The concept of the air mass factor is described within the next section. Results of the calculations are presented in section 2.3 and 2.4 and used for relevant discussion purposes.

1.8 Differential Optical Absorption Spectroscopy

For the retrieval of trace gas amounts, the technique of Differential Optical Absorption Spectroscopy (DOAS) is a useful and well established remote sensing method which has been developed and improved over the last decades (Noxon, 1975; Platt and Perner, 1980; Solomon et al., 1987; Platt and Stutz, 2008). It was first used for measurements conducted with ground-based instruments, but can also be applied when observing the atmosphere from space (Burrows et al., 1999b). The DOAS method makes use of the individual absorption characteristics of molecules on the mathematical basis of Lambert-Beer's absorption law:

$$I = I_0 \cdot \exp\left(-\sigma\rho \cdot L\right). \tag{1.6}$$

I_0 and I are the light intensities of a direct light beam before and after passing through a region of length L containing molecules with absorption cross section σ and concentration ρ.

The fundamental difference between typical radiative transfer calculations and the point of view in the DOAS method is the way how the light is traced through the atmosphere. While the RTE considers an altitude grid parallel to the Earth's surface and integrates over all losses and gains at each grid point, the DOAS equation will in the basic step integrate the radiation affecting processes along the individual light path, which might be in first place largely unknown. Therefore, the typical vertical integration over the altitude z is replaced by an integration along the slant light path S with increments ds. Approximations of the average light path can be done in a second step. This way, the spectroscopic influences on radiation and the radiative transfer itself are separated. DOAS type measurements can be conducted either using an artificial light source (active DOAS, e.g. with xenon arc lamp) or the sun as natural light source (passive DOAS). In the latter case, either the sun is observed directly or the atmosphere is viewed in a different direction, monitoring scattered sun light. In the present study, scattered sun light is used as light source. In contrast to the active DOAS and the direct sun methods, the light path here is complex due to scattering events. The properties of the radiation arriving at the instrument is a weighted average over all possible light paths through the atmosphere. The starting point now for the development of the DOAS equation reads:

$$\frac{dI(\lambda, s)}{ds} = -I(\lambda, s) \cdot \varepsilon(\lambda, s) \tag{1.7}$$

1.8.1 The DOAS equation

For real measurements in the Earth's atmosphere, it is mostly not possible to measure I and I_0 as described above, where the two quantities only differ in the absorption structures from one special trace gas. Usually, two measurements are compared where both carry multiple spectral signatures from atmospheric processes. Ideally, the I_0 spectrum, also called the background spectrum or generally the reference spectrum, is at least not affected by the trace gas of interest.

In the DOAS method, molecules are identified by the differential part σ' of the absorption cross section instead of by the absolute magnitude which makes the separation of spectral absorption and scattering influences possible. All broad-band spectral structures are neglected for the identification process and only the spectral features of higher frequency are considered. The spectral resolution needs to be high enough to resolve these structures. While some other absorption methods use, e.g., only three distinct wavelength positions for analysis (Brewer et al., 1973), the present DOAS method works with a wavelength window at moderate spectral resolution typically on the order of 0.1-1 nm. All broad band influences on the light spectrum are modelled by a polynomial of suitable degree, a procedure which can be regarded as high pass filtering of the spectrum.

For the task of measuring atmospheric absorbers under atmospheric conditions by using scattered sunlight, the initial simple form of Lambert Beer's absorption law is modified in several aspects:

- In most cases, there will be more than one substance present along the light path with absorption features in the same wavelength region. The extinction term has to be extended to

a sum over all relevant absorbers i with individual absorption cross sections σ_i and densities ρ_i.

- For scattering at objects of different sizes (i.e., molecules or particles), the two scattering modes Rayleigh and Mie scattering have to be considered (cp. Sec. 1.6.2). Their wavelength dependency is essentially smooth, so that when concentrating the analysis on a small wavelength window of typically around 20-50 nm width, the spectral influence of scattering can be well described by a polynomial.

- Also the broad band part σ^b of the absorption cross sections $\sigma = \sigma^b + \sigma'$ will be described by a polynomial. All occurring spectrally broad band functions independent of their origin will be summarised and approximated by one polynomial of order p.

- Molecular absorption cross sections normally are pressure and temperature dependent. With changing altitude above the Earth's surface, therefore, the cross sections of atmospheric species might change. Then more than one cross section needs to be considered per trace gas. In some cases though, especially in the visible spectral region, this can often be neglected.

- Most of the parameters and values in the equation are wavelength dependent. This is sometimes not written explicitly but needs to be kept in mind.

These modifications will now be implemented in the DOAS equation and the integration along the light path S from location L_0 to L_1 is performed:

$$
\begin{aligned}
\frac{dI(\lambda)}{ds} &= -I(\lambda) \cdot \left(\sum_i \sigma_i(\lambda, s) \cdot \rho_i(\lambda, s) + \sigma_{Ray}\rho_{Ray}(s) + \sigma_{Mie}\rho_{Mie}(s) \right) \\
\Rightarrow \quad \ln I|_{L_0}^{L_1} &= -\int_S ds \left(\sum_i (\sigma_i'(\lambda, s) + \sigma_i^b(\lambda, s)) \cdot \rho_i(\lambda, s) + \sigma_{Ray}\rho_{Ray}(s) + \sigma_{Mie}\rho_{Mie}(s) \right) \\
\Rightarrow \quad \ln\left(\frac{I_0}{I_1} \right) &= \int_S ds \left(\sum_i \sigma_i'(\lambda, s) \cdot \rho_i(\lambda, s) \right) + \sum_{k=0}^{p} a_k \lambda^k.
\end{aligned}
\tag{1.8}
$$

In case the absorption cross sections are largely independent of position s they can be detached from the integral. The remaining term is substituted by $SC := \int_S \rho_i(\lambda, s) ds$, where SC is called the slant column and is given in molecules per cm^2.

$$
\ln\left(\frac{I_0}{I_1} \right) = \sum_i \sigma_i'(\lambda, s) \cdot SC_i + \sum_{k=0}^{p} a_k \lambda^k.
$$

As the above equations only consider the ideal case, differences between measurement and theory still need to be taken into account. In any case, the measurements are affected by noise, which can not be calculated. The above considered measured optical depth $OD = \ln\left(\frac{I_0}{I_1} \right)$ needs to be replaced by the fitted, theoretical optical depth OD_{fit} which differs from the measurement by the left-over signals $r(\lambda)$:

$$\ln\left(\tfrac{I_0}{I_1}\right)(\lambda) \quad \rightarrow \quad OD_{fit}(\lambda)$$

$$\ln\left(\tfrac{I_0}{I_1}\right)(\lambda) \quad = \quad OD_{fit}(\lambda) + r(\lambda)$$

$$\Rightarrow \quad \ln\left(\tfrac{I_0}{I_1}\right)(\lambda) \quad = \quad \sum_i \sigma_i'(\lambda, s) \cdot SC_i + \sum_{k=0}^{p} a_k \lambda^k + r(\lambda). \tag{1.9}$$

The slant column amounts SC_i and the $p + 1$ polynomial coefficients a_k are the main retrieval parameters being adjusted in the DOAS fit routine to yield the best fit result OD_{fit}, as close as possible to the measured OD. The best parameters are determined in the fit routine by the request:

$$\text{Minimise}(\delta), \quad \text{with } \delta \; := \; \sum_j r_j^2$$

The sum runs over all wavelength positions j of the instrument detector included in the spectral fitting window. The above equation represents the quality criterion of a least squares fit. The difference spectrum $r(\lambda) = (OD - OD_{fit})(\lambda)$ is called the residual spectrum and is of central importance in the improvement processes of a retrieval. The success of a retrieval is in part judged by the magnitude of δ and the appearance of the residual spectrum. Small values of δ and unstructured residual spectra without remnants of absorption features or other spectral structures are requested for a successful retrieval. In later discussions of the fit quality the root-mean-square (rms) of the residual is used as quality criterion, which describes the deviation of measurement and theory per pixel, where N is the total number of pixels in the wavelength window:

$$rms \; = \; \sqrt{\frac{1}{N} \sum_j r_j^2}.$$

1.8.2 The Ring effect reference spectrum

Due to strong Fraunhofer features in the UV and visible wavelength regions, the Ring effect has to be taken into account if scattered sun light is analysed for atmospheric trace gases (cp. Sec. 1.6.3) and turns out to be crucial for the retrieval of iodine monoxide.

As rotational Raman scattering in the atmosphere leads to the filling-in of absorption lines, the effect on the resulting spectrum is similar to an emission process. An additional reference spectrum σ_{RRS} describing the spectral features of the Ring effect may be implemented in the DOAS retrieval and used in the same way as the absorption cross sections σ_i' in Eq. 1.9. The Ring-effect is therefore also referred to as a pseudo-absorber.

The Ring reference spectrum can be calculated using a radiative transfer model. In the present study, the SCIATRAN code (Rozanov et al., 2005b) was applied and the required intensity spectra were computed for different cases. Details on SCIATRAN are provided in Sec. 1.7. In this radiative transfer model, the light intensity at a given wavelength (λ) traveling through the atmosphere is calculated in two ways - with the presence of the Raman scattering effect (I^+) as well as without (I^-) (Vountas et al., 1998). I^+ is the intensity one actually records when observing scattered sun

light. All other atmospheric effects such as the absorption by various trace gases are already present in the spectrum given by (I^-). The physical quantity under investigation in the DOAS method is the optical depth. In general, with the irradiance I_0, the total optical depth τ^+ in presence of the Ring effect is given by:

$$
\begin{aligned}
\tau^+ &= \ln \frac{I^+}{I_0} \\
&= \ln \frac{I^+}{I^-} + \ln \frac{I^-}{I_0} \\
&= \sigma_{RRS} + \tau^-.
\end{aligned}
$$

The optical depth without the influence of the Ring effect is τ^-, and in this way the Ring effect is described by the additive quantity σ_{RRS}:

$$
\sigma_{RRS} = \ln \frac{I^+}{I^-}. \tag{1.10}
$$

In Fig. 1.7, the procedure of generating the effective Ring spectrum is demonstrated. The top panel shows two simulated intensity spectra, which where calculated with the SCIATRAN radiative transfer code, the black curve representing the intensity spectrum neglecting the infilling by Raman scattering and the red curve taking this effect into account. For the radiative transfer calculations an albedo of 0.9, a surface elevation of 0 km (sea level) and 70° SZA were chosen. For test purposes, also different settings were examined (cp. Sec. 2.8). The smaller inset magnifies the spectral region from 415 to 440 nm as the difference between the two spectra is rather small so that it is hardly visible in the large graph. In the zoom-in, the infilling of the absorption line around 430 nm (the Fraunhofer G-band) can be just recognised as the feature is slightly less pronounced in the red curve than in the black one (marked by grey circle). The Fraunhofer G-band consists of many absorption lines, mainly originating from Iron (Fe) and Calcium (Ca) ions.

The lower panel shows the resulting Ring effect calculated from the top curves following Eq. 1.10. It becomes clear from these figures, that the effect is small in comparison to the total intensities, but in terms of optical depth, the magnitude of the Ring effect is considerable. As will be shown later, the Ring effect constitutes one of the most influential impacts in the spectral region of the IO retrieval. The encircled feature around 431 nm will be important for later discussion (cp. Sec. 2.8).

1.8.3 The Air Mass Factor

If the vertical column of an atmospheric species or even its concentration is needed rather than the slant column, some additional calculations and a priori information are necessary. While the slant column is the integrated trace gas amount along the actual, specific light path, the vertical column (VC) represents the vertically integrated trace gas amount from Earth's surface to the top of the atmosphere. The relation between these two quantities is called the Air Mass Factor (AMF) and describes the light path enhancement as compared to the direct light path due to slant irradiation and observation angles and because of scattering processes. It is necessarily wavelength dependent:
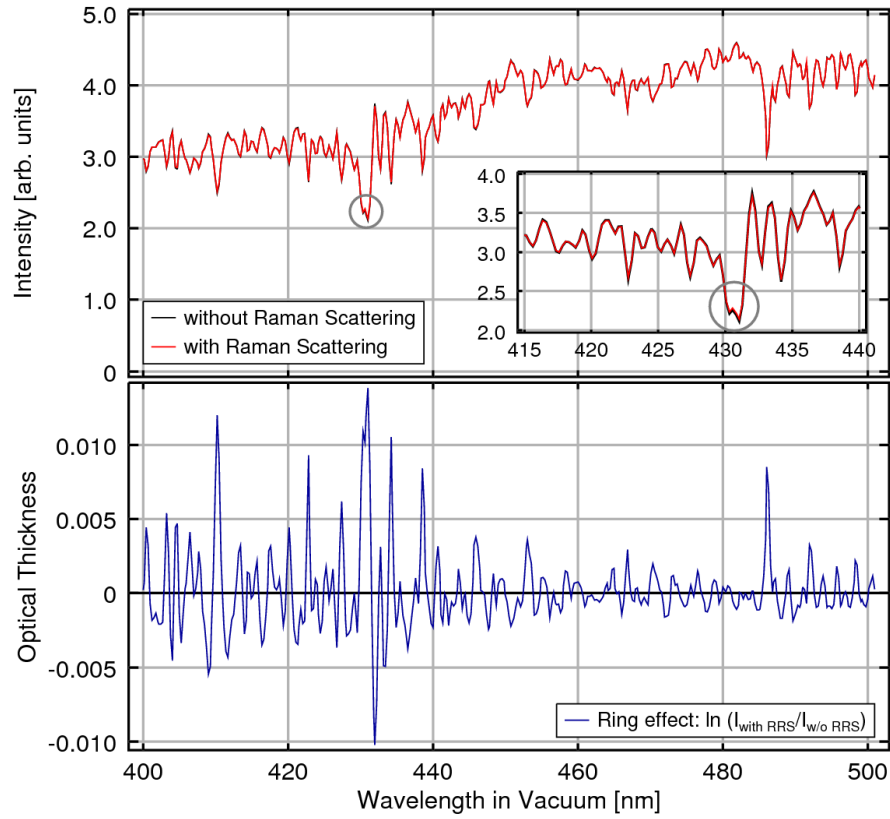
Figure 1.7: The intensity spectra in the top panel were calculated using the SCIATRAN code and they represent the electromagnetic spectra between 400 and 500 nm as they would be measured at the position of SCIAMACHY. While the black curve disregards Raman scattering, this is considered in the red curve. In inset zooms in on the region from 415 to 440 nm. The Ring effect spectrum determined from these simulations is shown in the bottom graph. The grey circle points out the Fraunhofer G-band.

$$\mathrm{AMF}(\lambda) = \frac{SC(\lambda)}{VC}$$

If the AMF can be computed, then the SC can directly be transferred into a VC. Due to scattering incidences though, the average actual light path is usually not explicitly known, so that the calculation of the AMF becomes elaborate and needs to be performed using radiative transfer models.

Rayleigh and aerosol scattering as well as surface reflectivity lead to the wavelength dependency of the AMF. This dependency can be neglected only as an approximation in small wavelength windows and only for sufficiently small amounts of a trace gas. If the absorption by a trace gas amount becomes too strong, then the AMF will vary between wavelengths with strong and weak absorption of the species. In that case, the computation needs to be altered to include an iterative algorithm. For the case of iodine monoxide, this extension is not needed.

The AMF is influenced by the trace gas profile, as the typical light path enhancement changes

with altitude. In the computation of the AMF, therefore, an a priori assumption on the profile shape is needed. If the profile of the species is not known, considerable uncertainties are introduced in the process of conversion from SC to VC. Only very sparse information on the profile is available for iodine monoxide, so that a calculation of the VC bares the risk of systematic errors. Nevertheless, the calculation of a probable AMF makes sense in order to estimate the magnitude of the VC and also of the surface concentration. One should keep in mind, however, that the unknown profile shape has a substantial influence and that results in terms of VC or concentrations that are derived from scattered light DOAS measurements are subject to certain assumptions.

In addition to the total AMF, the light path enhancement in a certain altitude range is of interest. This is described by the block AMF (BAMF) and can be related to any altitude and layer thickness. The BAMF is the discrete change in slant column density δSC_i of trace gas i, which one would detect with the applied instrument, if the vertical column changes by $\delta VC_{i,j}$ at a certain altitude interval number j of the discrete altitude grid:

$$\mathrm{BAMF}_{i,j} = \frac{\delta SC_i}{\delta VC_{i,j}}.$$

BAMFs are calculated in this study with a typical layer thickness of 200 m in the boundary layer and increasing layer thickness above. In the applied radiative transfer code, the BAMF is calculated via the weighting function. Weighting functions describe the sensitivity of the measurement method with respect to any atmospheric parameter, e.g. the absorption of trace gases, in dependence of the altitude. They may be defined in different ways, and in the present case the weighting functions describing the intensity change (δI) seen by the instrument with respect to a change in mixing ratio (δVMR) in the altitude interval h_j are used, i.e.:

$$W_{i,j}^{I,\mathrm{VMR}} = \frac{\delta I}{\delta \mathrm{VMR_i} h_j}.$$

As a linear change of the intensity with varying trace gas amount is assumed, this approach is only valid for an optically thin atmosphere. The intensity change is calculated by $\delta I = -I_0 \sigma_i \delta SC_i$. Using the above equations, the density of air $\rho_{air,j}$ at altitude j, and the conversion of the VMR to vertical column $\delta VC_{i,j} = \delta \mathrm{VMR} \cdot h \cdot \rho_{air,j}$, the BAMFs can be directly calculated from the intensity weighting functions:

$$\mathrm{BAMF}_{i,j} = \frac{W_{i,j}^{I,\mathrm{VMR}}}{I_0 \cdot \sigma_i \cdot \rho_{air,j}}$$

A measurement is especially sensitive to an atmospheric layer were the BAMF is large, as the average light path through this layer is comparably long and the absorption signature picked up by the radiation during its way through this specific layer is enhanced. This reduces the detection limit. Averaging the block AMF over the altitude and weighting the single layers by the respective relative trace gas amounts yields the total AMF.

1.8.4 The DOAS fitting routine

After atmospheric light spectra are recorded, the next step in obtaining the trace gas amounts from these measurements is the DOAS retrieval routine itself. For this purpose, the fitting programme NLIN is available, which has been developed at the Institute for Environmental Physics, University Bremen (Richter, 1997).

The programme incorporates the DOAS retrieval method as described above and can be used for the analysis of satellite as well as ground-based measurements. The fitting routine needs specific parameters and data files as input information and yields output files with the retrieval results, especially the trace gas slant columns of all chemical species included in the fit. In addition the spectral fit results can be saved. The structure of the programme, the incorporated algorithms, routines and some important computational aspects as well as the necessary input files will be explained in the following.

The retrieval routine starts with reading in all relevant input data. This includes, e.g., the measurement spectra I and reference spectrum I_0 as well as the laboratory cross sections σ for all included trace gas absorptions. In addition, a parameter file provides detailed information on the required fit parameters, such as fitting window, included trace gas spectra, polynomial degree, file paths and other retrieval settings.

After the input data is read in, first the spectral calibration of the selected background spectrum I_0 is performed. This step uses the Fraunhofer atlas (Kurucz et al., 1984), a high resolution spectrum of the solar flux, and is governed by the strong Fraunhofer lines. The spectral axis of I_0 is adjusted using two parameters. One parameter generates a spectral shift and the second factor may stretch or compress the wavelength axis. The Fraunhofer reference spectrum needs to be convolved with the instrument's slit function. The shift and squeeze parameters, a polynomial for the broad-band effects and a rough correction for the filling-in of the Fraunhofer lines (the Ring effect) in the background spectrum are retrieved by using the non-linear Levenberg-Marquard method.

The individual measurement spectra are adjusted within the main DOAS retrieval as described below. For their adjustment also two shift and squeeze parameters are applied. Both parameters are not allowed to exceed a selectable limit. The wavelength grid of the laboratory cross sections, however, is kept fixed. Shifting and squeezing is also possible for these spectra and was applied in some test cases, but was not used for the final results in the present study.

The treatment of the absorption cross sections is slightly different for satellite and ground-based data here. For the satellite retrievals, laboratory spectra measured with the instrument itself or spectra which are convolved with the appropriate slit function prior to read-in are used. For the ground-based measurements, all laboratory cross sections have been measured by different instruments and need to be convolved with the instrument slit functions. For this case, a daily measured slit function is read-in, and the cross sections are convolved as part of the retrieval routine.

In the main DOAS retrieval process solving Equation 1.9, first the logarithm of the measurement data is formed, calculating the optical depth. The quantity δ is then minimised in a two-part fit. Iteratively, a non-linear and a linear fit are repeated until the alignment of experiment and theory judged by the magnitude of δ is optimised. A non-linear fit is performed for the spectral alignment of

the individual measurement spectrum with respect to the background spectrum. For a given choice of shift and squeeze parameters for the current measurement spectrum, a linear fit for the slant columns and the polynomial coefficients is performed, following Eq. 1.9. These retrieval parameters are determined simultaneously. Both steps, the non-linear and the linear part, are repeated until the alignment does not further improve.

In addition to the trace gas absorption spectra some other spectral effects are taken into account:

1. The Ring effect discussed above in Sec. 1.6.3 and Sec. 1.8.2 is considered by using a pseudo-absorption cross section σ_{RRS} (Eq. 1.10) which is treated in exactly the same way as the absorption cross sections. The fitting parameter in the DOAS retrieval is then called a fit factor instead of a slant column.

2. Stray light may enter the instrument and affect the retrieval, as the DOAS equation in its ideal form does not consider any stray light. A constant amount C of stray light changes the optical depth to read $\ln(\frac{I+C}{I_0})$. This can be rewritten as $\ln(\frac{I}{I_0}) + \ln(1 + \frac{C}{I})$ and approximated by $\ln(\frac{I}{I_0}) + \frac{C}{I}$. The second term may be treated as an additional cross section. The constant C is chosen as the maximum intensity in the fitting window times a certain factor, in the present case 0.03. The resulting reference spectrum reads: $\sigma_{stray,offset} = \frac{0.03 \cdot I_{max}}{I}$.

A second stray light term takes into account a linear wavelength dependency of C, i.e. a linear change of the stray light amount over the detector. The optical depth becomes $\ln(\frac{I+C+D(\lambda)}{I_0})$, with $D(\lambda) = 0.03 \cdot I_{max} \cdot \frac{\lambda_2 - \lambda}{\lambda_2}$ for a fitting window $[\lambda_1, \lambda_2]$. Again a factor of 0.03 is applied, which has in both cases no large influence. This yields a second reference spectrum: $\sigma_{stray,slope} = \frac{0.03 \cdot I_{max}}{I} \cdot \frac{\lambda_2 - \lambda}{\lambda_2}$. Both stray light effect spectra are then scaled by a fit factor retrieved in the DOAS fit. Due to the dependence of $\sim \frac{1}{I}$, the spectral shape is similar to the Ring effect spectrum.

3. Furthermore, an undersampling correction (Chance, 1998) is included. A narrow slit function with a small number of pixels per FWHM may introduce errors into the fit in form of very highly structured spectral patterns. This may occur if a shift for the spectral alignment is necessary in the fit. A fixed reference spectrum is used for this correction.

1.9 Description of instruments

Several different instruments and measurement data have been used within the scope of this study. In this section, overviews and details for the employed instruments are presented. The main part of the work is concerned with observations from the SCIAMACHY satellite sensor, which will be described first.

In field campaigns, especially for validation purposes (Sec. 4) and for a specific study for the improvement of satellite retrievals (Sec. 6), measurements from one certain type of ground-based (and ship-based) instrumentation were used.

In addition, further satellite products were applied for specific discussion purposes and are described at the end of this section.

1.9.1 The satellite instrument SCIAMACHY

The satellite instrument SCIAMACHY (SCanning Imaging Absorption spectroMeter for Atmospheric CHartographY) is mounted on the Environmental Satellite (ENVISAT) of the European Space Agency (ESA). ENVISAT was launched in March 2002 into a sun-synchronous, near-polar orbit with a local equator crossing time of 10 am in descending node. The objective of the SCIAMACHY mission is to provide global measurements of relevant atmospheric compounds in order to enhance the knowledge and understanding of atmospheric processes and also of global climate change. The analysis of data measured by SCIAMACHY yields information about Earth's atmosphere, including the troposphere, stratosphere and also the mesosphere. The amounts of various atmospheric parameters and compounds, trace gases and aerosols can be determined by inversion of the electromagnetic radiation spectra recorded by SCIAMACHY. With this, the chemical composition and the pollution of the atmosphere, the ozone chemistry and ozone depletion in the stratosphere, as well as the solar variability and many other aspects are studied. The instrumental properties and mission objectives have been described in detail in Burrows et al. (1995) and Bovensmann et al. (1999). An overview over the instrument and some mission successes are summarised in Gottwald et al. (2006).

SCIAMACHY is a combined prism and grating spectrometer and records electromagnetic radiation from scattered sunlight in a wide spectral range (UV-vis-NIR-SWIR) and in different viewing geometries. In nadir viewing geometry, the instrument views downwards - sunlight backscattered and reflected from the Earth's atmosphere and surface is recorded. Measurements from this viewing geometry will be analysed in the following chapters for the spectral absorption signatures of iodine monoxide. Additionally, measurements in limb viewing geometry are performed, where the instrument's viewing angle points in flight direction tangential to the Earth's surface in different altitude steps in order to resolve profiles of trace species. In the solar and lunar occultation modes, the direct sunlight or sunlight reflected at the moon's surface are recorded. Combining more than one of these geometries allows additional analyses. Limb and nadir measurements can be utilised together to determine the tropospheric columns of relevant trace gases. Due to the alternating limb and nadir viewing settings and a swath width of 960 km, global coverage at the equator is achieved within six days. For an impression of a typical sequence of nadir data, Figure 1.8 displays the locations of nadir viewing measurements for one sample day, Sep 1st 2005. All locations marked in green are within the field of view of the nadir data on this day. One of the green marked areas is also referred to as a "state" of measurements.

The optical properties are determined by the design and characteristics of the Optical Unit of SCIAMACHY. An overview of the optical setup is provided in Fig. 1.9. In Earth observing nadir configuration the radiation is guided into the instrument by the Elevation Scan Mirror (ESM). For these measurements, the optional Aperture Stop is kept large and the Neutral Density Filter is moved out of the optical path for optimised intensity throughput. Following the ESM, the light is focused by the telescope mirror on to entrance slit of the spectrometer. Determined by the optics and the slit dimensions, the Instantaneous Field of View (IFoV) has a size of 1.8° × 0.045°, i.e., approximately an instantaneous ground scene size 25 km×0.6 km (along-track × across-track). This pixel size is enlarged during measurement operation by scanning movement of the ESM to ground pixels of typically 30 km×60 km. The scan covers a total swath width of 960 km which means
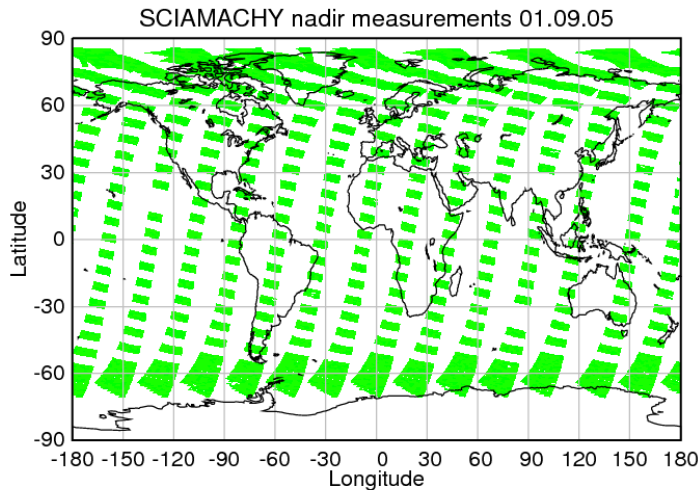
Figure 1.8: Shown in green are the locations covered by nadir measurements on one day, the 1st of September, 2005, demonstrating the typical daily coverage and data amount SCIAMACHY provides. The Solar Zenith Angle is restricted to $<84°$ here.

viewing within angles of $\pm 32°$ across track.

After the radiation has entered the instrument, the spectral dispersion within the spectrometer is achieved in two consecutive steps. Prisms are used for pre-dispersion of the spectrum, which is then split into eight spectral channels and guided to eight individual detector units. Reflection gratings then provide the appropriate final dispersion. Measurements in the eight spectral channels are therefore performed simultaneously. Six contiguous channels are present between 214 and 1773 nm and two additional short wave IR channels (1934 - 2044 nm and 2259 - 2386 nm). Silicon photodiode arrays (1024 pixels) are used in channel 1 to 5 for detection of the photon signal, while the short-wave IR channels require the use of Indium Gallium Arsenide (InGaAs) as detector material.
The individual channels are again subdivided into clusters which may have varying exposure times. The division of the eight channels, their spectral range and the typical trace gases which can be retrieved from the respective measurements are given in Tab. 1.3. Depending on the respective wavelength region, the spectral resolution lies between 0.2 nm and 1.5 nm. For the retrieval of iodine monoxide in this present study, measurements from channel 3, specifically from clusters 14 and 15 (404 - 527 nm), in nadir viewing geometry have been investigated. In this channel the spectral resolution is 0.44 nm.

In addition to the main channels, SCIAMACHY comprises the Polarisation Measurement Devices (PMDs). The original purpose of the PMDs is to provide corrections for polarisation effects in the SCIAMACHY science channels 2-6 and 8. While the main SCIAMACHY measurements record radiation from both polarisation directions, the PMDs are mainly sensitive to light which is polarised parallel to the entrance slit of SCIAMACHY. The PMDs record the intensity of radiation in seven different bands, involving six distinct wavelength intervals given in Tab. 1.4. Recordings from the PMDs become important for Sec. 2.7, as they can provide information on cloud cover and the underlying surface type in different ways.
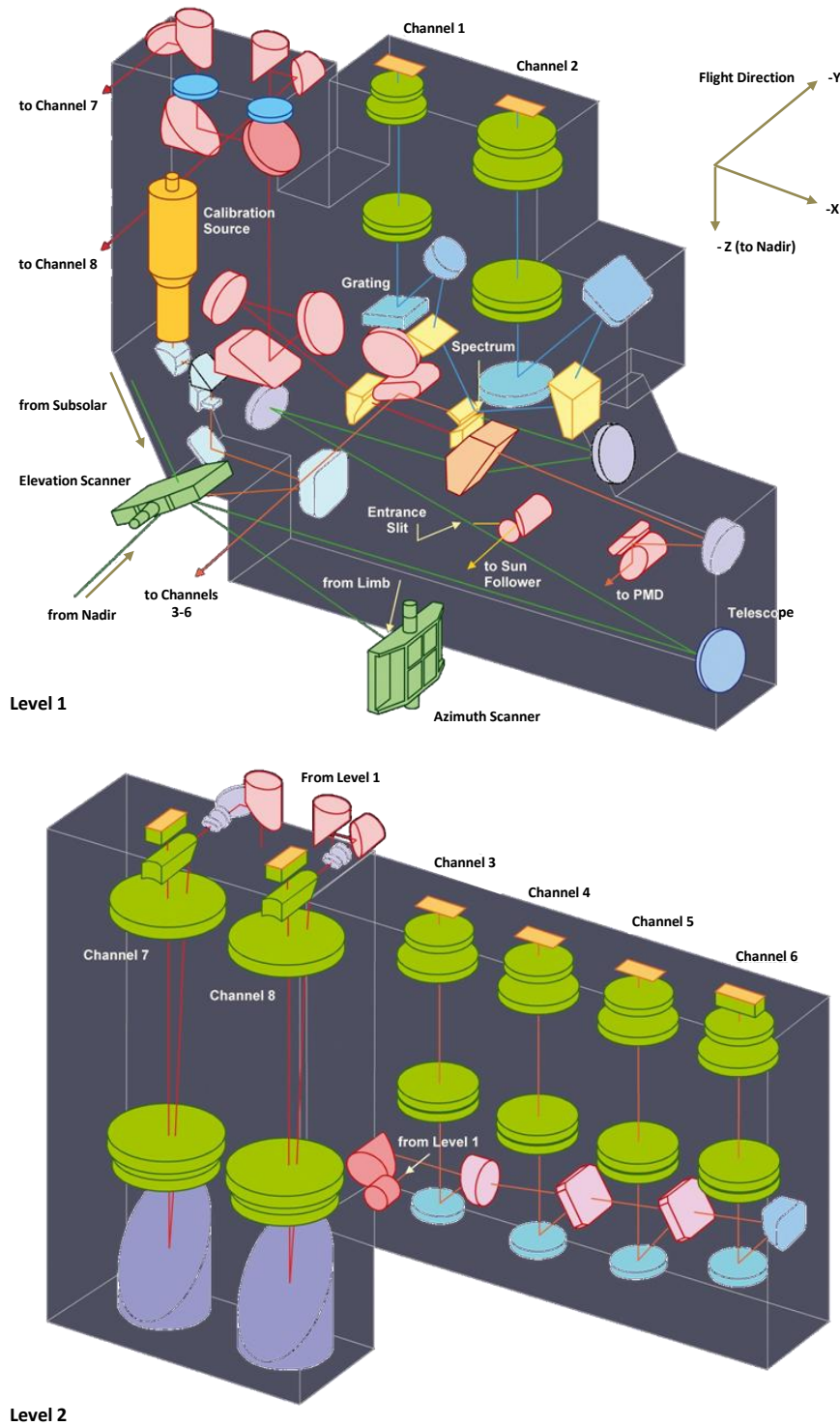
Figure 1.9: Schematic of the optical configuration of SCIAMACHY. The spectral dispersion is achieved by prisms (pre-dispersion) shown in yellow in Level 1 (top) and individual reflection gratings (blue) in the eight spectral channels (channel 3-6 in Level 2, the others in Level 1). In this work, data from channel 3 in nadir direction is used, which is guided into the instrument by the ESM mirror. The channel 3 detector unit is part of Level 2 (bottom graph). Figures adapted from Gottwald et al. (2006).

Channel No.	Wavelength Interval	Trace Gases
Channel 1	214 - 334	NO
Channel 2	300 - 412	O_3, BrO, SO_2, OClO, HCHO
Channel 3	383 - 628	NO_2, O_4, CHOCHO, IO
Channel 4	595 - 812	H_2O, O_2, NO_3
Channel 5	773 - 1063	
Channel 6	971 - 1773	CO_2, CH_4
Channel 7	1934 - 2044	
Channel 8	2259 - 2386	CO

Table 1.3: Overview over the Sciamachy main channels. For each channel, the wavelength region and some trace gases typically retrieved in this spectral window are given. Apart from these trace gas amounts, several aerosol and cloud parameters may be retrieved from the Sciamachy measurements.

PMD band	Wavelength intervall
1	310-365 nm
2	455-515 nm
3	610-690 nm
4	800-900 nm
5	1500-1635 nm
6	2280-2400 nm
7	800-900 nm (45° polarised)

Table 1.4: List of channels and covered wavelength bands of the PMDs belonging to Sciamachy.

1.9.2 Ground-based MAX-DOAS systems

Multi-AXis-DOAS (MAX-DOAS) instruments are able to view light in different elevation angles. The DOAS instruments operated by the IUP Bremen observe scattered sun-light and are therefore considered passive DOAS systems, in contrast to active systems using artificial light sources. Spectra in the UV/visible wavelength regions are recorded. Several studies of atmospheric constituents have been conducted with these systems (Wittrock et al., 2000, 2004; Heckel et al., 2005). The basic DOAS setup consists of three main components, the light gathering unit, a wavelength dispersing element and a detector. The Bremen instruments receive light from a custom-built telescope which focuses the incoming light into an optical fibre bundle. The fibre bundle reduces the polarisation sensitivity of the measurements. The light is then guided to the entrance slit of a grating spectrometer (Czerny-Turner type). Different sizes and types of grating spectrometers are used, typically with a focal length between 275 and 500 mm and planar reflection gratings with 300 or 600 lines/mm.

Two dimensional CCD cameras are used for radiation detection, one dimension giving the spectral information. The second dimension is usually not used for additional information, but the final spectrum is received by integration over the second dimension significantly improving the signal to noise ratio of the measurements. The size of the CCD chip, the focal length of the spectrometer and the grating constant determine the bandwidth of the system. Typically, bandwidths between 80 nm and 300 nm are achieved. A computer is used to control the instrument's measuring sequence and stores the recorded spectra and calibration measurements. For spectral calibration and slit function
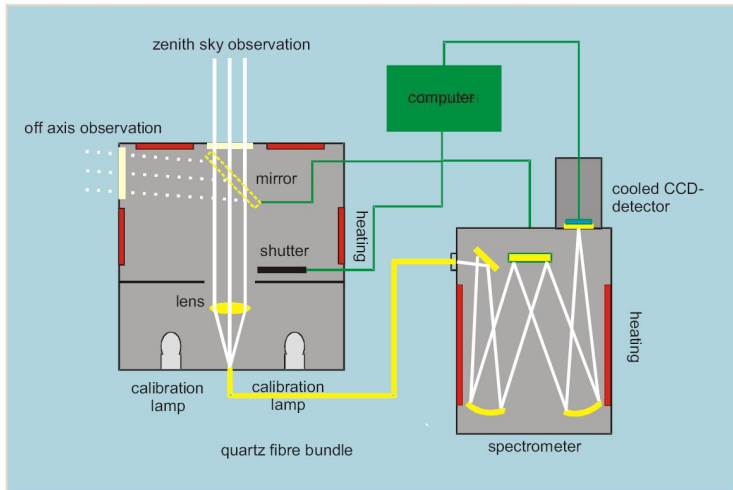
Figure 1.10: Sketch of the MAX-DOAS instrument setup with the main parts: telescope, glass fibre bundle, spectrometer unit, CCD camera and computer. Additionally, calibration lamps are used for wavelength calibration and determination of the instrument's slit function. The fibre bundle is of Y-form, i.e. the incident light is divided into two equal parts and is fed into two spectrometer units at the same time. Sketch kindly provided by Folkard Wittrock, IUP Bremen.

measurements, a mercury-cadmium (HgCd) calibration line lamp is installed in the telescope box. A sketch of the general instrument setup is given in Fig. 1.10.

The telescope system determines the viewing direction of the instrument in two dimensions, the azimuthal angle and the polar angle (elevation angle or line of sight, LOS). Here, the LOS is measured by convention with respect to the horizon, so that horizontal viewing corresponds to 0° and the zenith is observed at a LOS of 90°. Operated from the ground, the Bremen DOAS systems observe at several elevation angles, angles other than the zenith being selected by a rotatable mirror within the telescope box. Typical sequences include the zenith-sky direction, a fixed elevation angle at 30° above horizon and a scan from LOS 0° (horizon) in 1° or 2° steps to 15° or 16° above the horizon. The exact settings depend on the site and objectives of the observations. The viewing geometries from ground and the sensitivities towards different atmospheric layers are depicted in Fig. 1.11, showing the telescope (TS) - spectrometer (SP) unit and light paths for different solar positions, i.e. at high sun/low solar zenith angle (θ_1) and for lower sun (larger SZA θ_2). Light is scattered in the atmosphere by particles and molecules (SC). Two important influences of SZA and elevation angle become clear in this picture:

1. With increasing SZA ($\theta_1 \rightarrow \theta_2$), the path length through a stratospheric absorber layer (StAb) increases and with it the sensitivity towards trace gases in the stratosphere.

2. With lower elevation angle ($\beta_a \rightarrow \beta_b$), the path length through a tropospheric absorber layer (TrAb) increases, while the light paths through the stratosphere (following ray 1a and 1b) remain the same. The sensitivity towards trace gases in the troposphere and especially in the boundary layer is thus enhanced. This fact leads to the importance of the lower elevation angles additionally used in the MAX-DOAS technique as compared to zenith-sky DOAS.

1.9.3 Additional satellite instruments

SeaWIFS

NASA's Sea-viewing Wide Field-of-view Sensor (SeaWIFS) onboard the SeaSTAR satellite was launched in 1997. SeaWIFS records electromagnetic radiation in eight discrete wavelength bands of 20 or 40 nm spectral width between 400 and 900 nm. Amongst other bio-optical properties, infor-
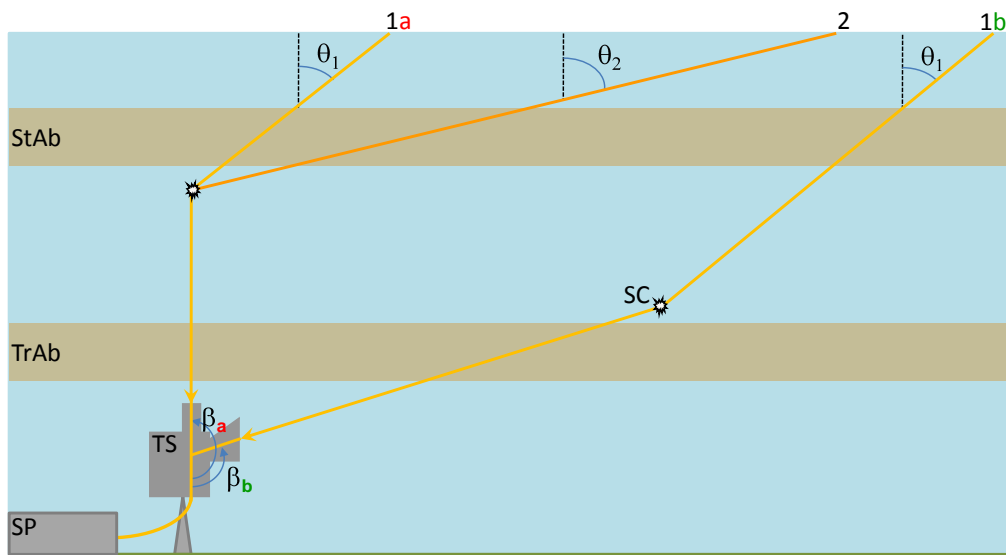
Figure 1.11: Simplified sketch of the MAX-DOAS light path geometries at different elevation angles $\beta_{a,b}$ and at different SZA $\theta_{1,2}$. Lower sun (SZA $= \theta_2$) leads to higher sensitivity for stratospheric absorbers (StAb) for a given elevation angle, while a lower elevation angle (β_b) leads to enhanced sensitivity towards tropospheric absorbers (TrAb).

mation on the oceanic chlorophyll-a concentration is retrieved. In the data set used for comparisons in the present study (Chapter 3), the information is provided on a grid with 9 km resolution. If the field of view partly contains ice cover on Earth's surface, the measurement is discarded from the product due to saturation. Data and maps from SeaWIFS are freely available from the Ocean-Color webpage (http://oceancolor.gsfc.nasa.gov) from NASA, the National Aeronautics and Space Administration of the United States of America.

AMSR-E

The Advanced Microwave Scanning Radiometer for EOS (AMSR-E) instrument is installed on the AQUA satellite, which is operating in space since May, 2002, and belongs to NASA's Earth Observing System (EOS). AMSR-E is a passive microwave radiometer, recording radiation at several distinct microwave bands. A multitude of parameters is observed, such as sea surface temperatures, ice concentrations, atmospheric water vapour and several others. In the present study, information about the ice coverage on Earth's surface is used for discussion purposes in Chapter 3. The analysis of ice concentration is performed with the 89 GHz channel (Spreen et al., 2008), and the data version utilised in this study is the "AMSR-E ASI 6.25 km Sea Ice Concentration Data, V5.5i". The sea ice maps were obtained from Gunnar Spreen and Lars Kaleschke (2008), Institute of Oceanography at the University of Hamburg, Germany, digital media (ftp-projects.zmaw.de/seaice) in June 2009.

GOME-2

The Global Ozone Monitoring Experiment-2 (GOME-2) is a scanning optical spectrometer covering the UV and visible spectral regions from 240-790 nm. It has been launched in October 2006 on the MetOp-A satellite (the first of its kind in a series of three). GOME-2 is a successor of the GOME instrument still in orbit on the ERS-2 satellite. The main objectives of GOME-2 are measurements of O_3 and other trace gases which are important for O_3 chemistry, as well as several trace gases of air pollution. GOME-2 is viewing in nadir geometry and has the big advantage of a near-global coverage every day due to the wide swath of 1920 km. The ground resolution of 40×80 km^2 is similar to that of SCIAMACHY. The present work uses results from GOME-2 in Chapter 6 for the liquid water path in ocean regions, as well as a test measurement using a newly generated correction spectrum. In future studies, the retrieval of an IO product from GOME-2 might be achieved.

2 Developing the retrieval of iodine monoxide from satellite

Until recently, measurements of iodine species have exclusively been conducted using ground-based and in some cases balloon-borne instruments. These represent point measurements of trace gas amounts at specific locations and give some insight into the temporal evolution. Information on a spatially larger scale may be obtained from aeroplane or satellite measurements. The objective here is to use satellite data analysis to observe iodine monoxide columns from space and therewith enhance the knowledge and understanding of iodine abundances on a more global scale. The satellite sensor SCIAMACHY was introduced in Sec. 1.9.1 and is of valuable help in this respect.

In this chapter, the technical details of the satellite data analysis are presented. The description starts with the necessary data processing steps, before the specific DOAS settings for the IO retrieval, the fit results and the estimated detection limit are discussed. Data quality and consistency are investigated. Then possibilities and effects of cloud screening are presented, as well as example influences caused by certain changes in the retrieval settings.

Selected retrieval results and first examples of global maps in this chapter shall specifically serve for discussion purposes of fit quality and retrieval consistency, while the scientific discussion of the IO amounts, their distribution and approaches for interpretation will follow in the next chapter.

2.1 Satellite data configuration and selection

Before iodine monoxide slant columns can be retrieved from SCIAMACHY measurements, several data configuration and selection steps are required. The single steps shall be specified in the following.

Level 0 to Level 1b Processing

From all available measurements recorded by SCIAMACHY, a certain subset of data is needed for the analysis of iodine monoxide. The initial raw satellite readout in counts per pixel is commonly referred to as the Level 0 data. First of all, this Level 0 data is processed by the SCIAMACHY Data Processor, which uses control parameters, auxiliary data and orbit parameters and yields the general Level 1b product. This Level 1b data contains processed, geolocated observational data in scientific units. Additionally, instrument monitoring data, calibration measurements and also calculated calibration parameters are included in this product. The intermediate data Level 1a is only an internal data version with no purpose for the data user.

Usually, satellite instrument data is downlinked from the satellite to ground-based receiver stations, then processed and transferred to the science institutes within several hours. This first

version of the measurement data is called the near real-time (NRT) data, and is the commonly used version for first scientific analyses. Only data which is quickly available after the respective recording is contained in this NRT product. Consequently, some orbits or single measurements can be missing in this version. As another effect following from this immediate processing, in case of a missing dark measurement, the next best dark measurement is provided instead. Subsequent quality analysis and data activities often complete and improve the data set. At certain times later on, so called consolidated and reprocessed data sets become available, where some formerly missing orbits are supplied and non-optimal first choices for calibrations and correction steps are replaced. The advantage of the consolidated and reprocessed data is the usually larger data amount and possibly a higher data quality. A clear advantage of the NRT data is the almost instantaneous availability at an already good data quality.

From the beginning of this study up to May 22nd, 2006, Data Processor Version 5 was the implemented processing unit providing the Level 1b product. For data recorded later than this date, an updated Data Processor Version 6 was operated with improved calibration steps and additional changes, e.g. in the sequence of calibration and correction steps. Recently, the complete Sciamachy measurements were reprocessed using this revised Processor (latest Version number 6.03), from which now a consistent Level 1b data set is additionally available.

In this present study, two basic data versions are applied. All scientific results and analyses are gained on the basis of near real-time data for a time period of four and a half years, covering the time from January 2004 to July 2008. After the reprocessed data version became available, calibration steps (see paragraph below) were tested and a longer consistent time series with slightly different calibration and correction settings was generated. While focus is on the NRT data set in this thesis, some new analyses and comparisons have already been conducted with the reprocessed data. The two data versions will be described in more detail in the following sections on further data processing and the actual DOAS retrieval procedure.

Level 1b to Level 1c Processing

As only a certain subset of the available Sciamachy data is needed for each specific task, and as individual requirements need to be met, the extraction and further processing of data from Level 1b to Level 1c is facilitated by an extraction tool provided by ESA. Level 1c data contains user specific data subsets with individual selection and configuration settings. Users can select themselves which properties (wavelength region, dates, viewing geometry, calibration steps, etc.) are needed for a certain purpose.

For recordings prior to the processor change in May 2006, the extraction of Sciamachy Level 1b data subsets can be performed with the SciaL1C Command Line Tool (Version 2.5.0) from ESA. This tool was linked to the Data Processor Version 5, so that it could no longer be used after the processor exchange. Since the exchange, an updated SciaL1C Tool (specifically for data from Processor Version 6 onwards, programme Revision 1.23) is available, which mostly works in the same way as the former version, but incorporates some updates on the calibration steps.

The data utilised in this study for the retrieval of iodine monoxide is recorded in nadir viewing geometry by the third spectral channel of Sciamachy. Channel 3 is subdivided into several clusters,

and the current standard IO fitting window from 416 to 430 nm overlaps with clusters 14 and 15, both belonging to channel 3.

Considering the selection of calibration and data correction steps, for most purposes of DOAS retrievals in the UV and visible spectral range, it has proven to be the best choice to select only the dark current subtraction (calibration step 1) and to omit all other possibilities. Usually, the information for wavelength calibration (calibration step 5) is also extracted but not applied (cp. Sec. 1.8). This information is only written to the files without changing the data product. For the reprocessed data set, calibration step 0 for the correction of the memory effect was added to the usual settings. This step appears to yield slight improvement with respect to earlier processor versions and also slightly better results than without this setting. The relevant data calibration steps (programme options "-cal 0, 1, 5") have the following properties:

- -cal 0

  The memory effect is caused by left over electrons of a previous signal on the instrument detector affecting the subsequent measurement, especially at transitions between bright and dark surfaces (such as ice/water or cloudy/cloud free scenes). In the correction procedure, the signal intensity of the previous signal determines the action which is applied to the subsequent readout. Measurements following a weak signal are not corrected, while from recordings after intense signals above a certain threshold, a correction term is subtracted. This correction is calculated as a function of the previous intensity.

- -cal 1

  The dark current is obtained in several states on the dark side of every orbit from observations pointing into deep space at 250 km altitude where no Earthshine light is expected to affect the measurement. There are five Dark States covering all relevant exposure times used for measurements. The correction signal in channel 3 consists of a constant offset per readout and an additional part from the leakage current which is exposure time dependent.

- -cal 5

  Spectral calibration is performed using a hollow cathode lamp (Pt/Cr-Ne). The wavelength axis is calculated from a 4th order polynomial fitted to the spectral lines as a function of detector pixel. The polynomial coefficients are also modulated by a harmonic function of orbit phase and finally written into the orbit files of SCIAMACHY data. However, this calibration data is usually not further used in the present study. The wavelength calibration is conducted in a different way, as described in Sec. 1.8.

Other possible calibration/correction steps implemented in the extraction tool are corrections for the pixel-to-pixel gain, the etalon effect, the impact of stray light, polarisation influences and the radiometric calibration for computing the real radiance. In some quality tests, the additional calibration steps did not improve the IO retrieval and were therefore not applied to the data used in this study.

Figure 2.1 displays a typical spectrum measured by SCIAMACHY in channel 3, here showing the spectral region of cluster 14 and cluster 15 after the above processing steps have been undertaken.
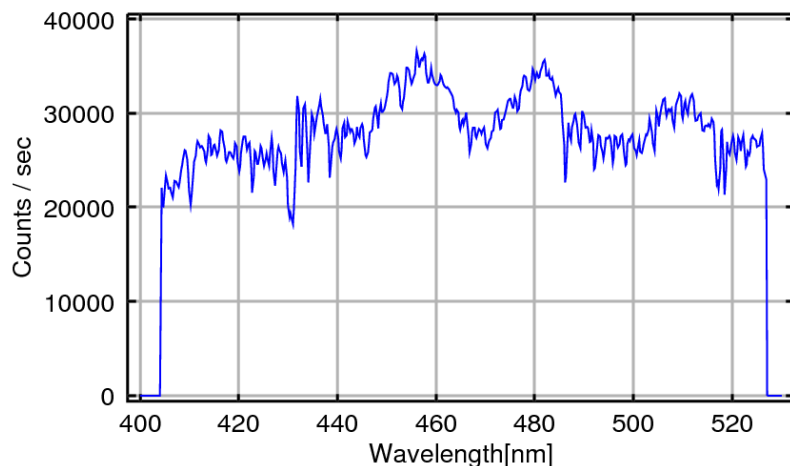
Figure 2.1: A typical spectrum measured by SCIAMACHY shown here after application of the dark current correction and spectral calibration including data from cluster 14 and 15 in channel 3. The spectrum was measured on Sep 1st , 2005, with a ground scene covering Bremen at a central position of 52.8°N, 9.2°E.

The dark current is subtracted and the spectrum is spectrally calibrated. Some features attract the attention. At the channel borders the light intensity drops abruptly to zero. In between, the prominent dips in the spectrum are Fraunhofer lines from atomic absorption in the solar atmosphere, and the broad intensity variation with a period on the order of 20 nm is caused by the etalon effect of the detector chip. Spectra of this type are utilised as starting point for the DOAS retrieval of iodine monoxide.

Data adaptation, formatting and additional conditions

Using data from two clusters at the same time, here cluster 14 and 15 from channel 3, attention needs to be paid to the integration times used in each cluster. The Pixel Exposure Time (PET) is constant for the entire channel, but for cluster 14, the coadding factor f_{coadd}, i.e., the number of subsequent recordings added up to one averaged measurement, and with this the integration time $IT = f_{coadd} \cdot PET$ is larger as compared to cluster 15. This has been decided in order to reduce the data amount due to the limited band width for the down-link of data from the satellite to receiver stations on ground. When using both clusters, the coadding has to be matched to the respective longer integration time to receive consistent spectra across the cluster borders. This adaption and a format change are accomplished in a next step by a separate programme where also the data format is adapted to the input format required for the DOAS fitting routine programme NLIN (cp. Sec. 1.8.4). Each file of satellite data contains one orbit of SCIAMACHY measurements. Important information such as geolocation, time of measurement, viewing geometry, applied calibration steps and other parameters are given for each spectrum in ASCII-headers, followed by the respective measurement spectrum in binary code.

During or after the fitting routine, some additional data selection steps are performed. The following settings have been chosen:

- The ground scene size is increased to a minimum of 60 km along and 120 km across track by averaging several individual measurements in order to improve the signal-to-noise ratio. As the integration time in cluster 14 is usually longer than for cluster 15, the ground scene size may be already increased due to the matching of the integration times.

- A restriction for the solar zenith angle (SZA) to less than 84° was applied. This excludes observations with a low position of the sun and therefore intrinsic low signal-to-noise ratio, reduced sensitivity to the lower troposphere and larger retrieval errors.

- The slant columns from the DOAS fit result are subjected to a defined quality criterion. In the final product of a trace gas column, only those data where the residual exhibits a sufficiently small root-mean-square (rms) are included and utilised for regional or global maps.

- In the visible spectral region, clouds between the satellite instrument and the part of atmosphere under investigation can affect the trace gas retrievals. In many cases the application of cloud screening algorithms is useful or necessary. Information about the cloud fraction in a satellite measurement can be obtained, e.g., by accessory information from other instruments or analyses. Elsewise, an intensity criterion can be applied, which simply rejects data from too bright scenes. In the present study, no cloud screening is applied by default for specific reasons, as explained later. However, some tests and case studies for cloud screening were conducted to investigate possible cloud effects on the IO retrieval even in ice covered regions by using a recently developed data product. More details follow in Section 2.7.

A summary of all selection and configuration parameters for both data versions - the NRT product and a reprocessed data set - is given in Tab. 2.1. A majority of the analyses is conducted on the NRT data, whenever the reprocessed data set is used, this is indicated.

2.2 The DOAS retrieval of iodine monoxide

As discussed in Chapter 1, all trace gases and atmospheric spectral effects affecting the transmission of light need to be simultaneously accounted for in the DOAS retrieval. In the following sections, the specific effects which are of relevance in the spectral region of IO absorption are presented and the retrieval settings, fit quality and consistency tests are discussed in detail.

2.2.1 The developed IO standard fit

The retrieval which showed the best and most consistent results is referred to as the standard fit. The results from this retrieval have been described and used in Schönhardt et al. (2008). First of all, the parameters and settings chosen for this case will be mentioned and discussed. Tests with further considerations of trace gases and different settings have also been performed and the most important results from those test runs will be presented in Sec. 2.8. One important aspect in the following is the judgement of the quality of a fit.

Labeling definition for IO product versions

Apart from the specific standard IO product, several other IO retrieval versions have been generated, differing from the standard product in several aspects, e.g., in the SCIAMACHY data version or the choice of the wavelength window or more. In most of the figures and calculations, results from the

Parameter	Settings NRT data	Settings reprocessed data
Processor (0-to-1b)	Version 5.0	Version 6.03
Extraction Tool (1b-to-1c)	5.0 V2.5.0 and 6.0 Revision 1.23	6.0 Revision 1.23
Calibration	1 and 5	0, 1, and 5
	(dark current, spectral calibration)	(memory effect, dark current, and spectral calibration)
Time interval	01/2004 - 07/2008	01/2003 - 02/2009
Viewing geometry	nadir mode	
Spectral region	cluster 14, 15 in channel 3 (404-527 nm)	
Spatial resolution	averaged to 60×120 km^2	
SZA	$< 84°$	

Table 2.1: Overview of relevant configuration and selection parameters applied to the satellite data scheduled for the retrieval of IO slant columns.

defined standard IO retrieval will be shown unless stated otherwise. For the applied versions, a shorthand notation becomes useful. In this scheme, the standard IO product based on SCIAMACHY NRT data from the retrieval defined above is labeled version V1.28. A second important data set is based on the reprocessed SCIAMACHY data but uses the same DOAS retrieval settings, where only minor changes in the background spectrum were necessary. This version is defined as version V2.54. The first digit marks the respective SCIAMACHY data release (with 1 for the NRT data, 2 for the reprocessed data set). A zero as first digit is used for data sets which have not passed the consistency checks. The second number is a running value for the respective parameter set used in the DOAS retrieval. In this scheme, V0.27i is a product showing systematic retrieval errors and will be used for technical discussion purposes only (cp. Sec. 2.8).

Choices of retrieval settings

The absorption cross section spectrum for iodine monoxide exhibits strong differential structures in the wavelength region around 400 to 460 nm. In this spectral region additionally other processes alter the solar radiation before being recorded by the satellite instrument. These effects have to be taken into account in the fitting procedure.

Version	SCIAMACHY data	IO retrieval	Remarks
V1.28	NRT data	standard (cp. Tab. 2.3)	standard product
V2.54	reprocessed data	standard (cp. Tab. 2.3)	new product under development
V0.27i	NRT data	alternative settings discussed later (cp. Tab. 2.7)	corrupt retrieval with systematic errors, used for discussion purposes

Table 2.2: Overview over the main retrieval versions relevant for the present thesis.

First of all, the applied IO absorption cross section shall be introduced. While for most other trace gases direct cross section measurements with the SCIAMACHY instrument are available, this has not been performed for minor trace gases as IO. However, laboratory measurements of the IO absorption have been conducted at high spectral resolution by Gómez Martín et al. (2007) and Spietz et al. (2005) at the University of Bremen. The associated temperature for the absorption cross section is 298 K. This temperature differs from the temperatures in some locations on Earth where IO has been detected. The impact is a source of systematic error, but can be considered minor in comparison to others (cp. Sec. 2.5). The laboratory absorption spectrum $\sigma_{IO}(\lambda)$ needs to be convolved with the SCIAMACHY slit function f_{SCIA} before entering the DOAS fit. This procedure is demonstrated in Fig. 2.2, resulting in the cross section spectrum $\sigma_{IO,SCIA}(\lambda)$ which is used in the following retrievals for IO:

$$\sigma_{IO,SCIA}(\lambda) \;=\; \sigma_{IO} * f_{SCIA}(\lambda) \;=\; \int_{\lambda-\Delta\lambda}^{\lambda+\Delta\lambda} \sigma_{IO}(\lambda') \cdot f_{SCIA}(\lambda - \lambda') d\lambda'$$

The Ring effect introduced in Sec. 1.6.3 is included in all retrieval runs. The impact of the Ring effect on the measured spectrum is substantial for the viewing geometry and the wavelength region here. As a focus lies on the Antarctic region, the standard Ring spectrum used in the present study is calculated for a solar zenith angle of 70° and a ground spectral reflectance of 90%. Two trace gases that need to be considered in the IO retrieval are nitrogen dioxide (NO_2) and ozone (O_3). The absorption cross sections of both species were measured by Bogumil et al. (2003) at different temperatures, from which the spectra at 223 K were chosen here. The major part of the O_3 resides in the stratosphere where temperatures are rather low. In remote sites, a similar consideration holds for NO_2 as tropospheric amounts are small. The changing absorption cross section of NO_2 for higher temperatures was also considered in test retrievals with no large effect on the IO column.
The species taken into account in the current standard fit are listed in Tab. 2.3. References to the respective laboratory studies of the cross section measurements are included. The particular absorption cross section spectra and the optical depth of the Ring spectrum are shown in Fig. 2.3, where they can be directly compared.
Apart from the choice of the absorption features to be considered, several fit parameters have to be adjusted adequately.
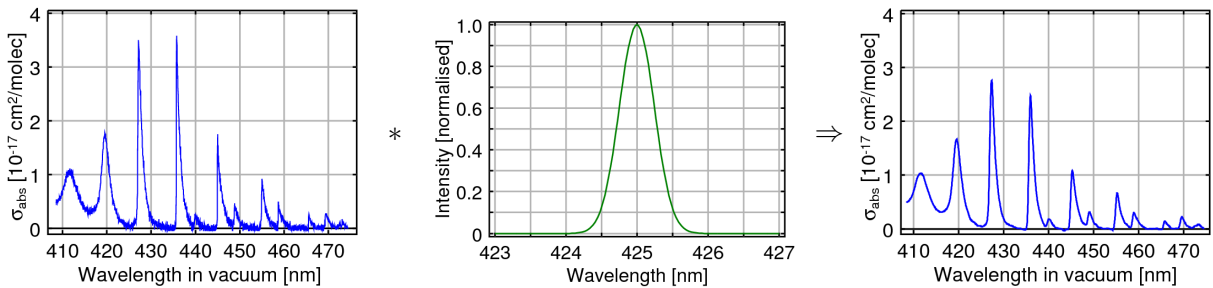
Figure 2.2: The high resolution IO spectrum (left) is convolved with the SCIAMACHY slit function (green curve in the center figure). The resulting IO spectrum with slightly broader absorption peaks and smaller maxima is then used in the DOAS retrievals of IO from SCIAMACHY data.
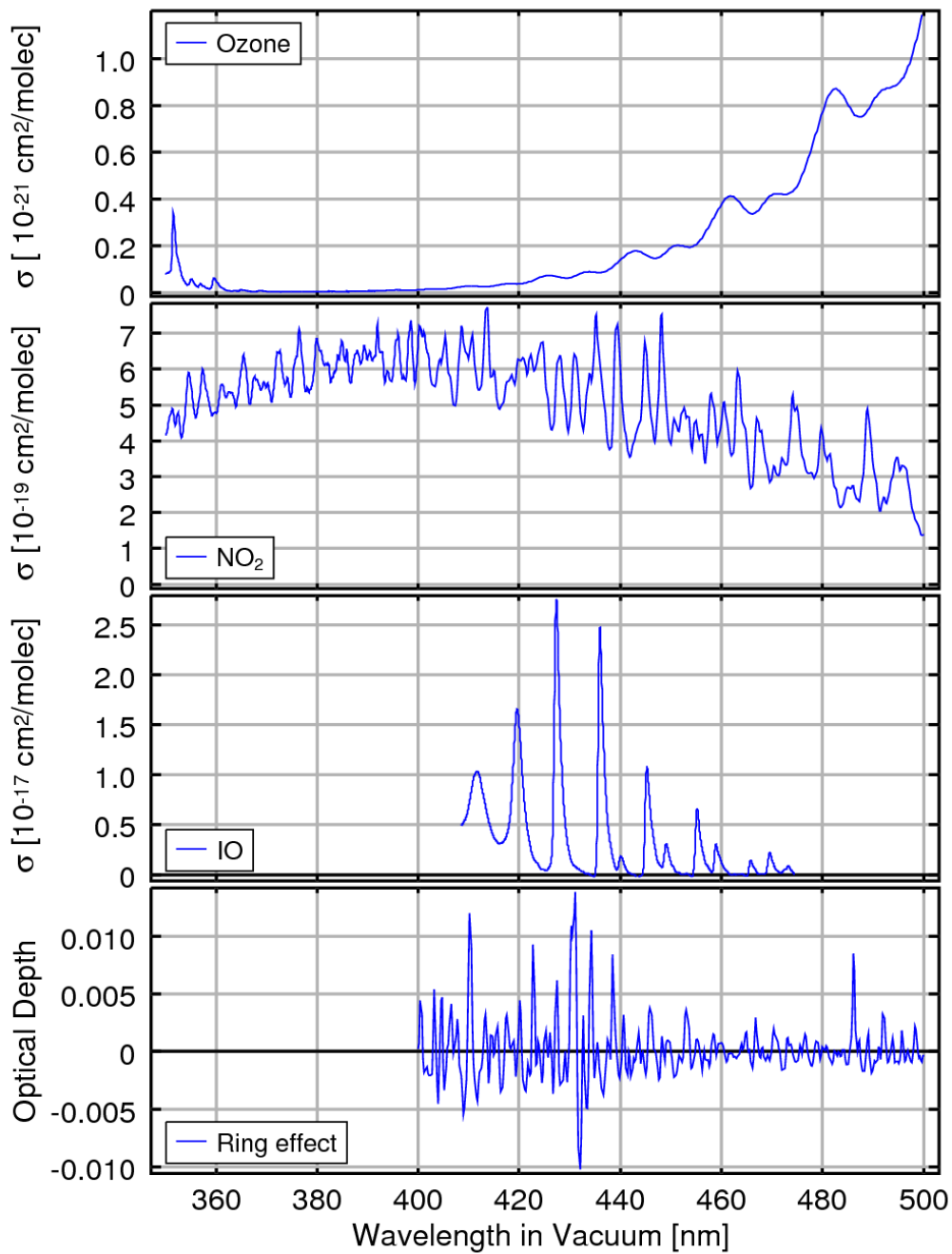
Figure 2.3: Spectra of the absorption cross sections of O_3, NO_2, and IO and the effective optical depth of the Ring effect. While the absorption cross sections are results of laboratory experiments (see references in Tab. 2.3), the Ring spectrum follows from theoretical considerations.

- Broad-band influences are accounted for by a polynomial which is subtracted from the measured optical depth (cp. Sec. 1.8). The polynomial degree, which yields the best retrieval results, depends on the size and position of the wavelength window and also on the trace gas in question. A second order polynomial turned out to be suitable for the finally chosen standard fitting window. In test fits, also higher order polynomials were used, but the fitting window of 416-430 nm is rather short, so a low degree is appropriate here.

- For the correction of possible residual stray light in the instrument during measurements, a spectrally linear stray light intensity is assumed. The stray light reference spectra are generated from the actual measurement by using factors of 0.03 for the offset and slope parameters (cp. Sec. 1.8). The resulting spectra are scaled during the fitting procedure in the same way as absorption spectra.

- An undersampling correction (Chance, 1998) is included. This is useful in case of SCIA-MACHY retrievals, due to a rather narrow slit function and low sampling per FWHM. This can cause fast varying features at the shoulders of spectral lines. The resulting influences on the measured spectra need to be corrected.

- Another important choice in a DOAS-Fit is the background spectrum to which each individual measurement is compared. In the standard IO fit, an Earthshine spectrum is chosen as background. This choice is preferred over a solar measurement in order to minimise the Ring effect and residual instrumental effects caused by differences in the viewing of Earth and Sun. The reference region was selected in the Pacific at 40°S and 160°W and within ±10° in both directions as illustrated in Fig. 2.4. This location is specifically chosen as a region where the IO signal is expected to be small, which was confirmed by fitting the Earthshine against the solar reference spectrum. Resulting IO columns from the respective DOAS fit are then differences between the current measurement and the averaged reference region. Effectively, the IO amount in the reference region is set to zero. The procedure is implemented as fit with respect to a constant Earthshine spectrum and subsequent subtraction of the daily average within the assigned reference region. This is the same as using the daily average Earthshine spectrum from the reference region. Further considerations are presented in Sec. 2.9.
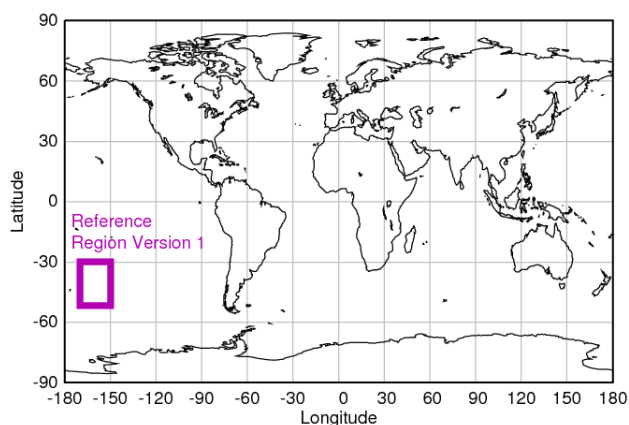
Figure 2.4: Global map showing the reference region over the Southern Pacific at 40°S and 160°W with a side length of 20° in each direction. This background region is used for all Version 1 data, e.g. the standard retrieval V1.28.

Influencing effect	Comments	Reference
IO absorption	laboratory spectrum, 293 K	Gómez Martín et al. (2007)
NO$_2$ absorption	laboratory spectrum, 223 K	Bogumil et al. (2003)
O$_3$ absorption	laboratory spectrum, 223 K	Bogumil et al. (2003)
Rot. Raman scattering	SCIATRAN calculation, (Sec. 1.6.3)	Vountas et al. (2003)

Retrieval parameter	Settings
Wavelength region	416 - 430 nm
High-pass filter polynomial	2nd order
Stray light correction	
offset parameter	0.03
slope parameter	0.03
Background spectrum (I$_0$)	constant Earthshine spectrum

Table 2.3: Overview of the retrieval settings valid for the current standard fitting routine of IO columns from SCIAMACHY, as applied for product version V1.28. Top panel: Absorption effects by trace gases and Raman scattering. Bottom panel: Additional retrieval parameter settings.

2.2.2 Fit quality and consistency of the IO standard fit

The quality of a retrieval needs to be judged in different ways. Apart from checking the results for consistency and for absence of artefacts, one important test for the fit quality is the magnitude of the residual. Only if the remaining residual is reasonably small, the fitting procedure has been successful. Additionally, it is necessary that the residual spectrum is also free of regular structures, but mostly consists of a noise signal. Therefore, if different retrieval settings are compared, an improved fit should reveal a reduced and less structured fitting residual.

Judging the quality of a satellite DOAS retrieval

When the overall product quality of a DOAS retrieval from satellite data is assessed, there are several considerations that should be taken into account. First of all, the retrieval quality itself, i.e., the rms-value is important (cp. Sec. 1.8). When the fit is improved, the magnitude of the rms will decrease, but this does not suffice as a quality check. Other inspections are necessary, which are mostly consistency checks:
- Physically not logical results, e.g., negative trace gas columns, need to be avoided. This applies to the trace gas in question, but also to all other included absorbers and effects in the fit.
- The results for the other trace gases included in the fit routine, which are already well known, need to be reasonable, i.e. reasonable amounts and the known tendencies, spatial variations, special regions etc. should be reproduced.
- The applied correction effects, especially the Ring effect in the present study, need to receive the correct algebraic sign in the different regions and reasonable magnitudes.
- Another important test involves additional measurements. Good agreement with ground-based

measurements and results from other studies is desired. This requires available studies for comparison and is discussed separately in Chapter 4.

These considerations have been taken into account when judging the fit quality of the different IO retrievals. According to the respective results, the current standard IO retrieval performed satisfactorily and example results of the performed tests are presented in the following paragraphs.

Two example fit results for the IO absorption

From the aforementioned standard IO fit V1.28, example fit results are displayed in Fig. 2.5 for two individual SCIAMACHY measurements. Both spectra were selected from orbit number 20051001_110 on the first of October, 2005, on the Southern Hemisphere. Exact data is given in the figure caption. The two examples are chosen for two different amounts of IO, i.e., 2.1×10^{13} molec/cm^2 (a) and 1.3×10^{13} molec/cm^2 (b). The figure shows the differential absorption of the specific measurement at the top in terms of optical depth. This spectrum still includes all absorption features, but the fitted polynomial has already been subtracted. The bottom panel shows the final residual, where all assigned effects have been eliminated from the spectra. Only the unassigned structures remain and it is visible, that the residual does not exhibit any large left over absorption features and mainly consists of measurement noise. The rms values of the residual given in the figure caption are very close to the theoretically calculated limit which is possible with SCIAMACHY recordings in this wavelength region. The three graphs in the middle show the retrievals of NO$_2$, the effective Ring structure (sum of Ring and stray light effects) and IO. The blue solid line represents the scaled reference spectrum, while the red dotted line is the reference spectrum plus the residual structure. The retrievals show that IO is detected in these cases and that the residual does not contain noticeable systematic structures. This gives confidence to the chosen fit parameter settings.

Results for NO$_2$ in the IO standard fit

The IO retrieval settings are not optimised for the retrieval of NO$_2$ of course, but nevertheless the fits of the other included trace gases apart from IO need to perform reasonably well. The two presented measurement results above originate from the Southern Ocean close to Antarctica. Here, one is concerned with relatively small optical thicknesses of all included absorbers in general. In comparison to the background region in the Pacific, e.g., the retrieved NO$_2$ amount is hardly different in this remote site and also the optical depths of the other effects are small. This naturally causes the noise level to be more prominent than in cases of strong absorption signals. Moving over to a completely different area on Earth, e.g. to the highly industrialised Asian cities, the fit results for NO$_2$ look quite different. One example is displayed in Fig. 2.6(a) for a total NO$_2$ slant column of $2.64\pm0.05\times10^{16}$ molec/cm^2 ($rms = 1.6\times10^{-4}$). This retrieval is taken from a measurement on March 1$^{\text{st}}$, 2006, at 40.75° N 124.25° E, and the spectral fit exhibits only a small relative error demonstrating a good performance of the NO$_2$ fitting. Figure 2.6(b) shows global results for tropospheric NO$_2$ averaged over three months (Mar-May 2006). The stratospheric NO$_2$ has been eliminated from the total column by subtracting the NO$_2$ amount from a reference sector (180°-200° East, where tropospheric amounts are negligible). This approximation assumes the

(a) **(b)**
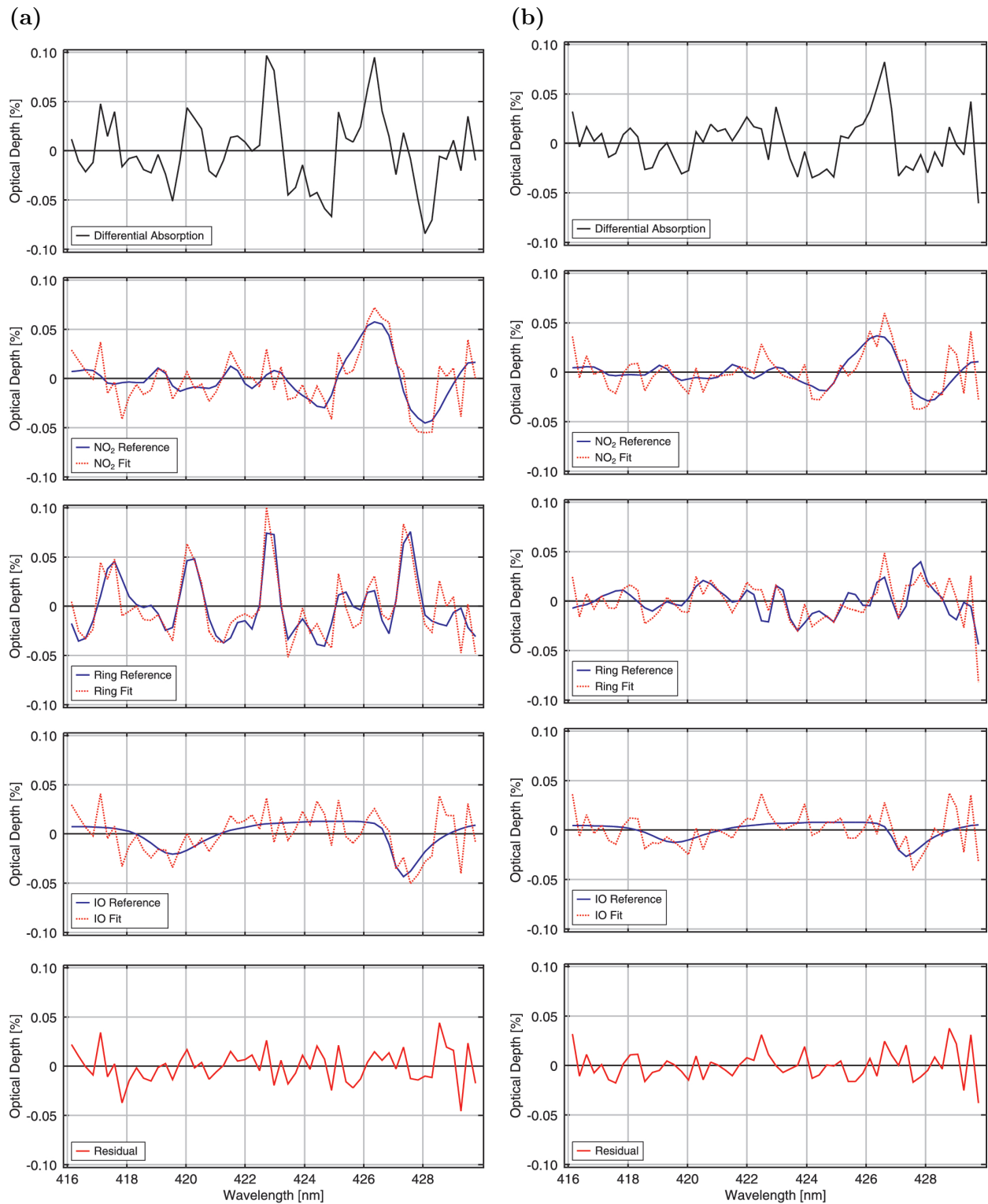
Figure 2.5: Two example fit results of the standard IO fit including graphs for the differential absorption (top), the remaining residual (bottom) and in between the trace gas fits for NO_2, the Ring effect and IO. The trace gas fits show two curves each - the actual fit from the measurement still containing the residual structure (red dotted lines) and the respective reference cross section scaled with the retrieved slant column amount (blue solid line). Both measurements belong to orbit 20051001_110. **(a)** was taken at 70.7° S, 53.7° W with an IO amount of $2.1\pm0.5\times10^{13}$ molec/cm^2 , $rms = 1.7\times10^{-4}$, and **(b)** at 64.7° S, 48.7° W with an IO amount of $1.3\pm0.4\times10^{13}$ molec/cm^2 , $rms = 1.5\times10^{-4}$.

stratospheric NO_2 amount to be constant with longitude, deviations from this assumptions occur but are not relevant in this case.

No detailed analysis of the NO_2 results shall be given, but it shall be recognised that the important features of NO_2 like the highly industrialised and polluted areas of Europe, America and Asia are captured by the retrieval. The spatial distribution agrees well with reported NO_2 retrievals (Richter et al., 2005), while the absolute values lie in the right order of magnitude, but are somewhat smaller in urban areas. This is mainly due to the use of a cross section at cold temperatures (223K), which is suitable for the IO retrieval but gives too small column amounts for NO_2, because the absorption cross section is stronger than at warmer temperatures (e.g., 293K). Additionally, only a rough consideration of the AMF has been performed without optimising the procedure for precise NO_2 vertical columns, but the main point here lies on fit quality and not on the absolute amount of the NO_2 vertical column. The NO_2 analysis shows that the standard IO fit performs well also for other trace gases.

(a)

(b)
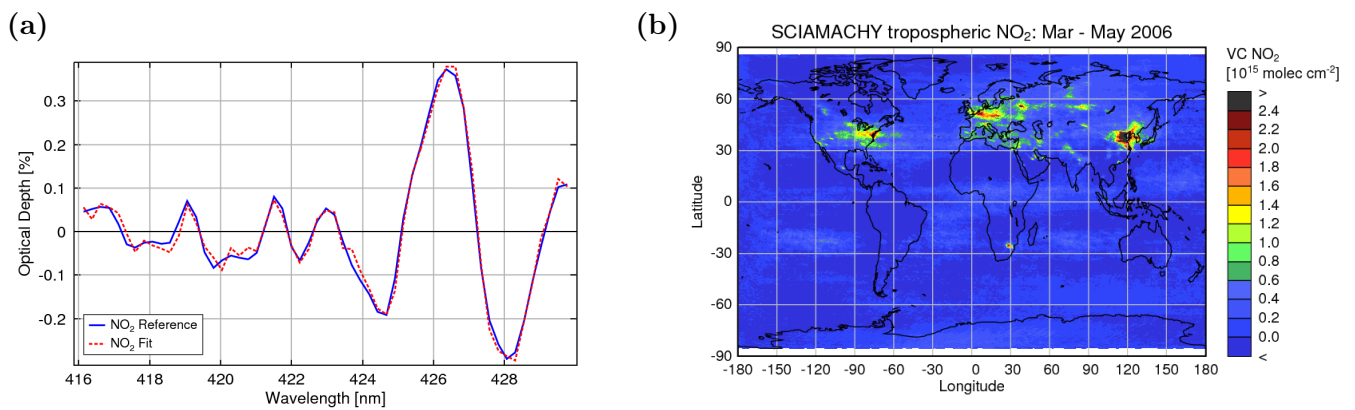
Figure 2.6: (a) A typical NO_2 fit result ($rms = 1.6 \times 10^{-4}$) where the scaled laboratory cross section and the measurement agree very well. **(b)** Global distribution of NO_2 for three months (March-May) in 2006, where industrialised areas and also single cities can be distinguished. The absolute NO_2 amounts are too small due to the chosen cross section temperature and the rough consideration of the AMF, but this is not relevant here, as this scaling has no influence on the quality of the IO retrieval.

Results for the Ring effect in the IO standard fit

The results for the Ring effect from the IO retrieval are a crucial part of this study. In several retrievals other than the IO standard fit, the spectral correlation between the IO absorption cross section and the Ring effect spectrum leads to erroneous slant columns and fit factors for IO and the Ring effect, respectively. The choice of unfavourable fit parameters then leads to an irregular spatial correlation between the IO and Ring patterns in several locations on Earth. There is no physical reason why atmospheric IO amounts should be well correlated to the Ring effect, although in some cases certain causalities may lead to similar behaviour in both effects. The detection of a generally strong spatial correlation between the results would point out an interference during the retrieval procedure. Consequently, the Ring effect results serve as an additional criterion for the judgement of the fit quality: the Ring fit factors should yield meaningful values and also the spatial

Ring pattern should not be detected in the IO result in the same form.
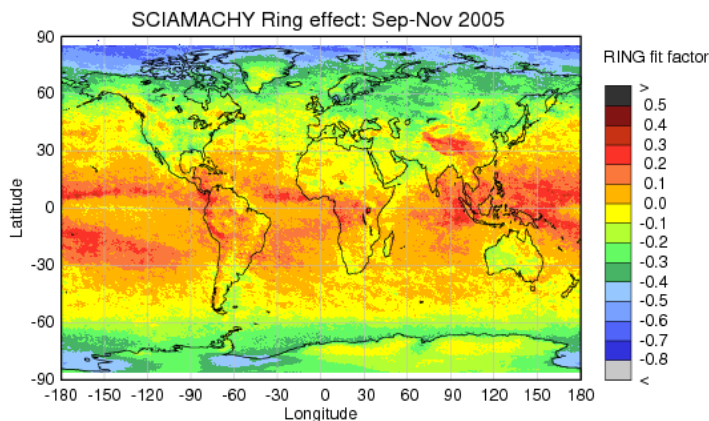
Figure 2.7: Global map of the Ring effect fit factor averaged over the three months from September to November 2005. Negative fit factors denote the occurrence of rotational Raman scattering while a positive fit factor is found if the RRS is smaller than in the background spectrum.

For the standard IO fit parameter set, an example of the retrieved fit factors for the Ring effect is plotted in Fig. 2.7. The data is averaged over a period of three months, September to November 2005. The Ring effect is expected to be strong over low ground elevation, while clouds and high surface elevations such as mountain ranges and plateaus lead to a smaller Ring effect. Additionally, the fit factor depends on the SZA with larger Ring effect for larger SZA. An additional small effect is induced by the surface reflectance with decreasing Ring effect for brighter surfaces, because the Raman scattered radiation is relatively reduced in comparison to the reflection at the ground. These dependencies originate from the individual photon path lengths through the atmosphere, especially from the path length in the lowest atmospheric layers, as the probability for Raman scattering becomes higher for higher air density. The infilling increases, for a large ratio of Raman to Rayleigh scattering.

Due to the definition of the effective pseudo-absorber spectrum for the Ring structure (Sec. 1.6.3), a strong Ring effect corresponds to negative fit factors. The filling in of absorption lines appears like an emission process. As an Earthshine background spectrum is used, the results are relative to the respective location over the South Pacific. Positive fit factors therefore mean a Ring effect which is weaker than at that location.
Regarding these considerations, the fit factors of the Ring effect in Fig. 2.7 show meaningful values. The fit factor tends to stronger negative values (green/blue) for higher latitudes due to the increasing solar zenith angle. In addition, several mountain ranges and regions with high surface elevation exhibit positive (red) values as expected. For example, the Himalaya and typically cloudy regions in the tropics can be distinguished. Even the Alps can be identified, especially in longer term averages, but already here as yellow area surrounded by green colour.

In conclusion, the retrieval yields sensible and explicable results for the Ring fit factors and is not disturbed by retrieval errors or systematic correlation with the IO amounts. As can be seen later in the global IO maps (cp. Fig 2.12), there are no prominent features in the IO result which would correlate only with the Ring effect. These observations give further reassurance to the quality of the standard IO retrieval.

2.3 Air mass factor considerations for the IO retrieval

As described in Sec. 1.8, the AMF transforms the slant column into a vertical column. In order to compute the vertical column from the satellite slant column results, several assumptions are necessary. In the present case, some factors are not well known and therefore the regular transformation of slant into vertical columns would introduce large uncertainties. Therefore, the slant columns are retained and a standard conversion into vertical columns needs to wait until the open questions have been answered. Nevertheless, the computation of AMFs is of interest. For a given vertical column, the present AMF describes the sensitivity of the satellite measurement for the trace gas detection. Therefore, some considerations on typical AMFs for some given cases are necessary for a better interpretation of the IO results.

In general, a large slant column amount may be enhanced due to (at least) two different causes. Either the trace gas amount might be large or, alternatively, the AMF may be enhanced. The first case is obvious and the second case evolves as a consequence of surrounding conditions. The light path through a trace gas layer is affected by, e.g., the solar zenith angle, the ground spectral reflectance, the aerosol load in the atmosphere, clouds and the trace gas altitude profile. These aspects need to be taken into account if absolute values are interpreted, and sometimes also if qualitative comparisons are made.

Block AMFs have been calculated for a pure Rayleigh atmosphere and several typical conditions. For iodine species, the mid-latitude marine boundary layer as well as Polar Regions, which are typically ice covered, are of special interest. The SZA and the albedo have been varied as well as the influence of a low and strongly reflecting cloud has been been investigated.

The influence of the SZA

For Antarctic locations like Halley Station (cp. Sec. 3.2.2), the mimimum SZA lies around 55° and maximum SZA used in the data product is 84°. Figure 2.8 shows the block AMF for SZAs of 55°, 70° and 80° at altitude levels between the Earth surface and 10 km for an albedo of 90%. For IO being situated at low altitudes, probably even in the lowest part of the boundary layer, the influence of the SZA on the near-surface block AMF is on the order of 10%. In the upper part of the troposphere the AMFs differ strongly (by a factor of 2). However, towards the ground, the block AMFs converge to values between 3.8 and 4.4.

The influence of the albedo

For a solar zenith angle of 70°, the influence of a changing albedo is demonstrated in Fig. 2.9. Especially for low altitudes, the effect is huge. Increasing the albedo from a typical value of 5% (e.g. over the ocean) to 90% (for bright snow or ice) changes the block AMF directly at the Earth's surface by a factor of 6 from 0.7 to about 4.1. The total AMF for an IO profile in the lowest 1 km, differs by a factor of 4.

This observation is important for IO retrievals as the amounts are often close to the detection limit, which is strongly influenced by the AMF. The determination of the detection limit is the topic of the next section. Considering a given IO amount, it might be below detection limit over a dark

Figure 2.8: Comparison of block air mass factors at different solar zenith angles calculated with SCIATRAN Version 2.0 (Rozanov et al., 2005b) for 425 nm and an albedo of 90%. The influence of the SZA is large in the upper troposphere but rather small towards the Earth's surface. For IO amounts in the lowest layers, the SZA therefore has not such a big relevance.

surface, but well observable over a bright underground.

Influence from the IO altitude profile

As oceanic areas belong to the interesting regions for IO, it is also important to note the strong altitude dependence of the block AMF for this case (e.g. Fig. 2.9, blue curve). If the block AMF changes a lot with height, the assumed trace gas profile will have an effect on the calculation of the total integrated AMF. For a SZA of 70° and an albedo of 90% (red curve), the block AMF is nearly constant with height. For all other examples of varying SZA and varying albedo, this is not the case and the trace gas profile will have a strong influence. Depending on the individual situation, the vertical column may change by a factor of ~ 3, between an IO profile confined to the boundary layer or distributed over the troposphere.

Impact of clouds on the AMF

The impact of clouds on the AMF and especially on the block AMF profile can be quite large. The exact calculation also depends strongly on cloud parameters like liquid water content, cloud structure and droplet sizes. No detailed analysis of cloud influences on the AMF shall be given here, but one central aspect shall be pointed out. The typical light path enhancement within the

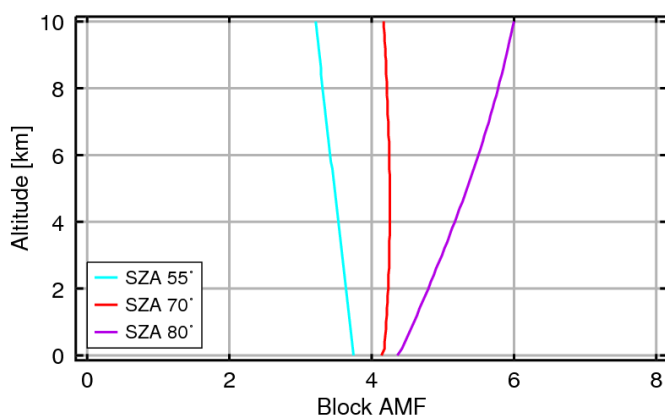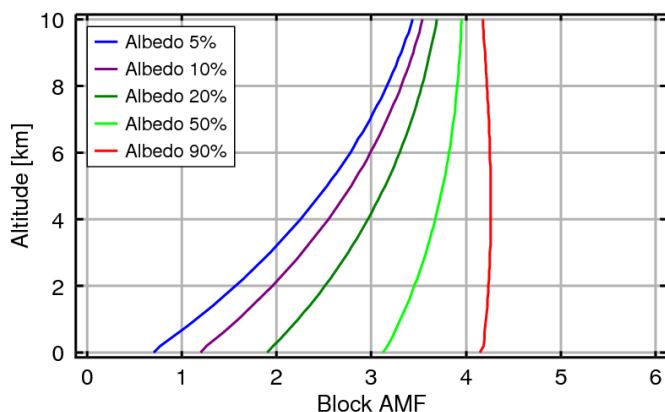**Figure 2.9:** Comparison of block air mass factors for different albedo situations calculated with SCIATRAN Version 2.0 (Rozanov et al., 2005b) for 425 nm and a SZA of 70°. The strong influence of the ground reflectance on the block AMF close to the surface, and consequently also on the sensitivity towards IO detection is visible - the block AMF close to the surface increases from 0.7 at 5% to 4.1 at 90%.

cloud top is also neglected here, only the effect on the path above the cloud shall be considered. Three block AMFs are compared for this purpose in Fig. 2.10. All curves are calculated for equal conditions, except for the albedo and the presence of a cloud. The SZA is 55° in all three cases. Two curves reach down to the ground and are calculated for an albedo of 5% (green) and 90% (light blue). The strong blue curve is calculated for a bright 100% reflecting cloud (no visibility below the cloud) at 1 km. The comparison shows that the difference between the 90% albedo case and the cloud covered situation is small above 1 km. The sensitivity towards IO in the upper layers would be the same and IO amounts below the cloud would simply be ignored. The situation is different over a dark surface. The block AMF above 1 km changes strongly between the 5% reflecting ground and the cloudy scene. The AMF above 1 km is much larger above the cloud. Considering satellite measurements, this means that a partly cloudy pixel will carry most information from the cloud covered part dominating the information content coming from the cloud-free portion. For the 90% albedo case, IO amounts in the cloud-free part would stand a larger chance to be observed in spite of some masking in the cloudy region.
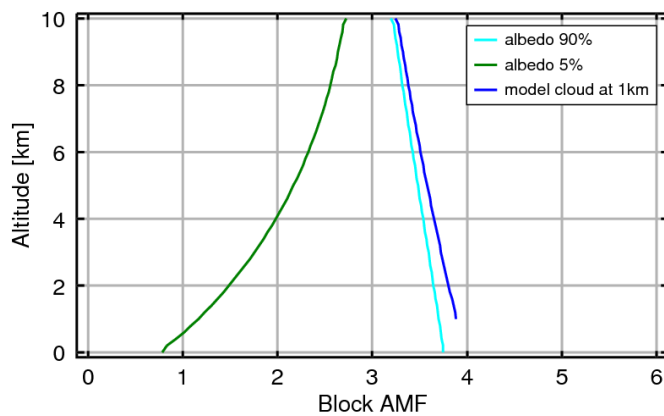
Figure 2.10: Comparison of block air mass factors for three different cases, an albedo of 5%, an albedo of 90% and for the case of a 100% reflecting cloud at 1 km altitude. While the difference above 1 km is very small between the cloudy case and the highly reflecting surface case, the change is large over a dark surface when a cloud is present.

Summary

The main outcome of the analysis of the AMF are the following points:

- The overall AMF for IO can vary strongly depending on conditions.

- The solar zenith angle has only a small influence on the AMF for trace gases close to the ground, as long as the SZA does not exceed 80°. The SZA influence is much larger at higher altitudes, and is therefore probably not highly relevant for IO.

- The albedo, in contrast, shows a strong influence especially close to the ground, where the block AMF may vary by a factor of 6 between extreme conditions. The integrated AMF for IO will typically vary between 1 and about 4.

- Strongly reflecting clouds, which hide the atmosphere below from the view of the satellite, provoke largest changes if the surface below is dark (albedo of 5%), while for a bright surface the main effect is the simple disregard of the low layers.

- Due to the uncertainties introduced by the unknown vertical profile of IO, the slant columns will not be converted to vertical columns in the standard IO product. However, the AMF considerations above are valuable information needed for the interpretation of IO amounts, temporal/spatial variances and detection limits in individual cases.

2.4 Detection limit for IO

The detection limit of a measurement states the smallest amount of a trace gas, which can still be identified by the respective method. This is an important value to be considered for the judgement if a measurement task is promising.

In order to estimate the detection limit of SCIAMACHY for the identification of IO slant columns, several factors determined by the instrument, the measurement procedure and algorithm as well as the physical processes need to be considered. A relevant parameter in this respect is the signal-to-noise ratio (S/N) of the measurement. The minimal optical depth OD_{min} still detectable by the instrument is determined primarily by the inverse of this value, the ratio of the noise w.r.t the signal (N/S), which will be shown below.

The signal-to-noise ratio

The signal S is given by the number of electrons generated by incoming photons with photon flux F_γ (in photons/s/pixel) at the detector during the measurement integration time t (in s) and with quantum efficiency q_e (electrons/photon):

$$S = q_e \cdot t \cdot F_\gamma$$

The signal strength therefore depends on parameters like the spectral region, the surface spectral reflectance and the solar zenith angle in combination with the respective integration time. The noise amount N is the value for the total noise per detector pixel arising in the measurement process and contains all disturbing effects, mainly from three different processes generating additional signals on the detector. These noise signals are the statistical photon noise N_i, the read-out noise N_r and the noise of the dark current N_d. As the physical emission process is of statistical nature, the photon signal is determined by Poisson statistics and is therefore described by a Poisson distribution, which converges to a normal distribution for large photon numbers. Consequently, the statistical noise N_i (shot noise) is given by the square root of the signal $N_i = \sqrt{S}$. The read-out noise is generated by the electronics during the read-out procedure and is independent of integration time and signal strength. The dark current which is present also if no radiation meets the detector has a statistical noise signal as well. The magnitude of N_d increases with integration time of the measurement and strongly depends on the detector temperature. It is effectively suppressed by detector cooling. In total, the signal-to-noise signal is given by:

$$\frac{S}{N} = \frac{S}{\sqrt{N_i^2 + N_r^2 + N_d^2}}$$

In the present case, the read-out noise is small and, especially with the given large photon flux in the visible spectral region and a well cooled detector, the dark current noise is mostly negligible in comparison to the signal noise $\sqrt{S}$. This yields: $\frac{S}{N} \approx \sqrt{S}$.

The minimum detectable optical depth

The optical depth OD between the actual intensity measurement $I = S \pm N$ and the background measurement I_0 is calculated in the following way:

$$
\begin{aligned}
\text{OD} \quad &= \quad \ln \frac{I_0}{I} \quad = \quad \ln(I_0) - \ln(S \pm N) \quad = \quad \ln(I_0) - \ln(S) - \ln(1 \pm \frac{N}{S}) \\
&\approx \quad \underbrace{\ln(I_0) - \ln(S)}_{\text{OD}_{\text{real}}} \quad \mp \quad \underbrace{\frac{N}{S}}_{\text{OD}_{\text{error}}}
\end{aligned}
$$

The first term in this sum is the undisturbed optical depth OD_{real}, while the second is the error in the optical depth. The approximation made in the last step holds if $N \ll S$, which is valid for a sufficiently high measurement intensity. If I_0 is chosen from an Earthshine measurement, the noise can be reduced by averaging and in that case be neglected in comparison to the noise of each individual measurement I. Otherwise, the noise in the background measurement will, of course, further increase OD_{error}. Demanding a stronger OD signal than the error OD for reliable detection, leads to the requirement of the minimum detectable optical depth OD_{min} :

$$
\text{OD}_{\text{min}} \quad \approx \quad \frac{N}{S} \quad \approx \quad \frac{1}{\sqrt{S}}
$$

For the wavelength region under consideration here, the theoretically expected S/N-ratio is on the order of 5000 for an albedo of 90% and 2000 for 5% albedo (Noël et al., 1998). The error or root mean square of the optical depth (OD_{rms}) is then on the order of 10^{-4} depending on conditions. Typical experimental OD_{rms} values from the IO retrieval (cp. Sec. 2.2.2) lie around 2×10^{-4} (between $1\text{-}3 \times 10^{-4}$).

The comparison between the experimental detection limits and the theoretically estimated numbers allows the conclusion that the retrieval is close to optimal performance. The theoretical limit is only slightly smaller than the experimentally identified values. Much stronger reduction of the residual rms value is most probably not possible. Some remaining influence on the residual is also caused by systematic effects and is hence independent of averaging.

Consequences for the slant column detection limit

For an ideal measurement, the slant column detection limit (SC_{lim}) is given by the ratio of the residual optical depth OD_{rms} and the maximum differential absorption cross section value of the respective trace gas σ_{max}.

$$
\text{SC}_{\text{lim}} \quad = \quad \frac{\text{OD}_{rms}}{\sigma_{\text{max}}}
$$

This analysis assumes that a trace gas is detectable if its absorption optical depth becomes

larger than the residual *rms* value. For IO ($\sigma_{\max}$ =2.8×10^{-17}cm^2/molec) and a residual *rms* of 2×10^{-4} (typical for 90% albedo), the detection limit is given by SC$_{\mathrm{lim}}$ = 7×10^{12} molec/cm^2 for a single measurement. This limit can be further reduced by averaging, in time or space, provided the source of errors is random and systematic errors have been accounted for. The theoretical *S/N*-ratio at 5% albedo corresponds to an *rms* value of about 5×10^{-4} and an IO slant column detection limit of 2×10^{13} molec/cm^2 for a single measurement. For the spatially averaged ground scene of 60×120 km^2, used in this study, the theoretical SC limit is reduced by a factor of 2.

For experimental results (i.e. also for a ground scene size of at least 60×120 km^2), with the above mentioned OD$_{rms}$ values around 2×10^{-4}, the typical IO slant column detection limit is 7×10^{12} molec/cm^2. This limit is then further decreased by temporal averaging in a subsequent step. For monthly averages and for a SCIAMACHY overpass every six days, the SC detection limit is reduced to around 3×10^{12} molec/cm^2. This reduction obviously depends on the number of overpasses and the averaging time period.

The conversion to vertical columns and mixing ratios

The detection limit is useful for an estimation if the satellite observations are capable of identifying expected trace gas amounts. Many measurements of IO have specified the ground volume mixing ratio instead of a column amount. In order to judge if these amounts should be detectable by SCIAMACHY, the detection limit on the slant column needs to be converted to a detection limit for the surface mixing ratio. Naturally, this conversion will introduce the usual uncertainties discussed previously. Assumptions on the appropriate AMF, and in particular on the altitude profile of IO are necessary. The altitude profile enters the conversion twice, once in the AMF calculation and another time in the conversion from the vertical column to the mixing ratio. According to current knowledge (cp. Sec. 1.5), IO is primarily a tropospheric trace gas (Friess et al., 2001) with evidence for confinement to the lower part of the boundary layer Saiz-Lopez et al. (2007c). Assuming the IO to be situated in the lowest 1 km or in the lowest 100 m is consequently reasonable.
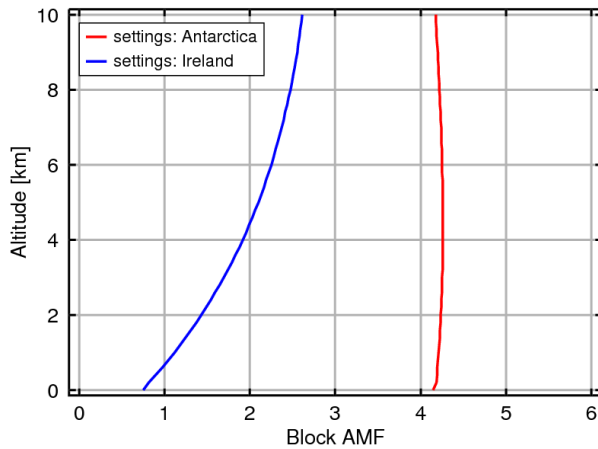
Figure 2.11: Block air mass factors calculated with SCIAMACHY Version 2.0 Rozanov et al. (2005b) for 425 nm, and two relevant example locations, red: 90% albedo, 70° SZA (typical for Antarctic coast), blue: 5% albedo, 55° SZA (typical for Ireland). The sensitivity for IO detection is several times higher for Antarctic conditions.

Following the AMF discussion in the previous section, two typical cases are chosen here as examples. For a typical situation at the Irish coast with 5% surface reflectance and 55° SZA the

total AMF then amounts to approximately 1.0, in contrast to 4.2 for a typical case for Antarctica at 90% albedo and 70° SZA. These values hold for an IO box profile within the lowest 1 km (with linear concentration decrease to zero up to the next altitude grid point at 1.2 km). Figure 2.11 shows the block AMF for the two different settings, similar to the general cases discussed in Sec. 2.3. The larger sensitivity for the detection of IO under typical Antarctic conditions is again visible. For the Antarctic case, the AMF is hardly profile dependent, while for the mid-latitude coastal situation the AMF reduces to 0.8 if the IO is assumed to be well mixed only in the lowest 100 m.

Theoretical detection limits for individual measurements				
	Antarctic		Irish coast	
SC (molec/cm^2)	7×10^{12}	7×10^{12}	2.0×10^{13}	2.0×10^{13}
box profile height	1 km	100 m	1 km	100 m
AMF	4.2	4.2	1.0	0.8
VC (molec/cm^2)	1.7×10^{12}	1.7×10^{12}	2.0×10^{13}	2.5×10^{13}
VMR	0.7 ppt	7 ppt	8 ppt	100 ppt
Experimental detection limits for measurements averaged over 60×120 km^2				
	Antarctic		Irish coast	
SC (molec/cm^2)	7×10^{12}	7×10^{12}	7×10^{12}	7×10^{12}
box profile height	1 km	100 m	1 km	100 m
AMF	4.2	4.2	1.0	0.8
VC (molec/cm^2)	1.7×10^{12}	1.7×10^{12}	7×10^{12}	8.8×10^{12}
VMR	0.7 ppt	7 ppt	2.8 ppt	35 ppt

Table 2.4: Detection limits for SCIAMACHY observations of IO for some typical conditions. The detection limits for the slant columns (SC) result from theoretical considerations (top panel) and experimental evidence upper limits (bottom panel). Conversion of values yield the vertical column (VC) and the volume mixing ratio (VMR) in dependence of two assumed box profile heights (with homogeneous mixing below this height) and the calculated AMF (using the SCIATRAN 2.0 code). For monthly averages, typically additional reduction by a factor of around 2 can be achieved depending on the number of overpasses.

Using the slant column detection limits determined from theoretical considerations as well as from the experimental findings, the detection limits for the vertical columns and volume mixing ratios are calculated. For several relevant cases and assumptions discussed above, the results are summarised in Tab. 2.4. Strongly influenced by chosen conditions, VMR detection limits are highly variable and may lie between 0.7 ppt and 35 ppt.

Discussion of detection limits

The analysis shows that IO amounts reported by ground-based measurements (Sec. 1.5.5) are close to the IO detection limits for a single SCIAMACHY ground scene. Often the detection limit will inhibit

the IO observation from satellite. In some cases, especially in the Antarctic, reported amounts are indeed somewhat higher than the detection limit. For these cases, positive detection of IO from satellite can be expected under an additional condition. The spatial extent of the enhanced IO amounts needs to be on the order of a satellite ground-pixel. This is an important point, because the available ground-based and balloon measurements made so far are unable to determine the spatial extent of IO release and it is unknown how localised enhanced IO occurs. IO release related to algae emissions may be confined to very local spots. In that case, the mixing ratios would need to be much larger to enable SCIAMACHY to detect the IO absorption.

2.5 Precision and accuracy of the IO retrieval

Every measurement result is inherently affected by some uncertainties. These effects are caused by statistical as well as by systematic effects. While statistical errors may be reduced through averaging, systematic inaccuracies remain also after the averaging procedure. In general, the statistical errors of an experiment affect its precision, while systematic deviations determine the accuracy of a measurement.

Statistical errors

The discussion of the detection limit in the previous section already considers the statistical effects. Consequently, the determination of the detection limit concurrently yields the precision of an individual measurement. The values computed for the slant column detection limit can be directly transferred to the column precision as the noise in the optical depth considered above (OD_{error}) leads to statistically fluctuating slant column results. The IO slant column results from satellite measurements presented in the following chapters are typically averaged over at least 3 months and therefore exhibit better precision. This may improve the precision by a factor of 4 as compared to the experimental error values which are used for the detection limit calculation from individual spectra above.

From the findings in the previous section that the experimentally identified residuals are at most two times larger than theoretically possible, it can be followed that a major part (at least 50%) of the remaining residual is usually caused by statistical fluctuations. The statistical error in seasonal averages of IO slant columns is then calculated to be at least 1×10^{12}molec/cm^2.

Inaccuracies due to spectral correlations and scaling errors

The accuracy is basically determined by three different types of systematic effects. The first type causes interferences during the retrieval process. A typical example is the spectral correlation between two or more trace gases considered in the retrieval. Inaccuracies in the cross section spectra, approximations in the calculation and consideration of the Ring effect and stray light as well as unidentified spectral structures and left over instrumental effects (such as the memory effect or similar) also belong to this category. The consequence are residual features, which increase the possible error in the retrieved trace gas amounts.

This part of the systematic errors is minimised by the specific choice of retrieval parameters. Largest

systematic error sources are thus largely excluded by the consistency checks presented in Sec. 2.2, but some particular inaccuracies might remain. In Section 3.1, some irregular, negative slant column values will be pointed out. These values are on the order of 3×10^{12} molec/cm^2 in averaged data, so some systematic influence on this order of magnitude from spectral correlations is possible, but can be largely prevented by consistency checks.

A second type of influences are scaling errors, which are not attributed to disturbing effects during the retrieval process. These errors would even occur under perfect measurement and retrieval conditions, i.e., especially also for simulated measurements without noise. One prominent example of this class of errors is the temperature choice for the cross section reference. All absorption cross sections depend on the temperature of the absorbing molecules. Due to thermal energy and the resulting occupation probabilities of energy levels, line strengths typically decrease with rising temperature. The applied IO cross section in this study has been measured in the laboratory at room temperature, 298 K (Gómez Martín et al., 2005; Spietz et al., 2005). Temperatures in Antarctica, e.g., are colder and therefore the absorption strength per molecule is stronger. As a consequence, the retrieved IO amount will be systematically too high by some percentage. IO spectra at other temperatures are not available, but estimations using BrO as measure for comparison are possible, for which cross sections have been determined by Fleischmann et al. (2004) at various temperatures. Adjusting the differential absorption line magnitude measured at 298 K to the one at 243 K, e.g., requires a scaling by 17%. Depending on region and temperatures, the effect may be differently strong, but generally ranges between 0 and 20%.

Additionally, a third category of individual influences can be distinguished, with mostly varying impact and typically leading to offsets on the retrieved amounts.

The presence of clouds may introduce such additional errors. The impact of clouds on the AMF has been mentioned in Sec. 2.3 and the effect of clouds on the retrieved IO slant column maps will be discussed separately in Sec. 2.7. In principle, clouds may obstruct the IO column partly from the satellite's view, so that the retrieved IO columns are expected to be too low in the presence of clouds above the IO layer. In case of overlapping volumes of clouds and IO presence, the influence is less definite.

An additive slant column offset may result from the choice of the background Earthshine spectrum. In case some IO is present at the chosen location, this will be subtracted from the other regions. However, the background reference location has been chosen such that no IO is recognised there. Depending on how the background spectrum is considered and calculated, the resulting IO column can vary slightly. Calculations show, that the impact is on the order of below 1×10^{12} molec/cm^2. However, this is the same for all regions on Earth and does not influence an individual measurement or location. Spatial comparisons remain entirely unaffected by this source of uncertainty.

Summary of error estimates

Statistical errors: $\pm$ 1×10^{12} molec/cm^2.

Systematic errors: $\pm$ [20% + 1×10^{12} molec/cm^2 + (3×10^{12} molec/cm^2)].

The last term of (3×10^{12} molec/cm^2) is set in parentheses as this contribution can be largely suppressed and avoided by consistency tests and quality inspection of the overall fit result. Including

the additional term, the overall error could exceed 5×10^{12} molec/cm^2. Typical overall errors, however, lie on the order of $\pm$ 2-3$\times 10^{12}$ molec/cm^2. On the colour coded maps of satellite data the error sources and resulting error bars are not representable, so the above discussion needs to be kept in mind.

2.6 Example results of global IO columns

In the next sections, spatially resolved maps of IO are used for discussions and comparisons of the quality and consistency of the final IO product. As a point of comparison, a first map of the standard IO columns discussed above is placed in Fig. 2.12, also as published in Schönhardt et al. (2008). In the following discussions, influences on the IO results and potential irregularities in the product can then be assigned and highlighted accordingly. No scientific interpretation and discussion of the observed IO values themselves or the spatial and temporal distribution is given here. This is subject of Chapter 3.

In Fig. 2.12, the results of the IO slant columns are shown on a global map of the Earth. For the results of the standard IO retrieval, the same colour scale (given on the right in Fig. 2.12) is used throughout this study. The chosen colour scale combines values below 3×10^{12} molec/cm^2 into larger intervals and is followed by smaller and linear steps above. The map shows an average over three months of the year 2005, from September to November. This time period of Southern Hemispheric Spring will become important in the scientific analysis and discussion (cp. Sec. 3.2). The values entering these final maps of IO amounts obey a quality criterion limiting the optical depth rms to values better than or equal to $4 \cdot 10^{-4}$. (This causes results to be discarded, if the fit residual becomes larger than twice that specific noise level which would lead to the typical experimental detection limit of $7 \cdot 10^{12}$ molec/cm^2 for the IO slant column.)

2.7 Cloud screening

While clouds are no problem in some other wavelength ranges such as the microwave, visible radiation experiences scattering and reflection at clouds, so that measurements are in some cases considerably affected. Clouds in the field of view can cause a positive or negative bias for the retrieved trace gas amount depending on the altitude profile of the trace gas and on cloud properties, or might introduce other systematic problems. In principle, it is desirable to apply a cloud screening algorithm to the satellite data, which filters out scenes where clouds have a considerable impact.

Nevertheless, no cloud correction scheme was routinely applied to the standard IO product for specific reasons. One special interest is the investigation of IO in the high latitude regions. Some reflectivity properties of ice and snow are very similar to those of clouds so that a reliable separation of clouds from ice and snow is not routinely available yet. Of course, it is possible to apply some cloud criterion in the other regions on Earth, but not for a consistent global data set. While the advantage of applying a cloud screening is the reduction of possible systematic errors, an essential disadvantage, which is especially present for retrievals of small optical depths, is the loss of data and therefore a reduced benefit from the averaging procedure. It needs to be judged individually,
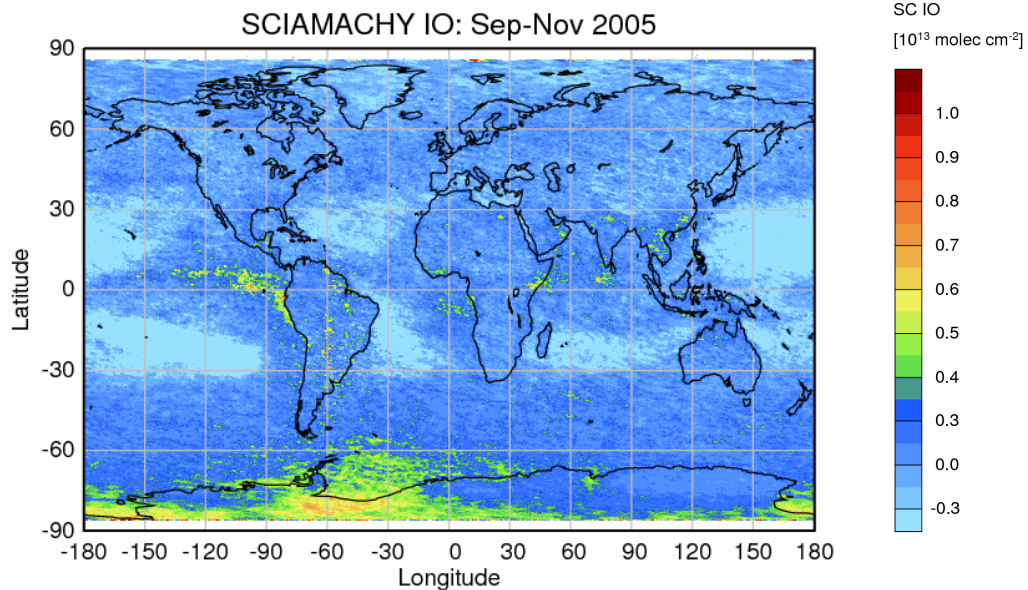
Figure 2.12: Global map showing slant column results of the standard IO fit. The IO columns are averaged over the time period of September to November 2005 and the colour code applied is shown on the right. Scientific discussion of these results is topic of Chapter 3.

which cloud screening settings are appropriate for which task.

The potential influence of clouds on the IO product was investigated in two test studies presented in the following. First, a simple cloud screening method was used for lower latitude regions, where measurements are not influenced by snow and ice. In a second test, a new and promising surface classification method, which has recently been developed at the IUP Bremen, will be applied to observations also above highly reflecting regions like the Antarctic. Distinguishing ice surfaces from bright clouds is supposed to be possible with this method, which consequently shows a high potential for cloud screening in high latitudes for the future.

2.7.1 Cloud screening with an intensity criterion

Concerning radiation in the visible wavelength region, one basic property of clouds is their high reflectivity. The overall intensity of a recorded spectrum is influenced by the amount of reflecting clouds within the field of view. From this simple consideration cloudy scenes may be roughly distinguished from cloud free ones.

The reality is more complex, as the reflectivity properties of clouds can be extremely variable, high and thick clouds reflect and scatter photons differently than low and thin clouds. Additionally, the variations of scattering and reflection properties are not clearly linked to the effects on the trace gas product, i.e., a highly reflecting cloud does not necessarily affect the trace gas retrieval most. The application of an intensity criterion nevertheless shows if the measurements are systematically affected by clouds and if artefacts are introduced.

A suitable limit for the overall intensity needs to be chosen, from which value onwards a scene is defined as too cloudy and is discarded from the product. The limit needs to lie between the lowest and highest occurring intensities, where under comparable conditions the lowest intensity

corresponds to a completely cloud free view and the highest occurs for a closed cover of bright reflecting clouds. The lower the threshold is set, the clearer the view needs to be for the measurement to pass the criterion. There is no fixed definition for the magnitude of this limit and it will in any case depend on the wavelength region in which the analysis is performed.

In the present case, a value of 1×10^5 Counts/s provided a suitable intensity threshold. In order to apply this criterion, two steps need to be taken. First of all, the recorded intensity in the respective fitting window is averaged over all spectral detector pixels. Secondly, the intensity value is divided by the cosine of the solar zenith angle (valid for Lambertian reflection) to account for the relative darkening per ground area of a scene at low sun.

In order to determine the above threshold, SCIAMACHY's PMD channels are helpful. From their different wavelength bands (cp. Sec. 1.9.1), a visual colour in the sense of an RGB (Red-Green-Blue) code can be calculated. This data is readily available and could be used without further processing within this study. When plotting the visual impression from the PMD values, cloudy scenes appear bright white over dark land or ocean regions. Figure 2.13 compares SCIAMACHY measurements over Europe on 1st September, 2005. The left map (a) shows the visual impression determined by the PMD data. Clouds can be distinguished from water and land in this figure, as the underlying surface is dark. This is not possible for snow and ice covered regions. In comparison, the right map (b) displays the intensity value recorded by SCIAMACHY in the standard IO fitting window according to the colour scale on the right. Low intensities appear green, and higher values are plotted in orange/red. The colour change to red is intentionally set at the chosen limit of 1×10^5 Counts/s. The agreement between red scenes in map (b) and cloudy areas in map (a) is reasonably good, the cloud covered areas, e.g., Northwest of Norway and over France can be determined in both pictures. It can also be recognized that some SCIAMACHY pixels where only a small fraction is affected by visible clouds will not be discarded from the final product. The intensity criterion is thus not absolutely strict and certain percentages of clouds are still allowed.
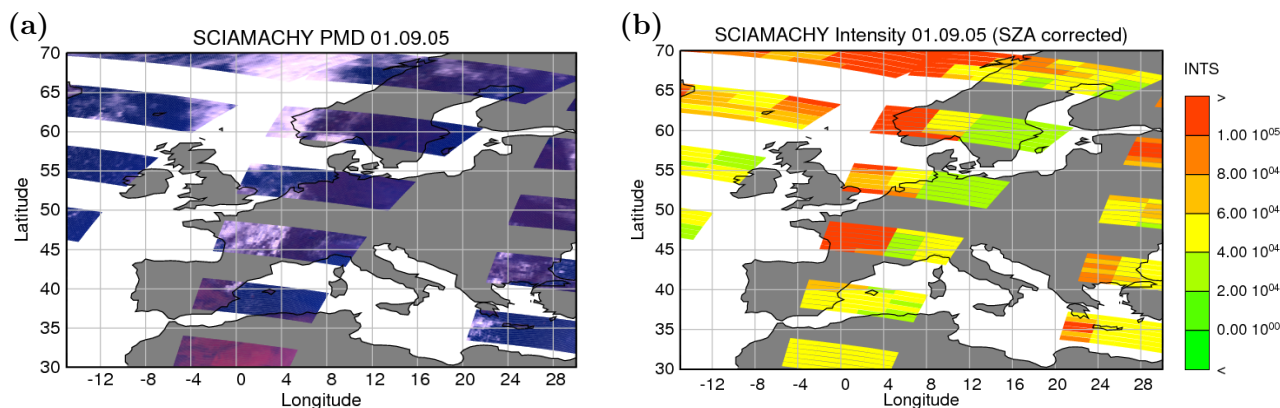
Figure 2.13: The left map **(a)** shows the visual impression of the ground scene as determined from the different PMD bands, where clouds (appearing white) can be distinguished from cloud free areas. In the right map **(b)**, the SZA corrected intensity as average within the IO fitting window is plotted for the same day and region. The highest intensities (red) occur over cloudy areas and would be discarded in the intensity limited product.

As an example of how the IO product is affected by this intensity criterion, Fig. 2.14 compares

the IO product without an intensity limit (a) to the result after application of the threshold (b). All bright regions are missing in the right map, especially the snow and ice covered Polar Regions and Greenland are completely masked. When applying the intensity criterion many measurements are discarded. This leads to a substantial increase in the final noise of the product, which is recognised by strongly varying values in low latitudes. It can be seen that the overall IO values do not change systematically and no specific artefacts are introduced when cloudy scenes are kept in the final data product. Before this is not checked, one cannot know if some enhanced IO values might be due to cloud related interferences in the measurements. However, this is not the case here.

This type of cloud screening is not useful in general for the IO product, as all ice and snow scenes are completely lost. The main result of this comparison is that no large systematic errors or even artefacts are introduced when omitting a cloud screening procedure.
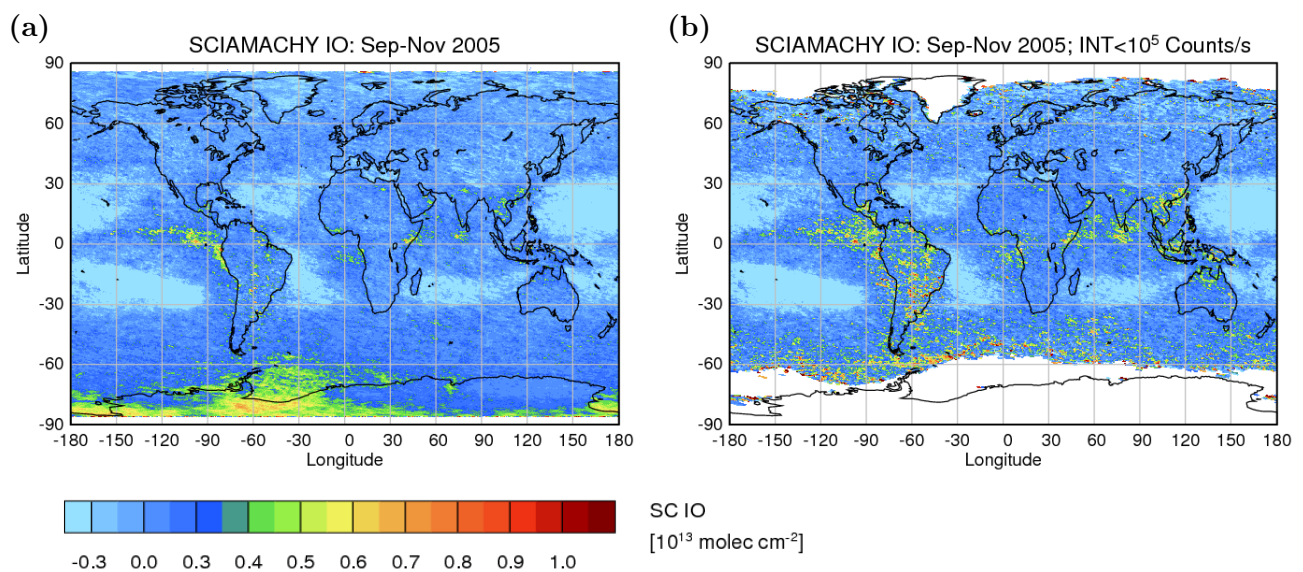
Figure 2.14: Comparison of the IO final product without a cloud screening procedure (a) and after application of an intensity criterion (b) which only leaves measurements with intensities below 1×10^5 Counts/s in the result. This way, cloudy scenes but also snow and ice covered regions are removed and the spatial noise is markedly increased.

2.7.2 Cloud screening using the PMD based classification scheme

Only recently, a new method has been developed which classifies the underlying surface and cloud type of each SCIAMACHY measurement (Lotz et al., 2008). The different categories which are considered in this classification scheme are listed in Table 2.5.

The method is called SPICS (SCIAMACHY-PMD based Identification and classification of Clouds and Surfaces) and uses the Polarisation Measurement Devices (PMDs) of the SCIAMACHY instrument (cp. Sec. 1.9.1). The PMDs have an overlapping field of view with the measurements in the main channels. This is important, as the measurements by the PMDs are hence performed at the same time and location as the nadir observations of channel 3 which are used for the IO retrieval. As the PMDs measure at higher frequency, the ground resolution is higher than for the spectral channels. From the PMD information, each SCIAMACHY measurement in the science channels is

Surface type	Cloud type	Other
water	ice clouds	sun glint
vegetation	water clouds	
snow/ice	generic clouds	
land/soil		
desert		

Table 2.5: Surface and cloud types considered in the SPICS algorithm.

classified for a certain category and can in principle receive up to one classification from each of the three columns (surface type, cloud type, sun-glint yes/no).

The principle of the surface type classification is based on the fact that the reflectivities of different surface types have different spectral characteristics. Several constraints and thresholds are applied for the classifications. Ratios of radiances measured by different PMD bands as well as the reflectance values at certain wavelengths and also further derived quantities are used. For details the publication by Krijger et al. (2005) and Lotz et al. (2008) should be considered. For each SCIAMACHY measurement in a certain time period, the information about the allocated surface types was provided by the developers of the SPCIS algorithm, W. Lotz and M. Vountas from the University of Bremen. With this data, tests could be performed for several months in the year 2005.

In order to observe the effect of cloud screening on the satellite IO observations, all scenes which SPICS classifies as water cloud, ice cloud or generic cloud are discarded from the IO product. The outcome of this procedure shall be compared to the unscreened results. In Figure 2.15, global maps of the IO slant column average for the three months of September to November 2005 are plotted in the top panel. In the left map, the standard IO product is shown, and the right map contains only those results which have not received any possible cloud flag. The scientific analysis of the IO results themselves will follow in Chapter 3. The bottom panel of Fig. 2.15, shows the same IO products as the maps at the top, but as a closeup of Antarctica. The performance over the Antarctic region is of central interest as the discrimination between clouds and ice is a special capability of the SPICS algorithm. This is important for the present study as one focus lies on observations of IO in the Polar Regions.

One immediate perception is the reduced data amount in the right maps. Naturally, these figures must contain less data and it becomes obvious that the data reduction has a noticeable influence on the noise level and consequently on the spatial scatter. The maps without cloud screening make a smooth impression in comparison to the maps where cloudy scenes were eliminated. Apart from this finding though, the main features persist also after cloud screening. In the Southern Hemisphere maps, the regions with highest IO values agree well for both cases and the overall column amounts lie in the same range. This observation also holds true for the global plots. From the similarity of the pattern one can conclude, that a missing cloud screening does not lead to systematic artefacts in the standard product. Especially, no appearances of outstanding values over cloudy scenes is observed.

The exact values of IO columns differ only slightly between the two results, when comparing the average amounts in certain regions. Typical differences only lie below $1 \cdot 10^{12}$molec/cm^2. For

Global Maps:
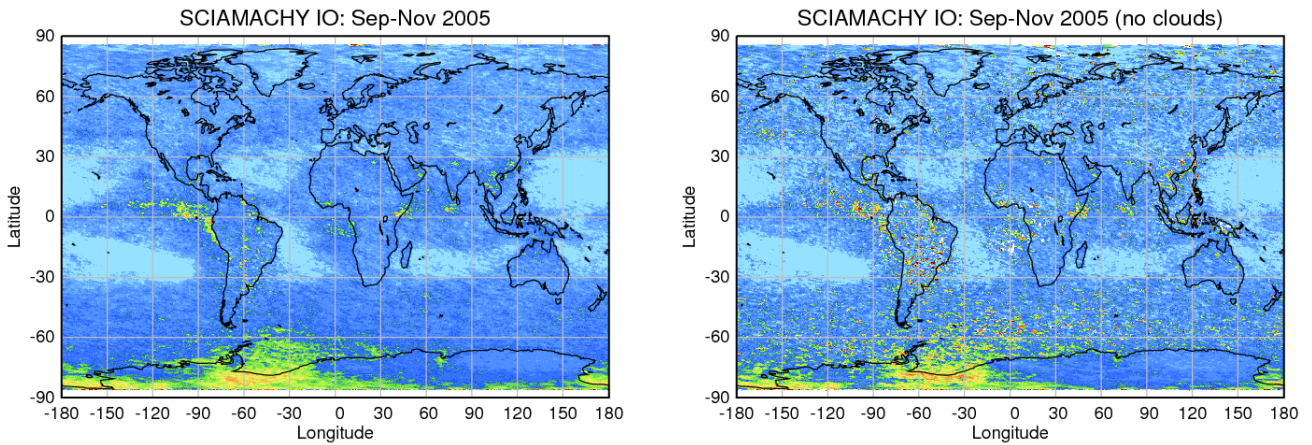
Southern Hemisphere:
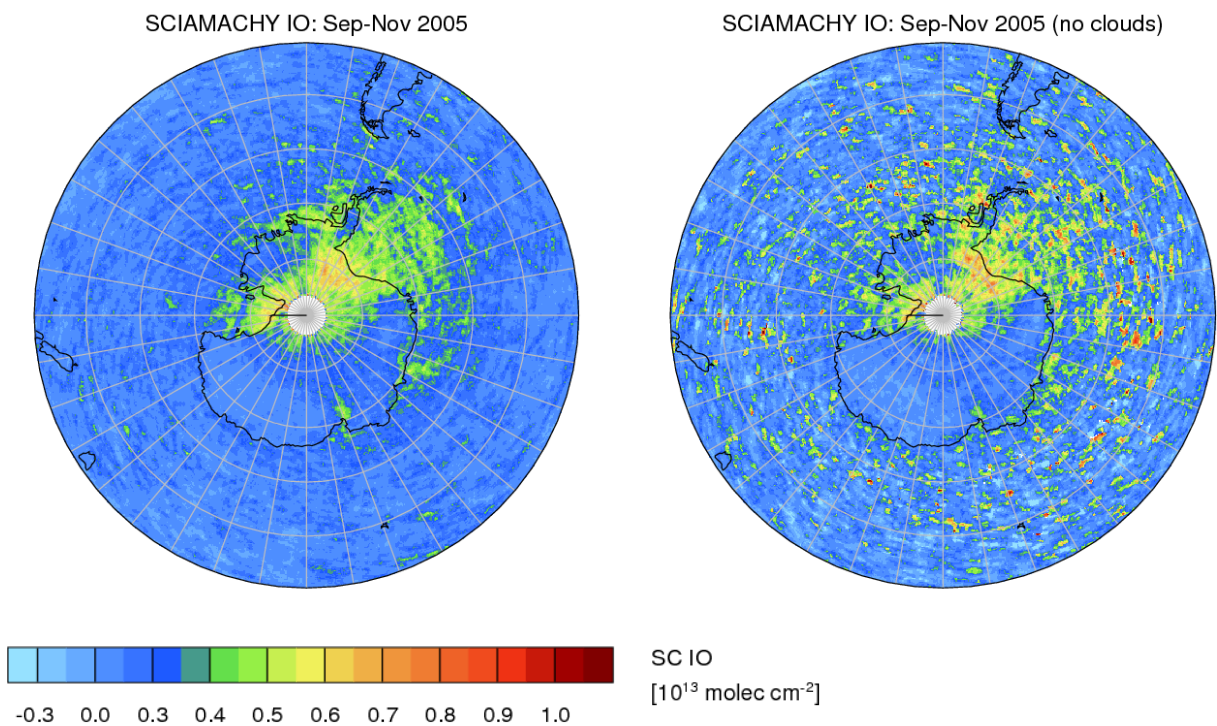
Figure 2.15: Global maps and close ups of the Southern Hemispherie for the standard IO results (left) and cloud screened results (right) using the SPICS algorithm. The spatial noise is increased noticeably in the right maps, apart from that the systematic differences are only small, and no artefacts are induced in the left maps by not rejecting cloudy scenes. Due to the new SPICS algorithm, it becomes possible now in principle to use cloud screened products also above the Polar Regions.

tropospheric trace gases like IO, especially when the substance is expected to be located rather close to the ground, the values received from an unscreened product should be lower than after cloud screening. In the presence of clouds, a part of the IO abundance is shielded from the satellite view and the average value would be reduced. The reason why the differences in the present comparison are rather small may have different reasons. However, the consideration above is generally true only for trace gases which do not vary much in time. IO amounts are usually temporally and spatially highly variable though, so the exact values seen by the satellite instrument can not be generalised easily. Scenes which are classified as cloudy often still exhibit partly cloud free regions. In the remaining area, still a considerable amount of IO may be detected if present. This measurement would then be missing in the screened product and would lead to a contrary influence than usual. In addition, the presence of some IO at higher altitudes, partly above clouds, cannot be entirely excluded. In order to see definite systematic differences between the uncorrected and the cloud screened product, a larger data amount would need to be considered. This will be done in future studies.

In Sec. 2.3 the difference between bright and dark surfaces in the presence of clouds has been mentioned. Pieces of clouds over ice scenes affect a satellite measurement less than cloud fractions over dark surfaces like oceans. For dark scenes, the intensity from the cloudy part is much stronger leading to an overbalance of this part with respect to the cloud-free part, whereas over ice, the weighting of cloudy and the cloud-free fractions is about the same.

The important result from this initial comparison is that no considerable artefacts are introduced when also the cloudy scenes are kept in the IO product.

2.8 Influencing effects on the retrieval

In the process of finding the most suitable retrieval settings for IO from the Sciamachy data, several parameters needed to be varied and the retrieval results needed to be analysed. A multitude of different retrieval parameter sets have been investigated, testing the influence of additional or modified fit settings and reference spectra. From the results of these test runs especially the fit quality and the consistency requirements as described above have been evaluated. Some options for alternative retrieval settings and their respective influences are reported here, and one especially important example retrieval is selected for a detailed discussion below.

2.8.1 Investigated retrieval settings

The following changes and additional options have been tested in the retrievals. The utilised data for the absorption features is listed in Table 2.6.

- Different fitting windows including different absorption lines of IO

- Additional trace gases like O_4, $H_2O_{(g)}$, and/or Glyoxal (CHOCHO)

- Different or additional cross section temperatures for NO_2

- Consideration of the vibrational Raman scattering in liquid water

Influencing Effect	Comments	Reference
Absorption by O_4	laboratory spectrum at 296 K	Greenblatt et al. (1990)
Absorption by CHOCHO	laboratory spectrum at 296 K	Volkamer et al. (2005)
NO_2 temperature effect	laboratory spectra, 293K & 223 K	Bogumil et al. (2003)
Absorption by water vapour	laboratory spectra	HITRAN data base
Vib. Raman scattering on $H_2O_{(liq)}$	SCIATRAN calculation	Vountas et al. (2003)

Table 2.6: Additional atmospheric effects on transmitted radiation considered only in selected test retrievals

From the tested retrieval settings, the fitting window leading to lowest errors and interferences lies around 416-430 nm. In this region, the oxygen dimer O_4 and H_2O vapour absorption are not significant and therefore don't need to be included. It is inevitable to include these gases when using wavelength windows exceeding 440 nm. The consideration of CHOCHO in the retrieval leads to apparently incorrect results for high latitudes, also the strongest absorption lines lie beyond the selected wavelength window.

The different temperatures of NO_2 show little impact on the fit quality and the IO amounts in the chosen spectral range, therefore only one temperature is taken into account in the standard fit. In some retrievals, the VRS showed the wrong algebraic sign in some locations. In the current fitting window, VRS does not show a large influence on the retrieval and is therefore omitted in the standard product.

When selecting the retrieval parameters, the number of variables in the fit should be kept small in order to avoid over-determination of the system of equations. Especially for small wavelength windows this is an important issue. From the number of spectral points in the measurements (corresponding to detector pixels) and the width of the slit function, the number of independent pieces of information is determined. The number of free variables in the fit should not exceed this value and also should not lie too close due to the remaining noise in the measurements. Therefore, the numbers of fitting parameters is kept as small as possible.

Of all tested parameter combinations, some retrieval results and retrieval failures of one selected parameter set are presented in the next paragraph. This specific retrieval is chosen as example here for several reasons. Straightforward and likely choices of parameters have been made, so initial retrieval attempts used parameter sets similar to this one. The retrieval results show interesting error features and correlations. Furthermore, the considerations connected to this retrieval are of importance for later comparisons to an independent study (cp. Sec. 4.2).

2.8.2 Retrieval in the 418-438 nm window

The retrieval version discussed in this paragraph is Version 0.27i. In principle it would be desirable to select a fitting window that includes at least the three most intensive absorption features from the absorption cross section spectrum of IO. These are the absorption bands from $(\nu' = 3 \leftarrow \nu'' = 0)$ to $(\nu' = 5 \leftarrow \nu'' = 0)$ of the $A^2_{3/2} \leftarrow X^2_{3/2}$ transition, cp. Fig. 1.4, and lie between 418 and 438 nm.

In several test runs therefore, this fitting window was chosen for the retrieval of IO.

Parameter	Settings
Fitting window	418 - 438 nm
Additional trace gases	NO_2 temperature effect (293K - 223K)
	O_4 absorption
	vibrational Raman scattering in H_2O_{liq}

Table 2.7: Fit settings for the problematic retrieval V0.27i different from the standard fit.

The results for this window showed some problems, which do not allow proper IO retrieval in this spectral range. For the problematic retrieval, the relevant settings which are different from the standard fit are listed in Tab. 2.7. First evidence of irregularities in the fit can be seen in Fig. 2.16. Global maps of the retrieval results for IO from the problematic retrieval settings are shown, averaged over the month of October 2005. In the left map, the fit quality is limited corresponding to an optical depth rms of 5×10^{-4}, and some regions with high IO slant columns are visible. After applying a more strict criterion of $rms < 2 \times 10^{-4}$ in Fig. 2.16(b), the results look completely different, as all high IO results vanish. A correlation between lower fit quality and the detection of high IO amounts is thus identified. This is the most direct evidence for fundamental retrieval difficulties.

An additional observation is that the regime of specific fit parameters here is highly unstable with respect to certain fit settings. In similar retrieval runs, where only minor setting changes were applied (e.g. a different choice of the calculated VRS spectrum), the IO signatures flip their sign, i.e., locations with high IO in Fig. 2.16(a) then exhibit strongly negative IO slant columns. The spatial correlation of IO and high rms-value in the global picture remains in all similar retrieval runs.
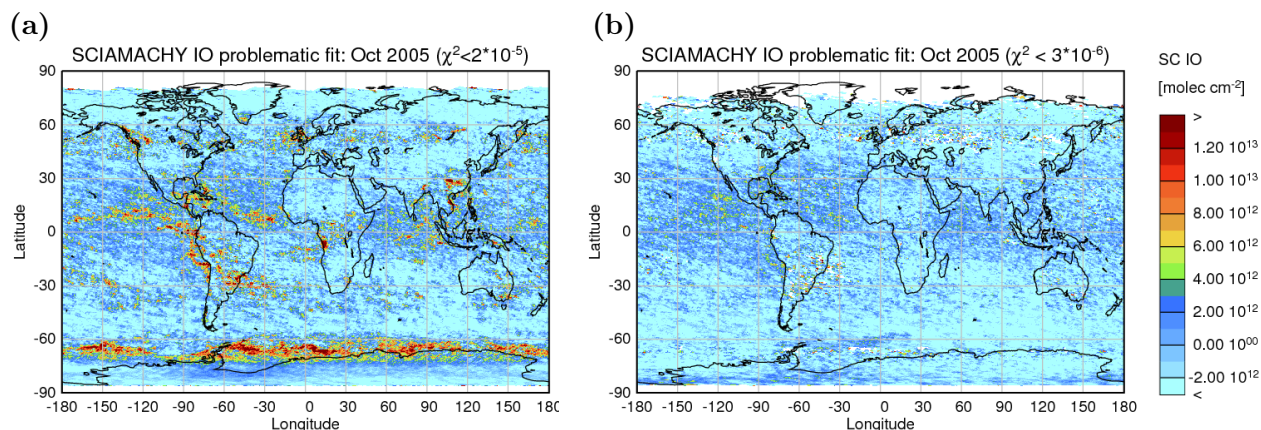
(a) **(b)**

Figure 2.16: Global maps of IO results from the retrieval in the problematic 418-438 nm window. The two cases show results after application of differently strong quality criteria. A correlation of lower fit quality and higher IO amounts is identified.

(a)

(b)
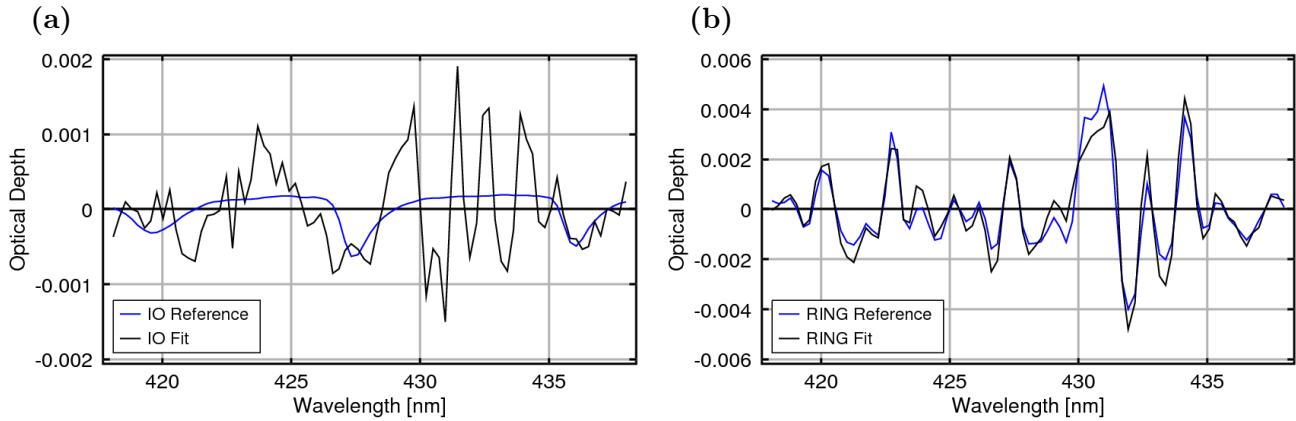
Figure 2.17: (a) shows the spectral IO fit result with the scaled laboratory cross section in blue and the fit result including the residual spectrum in black. The detection of a high IO amount is the consequence of a strongly structured residual. (b) shows the result from the same measurement for the poor fitting of the Ring effect. It becomes clear that several features in the spectrum are not properly captured.

Spectral fit results

A spectral fit result of a typical failed retrieval is displayed in Fig. 2.17 for a measurement where high IO was detected. The figure contains two curves, the blue curve is the scaled laboratory spectrum of the absorption cross section, the black line is the respective measurement fit result of the absorption spectrum containing the residual spectrum. Strong spectral structures appear in the residual, which are clearly not related to pure noise. Partly, the IO cross section coincides spectrally with otherwise unassigned structures so that an IO signal is picked up. From this poor fit result, it must be concluded that the retrieved IO amount here is the result of an improper retrieval process.

The shape of the fit residual displayed in Fig. 2.17(a), occurs persistently whenever especially high IO amounts are detected. Such a stable, highly structured residual indicates an underlying fundamental problem. The most probable cause here was identified to be the fitting of the Ring effect. The respective fit result for the Ring effect is displayed in Fig. 2.17. The differences between the fit and the calculated spectrum are especially strong at the pronounced features of the Ring effect. In many places, either the peaks or the minima are not well captured.

Circumstances for scenes with large fitting errors

The fact that high IO amounts are connected to the persistent structure, is demonstrated in Figs. 2.18 - 2.20. The visual colour from the PMD measurements is shown in Fig. 2.18(a), where clouds appear in white, for the 1st of September, 2005, over East Asia and the IO slant column results on the right (b) for the same time and scene. In several cases, the high IO amounts coincide with the occurrence of clouds. The central measurement state over Asia from Fig. 2.18 is picked out in Fig. 2.19 with four single measurements selected and numbered for closer investigation. Fig. 2.20 shows the fit results of four SCIAMACHY measurements in comparison. The measurements number 1 and 3 are not strongly affected by clouds and the residual of the retrieval is comparably small and only slightly structured. For measurements number 2 and 4, where bright clouds cover the field of

view, the residual is significantly larger and strongly structured. In particular, the structures are strikingly similar in both cases. Obviously, a systematic irregularity in the retrieval occurs above bright surfaces such as clouds and ice (Fig. 2.16), prohibiting reasonable IO retrieval with these parameter settings.

(a)

(b)
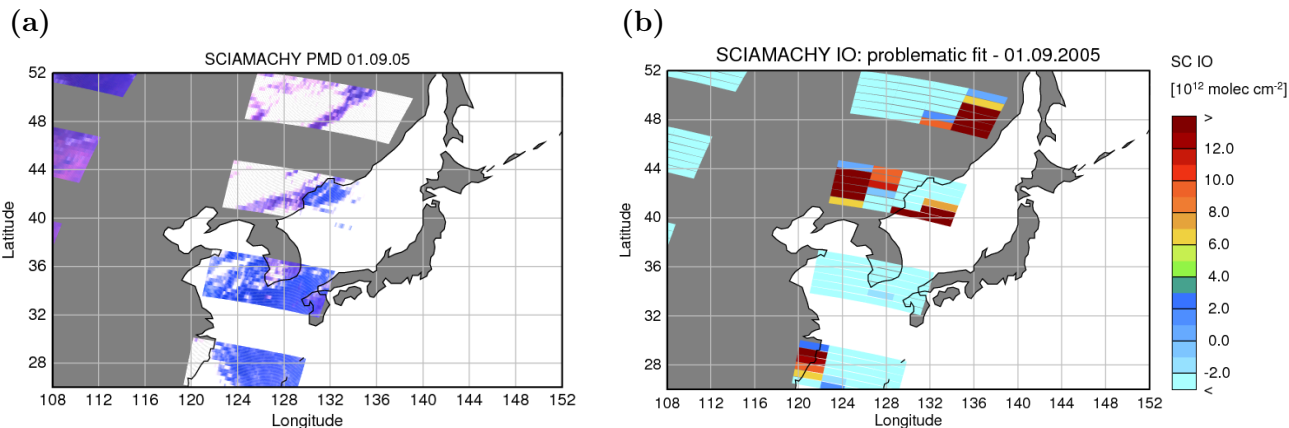
Figure 2.18: Satellite measurements for which spectral fitting results are shown in Fig. 2.20. (a) shows the PMD visual impression, where clouds are seen in white, and (b) gives the IO results from the problematic fit, where in most cases, high IO values are correlated with cloudy scenes.

Possible physical reasons for the fit errors

The systematic occurrence of the stable residual shown in Figs. 2.17 and 2.20 asks for explanations of its origin. The IO results in Fig. 2.16 and 2.18 show the relation of IO detection in scenes with either bright clouds or bright (ice) surfaces. However, not all ice covered regions and cloudy pixels are affected. Additional circumstances must play a role.

The spectral structures in the strong residuals are prominent around the 430-431 nm region and vanish if the fitting window is restricted to wavelengths below. This hints at a possible connection between the inaccurate fitting and the Fraunhofer G band (cp. Fig. 1.7). Being the most prominent Fraunhofer feature in the considered fitting window, the G band also exhibits the strongest infilling (Sec. 1.6.3). The Ring effect must be well described at this spectral position, otherwise errors are induced. One possible explanation is that the Ring effect spectrum used in the retrieval does not capture this position well in certain situations. In addition to the Ring effect, the Fraunhofer lines play a role also for other effects, like the impact of instrumental stray light on the measurements or the polarisation sensitivity of the instrument.
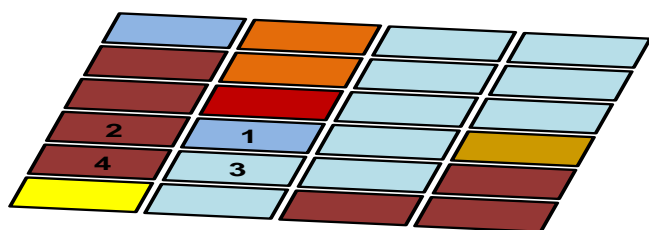
Figure 2.19: SCIAMACHY state from the map shown in Fig. 2.18 with four numbered ground pixels, for which retrieval results are shown in Fig. 2.20 to demonstrate the connection of incorrect fitting with cloud cover.
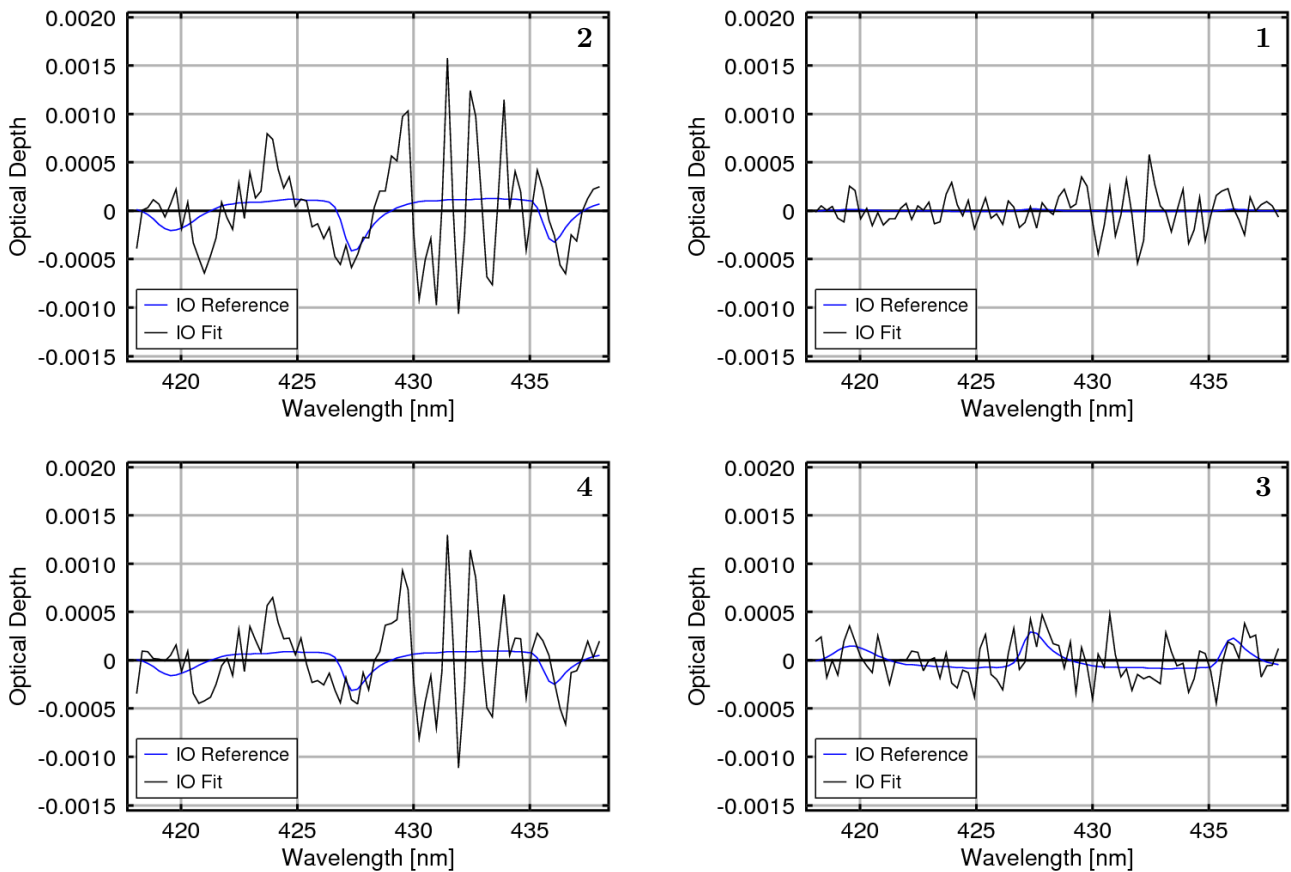
Figure 2.20: Fit results for the four ground scenes numbered in Fig. 2.19. Cases 1 and 3 are above cloud free scenes, the IO values are small and the residual largely unstructured. Cases 2 and 4 however, are chosen over cloudy satellite pixels and both show the same highly structured residual spectrum. These systematic effects lead to improper fitting and erroneous results here.

The Ring effect changes its shape and strength as consequence of several effects. One straightforward influence of clouds is the shielding of the lowest part of the atmosphere, where most scattering molecules are situated, thereby reducing the Raman scattered portion in the radiation. The infilling of absorption lines will be smaller in case of a high cloud. This effect can actually be used to derive the cloud top height from satellite measurements (Joiner and Bhartia, 1995; de Beek et al., 2001). Also above bright scenes such as ice on the Earth surface (which is a similar situation to very low clouds) the Ring effect is slightly weaker than over very dark surfaces, as the Raman scattering is overbalanced by Lambertian reflection and infilling is somewhat reduced. In the case of a bright cloud, if part of the atmosphere is shielded and all other parameters are kept constant, the major influence on the Ring effect is a change of the strength. In addition, the spectral shape of the Ring effect may change in dependence of the surface albedo, as the albedo impacts on the typical light path length through the surface layers. Different wavelengths will then experience differently strong Raman scattering. This effect is not taken into account in the retrieval, as it does not lead to any noticeable problems. The Ring effect used in the retrieval is calculated for an albedo of 90%, and there are no systematic irregularities for dark surfaces. Also, the problems over bright scenes

are restricted to certain situations. Tests with Ring spectra calculated for varying conditions (e.g., changing surface height, SZA, ground spectral reflectance) did not improve the situation in the large wavelength region. A pure influence from the Ring effect as single cause for the fitting difficulties in the 418-438 nm window calculation is regarded unlikely, mainly due to the selective appearance of the problem. However, a combined influence of the Ring and other effects might become relevant.

One aspect which is affecting both situations similarly, the cloud case and the bright surface, is the enhanced stray light influence. This occurs especially if a spectral part outside the fitting window is increased. Above visually bright surfaces, the longer wavelength part of the spectrum is enhanced relative to the shorter wavelengths as compared to darker scenes where the shorter wavelengths dominate due to the λ^{-4}-dependence of the Rayleigh scattering probability. The spectral shape of the stray light influence resembles that of the Ring effect (and is therefore most prominent at the Fraunhofer line positions), which may be illustrated in the following way. The intensity I recorded by the instrument is generated by the sum of elastic and inelastic scattering: $I = I_{el} + I_{inel}$, and $\ln(I) = \ln(I_{el}) + \ln(1 + \frac{I_{inel}}{I_{el}})$. For the case of dominant elastic scattering $I \approx I_{el} >> I_{inel}$, the following approximation is valid:

$$\ln(I) \approx \ln(I_{el}) + \frac{I_{inel}}{I_{el}} \approx \ln(I_{el}) + f \cdot \frac{1}{I}$$

In the last step, by applying a constant factor f, the wavelength dependence of I_{inel} is neglected in comparison to the wavelength dependence of I_{el}, which is strictly not true but may be used as an approximation. Considering the DOAS fitting method, this corresponds to using $\frac{1}{I}$ as pseudo absorber for the Ring effect and f as the associated fit factor. Before the Ring effect was calculated by radiative transfer models, the inverse of the radiance was used to account for the infilling in ground-based measurements (Johnston and McKenzie, 1989; Noxon et al., 1979). Although this is only a rough approximation, the similarity to the stray light approximation in Sec. 1.8 is apparent, for the case of constant stray light amount. Due to these relations, spectral features at the positions of the Fraunhofer lines are always most prominent in both effects. The resulting spectral correlation between Ring and stray light effect may generate fitting errors if one or both effects are strong and not precisely accounted for. Possibly, the consideration of the stray light is not sufficient in the presently implemented way. However, the distinctive features in the retrieval do not occur above all bright scenes where stray light is large, but only over some of them. If stray light is one cause of the error features, again there needs to be a combination with a further influence.

A third process which leads to spectral structures at the Fraunhofer lines is the polarisation sensitivity of the instrument. In general, light transmission through a grating spectrometer is polarisation sensitive due to polarisation dependencies of the optical components (mirrors, grating). Therefore, the recorded signal at the detector will depend on the polarisation degree of the incident radiation. The polarisation state of the radiation field is described by the Stokes vector $S = (I, Q, U)$, where I is the total intensity, $Q = I_p - I_s$ is the intensity difference between horizontal and vertical polarisation (with respect to the spectrometer entrance slit) and $U = I_+ - I_-$ is

the intensity difference of the radiation polarised at angles of ±45° (Gottwald et al., 2006). The polarisation sensitivity of a system may be specified by a Mueller matrix M (Hecht, 2001; Gottwald et al., 2006). With the radiation terms at the detector marked with subscripted *det* and the incident radiation terms with *in*, the transmission of radiation through the instrument follows the equation:

$$
\begin{pmatrix} I \\ Q \\ U \end{pmatrix}_{det} = M \cdot \begin{pmatrix} I \\ Q \\ U \end{pmatrix}_{in}
$$

The first entry in the detector Stokes vector is the actually recorded intensity I_{det}, which enters the DOAS analysis procedures. With the matrix elements M_{ij} the recorded intensity reads:

$$
I_{det} = M_{11} I_{in} \cdot \left(1 + \frac{M_{12}}{M_{11}} q + \frac{M_{13}}{M_{11}} u \right) \qquad \text{with } q = \frac{Q}{I}\bigg|_{in}, \ u = \frac{U}{I}\bigg|_{in}
$$

In the following, the considerations are restricted to the dependence on q for simplicity, as the u-dependency is equivalent. The quantity q is the standard polarisation degree. For optical sensors often the function η is determined in pre-flight tests, from which the matrix elements M_{11} and M_{12} are calculated by $\frac{M_{12}}{M_{11}} = \frac{1-\eta}{1+\eta}$. Considering the optical depth between the recorded intensity and an reference intensity I_0, which is the term analysed in the DOAS-algorithm, this can be written as:

$$
\ln\left(\frac{I_{det}}{I_0} \right) = \ln(M_{11}) + \ln\left(\frac{I_{in}}{I_0} \right) + \ln\left(1 + \frac{1-\eta}{1+\eta} q \right) \tag{2.1}
$$

$$
\approx \ln(M_{11}) + \ln\left(\frac{I_{in}}{I_0} \right) + \frac{1-\eta}{1+\eta} q \tag{2.2}
$$

The approximation holds if polarisation is not too strong, otherwise the impact is even more prominent. The last term in the equation depends on the inverse intensity I_{in}^{-1} and is therefore similar to the effects discussed above. However, the wavelength dependence of the factor in front of the inverse intensity and especially that of Q_{in} are comparably strong and often cannot be approximated by a constant or linear function as this is done for the stray light effect (cp. Sec. 1.8). Furthermore, Q_{in} is typically not known.

The polarisation degree strongly depends on the ratio of the different scattering types (Rayleigh, Raman and Mie), because Rayleigh scattering is strongly polarising, Raman scattering is only weakly polarising and Mie scattering is not polarising. The polarisation degree of the backscattered radiation therefore depends on the respective scene. Over clouds, e.g., Mie scattering is strong. The reference spectrum I_0 over the Pacific is taken over a clear scene, so that mainly Rayleigh scattering contributes. The polarisation difference between the reference scene and the bright scenes over clouds and ice may lead to additional structures in the spectrum which are not described by the applied cross sections. In addition, the degree of polarisation also depends on the scattering angle, i.e. on the viewing angle of the satellite and the position of the sun. This may explain the observation, that the large residuals over clouds and bright surfaces only occur in some locations.

In conclusion, the fitting difficulties in windows covering the Fraunhofer-G line around 431 nm

are possibly generated by a combination of several influences which are strong at this wavelength position. Spectral correlations of the IO spectrum with remnants of the G-band, the applied correction spectra for Ring and VRS then cause products which are more the result of mutual correlations than of real atmospheric conditions. The most probable impact results from the polarisation sensitivity of the instrument and may be improved either by a better polarisation correction of the SCIAMACHY raw spectra or in future instruments by employing a polarisation scrambler at the entrance of the sensor.

Consequence for the choice of fitting window

In the 418-438 nm range, no fit parameter set has been found so far, where the deficiencies at the Fraunhofer-G line are properly eliminated. The fit either tends to strongly negative (not shown here) or strongly positive (cp. Fig. 2.16) IO amounts. These problems need to be solved before the retrieval of IO in a spectral window spanning more IO absorption lines can become successful. As a consequence of the difficulties in the 418-438 nm window, the IO retrieval has been restricted to the spectral range of 416-430 nm, yielding the standard IO retrieval. This way, the discussed problem of strong residuals resulting from a poor fit around 431 nm is avoided. An even better retrieval of IO might be achieved, if the measured radiances in this spectral range were better understood. Future investigations should consider the polarisation sensitivity of the instrument as one likely cause for the strongly structured and large residuals in certain cloud or ice scenes. As soon as the question is solved, which influences exactly provoke the retrieval inaccuracies, new retrievals in a larger fitting window may be conducted.

2.9 The choice of the background spectrum

Considerations in this section use results from the IO fit Version V2.54 (cp. Sec. 2.2.1). For this data product, the large Pacific region shown in Fig. 2.21 is chosen as reference, overlapping the Pacific reference region of the standard V1.28 product (cp. Fig. 2.4), but being larger causing a higher degree of averaging.
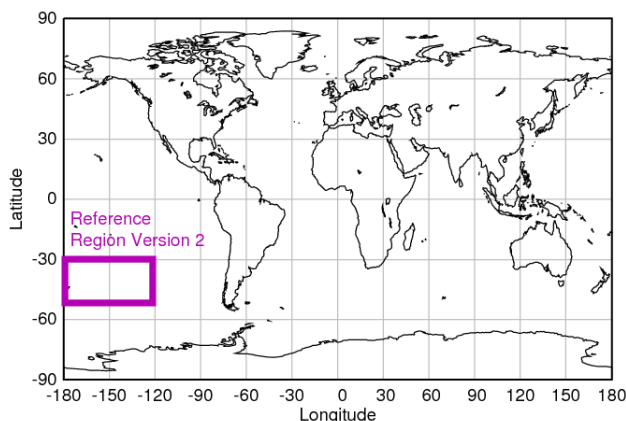

Figure 2.21: Map showing the large Pacific reference region (Version 2) used in this section and as standard reference region for the IO data version V2.54.

For the performance of a DOAS retrieval, the choice of the background spectrum (I_0) may be

crucial. While a solar reference spectrum containing no atmospheric absorber signatures would be one appropriate choice, this may cause decreased retrieval quality in some cases. This is due to two reasons - the noise level in SCIAMACHY solar spectra is higher than in an averaged earthshine spectrum and additionally the possibility for retrieval artefacts is higher. This can be caused, e.g. by a large spectral influence from the Ring effect, which is not present in direct sunlight but is prominent in Earthshine measurements of scattered and reflected sunlight in spectral windows with strong Fraunhofer lines (cp. Sec. 1.6.3). In addition, the impact of some remaining calibration inaccuracies, which are similar for individual Earthshine scenes but may be quite different for the Solar spectra, may be reduced this way. When comparing two Earthshine spectra, and forming their ratio in the DOAS retrieval (cp. Sec. 1.8), part of these effects cancels out. Therefore, the choice of an appropriate Earthshine spectrum as background usually leads to the most stable fit results here.

As instrumental characteristics and parameters might experience temporal drifts, a background spectrum close in time often is a necessary choice. Additionally, the location of this background spectrum has to be chosen carefully. The best choice is a location, where the specific trace gas under investigation is not present or, alternatively, where its amount is well known. Instead of using a new specifically generated Earthshine reference spectrum every day, a modified procedure can be used. A constant Earthshine spectrum from a fixed time and place is applied and in a second step, the influences of instrumental drifts on the retrieval are eliminated by subtracting the averaged daily fit result in the background location from the individual measurement. The mathematical basis for this procedure is given by the following equation:

$$\ln\left(\frac{I(t_i)}{I_0(t_i)}\right) \;=\; \ln\left(\frac{I(t_i)}{I_0(t_c)}\right) - \ln\left(\frac{I_0(t_i)}{I_0(t_c)}\right), \tag{2.3}$$

where I and I_0 are the intensities measured at any location on the Earth and in the background region, while t_i and t_c denote any time (day) of measurement and the fixed day of the constant background spectrum, respectively. The second term on the right hand side $\ln(\frac{I_0(t_i)}{I_0(t_c)})$ describes the differences in the background spectrum at different times and may contain a background offset of the trace gas of interest. The left hand side of the equation above refers to the retrieval with daily reference, while the right hand side uses the fixed reference in combination with subtracting the fit result in the background region every day. The second approach is used in most of the fits including the standard fit and from the basic principle, this procedure should be functional. For the real retrieval though, it shall be shown exemplarily that there is no big difference for the IO retrieval result between the two methods.

The pure Version V2.54C (tag C) uses a constant background Earthshine spectrum from the 1st September 2007, extracted from within the reference region. For everyday normalisation to the reference region, the daily average of IO in the reference region is subtracted. The final product is then referred to as Version V2.54C-AVE. The equivalent fit parameter set with the only difference of using a daily (tag D) reference is Version V2.54D. These two retrieval settings shall be compared in the following.

The comparison is now performed for two different days, the 20th September 2006 (different year than but same season as the constant background spectrum) and the 9th March 2006 (different year and different season). For these days, all recorded SCIAMACHY spectra within the reference

region are averaged to yield reference spectra for the specific days to be used in the fit V2.54D. Comparisons of the results are shown in Fig. 2.22, where the IO slant column results from the entire satellite orbit (20060920_183 and 20060309_190) are plotted versus the respective latitude of the measurement. The IO fit results with daily reference, $IO_D(lat)$, are marked by red squares, the blue triangles show the retrieval using constant reference, $IO_C(lat)$, and subsequent offset correction by the average IO in the reference region, $IO_{C,AVE}$. Differences between the two methods are small and cannot be distinguished in this graph.

(a)

(b)
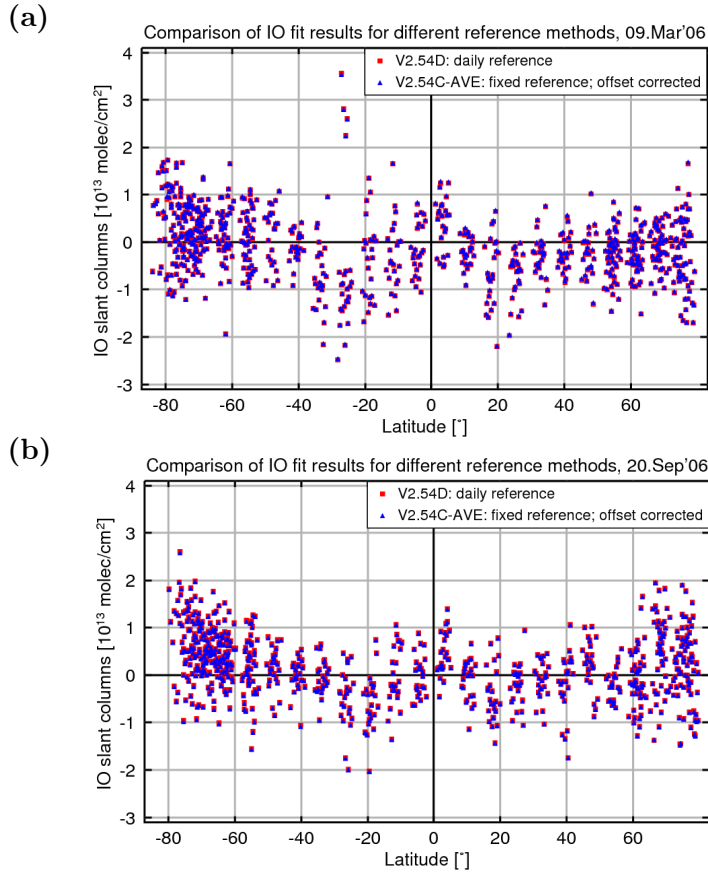
Figure 2.22: Resulting IO slant column amounts for two sample orbits in March (a) and September (b), 2006. In each graph, the results of two different methods are compared, which deal with the Earth-shine background spectrum in different ways. Retrieval V2.54D (red squares) uses the daily average Earthshine from the background region, while the version shown in blue triangles uses a constant reference from the 1st September, 2007. For the latter case, the daily average IO amount $IO_{C,AVE}$ in the reference region is subtracted in a second step, yielding the plotted version V2.54C-AVE. The two methods yield results which are equal within small deviations.

Day	Global mean $\bar{\Delta}$	Standard deviation $\sigma(\Delta)$	Reference offset ($IO_{C,AVE}$)
20.09.2006	-0.09	0.06	-5.74
09.03.2006	0.86	0.10	-7.11

Table 2.8: Statistical information on the difference Δ in IO results between Version V2.54C-AVE and Version V2.54D (Equation 2.4). The unit of the values is 10^{12} molec/cm^2 .

The difference in retrieved IO between the two methods is calculated by $\Delta(lat)$, where lat is the latitude:

$$\Delta(lat) = (IO_C(lat) - IO_{C,AVE}) - IO_D(lat) \qquad (2.4)$$

Some statistical information for $\Delta(lat)$ from the investigated orbits is given in Tab. 2.8. Remaining deviations on the order of $<1\times10^{12}$ molec/cm^2 (often $<1\times10^{11}$ molec/cm^2) are mainly caused by

statistical fluctuations and retrieval uncertainties (cp. Sec 2.5). Overall, the difference between the two methods is only small. Neither the trace gas results nor the fit qualities show specific deviations or problems.

One advantage may be the reduced risk of error when using a constant reference. Better inspection of the fit result is possible. Potential irregularities in the reference region can be seen in the pure result before subtraction of the averaged reference offset and will not affect the global results. However, both methods are regarded as suitable as long as no sudden instrumental change in the time series occurs. In that case, a daily (or renewed constant) Earthshine spectrum is necessary. Currently, the method of using a constant Earthshine reference is retained.

3 Observations of IO from satellite

After the retrieval of IO from SCIAMACHY data has been optimised, the detection of enhanced amounts of IO in some regions on Earth becomes possible. Due to the fact that abundances of IO are comparably small and often lie close to the detection limit (Sec. 2.4) of the satellite instrument, it is not possible to observe short term transport events or the localisation of emissions on certain days. It is necessary to average the resulting slant column values over certain time periods. Temporal averaging always means a trade off between an improvement of signal-to-noise and a loss of temporal resolution. With an averaging period of three months, e.g., the noise is considerably reduced as compared to monthly or even daily results, but some temporal variation can still be resolved. The strategy and period of averaging will be in each case adapted to the specific situation or objective of analysis.

In the following, global results for IO observations using the currently most consistent retrieval settings will be presented. All presented maps and time series of IO columns in this chapter show data from Version V1.28 discussed in Sec. 2.2, which have partly been published in Schönhardt et al. (2008). Alongside an overview over the global results, several interesting regions are highlighted. As one main focus of this study lies on iodine in the Polar Regions, IO amounts and seasonal variations over Antarctica are discussed. The new findings are presented and possible approaches for interpretation are explained. A further interesting region discussed in this chapter is the Eastern Pacific and finally some locations on the Northern Hemisphere.

3.1 Global observations

As an overview, complete global maps for certain time periods are considered. The global maps allow a view also onto regions where no iodine measurements have been undertaken before. Enhanced IO amounts above the respective detection limit are found in cases of widespread sources and favourable conditions.

Figure 3.1 shows the average of all retrieved SCIAMACHY IO observations over a time period of four years with a spatial resolution of $0.25^{\circ} \times 0.25^{\circ}$. The slant column amount is shown in colour code, which is displayed on the right. The colour code applied here is the same as introduced in Sec. 2.6 and will be consistently used throughout this study for the standard IO results, so that all plots can be directly compared with each other.

Over large areas of the Earth, IO columns are below the detection limit. Following the detection limit, precision and accuracy considerations (Sec. 2.4 and 2.5), mainly IO columns exceeding $3 \cdot 10^{12} \mathrm{molec/cm}^2$ are investigated and further discussed. Regions with sufficiently long lasting and widespread enhanced IO values can be distinguished. In this average over several years, the maximum values reach up to about $7 \cdot 10^{12} \mathrm{molec/cm}^2$. The largest and widest spread values are

found close to and over Antarctica, especially in the Weddell Sea, over shelf ice regions and at coast lines. There have been ground-based measurements in Antarctica also showing enhanced IO amounts in certain times of the year, which will be discussed in more detail in Sec. 4.1.
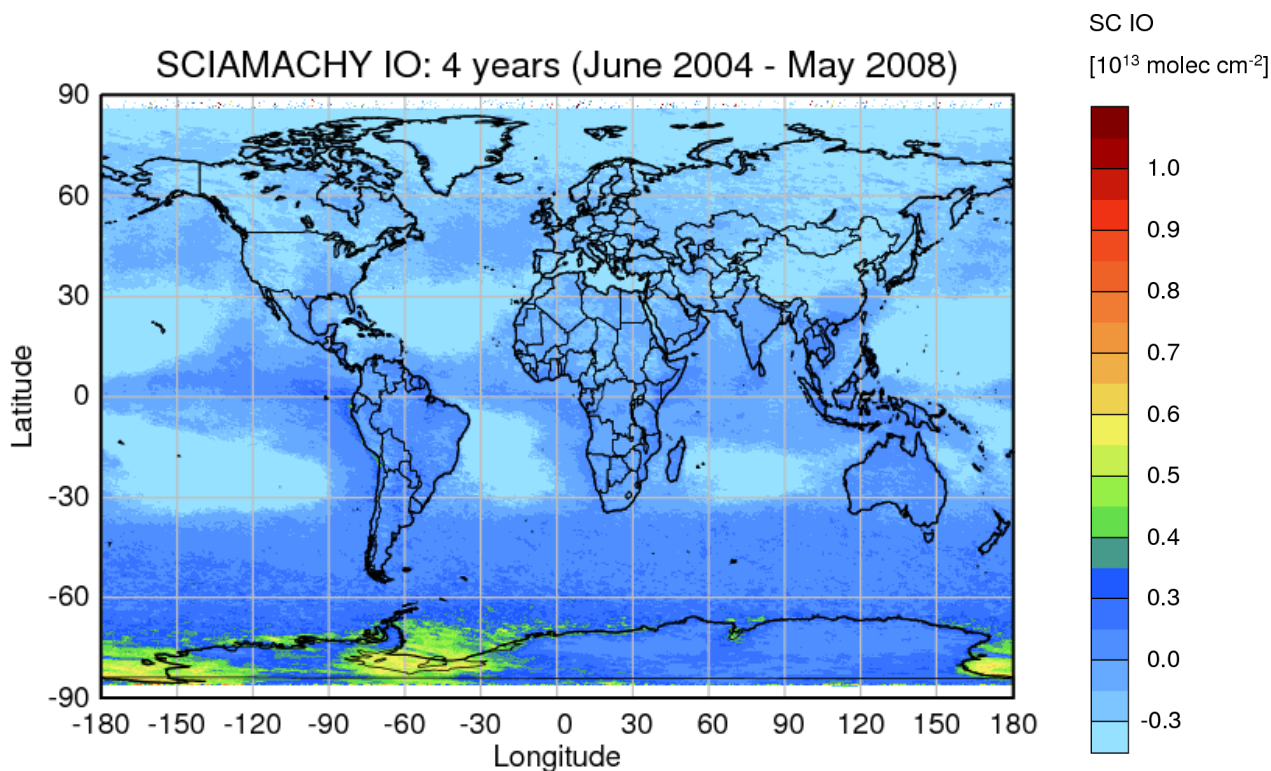
Figure 3.1: Global slant column amounts of IO averaged from June 2004 until May 2008.

Seasonal plots averaged over four years based on the same data are displayed in Figs. 3.2(a)-(d). It becomes visible, that the IO values around Antarctica are not constant over time, but exhibit annual variations. These findings are subject of Section 3.2 and 3.3.

Apart from the prominent South polar region, also other areas exhibit enhanced slant column values of IO. Looking at the equatorial Eastern Pacific Northwest of South America, enhanced IO values are observed. More details on this region follow in Sec. 3.4.

Not visible in the maps presented here, there are also notions of enhanced IO values on the Northern Hemisphere. Special aspects in the retrieval play a role for the results there and need to be discussed carefully (cp. Sec. 3.5).

Two irregularities need some attention. First, the IO values show a tendency to smaller and even negative values towards and on the Northern Hemisphere. This fact has influences on the choice of the reference region when analysing the results in Northern regions and will be discussed in Sec. 3.5.

A second point of concern are the clear ocean regions mainly in the Pacific and also in the Atlantic and Indian Ocean. In areas without biological production (*ocean deserts*) where the water is very clear, influences on the retrievals of several trace gases occur, probably by light that travels through the water for a certain distance before being backscattered into space. For IO, which is a minor
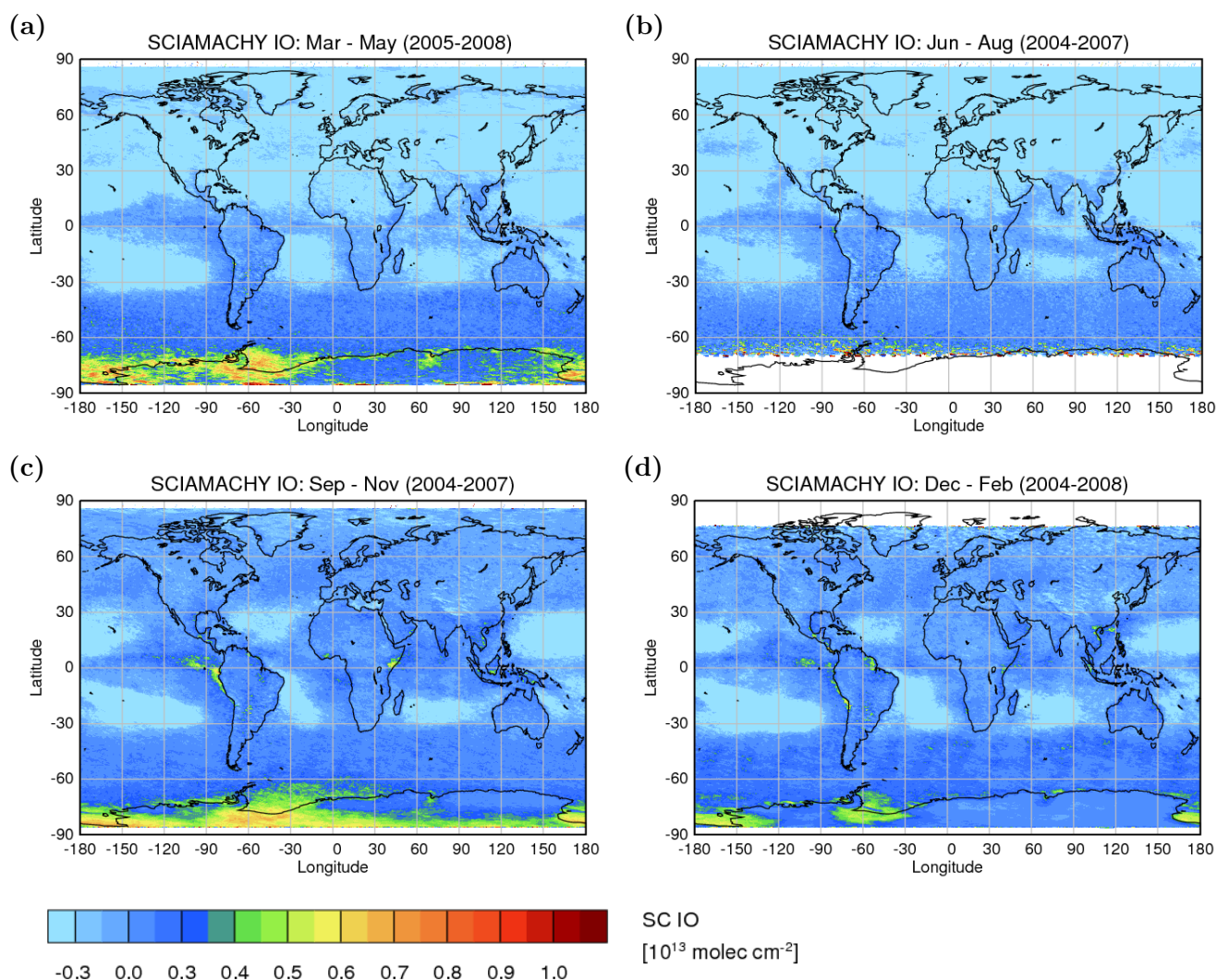
Figure 3.2: Global slant column amounts of IO averaged for different seasons. Taken from the overall time of June 2004 to May 2008, the periods cover (a) March-May for 2005-2008, (b) June-August 2004-2007, (c) September-November 2004-2007, (d) December-February 2004-2008.

absorber and where amounts are usually very close to the detection limit, the interference of light with processes in water may have a strong influence and cause systematic negative values over these ocean deserts. This perception has led to the analysis presented in Chapter 6.

3.2 Observations of IO in Antarctica

Some local measurements in Antarctica have reported observations of IO before (Friess et al., 2001; Saiz-Lopez et al., 2007b) and also of organic iodine components, e.g. CH_2I_2 (Reifenhäuser and Heuman, 1992; Carpenter et al., 2007). Measurements of iodine species in the Antarctic are generally sparse and it is a major interest to investigate this area further. Observations from space may be of great support in order to analyse amounts and variations of IO and also possible connections between IO and BrO, as well as between IO and ice cover.

3.2.1 Seasonal variation of IO in Antarctica

For the observations of IO in and around Antarctica, it is convenient to look at polar maps. The graphics in Fig. 3.3 cover the Southern Hemisphere up to 40° Southern latitude and show seasonal averages of the IO slant columns for the periods March-May, June-August, September-November and December-February. The overall time period of the data shown is June 2004 to May 2008, and each map represents an average over 4 subsequent years so that the noise level is strongly reduced. The temporal variations in the distribution of IO values in and around Antarctica show similar signatures every year which will be seen later. Therefore, the results can be averaged over subsequent years and meaningful conclusions can still be drawn.

Starting in Austral spring (i.e. from around September in the Antarctic), large values of IO occur in the Weddell Sea, in shelf ice regions and along the Antarctic coastlines (Fig. 3.3a). Also on the Antarctic continent, positive IO values are apparent. The largest average values reach up to about 8×10^{12} molec/cm^2. Single measurements can be considerably higher, e.g., a fit result of 2×10^{13} IO molec/cm^2 was presented in Chapter 2. The IO amounts are then lower in the summer, but still remain above detection limit in some areas. An increase of the amounts and the covered area towards the autumn period again can be recognised. In South polar winter, no light is available for this type of satellite observations. Regions without data appear white in the images. But also at the rim of the measurement region, no systematically enhanced values are observed. At this border of the measurement region in winter time and also in some extent for the autumn time, a larger amount of scattering is apparent in the data. This is due to a smaller amount of data points which fulfill the criterion of having a SZA below 84°.
Several aspects of this general seasonal variation found in the satellite IO observations shall be analysed in more detail now.

3.2.2 IO time series at Halley Station, Antarctica

The annual cycle roughly described above may be observed in more detail when looking at time series for certain locations. A time series extracted from around Halley Station (cp. Fig. 3.4), situated in Antarctica at 75.5° S, 26.5° W is shown in Fig. 3.5. Data from this time series forms the basis of a very important validation study presented in Sec. 4.1 where satellite and ground-based data are compared. For the data points in Fig. 3.5, all satellite measurements within a box of 500 km side length enclosing Halley Station have been taken into account and are averaged over one day each. These daily IO slant columns are plotted in blue and a weekly running mean is overlaid in black.

The evolution of the IO values is shown for four subsequent years and in each year, a similar development is observed. Largest IO amounts always appear shortly after polar sunrise in September with highest values in October around 6 to 7 $\times 10^{12}$ molec/cm^2 in the running mean. After a slight summer decrease down to values around 2×10^{12} molec/cm^2, the autumn again exhibits larger amounts. Towards winter, the IO indeed decreases again, and during winter time no data is available due to darkness.

In part, IO slant columns in summer are lower than in spring and autumn because of a higher
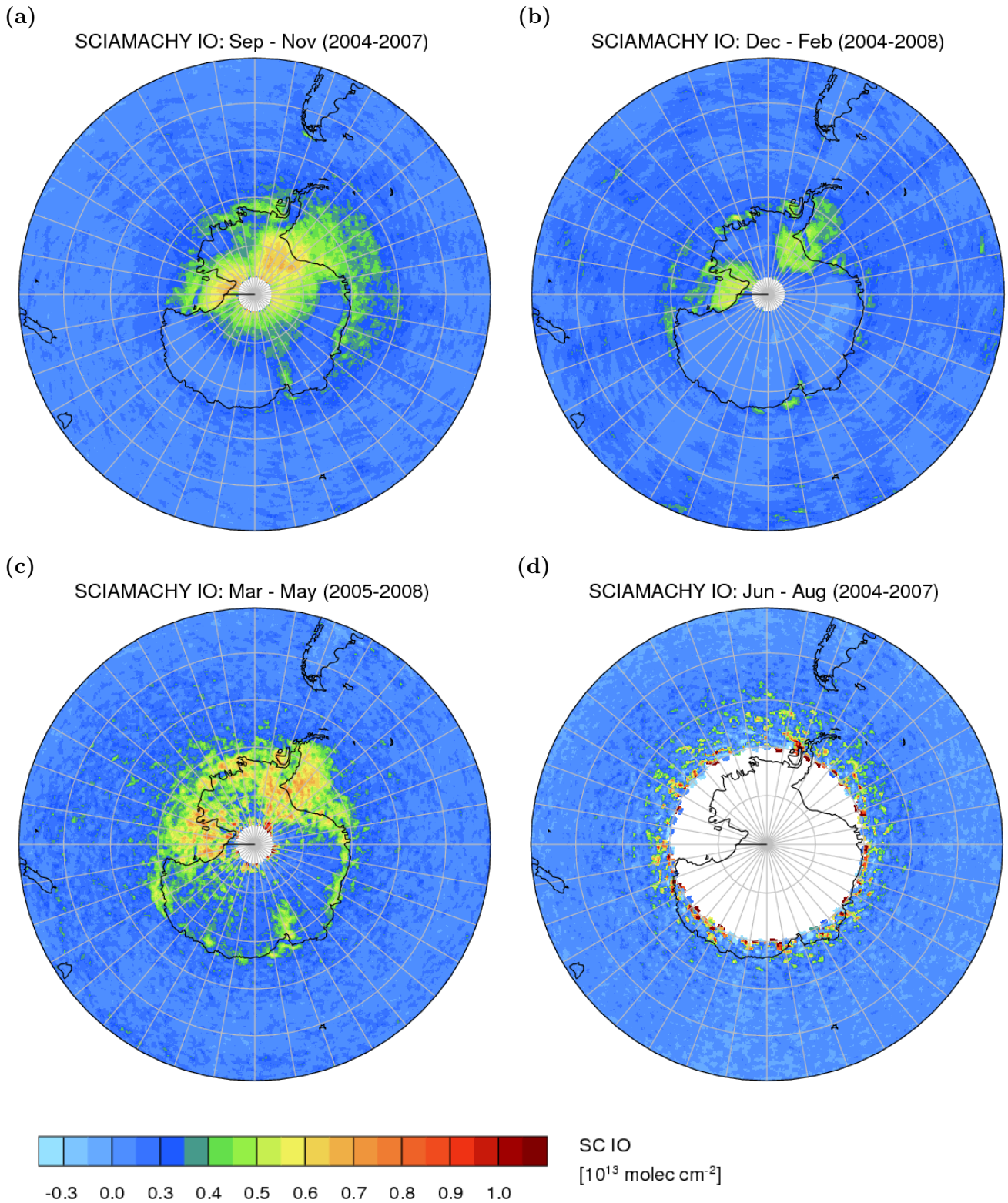
Figure 3.3: Seasonally averaged slant column amounts of IO above the Southern Hemisphere (up to 40°S) from Austral spring to winter. The data is taken from June 2004 to May 2008 for the periods of September-November (2004-2007), December - February (2004-2008), March-May (2005-2008), and June-August (2004-2007). Maxima in IO columns occur over the Weddell Sea, the Ross Sea and along the coast especially in spring and in autumn with lower levels yet remaining positive at some areas throughout the summer.
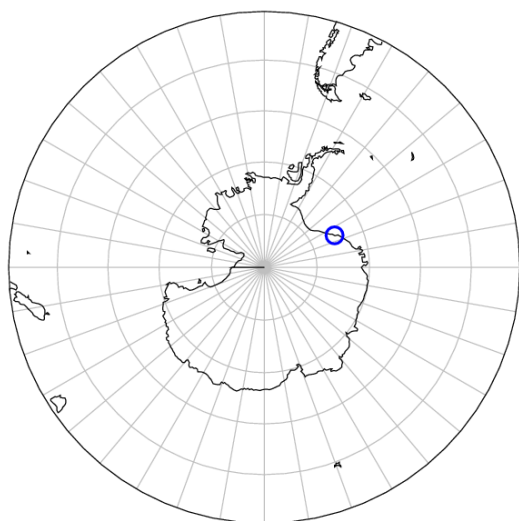
Figure 3.4: Map of the Southern Hemisphere showing the coast lines of the Antarctic continent. The location of Halley Research Station (75.5° S, 26.5° W) not far from the Weddell Sea is marked by the blue circle.
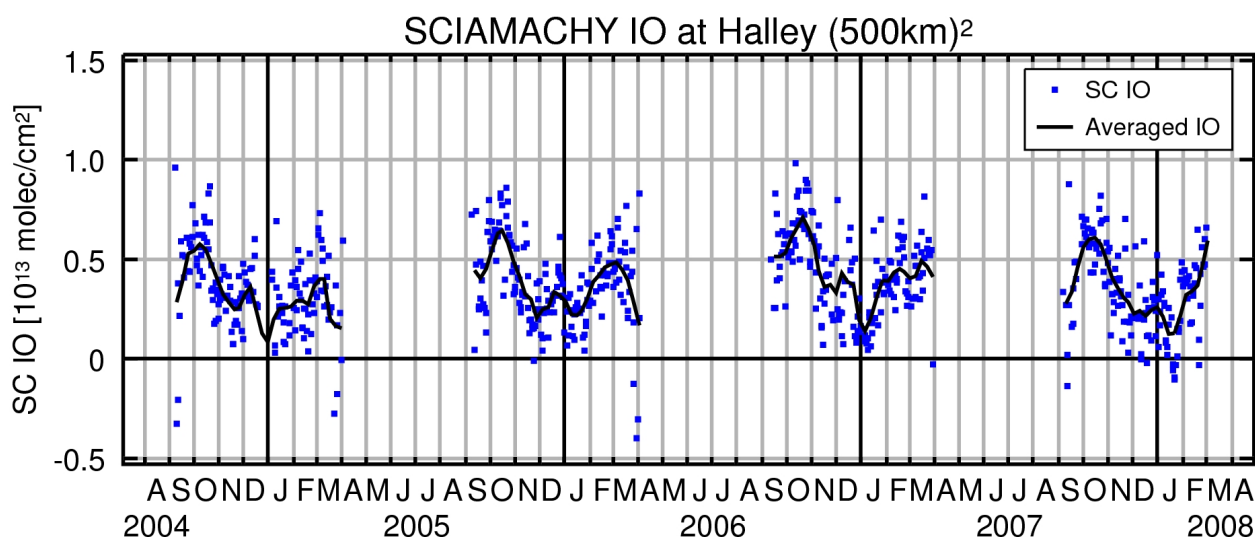
Figure 3.5: Time series of SCIAMACHY observations above Halley Research Station, Antarctica. All satellite measurements are considered which fall within a box with 500 km side length enclosing Halley Station. The blue dots represent daily values, the black solid line is a weekly running mean as a better guide to the eye.

sun (reduced SZA) and a resulting smaller AMF as discussed in Sec. 2.3. However, this effect is comparably small and may only explain a change by around 15% here and is not the cause for the observed decrease from around 7×10^{12} molec/cm^2 in October down to 2×10^{12} molec/cm^2 in summer. This must be caused by other reasons.

The interpretation of this seasonal cycle needs to take into account at least two different aspects - on one hand the amounts and availability of iodine containing precursor substances and on the other hand the photochemical conversions and other chemical pathways that lead to formation of IO. Direct sources of IO are not known up to date, so first of all, some precursor substances have to

be present. Their distribution and temporal evolution around the year will strongly influence the IO amounts. Although these substances have not been measured yet for an entire year anywhere near Antarctica, several pieces of information are available from different sources, which help to interpret the present findings (cp. Sec. 3.3).

3.2.3 Detailed analysis in higher temporal resolution

Seasonal variation for individual years

After the example of Halley Station showed that the annual cycle reappears in the same form every year, seasonal maps shall be investigated for single years, although the spatial scatter of the results becomes higher. Nevertheless, further information is obtained from these maps.

Figure 3.6 compares 16 maps, showing the four seasons for four single, subsequent years. The overall time period is the same as considered above. First of all, the similarity between the different seasons of individual years is visible. In principle, the same evolution with highest and widest spread IO amounts in spring time, lower values confined to a smaller region in summer and again higher but stronger scattered values in autumn is observed every year. The regions where the IO values are largest agree quite well between the four years, although the exact spatial patterns show differences. In all autumn and winter maps the aforementioned higher noise appears due to a smaller data amount.

Some noticeable differences are seen in the spring time map of 2006, where values are somewhat higher than in the other years and the enhanced values are somewhat more widespread around the Antarctic coast. Furthermore, the autumn map in 2007 exhibits lower values on a smaller area than the average autumn. As no accompanying measurements are available, the reason for this is currently still under investigation.

Despite these existing variations, the main conclusion from this comparison is the similarity of the regional and temporal pattern of IO, which is repeated in a comparable way in each of the analysed years. Observing an arbitrary example of one of these maps, one can easily judge which season is displayed. Averaging a certain time period over several years therefore leads to a representative result for the respective time of year.

Results in higher temporal resolution

Monthly plots averaged over four years each are analysed in the following. Figure 3.7 contains in total 16 maps for different times of year. The averaging periods are specifically chosen such that subsequent maps overlap by half a month. The start day is given in the individual headers of the maps, the second map hence contains data for the period of 15th September to 14th October, for the years 2004-2007. This way, a running average over the IO slant columns is obtained. More detailed evolutions now become visible.

Starting in early springtime, the September map shows enhanced values of IO around the Antarctic, especially in the Weddell Sea area, the shelf ice regions (the Filchner-Ronne, the Ross and the Amery ice shelves) and around the Antarctic peninsula. On the opposite side between 90° and 180° East and off the Antarctic coast, only small notions of IO are detected but no widespread

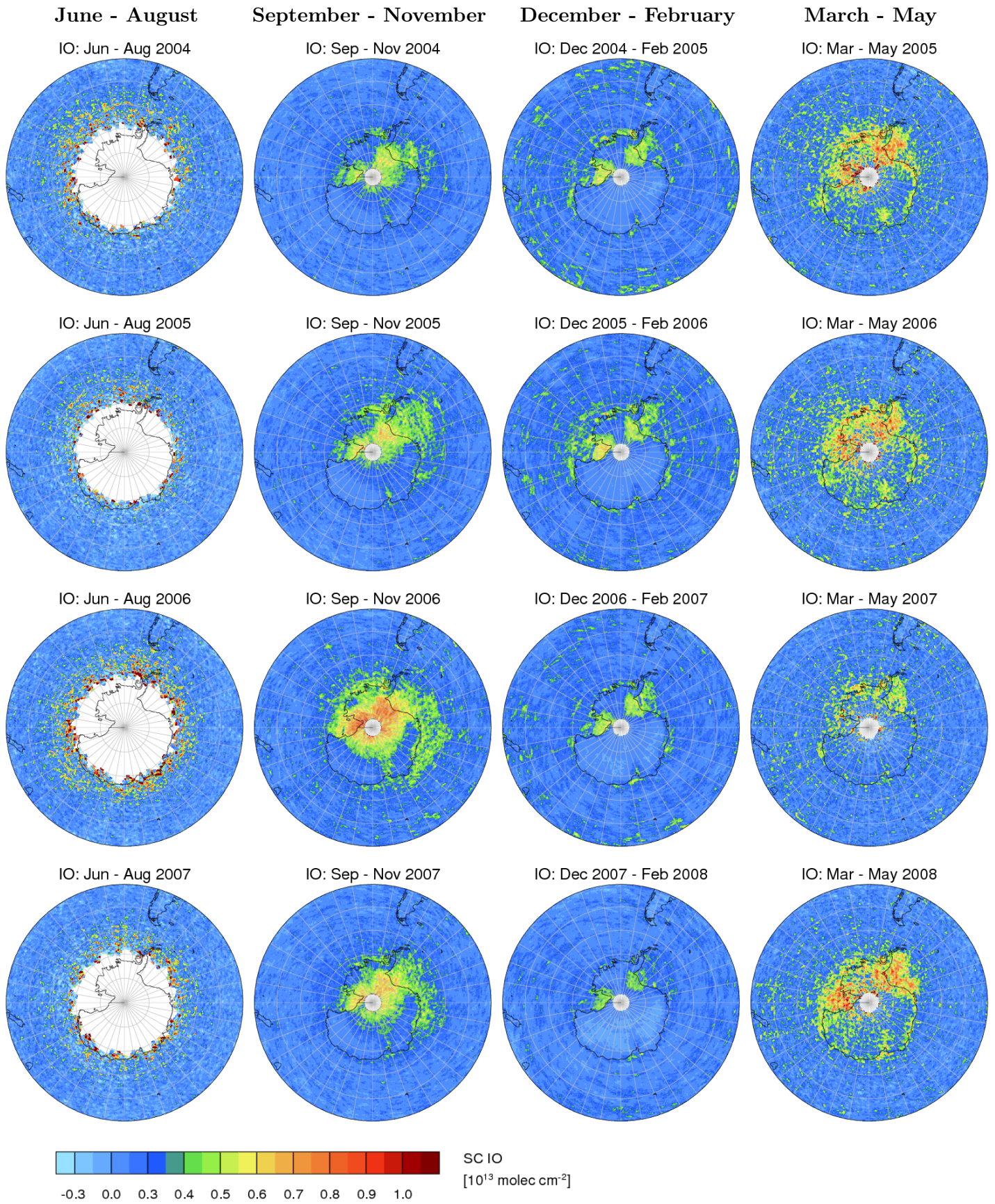| June - August	September - November	December - February	March - May

Figure 3.6: Seasonal maps of the IO slant column on the Southern Hemisphere separately for each year for an overall time span of four years from June 2004 - May 2008.
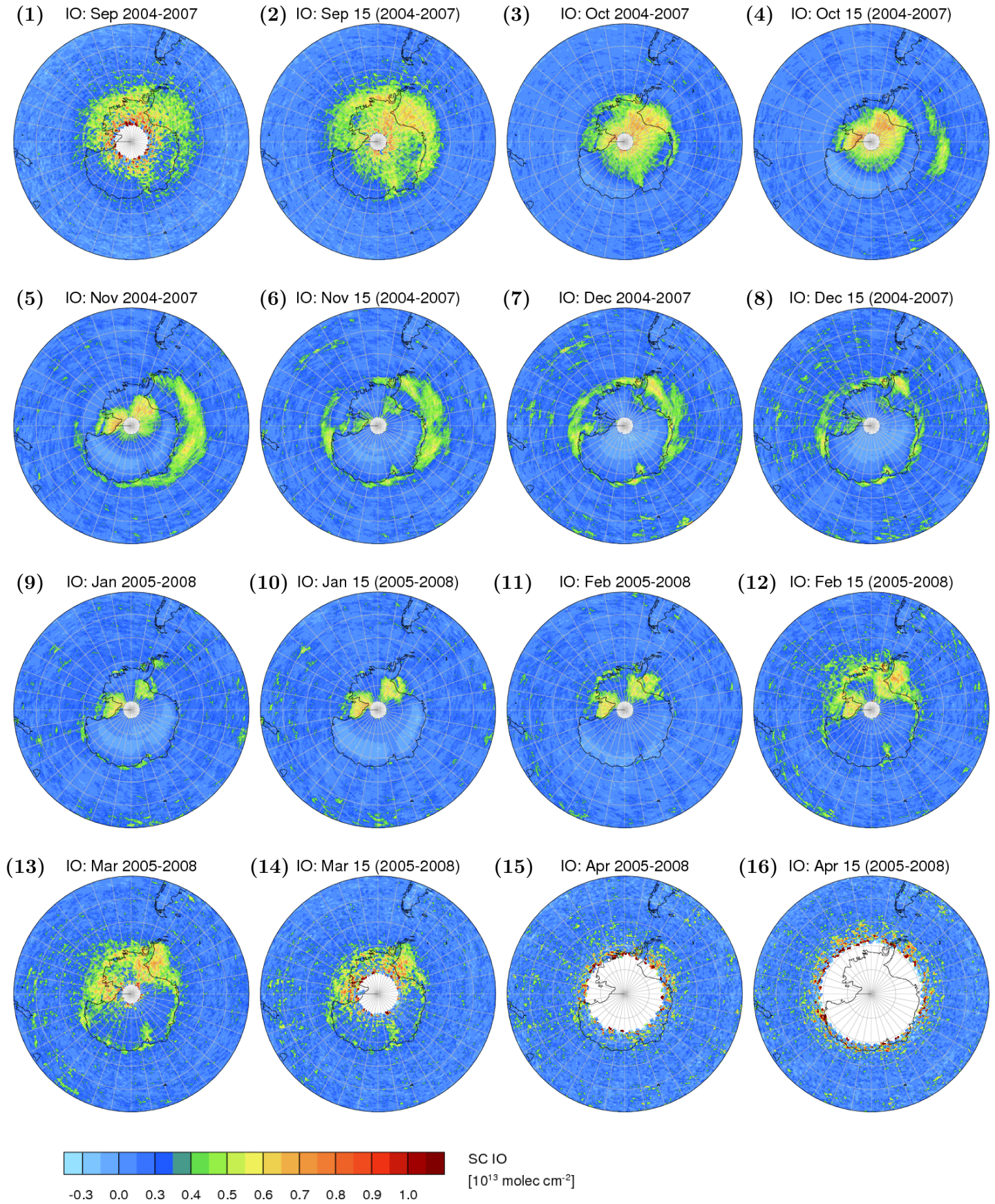
Figure 3.7: Monthly maps of the IO slant column results on the Southern Hemisphere averaged over four subsequent years each, starting on the date given in the individual headers.

amounts. As in the seasonal average, the slant columns are also enhanced on the Antarctic continent. Closer to the South pole the noise becomes higher due to the lower position of the Sun. Going one half month further, the IO values sustain their pattern and the magnitude grows, e.g., in the Weddell Sea from around 6 to 7×10^{12} molec/cm^2. Towards October, the highest values remain at their levels from before, but the region of enhanced IO is contracted closer to the Antarctic continent and does not reach as far off the coast as in the weeks before. Except for the continent and the shelf ice regions, now the direct coast lines East of the Weddell Sea and the Ross shelf ice regions show high IO amounts.

A completely new feature then appears in map (4) from mid October to mid November, where approximately 10° North of the Weddell Sea an extended regional band of enhanced IO develops. This band has a length corresponding to 70° in longitude around the Antarctic area, but is entirely disconnected from the enhanced IO values close to the continent. In November, the novel circular IO band extends even further around the Antarctic, the values grow and the width of the region of enhanced IO is also increased. It now reaches from the Antarctic peninsula at about 60° West in Eastward direction nearly up to the Ross shelf ice region at 180° East and lies between 70° and 60° South. This sudden appearance of widespread, enhanced IO amounts within a few days or weeks only strongly suggests the presence of a very efficient and fast release mechanism of iodine compounds in the respective area. Further scientific analysis about possible sources of iodine species in this area as well as comparisons with bromine oxide measurements and ice cover maps are subject of the following central section of this study.

During the following weeks up to the average from mid December to mid January (map no. 8), the circular structure is sustained but changes its exact pattern from week to week extending the band further around the Ross Sea region and nearly closing the circle in map no. 7 (December average). It is remarkable, that the enhanced IO values over the shelf ice regions and over the continent decrease and actually vanish up to December while the ringlike structure is developed. This independency of the two regions argues for different conditions and different ongoing processes - maybe even different iodine sources - in each case.

In January, eventually the IO band nearly vanishes, only small remnants at some coast lines are still visible, which two weeks later have disappeared also. Starting from January again, IO amounts reappear over the shelf ice regions (esp. the Ross shelf ice and at the Weddell Sea) and the continent close by. The region expands towards autumn and similar to early spring, enhanced IO values close to and over the Antarctic continent are observed.

From March onwards, similar as in September, a stronger spatial noise and scatter in the absolute IO amounts is apparent. This is in both cases due to less measurements at these times as compared to times closer to Southern summer. In April finally, no systematically enhanced IO amounts can be distinguished from the overall noise level and the region is partly affected by winter darkness already, so that no further measurements are possible in the Southern latitudes.

These novel observations of IO around Antarctica with a more detailed view on the temporal evolution of the abundances in the different areas provide a substantial basis for the interpretation of ongoing iodine release and chemistry at Southern high latitudes. The maps of Fig. 3.7 will be of valuable help for the following interpretations.

3.3 Discussion of observations in Antarctica

The observations of iodine monoxide over Antarctica are starting points for interpretations and discussions of potential sources and (chemical) pathways of iodine species. The relevant question is which processes and sequences may lead to the detected amounts of IO and to the observed seasonal cycle and spatial pattern.

After iodine species have been released, chemical conversions between the different iodine compounds take place. In estimating which processes may be relevant, the respective life times of the species, the known reaction kinetics and the surrounding conditions, e.g., other species, the photolytic situation such as the SZA and the time of year, as well as the physical environment (e.g. the present ice cover) may play a role. All these aspects influence the pathways of iodine chemistry. The combination of the most relevant factors must be able to explain the annual cycle and also the spatial variation which have been observed.

Considering the spatial distribution, two or even three different regions might have to be distinguished. The circular band of enhanced IO appearing around mid October/beginning of November around Antarctica may have different origin than the IO amounts on the shelf ice regions in certain times of the year. The high amounts on the continent in early spring (September to October) again need separate attention.

Organic release

Concerning the sources of iodine species, there are generally two different types of release processes, the organic and the inorganic release. Iodine release has been associated with organic precursors such as methyl iodide or diiodomethane and others (Alicke et al., 1999). These substances are of biogenic origin, e.g., emitted from certain algae types (Reifenhäuser and Heuman, 1992). This connection has directly been observed in the laboratory, but also in marine sites in mid latitudes. For the Southern Ocean, the release processes have not been clarified yet. No parallel measurements of IO in the atmosphere and potential precursor substances in the air as well as in the surrounding ocean or ice sheets have been undertaken.

In analogy to the observations of the mid latitudes, it is well possible, that organic release plays an important role also in the Antarctic. The Southern Ocean is biologically very productive and represents a habitat for many life-forms. In the ocean, high concentrations of phytoplankton types have been found. The cold and nutrient rich water is especially advantageous for certain species such as diatoms (Thomas and Diekmann, 2003). These organisms even live partly underneath the ice sheets and take advantage of the shelter and hold which is provided there. Therefore, Antarctic ice sheets have often been reported to be of greenish colour on their undersurface (Thomas and Diekmann, 2003). There is no doubt, that biological processes are taking place in the Antarctic region. Therefore, biogenic release of organoiodines has to be considered as one potential source of IO in the Antarctic atmosphere.

Iodinated methane species have been observed on ship borne campaigns in the Southern Ocean close to the Antarctic coast. Alongside the detection of the species in water, also measurements in the boundary layer above were conducted by (Carpenter et al., 2007) and substantial amounts

of, e.g., CH_2I_2 were detected. As these were spot measurements (taken in Antarctic summer), the situation on a larger spatial and temporal scale is not known, but the existence of iodinated species in the meltwater close to the coastal ice sheets and in the atmosphere has been proven.

If the phytoplankton species are close to the ocean surface, the emission can happen more or less directly. In case of an ice covered area, there are two different possibilities. Sea ice is often of poriferous structure with enclosures of liquid water (Thomas and Diekmann, 2003), so that substances may travel vertically through the ice if it is not too thick. On the other hand, there are always open leads and gaps in the sea ice cover which make the direct release in between the ice covered areas possible. So even if an ice sheet seems to be closed when observed from space, there may be open spaces allowing direct contact of the ocean water with the boundary layer above. Furthermore, large open leads (polynyas) cause a direct contact between the relatively warm ocean water and the colder air above, so that polynyas are typically accompanied by air convection. Concentration gradients across the ocean surface are influenced by the convective removal of the gaseous species. This way, the release of gaseous compounds from the water to the air is facilitated. Through convective motion, uplift of iodine species changes its vertical distribution, and additionally, horizontal transport processes may be thus initiated.
Considering this background knowledge, the IO along coast lines and above the comparably thin sea ice may indicate biogenic sources. Ice algae and diatoms are regarded the most probable candidates here, but also other sources should be kept in mind. Some further ideas are developed below.

Inorganic release

On the other hand, also inorganic pathways may be important for atmospheric iodine content in Antarctica. As some parallels between the different halogen species exist in general, the knowledge on the field of atmospheric bromine can give more insight to what might happen in the case of iodine.
Bromine oxide (BrO) can be measured with the DOAS technique in the ultraviolet wavelength range. For bromine species also both, organic and inorganic emission processes, are in discussion. However, for the polar regions, strong evidence has been found, that the inorganic pathways are of major importance here. Several field and laboratory studies lead to the conclusion that biogenic release would not be able to account for the observed amounts of BrO and the rapid O_3 destruction during ozone depletion events. The photolysis of organic bromine species is typically too slow to explain the sudden and strong occurrence of reactive bromine in the gas phase (Sec. 1.4.2).
The situation for IO might be different from that of BrO, even though similarities in the spatial and temporal patterns have raised the assumption, that the release processes may be connected in some cases. A similarity between the chemistry and sources of two halogen oxides has been suggested previously following ground-based measurements at Halley Station by Saiz-Lopez et al. (2007b).
An additional fact makes the comparison between IO and BrO observations even more important. Even if the release itself turns out to be different for iodine, the chemistry of both halogens is surely connected, as cross reactions take place and the presence of iodine might even lead to enhanced release of bromine (Vogt et al., 1999). Therefore, the comparison of observations may help in any case in the interpretation of the ongoing processes. For this purpose, the maps of IO and BrO will

be compared in the next paragraph. Inorganic release has its beginning within the ocean water, where various iodine and bromine species such as iodide (I^-), bromide (Br^-), iodate (IO_3^-), HOBr, HOI and several other compounds are present. Direct interaction on the ocean surface leads to the exchange between substances in the aqueous and the gaseous phase, such as $I_{2(aq)} \leftrightarrow I_{2(g)}$. Additionally, heterogeneous reactions on the ocean surface may take place involving gas phase and aqueous phase species at the same time. Apart from the ocean surface, sea salt aerosols, ice surfaces, frost flowers and brine are possible locations for relevant interactions and multi-phase reactions. Locations where inorganic release may become important include the ice edge of the ocean, fresh sea ice, but also all regions that can be reached by wind-blown aerosol coming from the ocean and sea ice. Especially interesting in this respect is the observation that sea salt aerosol is typically enriched in iodine as compared to sea water content (Murphy et al., 1997).

3.3.1 BrO observations and ice concentration in Antarctica

In order to compare the results of IO and BrO observations from satellite with each other, Fig. 3.8 shows 16 maps of the BrO vertical columns for the equivalent time periods as in Fig. 3.7 for the IO slant columns. The BrO data were provided by Mathias Begoin and Andreas Richter, University of Bremen (Richter et al., 1998). In these vertical columns, the stratospheric part of BrO is still contained (Sinnhuber et al., 2005; Rozanov et al., 2005a). This is not negligible, but spatially slowly varying. The stratospheric portion is covered by the green values from the colour scale for BrO starting at 4×10^{13}molec/cm^2 and not at zero. The stronger varying tropospheric portion appears in yellow to red. The conversion from the original slant columns to the depicted vertical columns was performed using a stratospheric AMF at an albedo of 90% and individual SZA and wavelength values. The AMF is valid for the stratospheric portion of the column and slightly underestimates the tropospheric amounts of BrO (Richter et al., 1998).

Although the maps of IO show slant and not vertical columns, a comparison is still meaningful, as not the absolute values but more the spatial distribution and temporal variations are of interest for the interpretation here. Without knowing the individual profiles of the trace gases and the ground spectral reflectances, the conversion between the SC and the VC for IO here is given by a factor, which changes only slightly throughout the year depending on the SZA.

For the case of BrO, the sea ice concentration is known to be of major importance for the interpretation of BrO observations in Polar Regions (Kaleschke et al., 2004). From the current new investigations in this study, it becomes probable, that also IO is in certain cases related to the sea ice cover.

In order to compare the halogen oxide maps to sea ice cover, Fig. 3.9 shows maps of the ice concentration in and around Antarctica from the AMSR-E sensor (cp. Sec. 1.9.3), provided by Gunnar Spreen and Lars Kaleschke, University of Hamburg (Spreen et al., 2008). In this plot, also 16 maps are displayed, but each map shows the ice cover situation for one certain day given at the top of each map. The chosen time is September 2006 to May 2007 and each day in this figure corresponds to the middle of the monthly averaging period from Figs. 3.7 and 3.8. The sequence of ice cover maps therefore starts on the 15th of September, while the IO and BrO maps show first an average from 1st to 30th September. Each following map in each sequence was taken two weeks
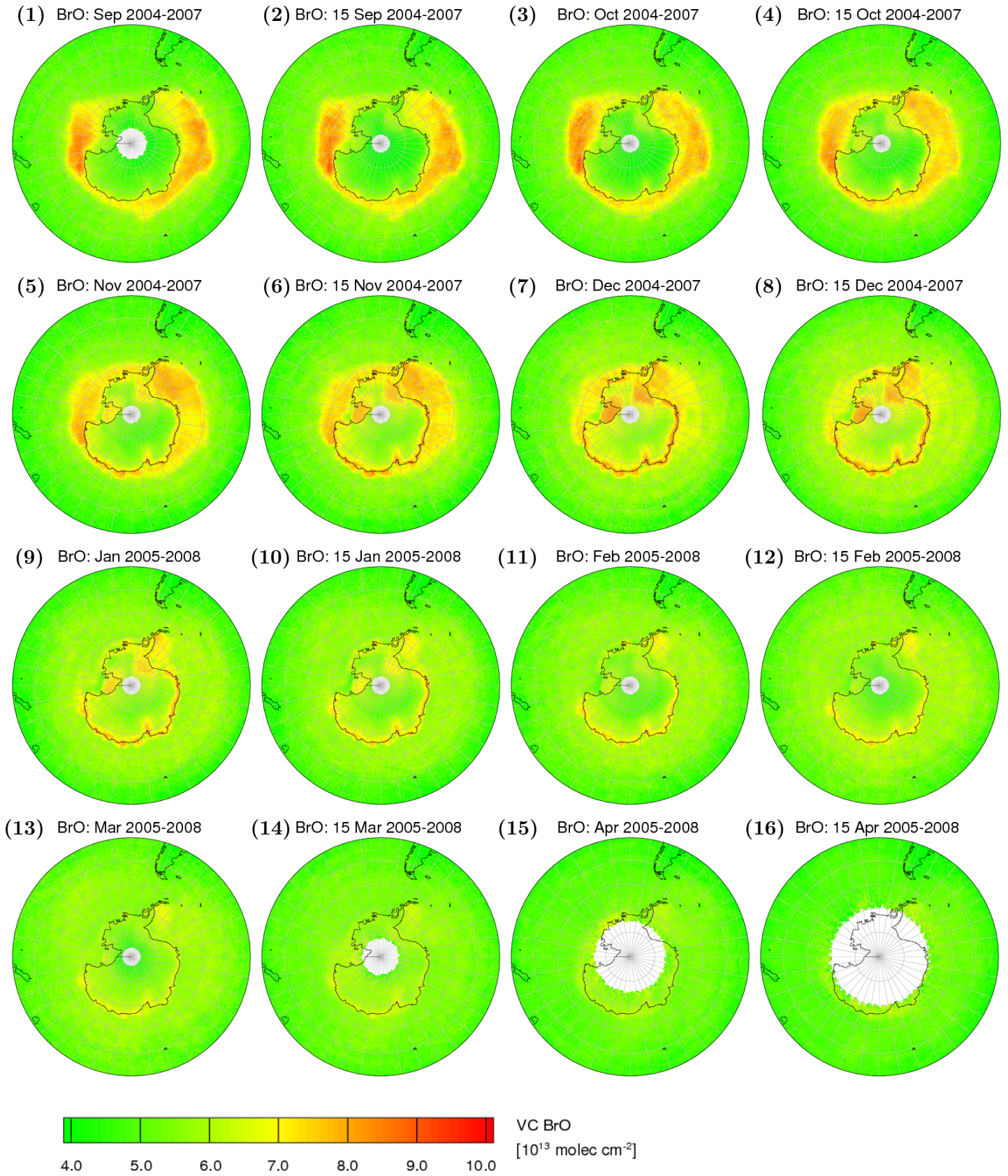
Figure 3.8: Monthly maps of BrO vertical columns for the same averaging periods as for IO in Fig. 3.7.

later.

The exact ice cover naturally varies from year to year, so that the spatial pattern exhibits deviations when comparing one specific time period with the same period of a different year. However, the seasonal changes are still larger than the year-to-year variations, and a typical ice cover may be allocated to a certain time of year. For the general comparison here, the exact pattern is not relevant, but more the general evolution. As the general patterns are roughly repeated annually, the comparison can be performed using daily maps.

BrO columns are already above the detection limit in August (not shown here), and a well pronounced circular pattern of enhanced BrO amounts around Antarctica is seen in September (Fig. 3.8, map no.1). By comparing the BrO and ice cover maps, the known observation can be reproduced, that the enhanced BrO columns correlate spatially with the extent in sea ice cover (Kaleschke et al., 2004). The circular structure in the BrO columns remains nearly unchanged with only slight variations until mid-October to mid-November (map 4). From map 5 onwards, additional regions with high BrO values appear - the Ross Sea around $180°$ East as well as the shelf ice area and some continental parts of Antarctica close to the Weddell Sea and further Southwards. Also, high BrO values around the coast lines of Antarctica become visible. This enhancement of BrO close to the coast remains present throughout the summer time until March (map 13). The broad ring of enhanced BrO however vanishes around December (maps 7-8). From this time, the shelf ice regions, some continental areas close by and the coast lines are the main regions of high BrO amounts. From mid-March onwards, hardly any BrO can be detected on the Southern Hemisphere in these averages.

Concerning the comparison to the sea ice cover, the largest areas of high BrO are found above the extended sea ice sheets. Up to the end of February, the pattern of enhanced BrO follows quite well the spatial extent of the sea ice cover. One exception are the shelf ice regions, where BrO is present for some months without direct contact to sea ice, e.g. in maps 4-8, for the shelf ice regions of the Ross Sea and the Weddell Sea. In autumn, the BrO does not correlate with the sea ice cover when this begins to grow again, but the BrO remains below detection limit (maps 14-16).

The detected correlations between BrO and sea ice cover and the high amounts of BrO have lead to the assumption, that BrO is most probable of inorganic origin from efficient processes which take place on salty surfaces and under certain conditions (Sander et al., 2006a; Simpson et al., 2007a). The concept of potential frost flowers and the connection to brine on sea ice were developed (Kaleschke et al., 2004). Up to now, it is not clarified which actual processes, conditions or specific locations on the sea ice are responsible for the bromine release. It is agreed that probably the so-called bromine explosion takes place (cp. Sec. 1.4.2). This auto-catalytic release mechanism leads to fast and efficient release of bromine atoms to the atmosphere, directly from the sea salt content without involvement of organic processes.

For the spatial pattern of BrO, also transport plays an important role. The enhanced values on the shelf ice regions for which no local release processes are proposed, are caused by transport processes. BrO may be carried over fairly large distances on the order of several hundred kilometres within several hours up to a few days (Begoin et al., 2009).

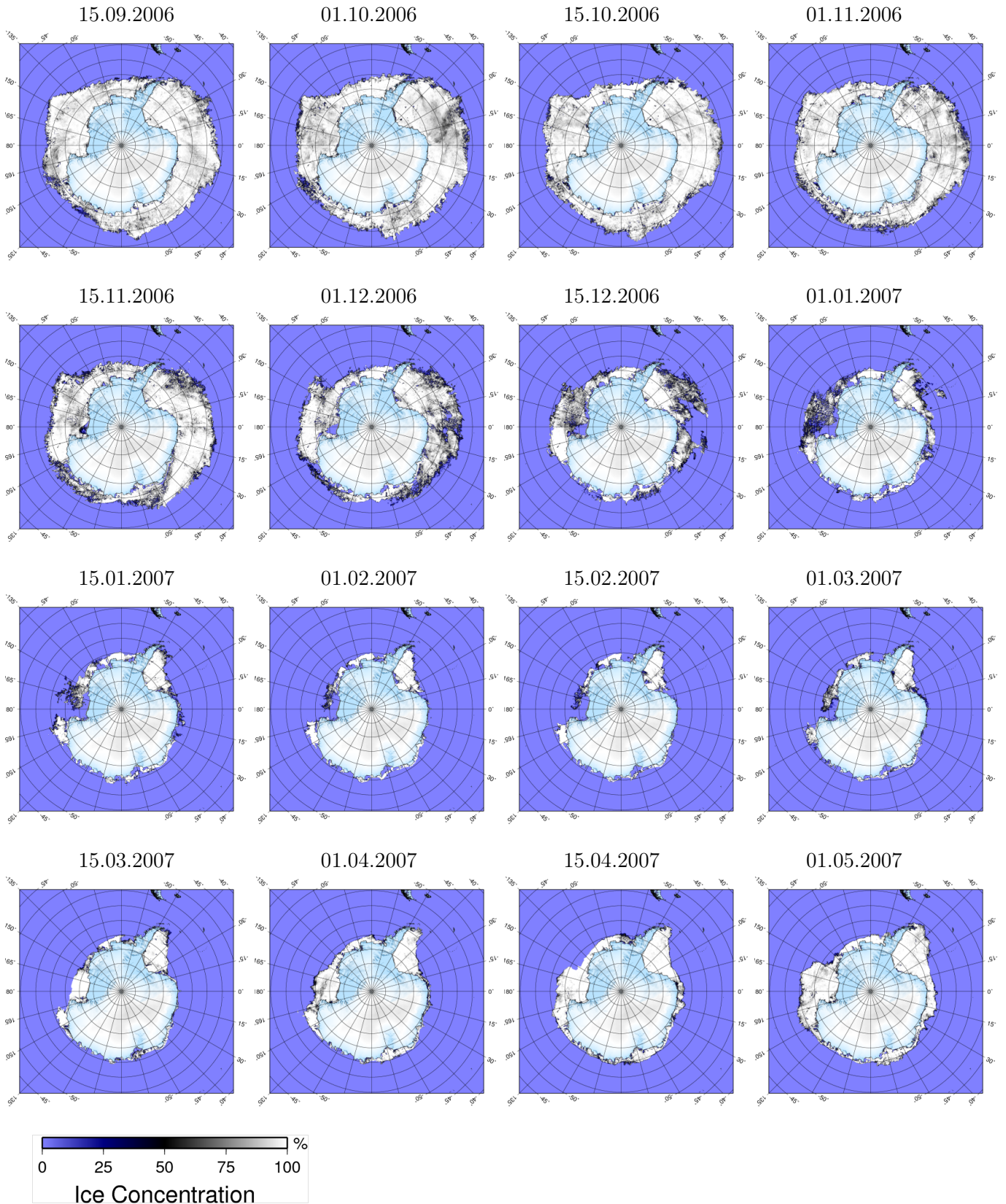**Figure 3.9:** Daily maps of ice concentration on the Southern Hemisphere retrieved from AMSR-E measurements in the 89 GHz channel at a resolution of 6.25 km (Spreen et al., 2008). The maps were obtained from Gunnar Spreen and Lars Kaleschke, Institute of Oceanography at the University of Hamburg, Germany in June 2009 (digital media ftp-projects.zmaw.de/seaice). The data version is "AMSR-E ASI 6.25 km Sea Ice Concentration Data, V5.5i".

3.3.2 Comparison of IO with BrO and sea ice maps

One similarity between IO and BrO observations in Antarctica is first of all the general overlap in time and space of enhanced columns. The largest amounts of IO globally are found in the spring time Antarctic. The same holds true for BrO, although columns of comparable magnitude are found in the Arctic also. Several similarities between the two species are observed:

- The circular structure which appears in both, the IO and the BrO maps, is of similar pattern and location approximately from mid-October to end of December (maps 4-8). Both halogen oxides show a connection to sea ice concentration during this period with highest amounts appearing above the present sea ice.

- Secondly, the enhancement over the Ross Sea and the Weddell Sea shelf ice regions occurs for both species. However, the times when high values are detected are not exactly the same.

- Although this is not as prominent for IO as for BrO, both trace gases show enhanced amounts along the coast lines. While BrO is detected around the coast for nearly all periods shown, the values drop below detection limit for IO around end of January and begin of February (maps 10 and 11). Nevertheless, smaller patches of IO amounts around the coast are seen in most of the maps.

On the other hand, the patterns of IO and BrO also exhibit some remarkable differences:

- IO values are enhanced above the continent in September and October, while no BrO appears above the continent at that times. The BrO is distributed at a further distance in the described circular pattern, whereas IO amounts are more confined towards Antarctica and do not reach as far onto the sea ice in September and October as later on. The connection between BrO and sea ice concentration seems to be stronger and valid for a longer period of time than for IO.

- Concerning the shelf ice regions, both species are detected here, but high IO amounts are seen nearly throughout the entire time series with lower values around December (map 7), while BrO shows the highest amounts in the shelf ice regions between November and January (maps 5-9).

- In March, IO values are nearly as wide spread as in September, but BrO amounts mostly drop below the detection limit except for small indications around the coast which remain until end of March.

3.3.3 IO in sea ice covered areas

The cases, where correlations between IO and BrO observations are detected suggest, that similar or connected release takes place. This may especially be true for the halogen oxides detected on sea ice and along the coast lines of Antarctica. In the central reaction of the inorganic bromine explosion, two inactive bromine species convert to Br_2 within sea water or sea salt aerosol:

$$HOBr \ + Br^- \ + H^+ \quad \rightarrow \quad H_2O \ + Br_2 \quad (R16)$$
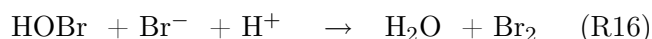
This may lead to an exponential increase in the concentration of BrO. One important prerequisite for this to happen is the necessary acidity (involvement of H^+ ions). In this central reaction, bromide may be exchanged for iodide and then also lead to completely inorganic release of iodine species:

$$\mathrm{HOBr} + \mathrm{I}^- + \mathrm{H}^+ \quad \rightarrow \quad \mathrm{H_2O} + \mathrm{IBr} \qquad \text{(R39)}$$
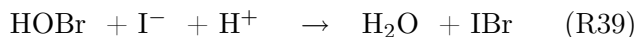
In this case, IBr is set free which yields an iodine and a bromine atom after photolysis. The above cross halogen reaction shows one of the existing links between bromine and iodine chemistry. Another important reaction is the reaction of IO with BrO, which also yields IBr in the gas phase. This is especially relevant for the recycling of Br atoms as the self reaction of BrO probably does not take place. This consideration suggests a strong correlation between the two species, as mutual amplification of their release and recycling processes is possible.

The circular pattern of BrO around Antarctica, however, occurs already earlier in the year than for IO. This argues for considerable differences in the release process. Possibly the iodine reactions need different conditions than the bromine reactions which are given only later in the year. A second possibility is the involvement of biology at this point. While the chemistry of iodine and bromine is surely related, the activation might still undergo different pathways. As stated above, sea ice is usually not a closed surface but exhibits cracks and large open leads (Thomas and Diekmann, 2003). As phytoplankton is present underneath the sea ice sheets, emission of biogenic substances may be enhanced in the presence of open areas, broken ice sheets and even just thinner ice sheets. The IO appears on the sea ice around late October, although sun light enters these areas several weeks earlier where no IO is detected on the distant sea ice.

Presumably, the iodine release requires the sea ice to be more porous and instable than it is in early spring time. From the beginning of spring towards the summer, the sea ice gets thinner and is more often interrupted by open water leads and polynyas. This can be followed in the ice maps of Fig. 3.9, where greyish colours mark reduced ice concentration. In this situation, possibly biological activity might become more prominent.

Discussing the potential biological source of halogens in the Antarctic it may be illuminating to consider the biological activity in the oceans. From space, this can only be measured in ice free areas. A potential indicator of active biology in the oceans is given by the chlorophyll concentrations. Chlorophyll, the initiator of photosynthesis, is a green pigment (absorbing in blue and red spectral bands) which is present in plants, and also in algae and cyanobacteria. Figure 3.10 shows the SeaWIFS monthly climatologies of chlorophyll a concentrations (cp. Sec. 1.9.3) for the six months of October to March (Hooker et al., 1992). Each map contains data from 10 years. The chlorophyll a (Chl a) concentration is colour coded as specified by the colour bar in the bottom of the figure. Regions without data appear black in the readily provided maps. With a ground resolution of 9 km side length, ocean data is only available for ice free areas of this size. The radiation reflected from ice sheets in the field of view otherwise overbalances the ocean signal. In the remaining months not shown here, the ocean surrounding the Antarctic is mostly ice covered and only smaller open leads and polynyas with less than 9 km size may exist.

October

November

December

January

February

March

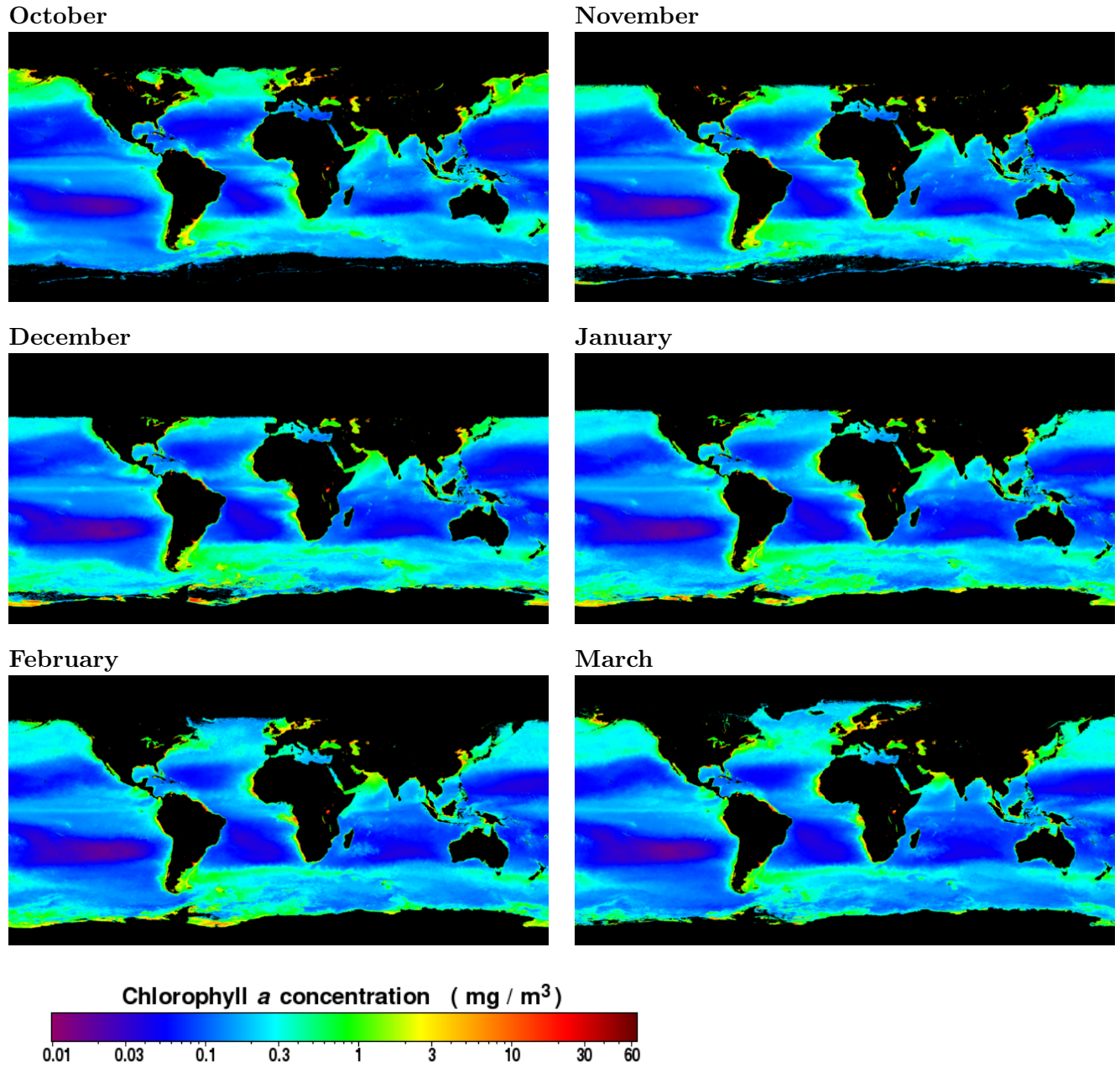**Figure 3.10:** SeaWIFS monthly climatologies of the oceanic chlorophyll a concentration, provided with 9 km spatial resolution by NASA (NASA, http://oceancolor.gsfc.nasa.gov, June 2009).

In the SeaWIFS images, the development of open water regions within the sea ice cover in Antarctica becomes visible as coloured regions appearing in the blackened space. It is interesting to note that these open water regions, especially in January and December but already in November, show enhanced chlorophyll concentrations indicating strong biological activity in these areas. In November, especially the ocean close to the Ross Sea exhibits enhanced chlorophyll amounts. In December and January, also enhanced chlorophyll in the Weddell Sea area can be clearly distinguished. The amounts are comparably large. These maps do not give information on the respective species which are responsible for the chlorophyll concentrations. In general, species which release iodine precursors as well as those which do not influence the atmospheric halogen levels contribute to the chlorophyll a signal. However, the maps prove that biological activity is high in many locations as soon as the ice opens. It seems likely that biological activity also occurs in smaller openings in the ice which are not resolved in these images, but which are definitely present (Thomas and Diekmann, 2003). For more detailed analysis on a smaller scale, e.g., in the sea ice covered regions still in October and even earlier in September, data in higher resolution needs to be considered in the future. The most important outcome of these images is the existence of high chlorophyll concentrations close to Antarctica in times, where also IO has been observed. These images therefore support the idea, that organic sources of iodine precursors may at least partly cause and influence the high iodine oxide content of the Antarctic atmosphere in certain times.

3.3.4 IO on Antarctic shelf ice regions and the continent

Unexplained so far are the high IO amounts on the Antarctic continent in early spring time (i.e. September to October). The original expectation was to find IO around Antarctica, similar to BrO, still in the vicinity of the ocean, but not on the continent. These result may need further investigations in the future. No direct sources inland on Antarctica are known up to now. Nevertheless, some existing processes would lead to high IO amounts on the continent also, and may explain the observations. Two important aspects need to be brought forward.

I. Transport processes of IO and iodine rich aerosols

First of all, transport processes from other regions need to be taken into account. After IO has formed in the atmosphere, it can be photolysed quite quickly back to iodine atoms. Therefore, its individual lifetime is short and one might rashly assume that long range transport consequently is not relevant. However, more detailed considerations point out the possible occurrence and significance of transport nonetheless.

IO and BrO are often detected on the ice shelves. Similar to the situation on the continent further inland, no direct sources of bromine or iodine have been reported for the shelf ice regions. Interestingly, transport processes reaching far inland can be regularly observed for the case of BrO (Begoin et al., 2009). BrO columns have larger optical depths and can be analysed on a daily basis, which is not possible for IO as values are much closer to the detection limit. Therefore, individual transport events can not easily be detected in the satellite IO data. Considering the observation, that BrO is transported over thousand kilometres inland, this may also be true for IO. The times involved in such transport processes are much longer than the typical photolytic life times of BrO.

The life times of the halogen oxides have a large influence on the possible pathways. And some important considerations should be made. BrO life times during strong exposure to sun light lie around two minutes, for IO around several seconds. This basic life time is much shorter than the effectively relevant lifetime (Simpson et al., 2007b), as the Br and I atoms produced by photolysis react with O_3 to form back BrO and IO. So the BrO and IO are not lost by photolysis. The effective lifetime is substantially longer and for the case of BrO_x ($BrO_x = BrO + Br$), life times around many hours were estimated by Simpson et al. (2007b).

The equivalent estimation was not performed for IO, but a similar consideration holds for reactive iodine. For similar situations, the lifetime of IO is effectively enhanced by the cycling of reactive iodine between I and IO, so that the lifetime of IO_x ($IO_x = IO + I$) is substantially larger than for an individual IO molecule.

In addition to the enhancement of the effective lifetime, further processes may take place which additionally sustain high levels of halogen oxides and enable transport processes. Concentrating on the case of IO, one special characteristic has substantial influence. IO forms higher oxides in a self reaction, first generating OIO molecules, and thereafter also higher oxides of the general form I_xO_y (cp. Sec. 1.5.3). Iodine oxides lead to the formation of fine particles themselves and they also undergo heterogeneous phase reactions on the surfaces of aerosols, snow and ice. This is facilitated by the the hygroscopicity of these gases. Being attached to the aerosol phase, the iodine atoms involved are not consumed but may be transported over longer distances than possible solely in the gas phase. Later on, the iodine species may be released from the aerosol phase again and the reactive iodine is recycled. The chemical reactions of this recycling are not known yet, but as the condensable iodine vapours and following particles are hygroscopic, some reactions in the following aqueous phase or on the aerosol surface may proceed. Depending on the available iodine compounds in the solution, some iodine molecules may transfer back to the gas phase, be photolysed and recover some IO. This way, the reactive iodine can effectively travel longer distances than initially assumed. All possible conversions and pathways need to be considered when estimating the effective lifetime of IO, and transport to regions, where direct sources are not known may well be possible. The significance of the combined recycling and transport processes needs to be evaluated more carefully in order to receive meaningful numbers of the possible amounts of IO transported a certain distance inland of Antarctica.

II. Unfamiliar and unusual sources

No inland sources of iodine in Antarctica are known up to now. However, this does not prove that such sources indeed do not exist and formerly unknown or not considered or even forgotten sources need to be (re)considered. Some ideas and proposals of probably minor importance shall be shortly mentioned here, of which many are still open for closer inspection, but they should not be excluded before their importance is properly assessed.

Several volcanoes are present in Antarctica such as Mount Erebus at 77.5°S, 167.2°E close to the Ross Sea. Volcanic activity is known to be a source of halogens and halogen oxides (Bobrowski et al., 2003). How important this might be for the Antarctic region is so far not known, but a major importance seems improbable as volcanoes in other location have no detectable influence on the IO

amounts, and the activity of Antarctic volcanoes has not been distinguished as especially strong. Also no direct evidence for BrO from the Antarctic volcanoes has been observed.

Futhermore, salt-rich dry lakes are common in some Antarctic locations. The salt content of these dry lakes is extremely high, for example, in the McMurdo Dry Valley close to the Ross ice shelf. The emission pathways from these places need to be point of further research as the details are not known yet. By erosion or other processes, salt-rich aerosols may enter the atmosphere. Extremely salty soils were found and they are expected to be developed by wind-blown sea salt (Mahaney et al., 2002). The ability of IO to form higher oxides and fine particles further on might influence the situation in favour of iodine compounds in these events. This additionally supports the argument above, that transport processes of sea salt aerosol need to be considered as a halogen source for the Antarctic continent.

Back in 1982, Rasmussen et al. have reported on methyliodide observed directly at the South Pole. Mixing ratios of 1.8 ppt CH_3I have been detected. Consequently, some unidentified local sources of iodine species in continental Antarctica are present or transport must be responsible.

Furthermore, bacteria might be of greater importance than previously assumed. Research efforts in quantifying iodine emissions from bacteria have shown that bacteria are capable of methylating iodide which is available in sea water. It is concluded that bacteria can strongly contribute to the transfer of iodine species to the atmosphere (Amachi et al., 2001). The distribution of bacteria in the Antarctic region would need to be analysed in this respect, as different bacteria have different capabilities of methylating iodide. The importance of bacteria for IO levels in Antarctica can not be estimated, but should not be disregarded.

3.4 Observations of IO in the Eastern Pacific

In the global maps (Figs. 3.1,3.2), some enhanced IO amounts over the Eastern Pacific were pointed out. Figure 3.11 shows a close up of the Eastern Pacific region, taken from the four year averaged IO map (cp. Fig. 3.1). Along the Pacific coast of Ecuador and Peru and also of Northern Chile, enhanced IO amounts around 4×10^{12} molec/cm^2 are identified. The enhanced values are concentrated over the ocean and do not extend over land. This finding indicates that some release process closely linked to the oceanic site takes place.

This region belongs to a highly interesting area, where biological production is strong. This will be further explicated below. However, the analysis in this region is more challenging than, e.g., for the Antarctic. As discussed in Sec. 2.4, detection limits and noise influences are stronger and play a larger role in oceanic regions than above high reflecting surfaces. The IO results in the East Pacific appear to be less stable with respect to changes in the retrieval settings than for the Antarctic. Nevertheless, the current results yield enhanced IO amounts and hint at some biogenic release processes in the Eastern Pacific region.

In the seasonal maps of IO, some annual variations have been visible in this region. However, some temporal variations are present in a wide surrounding area and not only at the locations where enhanced amounts are detected. As the area is affected on a large scale and the variation is systematic with the course of the year, this variation might not be a result of actual IO amounts but rather of a systematic retrieval impact caused by geometrical influences. The position of the satellite with respect to the sun is largely the same over the area for a given day, but the geometry changes with season. Depending on viewing geometry, the relevant scattering angles and with this the typical polarisation degree will vary and possibly impact on the retrieval.

A time series of IO columns has been selected in a region from 10° S to 5° N as well as from 100° W to 80° W. In order to remove the large scale temporal drifts, the average in the overall region contained in Fig, 3.11 has been subtracted. In Figure 3.12 the resulting IO slant column density is plotted versus time for the years 2005 to 2007, showing daily amounts (grey triangles) and the monthly mean (red lines and symbols). The typical standard deviation amounts to 4×10^{12} molec/cm^2, the error bars are not plotted to the data points for clarity. The overall mean of the time series amounts to 3.1×10^{12} molec/cm^2. The IO amounts perform only slight variations throughout the year, the
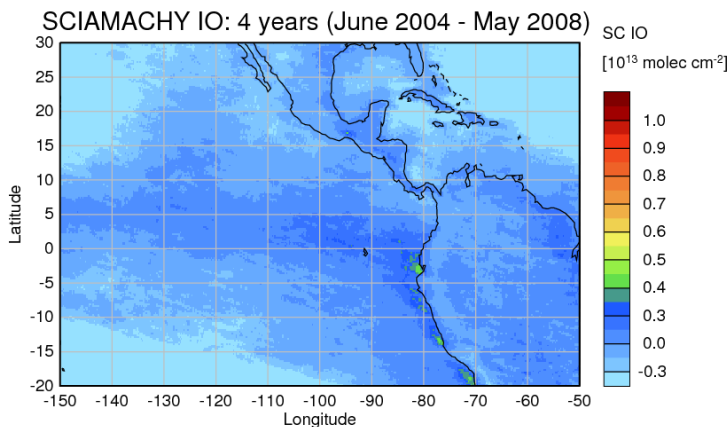

Figure 3.11: IO slant columns over the Eastern Pacific region averaged over 4 years from June 2004 to May 2008. Enhanced amounts are visible at locations along the Pacific coast lines of Ecuador, Peru and Northern Chile.
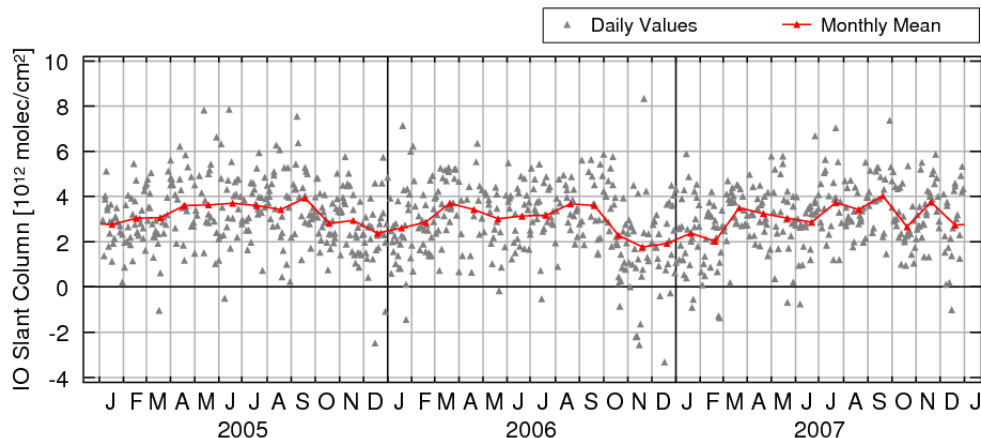
Figure 3.12: Time series of IO slant columns in the Eastern Pacific. From the original data set, the average in a wide surrounding area has been subtracted. Daily averages (grey triangles) as well as monthly means (red line and symbols) are plotted, while the standard deviations for the data points lie around 4×10^{12} molec/cm^2 and are not shown for clarity. The small seasonal variation is not significant.

difference between the summer and winter months lies around 1×10^{12} molec/cm^2. Taking into account the typical uncertainties (Sec. 2.5) and the standard deviation for the daily averages, this seasonal variation is not significant. The question for a seasonal trend in this region is therefore presently unclarified, but will need to be subject of further investigation. The fact that IO amounts are enhanced along the coast line, however, remains unaffected from this issue.

Connections to the ocean current and the biosphere

The most interesting consideration here concerns potential sources of iodine species in this location. The Eastern Pacific is well known for being a so-called upwelling region, where the typical ocean circulation is flowing upwards, bringing cold and eutrophic waters up from below. This is generally leading to an enrichment of surface waters with nutrients, generating a suitable environment for phytoplankton and other species. As a consequence, such areas are biologically very active. The upwelling region here is part of the Humboldt current, a cold ocean current in the West of South America coming from Antarctica and flowing towards the North and then turning Westwards (see also Fig.3.13). It is one of the largest upwelling systems of the world and a highly productive ecosystem.

The connection between the biosphere and iodine species was discussed in Chapter 1 and, according to current knowledge, several algae and phytoplankton types emit iodine compounds. So the nutrient rich upwelling regions are potential source regions of emissions of iodine compounds. Currently, no information is available, on how much iodine precursors are emitted in the Eastern Pacific. Considering the above thoughts though, enhanced IO amounts in this region could well be connected to the highly productive biosphere. The Humboldt current which flows past the Antarctic and surfaces at the South American West coast, partly connects the biospheres of the Antarctic and the Eastern Pacific, so that similar algae or phytoplankton species exist in the two regions. This
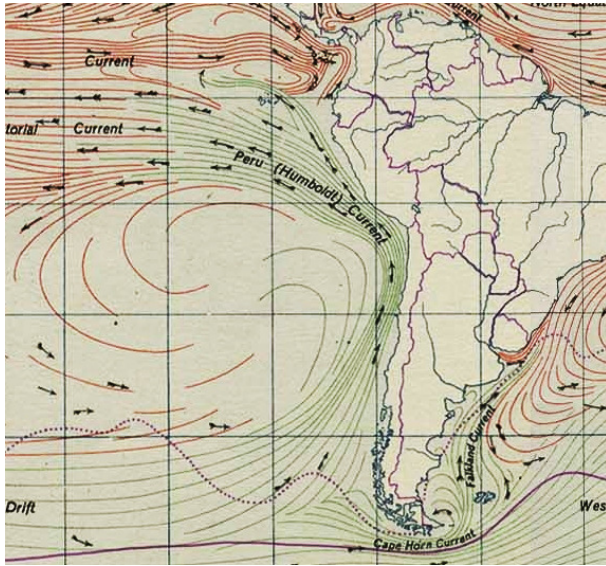
Figure 3.13: The flow of the Humboldt Current (also Peru Current). The excerpt is taken from a map of Ocean Currents and Sea Ice from the Atlas of World Maps, United States Army Service Forces. Army Service Forces Manual M-101 (1943).

may form a link between the high IO amounts in the Antarctic and the enhanced amounts over the Eastern Pacific.

As the Eastern Pacific is a region of strong biological productivity, the chlorophyll a concentrations are expected to be high there. To investigate this, a specific data set of SeaWIFS chlorophyll a concentrations has been extracted. Figure 3.14 covers the same time period and spatial region as Fig. 3.11. The color coded Chl a concentrations are clearly enhanced along the South American Northwest coast, overlapping with the locations of enhanced IO amounts. Biological emissions therefore are most likely the origin of iodine precursor compounds in this area.

Chl a from SeaWiFS Jun 2004 - May 2008

Chl a concentration [mg/m^3]
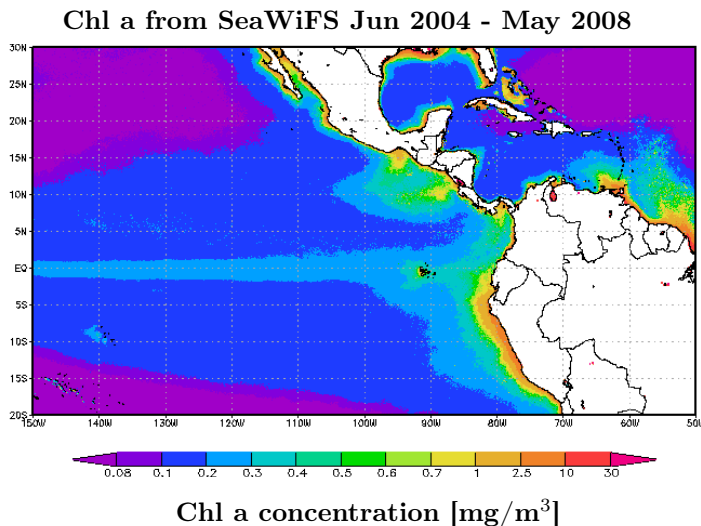
Figure 3.14: SeaWiFS chlorophyll a concentration in the Eastern Pacific, averaged from June 2004 to May 2008, i.e., over the same time period as shown in Fig. 3.11. This image was acquired using the GES-DISC Interactive Online Visualization ANd aNalysis Infrastructure (Giovanni) as part of the NASA's Goddard Earth Sciences (GES) Data and Information Services Center (DISC).

Considering the points of concern mentioned earlier, e.g, the irregularities over clear water regions (Sec. 3.1) where IO columns tend to be negative, and the lower stability of IO results over the ocean, some caution is necessary in the discussion here. Spectral correlations can in principle impact on the retrieved IO amount. The question is whether the apparent link of IO to biology in this area is a consequence of correlations or of causality. A spectral correlation of IO with chlorophyll a absorption may be excluded, as the global pictures show that high Chl a concentrations do not

necessarily imply high IO amounts. For this purpose, the mission composite of SeaWIFS cholorphyll a concentrations is shown in Fig. 3.15 containing data from Autumn 1997 to Summer 2009.

Figure 3.15: SeaWIFS mission composite from Autumn 1997 to Summer 2009 showing the chlorophyll concentration in the oceans.

Several coastal regions are coloured red due to high chlorophyll and hence strong biological activity. The so-called ocean deserts, e.g., in the middle of the Pacific and also the other oceans can be distinguished by their blue/purple colour. The area in the Eastern Pacific, where enhanced IO is seen in certain times is not as strongly pronounced as other regions, but exhibits m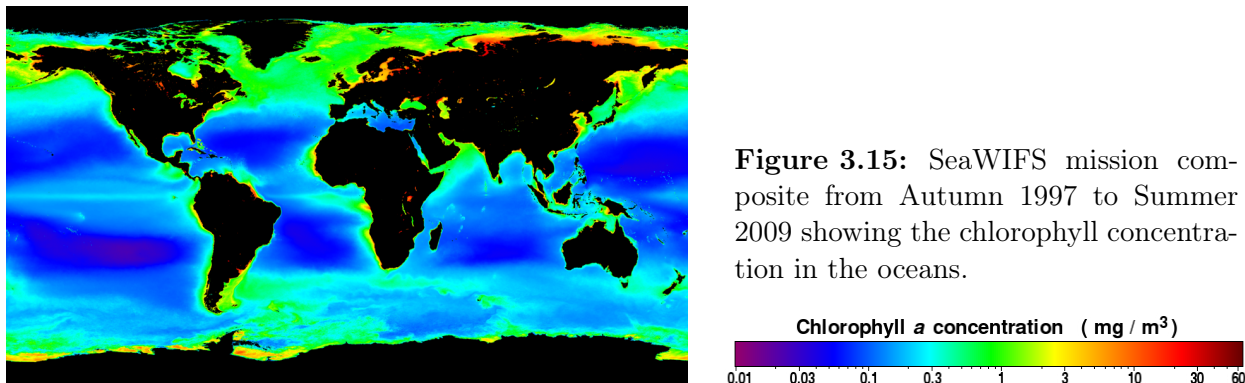edium amounts of chlorophyll. If a seasonal variation is present, amounts can well be higher for certain times. The spatial patterns of IO and Chl a are not correlated, a general dependency of the two quantities can be excluded, there are several locations, where Chl a is high and IO is not, but others where both quantities are enhanced, e.g., as in the East Pacific.

Due to the proposed link of IO amounts to the upwelling region, there should exist a dependence between the strength of IO emissions and the conditions within the East Pacific waters, like temperature, salinity and other parameters, which again influence the biosphere. Consequently, it is an interesting task for the future, to observe potential variations of IO between El Niño and non El Niño years. During years exhibiting the El Niño effect, the Humboldt current considerably weakens, sea surface temperatures are several degrees higher and biological production decreases. In a longer times series of satellite data, an effect on IO may become visible.

The question arises why IO is strong above one upwelling region but not over the others also, for example, at the Northwest coast of Africa (Mauretanian upwelling region), and also not over all regions of strong biological activity characterised by high Chl a concentrations. While in some of these regions, the IO columns may just remain below detection limit (cp. Sec. 2.4), one important reasons for the spatial differences are the spatially diverse biospheres.

IO spatial correlation with diatom concentration

It has been found that different types of algae and phytoplankton release different mixtures and amounts of organic compounds, some organisms are especially strong emitters for certain iodocarbons (Schall et al., 1994; Tokarczyk and Moore, 1994). Iodine species should only be released over regions which are populated by certain algae and phytoplankton groups, which again show individual spatial distributions in the world's oceans (Alvain et al., 2005; Bracher et al., 2009). Species such as diatoms or heptophytes can be distinguished by optical means because each species contains

different chromophores or different ratios of common chromophores leading to characteristic spectral signatures. The spatial distributions of different species may be retrieved using the DOAS technique in a comparably large wavelength window due to rather broad absorption bands (Bracher et al., 2009). Special attention is drawn to diatoms, which are reported to emit iodine species (Moore et al., 1996) with special activity of polar diatom cultures (Hill and Manley, 2009).

Figure 3.16 compares the diatom concentration retrieved by Bracher et al. (2009) with the IO slant columns in the oceanic regions of the world. Both data products are retrieved from the SCIAMACHY sensor. Some similarities in the spatial pattern can be seen. Especially, diatom concentrations are enhanced in the Eastern Pacific as well, similar to the IO amounts. The increase of diatom concentrations South of -30° latitude is not so prominent in the IO result. Future investigations will show if the link is provided by causality or not, i.e. if the diatoms are producing iodine precursors of if the products of Fig. 3.16 are the result of a third reason.
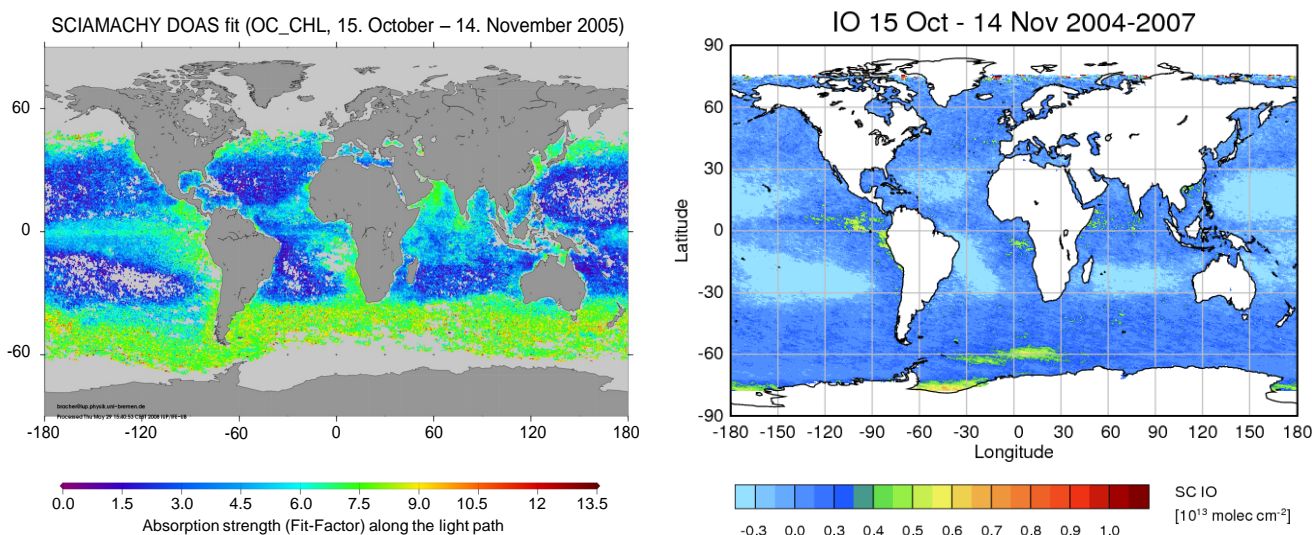
Figure 3.16: Left: Absorption strength (fit factor) of the diatom concentration in the world's oceans derived from SCIAMACHY measurements by Bracher et al. (2009) for October 15 to November 14, 2005. Reprinted from Bracher et al. (2009). Right: Composite of IO data for the same time of year but averaged over 4 years. The land is masked to match the left graph and to set focus on the oceanic regions.

Outlook

In Glyoxal results from SCIAMACHY, the Eastern Pacific also shows enhanced column densities in a region overlapping with the detected IO amounts. This has been reported by Wittrock (2006) and Vrekoussis et al. (2009) and additionally hints at biological production of atmospheric trace gases in this region. CHOCHO has various sources and is for example produced by oxidation of volatile organic compounds, which are expected to be present in biologically active areas. From ship-based measurements, enhanced amounts of CHOCHO and IO have been observed in the Eastern Pacific (Rainer Volkamer, personal communication). Comparisons between data from these independent studies will be further investigated in the near future. It is interesting to note, that similar to the

121

IO results, the Glyoxal amounts are not enhanced above the Northwest African upwelling region.

In any case, the East Pacific seems to be special with respect to iodine compounds. Comparisons with Glyoxal as well as with the spatial distributions of different phytoplankton species and also with measurements of organohalogens in the ocean waters will in the future give further insight into these initial findings, which reveal an interesting relation.

3.5 Observations of IO on the Northern Hemisphere

Up to know, results of IO mainly on the Southern Hemisphere were displayed and discussed. Before IO amounts and spatial distributions on the Northern Hemisphere can be examined, a change in the reference region needs to be performed. For globally consistent IO results it is desirable to use a constant reference region throughout a complete study. Unfortunately, this is not possible for the case of IO yet. It was already mentioned in the beginning of this chapter (Section 3.1) that the IO columns show a general tendency towards smaller and even negative values on the Northern Hemisphere. This is not due to real IO absorption but is caused most probably by geometrical influence on the measurement data. Changes in viewing geometry (especially the relative geometry between satellite and sun) may lead to changes in stray light amount or polarisation. These two processes show spectral signatures in the measurement data which are not perfectly corrected for. Until this is done more precisely than currently implemented, some solution needs to be found if results on the Northern Hemisphere shall be considered. The identified negative slope of IO columns towards the North is demonstrated in Fig. 3.17. The values calculated for this plot were taken from the four year global map (cp. Fig. 3.1) and were averaged over the longitude band from 30° to 150° East in 1° latitude steps. The minima around -20°, +15° and +35° originate from the detected interference over clear ocean regions (cp. Sec. 3.1 and Chapter 6). Apart from these minima, the negative trend can be seen. For the following data analysis and images on the Northern Hemisphere, a different reference region is chosen. The selected region in the Northern Pacific (at 180°±10° East and 30°±10°North) is displayed in Fig. 3.18. For future analyses, the possibility of correcting the decreasing trend towards the North - either by subtracting the effect (as temporary solution) or preferably by identifying and eliminating the cause - will be investigated in order to obtain consistent global results.

In the next figures, IO columns for regions on the Northern Hemisphere are shown. Figure 3.19
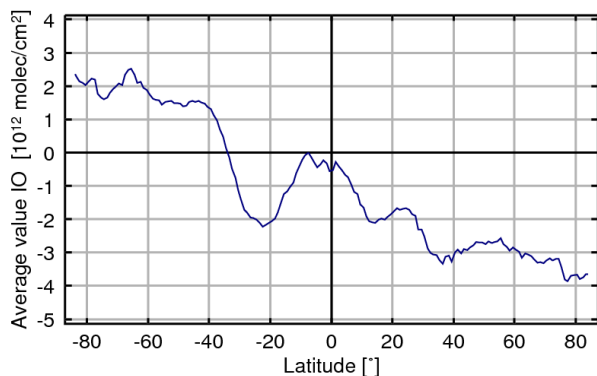

Figure 3.17: From the 4 year global mean, the IO values were averaged over longitudes between 30° and 150° East and latitude steps of 1°. The tendency towards negative values on the Northern Hemisphere becomes visible.
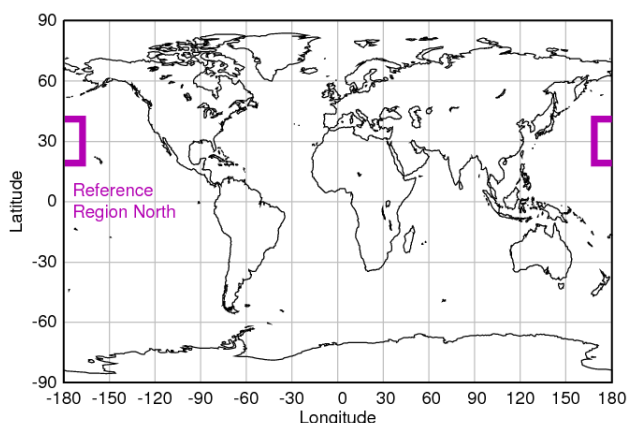
Figure 3.18: The rectangular area marked in purple was selected as suitable reference region for the analysis of IO results on the Northern Hemisphere.

contains four seasonal maps centered at the North Pole and reaching up to a latitude of 50° North. In each map, data of the respective season from four years each is included. Due to the usual light conditions and the limitation of the SZA<84°, the autumn and winter maps (c and d) contain a smaller data amount, than spring and summer (a and b), which leads to a larger spatial scatter. Interpretation of the amounts is therefore difficult here. Especially the autumn map exhibits enhanced values of IO, which will need further investigation. In the summer period (b), the IO amounts remain largely below 3×10^{12} molec/cm^2, apart for a few exceptions. At the Western coastline of Northern Greenland and at the coast of the Gulf of Alaska some notions of IO amounts appear with values around 4×10^{12} molec/cm^2.

The most prominent and clear features of IO are apparent in the spring time map (a), where several coast lines exhibit enhanced amounts of IO. These regions include the coasts of Southern Greenland, the West coast of Spitsbergen between 75° and 80° North, on the South coast of Novaja Zemlja (the North Russian archipelago between the Barents Sea and the Kara Sea), the coast line of the Gulf of Alaska and some smaller values also in the Bering Sea, over Iceland, and between the Hudson Bay and Baffin Island. A closer view for Spitsbergen/Svalbard follows in Chapter 4, Sec. 4.3, as the Bremen DOAS group maintains a ground-based instrument in Ny-Ålesund. Largest values at these coast lines reach 6×10^{12} molec/cm^2 in the averaged spring time period. Coast lines are familiar locations for the existence of increased algae population. Possibly, the main source in these regions is biological release of organohalogens also.

If the release is mainly of organic origin, the spatial distribution of regions showing enhanced IO values depends on the distribution of emitting species. The question if the iodine is released rather by macroalgae and/or phytoplankton at the Northern coast lines is not clarified yet.

In most of the cases where IO is enhanced on the Northern Hemisphere, the orientation of the involved coast lines seems to have a systematic component. Further North, the affected coast lines run from Southwest to Northeast, while further South, the respective coasts are rather facing towards the South, e.g. at the Southern coast of Greenland. In Fig. 3.20, this is displayed in addition to three selected SCIAMACHY orbits which pass over the respective coast lines.

The described tendency is either a result of coincidence or it might also be related to specific ocean currents and related accumulation of certain algae species. A third option might hint at an irregularity in connection with the orientation of the SCIAMACHY orbits. It is not clear which

(a) SCIAMACHY IO: Mar - May 2005-2008

(b) SCIAMACHY IO: Jun - Aug 2004-2007

(c) SCIAMACHY IO: Sep - Nov 2004-2007

(d) SCIAMACHY IO: Dez - Feb 2004-2008

SC IO
[10^{13} molec cm^{-2}]

-0.3   0.0   0.3   0.4   0.5   0.6   0.7   0.8   0.9   1.0
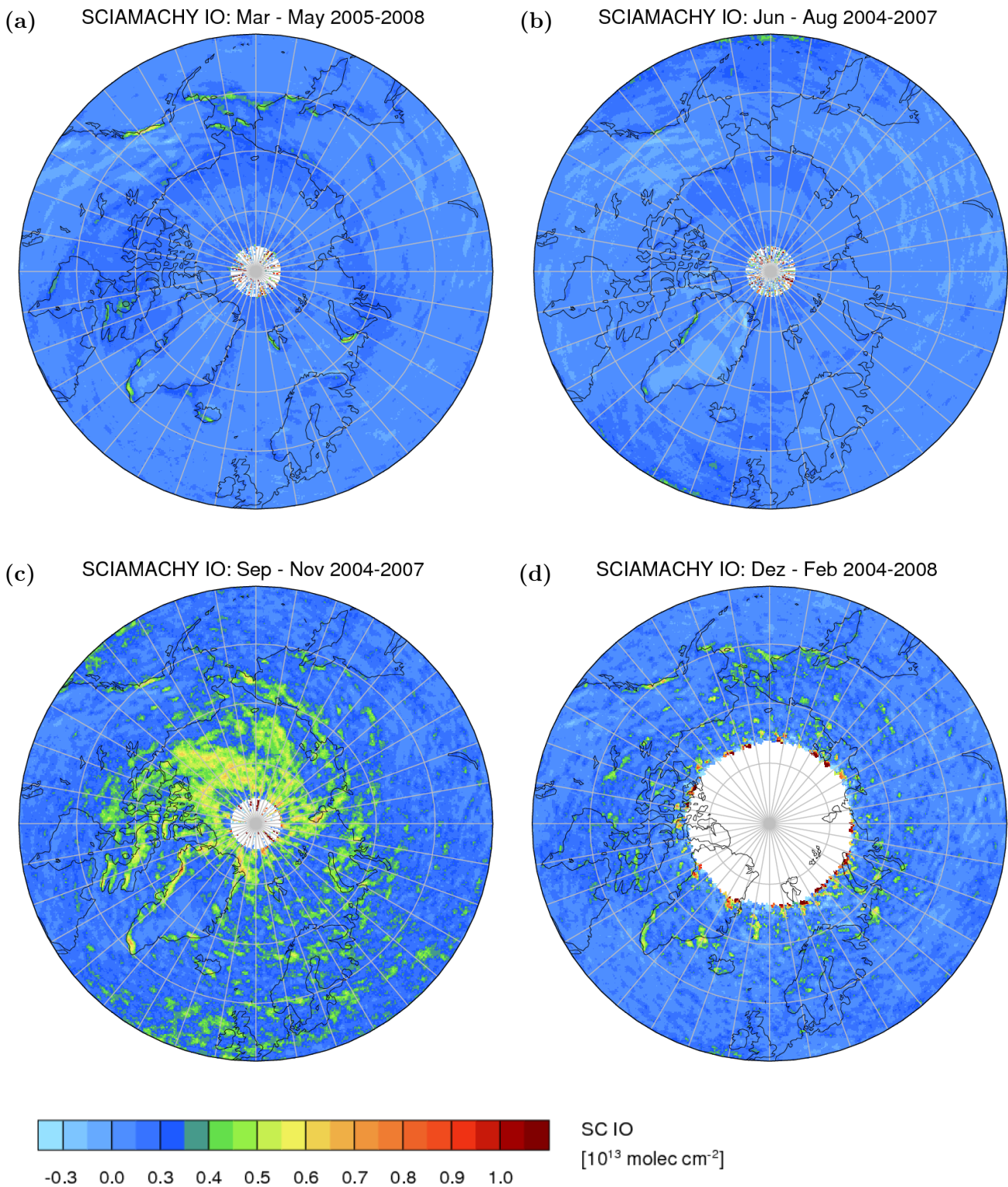
Figure 3.19: Seasonal averages of IO slant columns on the Northern Hemisphere, using data from four subsequent years each. While the spacial scatter in the autumn (c) and winter (d) maps is rather high, the spring (a) and summer (b) maps contain much more data points and show smooth results with low values in summer and enhanced IO at coastlines in spring time.

influence could provoke high IO amounts in this respect. Instrumental influences like the memory effect can in principle influence the measurements at certain regions. However, this possibility does not seem reasonable in the present case, as the sequence of SCIAMACHY measurements within one measurement state does not run from the possibly ice-covered land to the darker ocean at the affected coast lines, but along the coast. One possible effect is the improved sensitivity of satellite measurements towards patterns on the ground which are oriented in the same direction as the rectangular ground pixel. In this case, the respective feature is captured by one satellite measurement and not distributed over several pixels. A similar observation has been made in connection with ship emissions of NO_2, which become better visible if their direction is well aligned with the SCIAMACHY ground pixels (Richter et al., 2004). This would imply that the IO amounts at the indicated coast lines are better visible to the instrument than at differently oriented coast lines.

3.6 The difference between the Arctic and the Antarctic IO observations

When comparing the IO observations on the Northern and the Southern Hemisphere several differences can be identified.

- In the Antarctic, the detected IO amounts are relatively wide spread, and cover different areas from sea ice regions, to coast lines and ice shelves and also the continent. The IO remains enhanced over rather long periods of time with a variety of temporal and spatial variations. Highest amounts close to the continent appear in October each year, while the IO over the sea ice regions reaches its maximum later in November and December.

- The Arctic shows no evidence for widespread IO columns above the detection limit of SCIA-MACHY. Strongly confined coastal regions at several locations on the Northern Hemisphere exhibit enhanced IO mainly during spring time. In the Arctic sea ice regions, no IO is observed from space in spring time.

Overall, the comparison between the Arctic and Antarctic regions strongly supports the concept of organic release of iodine compounds.
For BrO, where maxima are found on both Hemispheres in Polar Spring, mainly inorganic sources are presumed. The suggested inorganic release processes can take place in the physical situations in the Arctic and the Antarctic. Inorganic pathways are in principle also possible for iodine release, but they will be different from the bromine mechanism then, because the temporal and spatial patterns are so distinct. Such pathways will necessarily be connected to some Antarctic specific property, e.g. of the (sea) ice structure, but are not known of yet.
Organic release of iodine compounds is known from algae, phytoplankton and also bacteria, and as the iodine release is species specific, the distinct biospheres of North and South may cause the difference in IO distributions. Some different ice properties might allow release of biogenic molecules more easily in the Antarctic. In the Antarctic, e.g., polynyas are typically large and also extend towards the open ocean, while in the Arctic they are generally smaller and more along the coasts
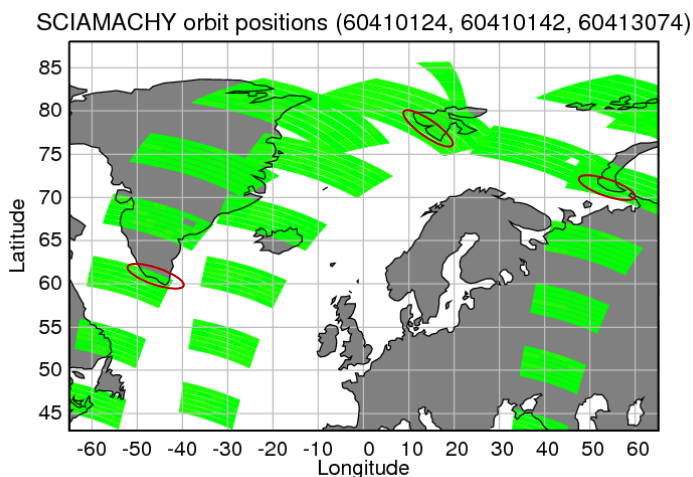
Figure 3.20: Three SCIAMACHY orbits from April 10th and 13th (see header for orbit numbers) for which the ground pixels within the field of view of the nadir measurements are marked in green. Some coast lines where high IO values were detected are encircled in red and it becomes evident that the relative orientation of the coast lines to the orientation of the SCIAMACHY ground pixels is approximately parallel.

(Thomas and Diekmann, 2003). This may facilitate closer contact of ice algae or phytoplankton species to the atmosphere above and hence, the release of gaseous substance into the polar boundary layer is more probable in the Antarctic.

3.7 Note on the relevance of the retrieved IO amounts

In addition to the discussions of probable sources as consequence of the spatial and temporal patterns of IO, the satellite observations of IO may also be used to estimate the potential impact of iodine chemistry on ozone loss and particle formation. These questions have been addressed by ground-based measurements (Dickerson et al., 1999; O'Dowd et al., 2002b; McFiggans et al., 2004; Read et al., 2008) and modelling studies (Vogt et al., 1999; McFiggans et al., 2000), and mostly conclude, that iodine has a substantial impact in both aspects at least locally. Following from the satellite observations, information on a larger spatial scale becomes available. If the satellite observations are used in this discussion it needs to be kept in mind though, that the retrievals yield column densities and assumptions are needed to determine local concentrations. These assumptions are accompanied by some typical uncertainties, but an estimation on an order of magnitude basis is possible and gives some insight into the potential importance nevertheless. As an example, the particle formation from iodine oxides is compared to that from sulphur precursors in order to estimate the relative importance of iodine oxides. For the calculations, rate coefficients are taken from Sander et al. (2006b).

Higher iodine oxides and iodine oxide clusters act as condensation nuclei for aerosol formation (Sec. 1.5.3), which is initialised by the IO+IO self reaction (R34 and R35). The rate of higher oxide production therefore depends on the square of the IO concentration, making this is a highly non-linear process. The rate of iodine particle formation $r(I_{part})$ is determined by the formation rate of higher iodine oxides. As the ratio of the reactions (R34) and (R35) with respect to the total rate of self reaction k_{IO+IO} is close to 1 (Bloss et al., 2001), the formation rate $r(I_{part})$ can be approximated by $r(I_{part}) \approx (k_{IO+IO})[IO]^2$. The rate coefficient for the self reaction is $k_{IO+IO} = 8 \times 10^{-11} cm^3/molec/s$.

For comparison, the formation of particle precursors from sulphur species is estimated. For this, H_2SO_4 is a crucial species. As subsequent reactions generating H_2SO_4 molecules are rapid, the rate determining step in the H_2SO_4 formation chain is the three body reaction of OH with SO_2 (OH + SO_2 + M → $HOSO_2$ + M). The formation rate of sulphate particles following the reaction of SO_2 with OH is then given by $r(S_{part}) \approx k(OH+SO_2+M)[OH][SO_2]$. To determine $r(S_{part})$, the reaction rate coefficient $k(OH+SO_2+M)$ for high pressure (large concentration of third body M) is chosen as well as daytime marine boundary layer conditions for SO_2 (100 ppt) and OH (1×10^6 molec/cm^3).

Using a typical observed upper limit of 3×10^{12} molec/cm^2 IO vertical column (from a slant column of 3×10^{12} molec/cm^2 and an AMF of 1 over the ocean) and profile heights of well mixed IO in the boundary layer between 1 km and 100 m, the IO concentrations lie between 1.2 and 12 ppt. This yields a range for the iodine to sulphur particle ratio of:

$$\frac{r(I_{part})}{r(S_{part})} = 18 \dots 1800$$

These numbers give a rough estimation on the rates of particle precursor substances from iodine and sulphur chemistry. The calculation of the actual numbers of CCN forming in the given atmospheric conditions needs to be performed using detailed atmospheric chemistry modelling, including precise information on crucial substances such as DMS for the sulphate chemistry and nucleation, and most importantly also the final clustering probabilities. This is required to assess accurately the relative importance of iodine chemistry as a global source of particles. The estimations above, however, already show that the production rates of direct iodine particle precursors range in the same and higher orders of magnitudes as compared to those of the sulphate aerosol. Exact numbers are in strong dependence of the individually chosen conditions, so that the result covers several orders of magnitude.

4 Validation and case studies of satellite IO

For the validation of satellite measurements, it is generally required to compare the results from space with other observations, such as ground-based or airborne measurements for as many locations and time periods as possible. If suitable conditions are used for both data sets and if then the results agree reasonably well, such a successful comparison lends confidence to the results of the compared observations. If no systematic error is induced when going to different times or locations, a comparison study also supports the credibility of the satellite retrievals for scenes where no other measurements have ever taken place before.

The following consideration is valid for all comparisons between satellite and ground-based measurements of IO. An exact agreement between the satellite observations and ground-based data cannot be expected. The reason for this is the different spatial coverage of the measurements. While typical ground-based measurements probe a rather confined region on the order of metres to a few kilometres at most, the satellite gathers all atmospheric information from a ground pixel of at least 30×60 km^2 size. Due to the high spatial variability expected for the sources of iodine species, differences between the different measurement platforms are expected. Nevertheless, validation with ground-based data is meaningful, if the focus is not set on the exact values but on the spatial and temporal trends and on the agreement within a certain range.

In the case of IO measurements, data sets for comparison from ground-based measurements or other platforms are sparse. Several studies have reported IO values below the detection limit of the satellite retrievals at the respective location. For these, zero point validation may be performed, which means to prove that the SCIAMACHY IO retrieval yields an IO value below detection limit for the respective time and location.
Some ground-based measurements, however, were conducted in regions where SCIAMACHY detects IO above the detection limit. Some individual comparisons have been performed with selected data sets of such independent studies.

4.1 Comparison with long-path DOAS measurements at Halley, Antarctica

For the Antarctic, where satellite observations reveal fairly large values of IO, ground-based measurements have been conducted during the CHABLIS (Chemistry of the Antarctic Boundary Layer and Interface with Snow) campaign (Saiz-Lopez et al., 2007b, and references therein) close to the aforementioned Halley Research Station from January 2004 until February 2005. IO volume mixing ratios were measured close to the ground (at a height of 4-5 m above the ice surface) by the active long-path DOAS technique using a xenon lamp as an artificial light source. The light beam travels

horizontally over a certain distance and is reflected back by corner-cube reflectors to a telescope and spectrometer unit. The VMR is determined as average over the total optical path length of the light beam, which has been 8 km in the considered case.

For a comparison with the ground-based data, the satellite IO results around Halley Station have been extracted. The four year time series for this location has been presented in Sec. 3.2.2, Fig. 3.5. All IO data falling into a box of 500 km side length with Halley Station in the center have been used for the time series. The area of the satellite observations is much larger, but covers that of the ground-based measurements. Spatial variations in IO amounts will therefore reduce the correlation between the two data sets, but using a much smaller region for the satellite data would reduce the data amount with according negative influence on the signal-to-noise ratio.

In order to compare the VMR values of the LP-DOAS results with the slant columns of the satellite observations, the air mass factor according to the satellite geometry and the IO profile is needed for the calculation of the vertical column and the ground VMR. The IO profile is not known for the respective location and time period, so that an AMF for the satellite measurements cannot be calculated exactly. No IO profile has been measured up to now and only some general estimates are available. However, with certain assumptions, meaningful comparison is nevertheless possible. Most importantly, assuming that the vertical distribution of IO does not change over the time period of the comparison, the conversion between the column amount and the VMR is given by a constant factor. In this case, the evolution of the two measurement time series can be compared.

In Fig. 4.1, the time series for both instruments from February 2004 until February 2005 are shown. The top panel contains an excerpt of the SCIAMACHY time series (cp. Sec. 3.2.2), with daily slant column values (black dots) and additionally a weekly running mean (black solid line). The bottom panel displays the IO VMR from the LP-DOAS measurements, as published in Saiz-Lopez et al. (2007b). Concurrent BrO measurements are also shown, but not further used here. In both IO data sets, a substantial day-to-day variability is visible. This scatter has several sources. Noise in the measurement data already leads to some spread in the results. In addition, however, the IO amount strongly depends on current conditions and actual emission rates and therefore is in deed variable itself. In some time spans within the shown period a direct comparison is not possible. During winter, e.g., no satellite measurements close to the pole are recorded due to a lack of sunlight. For the active LP-DOAS measurements, this is not a problem, but for other campaign related reasons, the LP-DOAS measurements of IO where only conducted on certain days.

The evolution of the two time series is very similar and some characteristics can be identified. In both data sets, the largest long lasting amounts of IO are observed in springtime, especially in October. Going from winter right in the middle of the time series towards this spring period, the IO values are increasing and after the maximum in October, somewhat reduced amounts are retrieved. This feature can be identified in spite of the aforementioned scatter in both data sets. In the ground-based data, the values truly range around zero in winter (e.g. in August) and go up to around 7 ppt during October with single spikes in the measurements up to 20 ppt. Such high IO amounts are rarely observed and probably are short-term events. Towards summer, IO VMR amounts drop to around 2 ppt and remain in this range for the whole season. The time series of the satellite results begins in September and rises from 3×10^{12} molec/cm^2 to about 6×10^{12} molec/cm^2 in mid-October
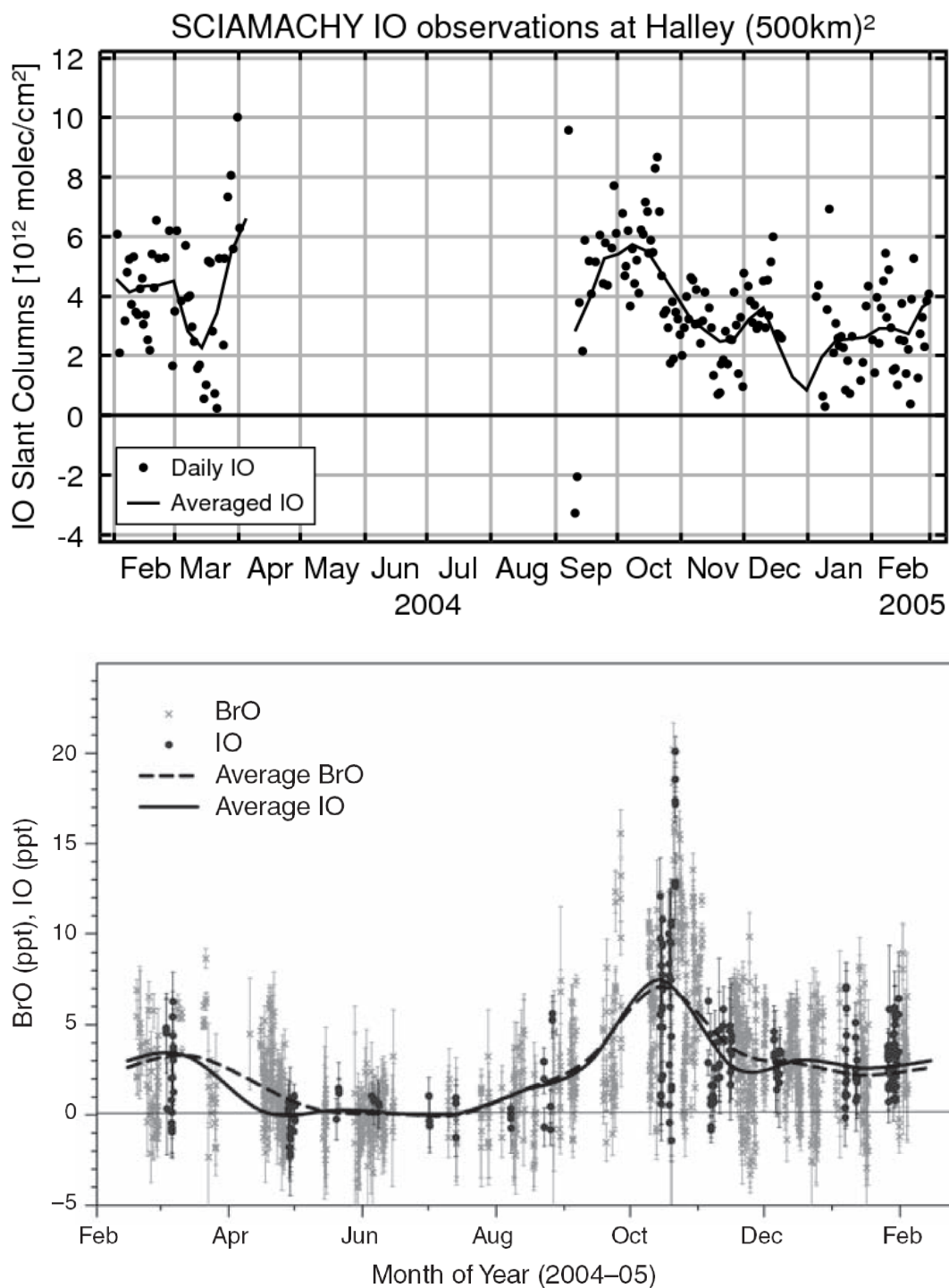
Figure 4.1: Comparison of the time series of SCIAMACHY observations (top) with long-path DOAS IO measurements from the CHABLIS campaign (bottom); bottom figure reproduced from Saiz-Lopez et al. (2007b). Both data sets are shown for the same time period, the ticks on the axes denote the beginning of the month in both cases. For the SCIAMACHY results, daily averaged IO data is shown as single points, a weekly mean as solid line. The standard deviation of the daily values lies between 1 and 5×10^{12} molec/cm^2, respective error bars are omitted for better visibility of the temporal evolution here. The long-path DOAS shows single measurements as points and a 10-day moving average as solid line.

with values up to 10×10^{12} molec/cm^2 on individual days. Consistent with the ground-based data, the values are lower in summer and remain positive. Both instruments show again higher values in autumn (i.e. around February-March), which is more pronounced in the satellite results. The dip in mid March is rather unusual, does not occur in the later years (Fig. 3.5), and is an indicator of the strong IO variability. The satellite still detects quite large amounts in April (some single high values cause a jump in the end of April), where no ground-based data are available for comparison (no data points between beginning of March and beginning of May). In other years (cp. Fig. 3.3), the satellite IO trend also shows decreasing values already from March to April towards polar winter. In conclusion, the evolution of the two co-located time series agrees with some expected differences in the details.

For a quantitative comparison between the two data sets, now a reasonable surface volume mixing ratio is calculated from the satellite slant columns. In spite of the missing knowledge about the exact IO profile, confinement of IO to the lowest layers is expected (Saiz-Lopez et al., 2007c) and an example profile shape may be assumed. The usual boundary layer height in Antarctica is low as compared to the marine boundary layer. A constant IO VMR in the lowest 100 m dropping to zero above as suggested by Saiz-Lopez et al. (2007c) is a reasonable choice. The maximum slant column amounts in Antarctic spring (around mid October) are around 6×10^{12} molec/cm^2 for the averaged SCIAMACHY observations (Fig. 4.1). Considering the typical AMF of 4 for Antarctic conditions (cp. Fig. 2.11), the vertical column amounts to 1.5×10^{12} molec/cm^2 . With the above chosen profile shape, these values corresponds to a surface VMR of approximately 6 ppt. The average value of the ground-based data set reaches 7 ppt around mid October. Although this type of comparison essentially addresses the order of magnitude of the results due to the required estimations, the deviation between the two VMR amounts is only 15%, demonstrating a good agreement between the ground-based and satellite results.

Overall, the comparison of the two individual studies, the satellite and ground-based observations at Halley Station on the Antarctic coast, are in good agreement regarding the temporal evolution of the IO amounts and also regarding the order of magnitude for the absolute VMR values. This conclusion is promising and strengthens the credibility of the satellite IO retrieval.

4.2 Comparison with an independent study using SCIAMACHY data

SCIAMACHY nadir measurements have been evaluated for the absorption structures of IO in one independent study, published by Saiz-Lopez et al. (2007a). Four selected days of data have been analysed and the IO vertical column densities for the Southern Hemisphere are reported. In agreement with the present study here, Saiz-Lopez et al. find enhanced values of IO in Austral spring time around the Antarctic. Apart from this general finding, most of the details show large differences to the present work though. The IO vertical columns for the four analysed days are reprinted in Fig. 4.2, as originally published (Saiz-Lopez et al., 2007a). The spatial maximum of IO lies around 60° South mostly over regions which are covered by sea ice during that time.

In short, the retrieval of the alternative study used a fitting window of 426 - 440 nm. The trace gases NO_2, O_3, O_4, $H_2O_{(g)}$, and the Ring effect as well as the VRS in water were included in the fitting routine. In a second retrieval run, the mean residual from the first run has been additionally included as "pseudo-absorber" in the fit. The spectral fitting results are shown only after the correction for this mean residual. The fit quality prior to the correction is therefore not known. Saiz-Lopez et al. state that the IO results differ only by 1% between the two retrievals (with and without including the averaged residual). This is actually not surprising as the residual is the remaining part of the measurement which does not exhibit any correlation with the respective trace gases anymore. In each fit of an individual spectrum, the residual spectrum is linearly independent of the included absorption structures (not considering noise). Consequently, this also holds true for the sum (average) of all residuals over one orbit and the inclusion should not affect the results of the other trace gases, but reduces the final residual. Consequently, such a correction procedure needs to be used with care as potential retrieval errors may be hidden. Therefore, this has not been applied in the present work.

Comparing the results by Saiz-Lopez et al. with the results in the present study in more detail, some points of discrepancies are identified.

First of all, the determined IO column amounts do not agree. The highest widespread amounts found by Saiz-Lopez et al. range around a vertical column of 20×10^{12} molec/cm^2 (cp. red colour code in Fig. 4.2). As a geometrical AMF is used (i.e., AMF = $1+1/\cos$(SZA) for exact nadir view), a light path enhancement of a factor of 3 for a SZA of $60°$ and exact vertical nadir viewing direction is considered. The high values therefore correspond to slant columns of at least 60×10^{12} molec/cm^2, individual pixels exhibit slant columns up to 80×10^{12} molec/cm^2. The present study detects no widespread slant columns over 10×10^{12} molec/cm^2 and only scattered values reaching as high as 20×10^{12} molec/cm^2.

Secondly, the spatial pattern differs, which becomes apparent when considering the monthly means for the standard IO product of slant columns which have been discussed above. In Saiz-Lopez et al. (2007a) the enhanced values of IO are concentrated at some distance from the Antarctic continent, where at that time of year the ocean is covered with sea ice, and also beyond the sea ice in patches over the open ocean. The four year averaged monthly means around October in the present study are also enhanced over sea ice, but closer to the Antarctic coast, and additionally over the ice shelves and some part of the continent. Enhanced IO values over the sea ice at further distance from the coast appear about one month later (cp. Fig. 3.7).

For one sample day (October 5th 2005), some views on the Southern Hemisphere are combined in Fig. 4.3 which are helpful for the following analysis. Field (a) in this figure shows the standard IO product (V1.28) for that day. For the purpose of better comparability, the same rough geometrical AMF (neglecting the influences of atmospheric scattering and surface reflectance) is applied and vertical columns are shown. Apparently, the daily values exhibit large discrepancies between the two studies, as no enhanced vertical columns can be distinguished for the standard IO fit in this colour scale. The colour scale in Fig. 4.3(a) is chosen to be the same as in Fig. 4.2 for the results
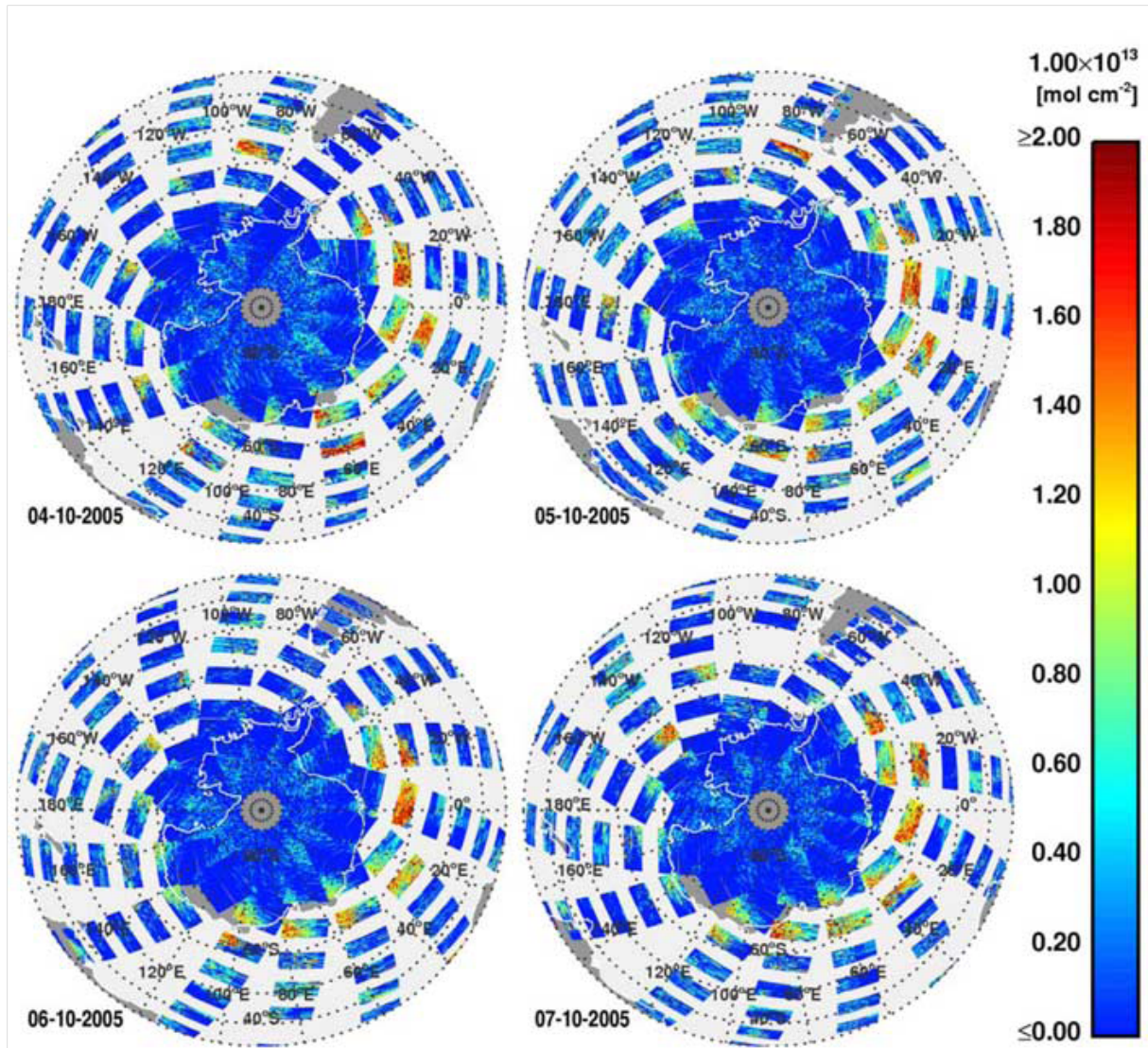
Figure 4.2: Figure reprinted from a publication by Saiz-Lopez et al. (2007a). Each map of the Southern Hemisphere (up to 30° South) shows one day of SCIAMACHY results of IO slant columns for four consecutive days (4th -7th October, 2005).

from Saiz-Lopez et al. (2007a). For direct comparison, Fig. 4.3(b) repeats the map for October 5th from that study.

The basic data set of satellite spectra is largely the same in both studies, although it is not known, which calibration steps (cp. Sec. 2.1) were set and which were omitted by Saiz-Lopez et al. (2007a). The question arises, which differences in the data analysis procedure may lead to the observed differences in IO results. As discussed in Sec. 2.8, the chosen wavelength range for the analysis may be a source of differences. The retrieval of Saiz-Lopez et al. can not be exactly reproduced, as some settings in the retrieval algorithm are not revealed. However, from the multitude of different retrieval runs tested in the present study, some parameter versions have similar settings and show similar results as compared to Saiz-Lopez et al.. One example of these is discussed in Sec. 2.8 as Version V0.27i and uses the spectral window from 418-438 nm. The fitting window of Saiz-Lopez et al. also includes the 430 nm region, where for V0.27i retrieval difficulties were identified.

Figure 4.3 contains results from the V0.27i retrieval in fields (c) and (d). Comparison with results from Saiz-Lopez et al. (2007a) highlights some points of concern as some similarities are revealed. The values of the V0.27i retrieval yield higher IO columns than the standard IO fit. Widespread amounts of IO reach up to about 10×10^{12} molec/cm^2 vertical column density, visible in Fig. 4.3(c). These amounts are by a factor of 2 smaller, but still comparable to the amounts observed by Saiz-Lopez et al.. The colour scale in Fig. 4.3(c) is also adapted to the one used in (b).

In most locations, the pattern of the V0.27i output agrees remarkably well with the results in field (b). The wide band of enhanced IO values is well reproduced in the V0.27i fit here. Except for very few pixels, most of the spatial structures of high IO in the individual states of satellite measurements can be seen in both data sets. In general, such a finding would give an indication that the two data sets capture the reality well, but following from the discussion in Sec. 2.8 it has been concluded, that the V0.27i fit exhibits considerable retrieval errors. Possibly, this holds also true for the external study. Figure 4.3(d) contains the residual rms values of the V0.27i retrieval. Comparison of field (d) with (c) and (b) demonstrates, how similar the spatial patterns of high rms (i.e. poor fit quality) from retrieval V0.27i are in comparison to the enhanced IO values seen by this retrieval as well as by Saiz-Lopez et al.. Comparable input information is used in both studies, so that similar problems may occur.

One additional curious finding is identified on the 5$^{\text{th}}$ of October. On this day, enhanced IO values are observed far outside the Antarctic, Southwest of South America in the state of satellite data between 70° and 90° West and 50° and 60° South (cp. Fig. 4.3 b and c). The columns here are just as large as those over the sea ice, but this region is ice free. For the case of an underlying ocean, the true vertical columns here will be even higher than those observed over sea ice due to a smaller AMF over dark surfaces (cp. Sec. 2.3). However, a bright cloud cover was identified for this scene exhibiting the same pattern as the enhanced IO values. For the V0.27i retrieval, the correlation of high IO amounts and the occurrence of clouds or similar cases with highly reflecting surfaces has been detected (cp. Sec. 2.8).

The conclusion is ambivalent. In any case, the actual quality of the external data set cannot be fully evaluated and judged here due to a lack of data amount and insight into the retrieval per-
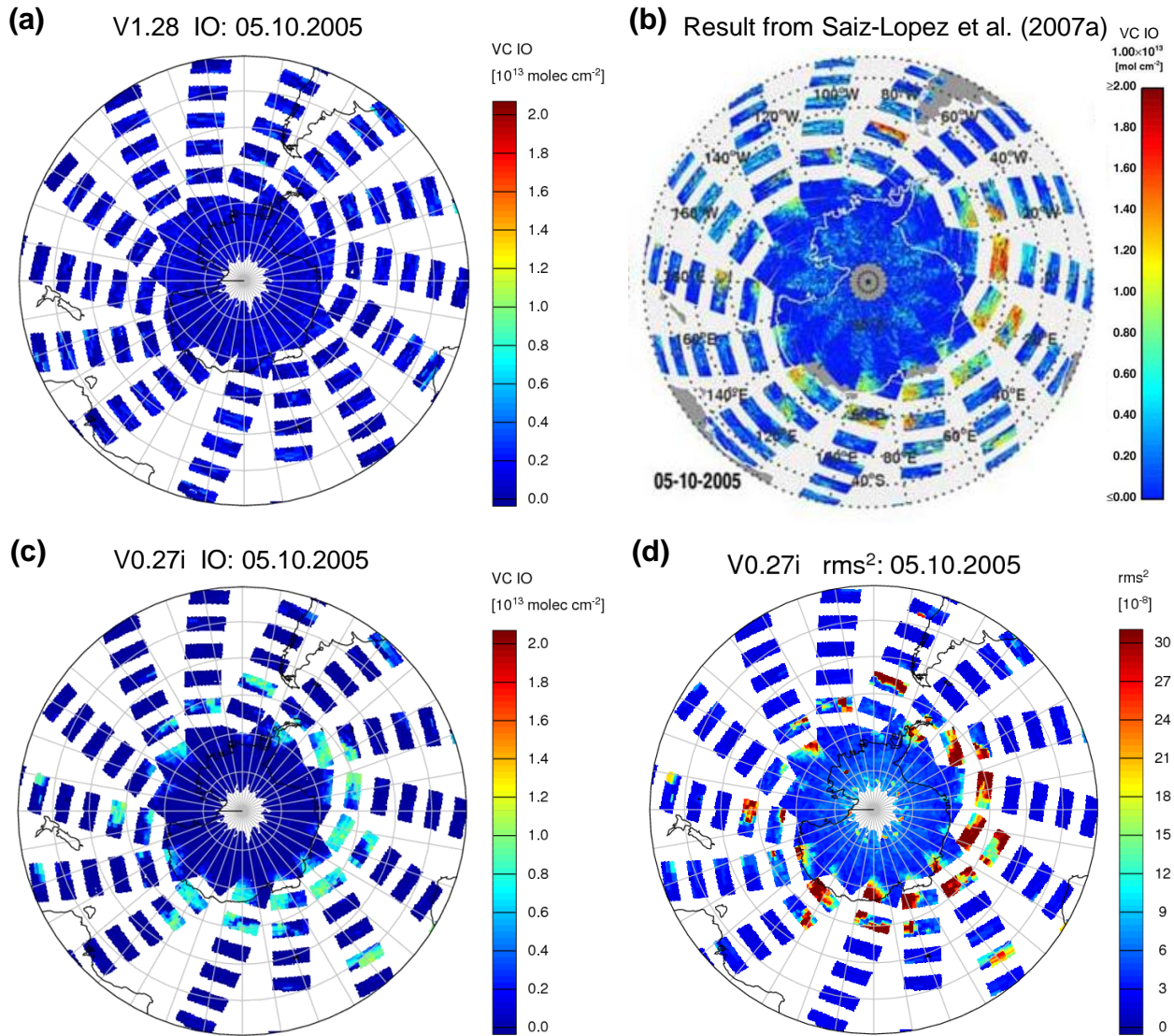
Figure 4.3: Combination of four plots comparing retrieval results on the Southern Hemisphere from different studies for the date of October, 5th, 2005. (a) shows the standard IO product (V1.28) transformed to vertical columns by the same geometrical AMF as used by Saiz-Lopez et al. (2007a), for which the retrieval result is reprinted in field (b). Fields (c) and (d) contain output from the retrieval V0.27i obtained in the present work and discussed in Sec. 2.8. (c) shows the IO vertical column in the same colour scale as (a) and (b), while (d) demonstrates the fit quality through the residual *rms* value. The *rms* reveals high values, where IO amounts are enhanced in fields (b) and (c).

formance. A main point of concern is the similarity with the corrupt V0.27 retrieval of the present study in combination with the identification of large residuals and unrealistic results over clouds and highly reflective scenes. This observation seems to be reproduced in the study by Saiz-Lopez et al.. Their results may prove to be accurate nevertheless. In that case it will be necessary to clarify how the V0.27i results can lead to comparable IO amounts in spite of systematic errors. The high values over clouds would introduce new questions on the production and pathways of iodine species.

Resulting from the above analysis, the discrepancies between the independent study by Saiz-Lopez et al. (2007a) and the present standard IO retrieval are respected, but should not lead to serious doubts in the V1.28 standard fit until more information on the independent study becomes available.

4.3 Comparisons with ground-based passive DOAS measurements

The University of Bremen DOAS group maintains ground-based DOAS instruments in several locations at various latitudes. Additionally, some instruments are operated on campaign basis at certain times and locations. One instrument is permanently installed at Ny-Ålesund on Spitsbergen, Svalbard (78°55' North, 11°57' East, cp. Fig. 4.4), providing a long-term data record since 1995 in zenith viewing geometry. After several upgrades of the instrument, further viewing angles were added with 5 viewing directions since 2002 and 11 directions since 2006.
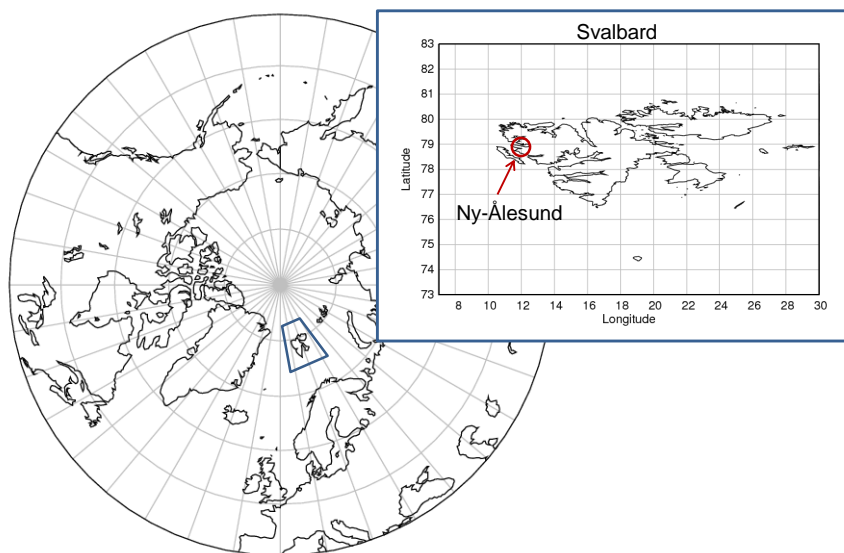
Figure 4.4: Map showing the location of the DOAS instrument at Ny-Ålesund on the island of Spitsbergen, belonging to Svalbard on the Northern Hemisphere.

Measurements from this station have been analysed for the absorption of IO, and on several days, amounts above the detection limit have been observed (Wittrock et al., 2000; Oetjen, 2009). The interpretation of the data suggests that small amounts of IO are present in spring and summer. Results from the IO observations in Ny-Ålesund are reprinted in Fig. 4.5, showing data retrieved by Hilke Oetjen (Oetjen, 2009). In this plot, the slant column amount of IO for viewing angles of 2° and 3° above the horizon are shown with respect to the time of year. The present IO values are rather low, so that out of the 5 years, only on 29 days reliable IO amounts above the detection limit

Figure 4.5: IO slant columns measured with the ground-based MAX-DOAS technique over several years in Ny-Alesund at 2° (2007-2008) and 3° (2004-2006) elevation above the horizon. The data is kindly provided by Hilke Oetjen* and Folkard Wittrock, University of Bremen, the plot was adapted from Oetjen (2009). *Now at the University of Leeds, UK.
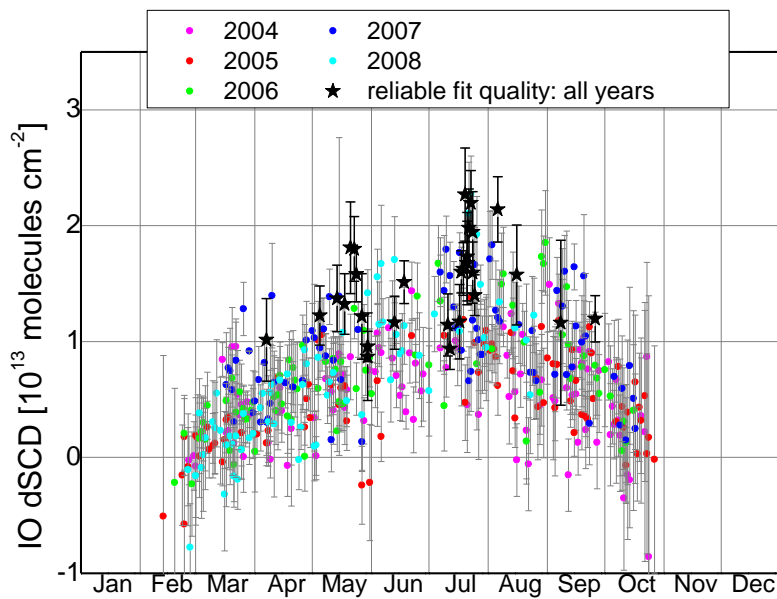
have been observed. The annual cycle apparent in the ground-based data has not been considered significant, so it will not be further interpreted here. The main focus lies on the retrieved IO amounts on days with reliable fit quality. The slant columns from Fig. 4.5 lie in the range of $1\text{-}2{\times}10^{13}$molec/cm^2.

In comparing the ground-based results with the satellite DOAS results, the most important issue and a source of errors is the estimation of the air mass factors for both cases. Both measurement geometries yield a case specific slant column as retrieval result. In order to calculate the vertical column and possibly the surface VMR for comparison, a suitable calculation of the air mass factor needs to be performed. The calculation is subject to the estimations of parameters like the surface reflectance and the not well known vertical profile of the trace gas. The calculation of a typical AMF for ground-based measurements at 2° and 3° LOS above the horizon yields 25.5 and 19.1, respectively. These values have been calculated using SCIATRAN with an SZA of 80°, an albedo of 90% for bright surfaces and a simple Rayleigh atmosphere. Consequently, the vertical column in the ground-based measurements is approximately $0.5\text{-}1{\times}10^{12}$molec/cm^2. This value is now compared to the satellite results.

The detection limit discussed in Sec. 2.4 has an upper limit of about $7{\times}10^{12}$ molec/cm^2 for a single SCIAMACHY measurement. The evaluation of the SCIAMACHY data shown in Sec. 3.5 yields a data amount of about 280 data points per location in the 4-year averaged seasonal maps. The reduction of the statistical error by a factor of $\sqrt{280}$, would indicate a minimum detection limit - ignoring all systematic effects - of around $4.2{\times}10^{11}$molec/cm^2. Consequently, the observations from the ground-based measurements are just slightly above the IO detection limit of the long-term

averaged SCIAMACHY retrievals. The systematic part of the uncertainties is of course not reduced by the long averaging period.
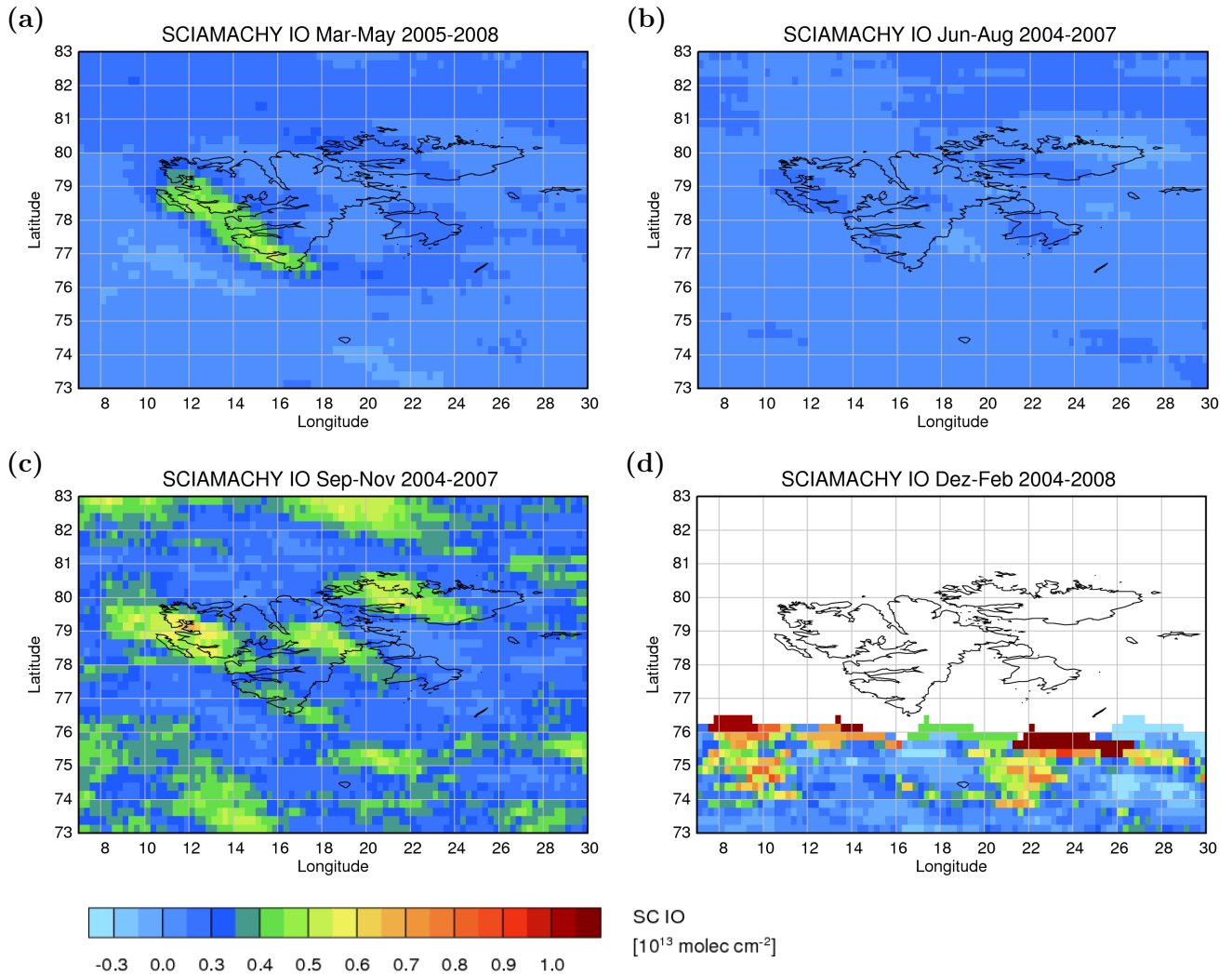

Figure 4.6: Seasonally averaged IO results for the area above Spitsbergen, Ny-Ålesund. In Spring (a), high IO amounts appear along the Southwest side of the island, while the amounts in summer (b) are below detection limit. In the other two seasons (c, d), the noise is much stronger, in winter most of the area is too dark for observations.

Concerning the IO amounts retrieved from the SCIAMACHY measurements over Ny-Ålesund, the seasonal averages for four years have been investigated in Sec. 3.5 as overview maps for the Northern Hemisphere (Fig. 3.19). A close up of the islands of Svalbard is plotted in Fig. 4.6, showing the same four year averages as in Chapter 3. The confinement of the high IO values to the coast in Fig. 4.6(a) is visible. There are only small IO columns in summer (b), strong noise influence in autumn and winter (c,d) with hardly any data in winter due to darkness. Maximum average values close to Ny-Ålesund lie around 4×10^{12} molec/cm^2. While the ocean surrounding Svalbard is mostly ice-free, the surface spectral reflectance over the snow and ice covered land is large. Depending on where the IO is mainly present in the satellite scene, the AMF is strongly influenced by the values of the surface reflectance. The AMF varies typically between about 1.0 and 4.0 for the satellite

measurements (cp. Sec. 2.3). For a slant column of 4×10^{12} molec/cm^2, the vertical column then lies between 1 and 4×10^{12} molec/cm^2.

Only a rough comparison is possible here, as for both instruments, the observed IO amounts are close to the detection limit. The vertical column for the ground-based observations of about 0.5-1×10^{12} molec/cm^2 is lower than the satellite value of 1-4×10^{12} molec/cm^2, but the two ranges meet at 1×10^{12} molec/cm^2. If the appropriate AMF is rather on the high side, the values agree within the statistical uncertainties of the satellite measurements alone, which are 0.4×10^{12} molec/cm^2 here.

Consequently, with vertical columns around 1×10^{12} molec/cm^2, the IO amounts seen by the two observations from the ground and from satellite, are comparably small. Especially, typical values found in the Antarctica are higher. This is in agreement with findings at other locations in the Arctic, for which low amounts of IO have been reported also (Hönninger et al., 2004).

4.4 IO in mid-latitude coastal regions

Several ground-based studies have revealed periodically enhanced IO in certain coastal cites, e.g. at Mace Head, Irish West coast (Alicke et al., 1999; Carpenter et al., 2001) and in Roscoff, French Atlantic coast (Whalley et al., 2007). In these locations, high amounts of IO in the boundary layer show a positive correlation with solar irradiation and a negative correlation with tidal height. Hence, the highest amounts of IO can be observed in sunlit periods and at low waters.

The question about the sources of the enhanced iodine concentrations under the mentioned conditions was answered by the discovery of large fields of algae along the coast. Certain types of algae were found to produce several different organohalogens, which are released to the atmosphere if the algae are exposed to oxidative stress. This arises at low tide when the algae field is no longer water covered but gets in direct contact to the boundary layer air. Halogenated organic compounds are then emitted as part of a defense mechanism of the plant to protect tissue from oxidative damage. Subsequently, the halocarbons are photolysed and atomic halogens enter the atmosphere. After reaction with ozone, species such as IO are produced and can be detected by spectroscopic methods in the visible wavelength region.

The satellite detection limit for IO in the mid-latitude coastal regions lies a few times higher than in the polar regions as discussed in Sec. 2.4. Nevertheless, the question arises, if the IO observations from SCIAMACHY show a significantly higher IO amount in low tide situations as compared to high tide periods. For this purpose, the SCIAMACHY IO data have been sorted according to the tidal phases. First of all, an IO timeseries has been extracted for a chosen location on Earth. The standard IO product (Version V1.28) is used here. In a second step, the tidal times of high water (HW) and low water (LW) have been generated as described in the next section. Each IO observation recorded in a certain time interval around this high or low water time is assigned to a respective HW or LW series of IO data. This sorting procedure is performed for more than four years of SCIAMACHY IO observations and for the two locations. Following from the ground-based observations, the LW series should exhibit higher IO amounts than the HW series.

4.4.1 Tidal data from SHOM

The time and height information about the high and low tides at some chosen locations was generated using a tool from SHOM, the French Hydrographic and Oceanographical service of the marine (Service Hydrographique et Océanographique de la Marine), provided on their data page[1].

The tidal data has a precision of a few centimetres for the heights and a few minutes for the times given. The tidal height in meters is given relative to a zero level which is roughly the level of the low tides. Predominantly, the times of high and low waters is of interest and not so much the exact height of the water line. Several minutes of inaccuracy can be accepted, as the timing of enhanced IO is not limited to a few minutes. The observations report maxima of IO which are present for periods on the order of a few hours (e.g. between 0.5-3 hours in the study of Carpenter et al. (2001)). In the selection procedure of satellite data for the respective location a certain time interval around the high and low tides will be allowed in any case. An example of the data format as provided by the SHOM data page is shown in Tab. 4.1. Data from the year 2004 until spring 2008 was selected.

SEPTEMBRE 2007								
Date	pleines mers				basses mers			
	matin		soir		matin		soir	
	temps	hauteur	temps	hauteur	temps	hauteur	temps	hauteur
sam 1	07h31	8.92m	19h50	8.97m	01h40	0.84m	13h56	1.12m
dim 2	08h08	8.58m	20h31	8.45m	02h20	1.28m	14h37	1.60m
lun 3	08h49	8.09m	21h17	7.79m	03h00	1.92m	15h20	2.26m
mar 4	09h39	7.51m	22h20	7.11m	03h45	2.68m	16h14	2.97m
mer 5	10h51	6.98m	23h57	6.67m	04h46	3.39m	17h32	3.52m

Table 4.1: Example of the tidal data provided by the Hydrographic and Oceanographical service of the marine (SHOM), here for the location of Roscoff on the French Northwest coast, listing the times (temps) of high tides (pleines mers) and low tides (basses mers) in the morning (matin) and the afternoon/evening (soir) of 1-5 September, 2007.

4.4.2 Case study for location Mace Head

Mace Head is an atmospheric research station on the Irish coast (53.3°N, 9.9°W) where several studies on atmospheric iodine have been conducted (Alicke et al., 1999; Carpenter et al., 1999; Saiz-Lopez et al., 2006). Here, an anti-correlation of IO with tidal height has been found by Carpenter et al. (2001) which approximately follows an exponential relation: [IO] = 2.6 × exp(-[TH]/1.7), with the tidal height TH given in meters and the IO mixing ratio in ppt. For the typical tidal variation between 0 and 5 m, the IO mixing ratio varies between over 2 ppt and close to 0 ppt.

In the satellite data, not only the exact point in time of high and low tides is considered, so the difference between the two cases will be somewhat smaller. Still a difference of around 1-1.5 ppt is expected.

2 ppt of IO would yield a typical slant column of 5×10^{12}molec/cm^2 in case of a 1 km box profile, or 5×10^{11}molec/cm^2 for a 100 m box profile (cp. to calculations presented in Sec. 2.3 and Sec. 2.4). As

---

[1]http://www.shom.fr/fr_page/fr_serv_prediction/ann_marees.htm

listed in Tab. 2.4, the detection limit of SCIAMACHY lies between 2.8 ppt and 35 ppt depending on the altitude profile. Only in case the IO is present over a considerable altitude and spatial ground range, the enhancement during low tides is expected to become visible in the satellite data.

From the IO standard product of the satellite data, first of all, an IO time series has been extracted around the respective research location and all measurements taken within a box of 100 km side length are used. The time series used in the following are based on the SCIAMACHY measurements between January 2004 and February 2008. In subsequent steps, the time series have been subjected to selection and sorting criteria in order to investigate differences between high and low tide situations. Each selection criterion reduces the data amount by a certain factor. An approximate reduction factor is given for each of the criteria:

- Only those observations within a certain time interval around the points of high and low tide are retained. For the interval either ±1 hour or ±30 minutes was chosen. The reduction factors for the individual series are 6 and 12, respectively.

- Either the time series of the entire year is retained or only data from the summer half-year (April-September), where ground-based observations reported the largest values. The reduction factor is either 1 or 2.

- The influence of clouds might be important here, so a cloud screening was implemented and could be switched on or off. The cloud screening is implemented by an intensity criterion, high reflective situations are excluded. This leads roughly to a reduction factor of 2.

Depending on the combination, the number of data points in the original time series of SCIAMACHY data is considerably reduced. This is part of the discussion in Sec. 4.4.4. The IO data sorted according to above criteria are finally averaged to one representative value so that the results of the high and low tide cases can be compared. The results are summarised in Tab. 4.2, stating the selection criteria and the resulting IO average slant column together with its standard deviation.

One important observation is that all resulting IO values are rather small. Taking the computed standard deviation into account, all of the IO slant columns are in agreement with zero. Regarding the above estimation of expected IO amounts in comparison with the satellite detection limit, this result is not surprising, as the expected amounts are close to or below the detection limit. Comparing the individual values of the HW and LW results, both situations occur, cases where the HW value is larger and others with higher LW value, while the ground-based observations find clearly higher IO amounts for the LW than for the HW situations. The two extreme tidal situations are in equal within their standard deviations in all tested cases. Consequently, no difference in IO amounts for high and low tides can be observed from the current SCIAMACHY observations. Further points of discussions follow below. Before, a second example of coastal locations is investigated.

4.4.3 Case study for location Roscoff

Roscoff is situated at the Atlantic coast in Northwest France (48.73°N, 3.98°W). In summer 2006, Whalley et al. (2007) measured IO by Laser Induced Fluorescence (LIF) in Roscoff, during the

Seasons included	Time interval	Cloud screening	IO at high tide	IO at low tide
all	±1 hour	no	1.55 ± 4.44	1.63 ± 4.37
all	±0.5 hour	no	0.72 ± 4.37	1.36 ± 4.90
summer	±1 hour	no	2.51 ± 3.23	1.53 ± 4.17
summer	±0.5 hours	no	1.27 ± 2.00	1.55 ± 4.31
all	±1 hour	yes	1.25 ± 5.91	1.21 ± 4.95
all	±0.5 hours	yes	-0.63 ± 6.60	0.85 ± 5.88
summer	±1 hour	yes	3.07 ± 3.47	0.81 ± 4.01
summer	±0.5 hours	yes	1.55 ± 2.04	0.76 ± 4.37

Table 4.2: Comparison of averaged IO slant columns (in units of 10^{12}molec/cm^2) for high and low tide at Mace Head, Ireland, based on satellite data recorded between Jan 2004 and Feb 2008. Different conditions concerning the included seasons (full year or only summer half-year), the time interval around the point of high and low waters (one hour or two hours) as well as cloud screening (via an intensity limit) have been investigated. The uncertainty ranges state the standard deviation of all involved IO data points and show that the values and differences are not significant.

project Reactive Halogens in the Marine Boundary Layer (RHaMBLe), at maximum mixing ratios around 30 ppt for short integration times of 10 s. Longer integration times yield much smaller IO amounts demonstrating the high variability of IO concentrations and the transitory nature of outstandingly high IO amounts.

The satellite IO data is processed in exactly the same way with identical selection criteria as chosen for the case study at Mace Head. An analogous overview lists the results of the selection and sorting procedures in Tab. 4.3. Like above, also for the location of Roscoff, all IO case averages are in agreement with zero IO load taking into account the respective standard deviations. In contrast to the Mace Head data, the IO amounts for low tide are in all but one combination higher than the HW data. Although this is in general agreement with the ground-based observations, this finding is not meaningful, because this difference between the high and the low tide IO amounts is not significant. All amounts agree within their standard deviations.

Seasons included	Time interval	Cloud screening	IO at high tide	IO at low tide
all	±1 hour	no	1.76 ± 5.21	1.89 ± 4.36
all	±0.5 hour	no	1.69 ± 5.90	2.67 ± 4.29
summer	±1 hour	no	-0.38 ± 5.37	1.87 ± 4.62
summer	±0.5 hours	no	0.27 ± 7.15	1.74 ± 4.32
all	±1 hour	yes	2.25 ± 6.76	1.74 ± 4.59
all	±0.5 hours	yes	2.06 ± 7.50	2.83 ± 4.98
summer	±1 hour	yes	0.43 ± 7.27	1.32 ± 4.43
summer	±0.5 hours	yes	1.07 ± 8.92	1.83 ± 5.03

Table 4.3: Comparison of averaged IO amounts for high and low tide at Roscoff. All settings are according to Tab. 4.2, IO slant columns are given in 10^{12} molec/cm^2.

4.4.4 Discussion of the tidal analysis

In the mid-latitudinal cases presented above, the satellite IO columns have been found to agree with a zero column amount within the respective standard deviations of the extracted time series. Reported ground-based mixing ratios are mostly below the detection limit of the satellite observations, so that the above results can be regarded as confirmation of two aspects. First of all, the satellite observations confirm that no large and widespread IO amounts above the detection limit of the satellite instrument are present at the investigated coastal locations. Secondly, the finding, that the detection limit is not significantly exceeded, argues for a confinement of the IO molecules either to the lowest atmospheric layers, or for strong localisation. If IO values in the range of surface levels were constantly mixed over a large altitude range (>1 km), the satellite data would contain some evidence of this. Additionally, the IO amounts observed by ground-based point measurements are effectively reduced by the size of a satellite pixel and detection of IO is most impeded by probably confined IO sources.

Although a long data set has been considered, the combination of necessary selection criteria strongly reduces the number of data points. The individual reduction factors have been stated above and following from this, one selected data series (either HW or LW) contains a number of data points reduced by a factor of 6 up to a factor 48. The largest original time series contains nearly 500 data points, so after the selection, on the order of between 90 (weak selection criteria) and 10 (strict criteria) remain. The data basis for analysis is thus not large and as the IO amount is close to the calculated detection limit, this data amount is not sufficient to reduce the influence of noise errors strongly enough. Consequently, in none of the investigated situations, the difference between the high and low tide is significant.

Concluding from the above findings, a different analysis strategy is needed for the observation of a tidal signal in the atmospheric IO loading and for the identification of sources as well as their spatial distribution and source strengths. Higher spatial resolution and more frequent measurements would be favourable for the analysis of these questions. The satellite instrument OMI (Ozone Monitoring Instrument), an imaging spectrometer installed on the Eos-Aura satellite (Levelt et al., 2006), observes in somewhat higher spatial resolution with a typical ground-pixel size of 13×24 km^2. However, up to now the observation of IO has not been reported from that instrument. For a purposeful investigation of the above tasks, specific aircraft measurements are proposed and planned for the near future. Aircraft observations form an intermediate between ground-based and satellite platforms.

5 Modeling of atmospheric IO with the CAABA/MECCA code

In addition to atmospheric measurements from different platforms it is of interest to apply atmospheric chemistry models to calculate concentrations and variations of atmospheric components for certain conditions. In the field of iodine research, still many open questions remain, especially on the sources of reactive gaseous iodine compounds and on some reaction pathways and their kinetics. For example, the sources and pathways leading to the observed Antarctic IO observations are not well known, although ideas for explanations certainly are being developed (cp. Sec. 3.3). In addition to these ideas, it is illuminating to use model studies to inspect the current knowledge which is incorporated in the model by analysing whether or not certain observations can be reproduced. Potential shortcomings in the current understanding may be identified in this way.

In the present study, the CAABA/MECCA model code developed at the Max Planck Institute in Mainz (Sander et al., 2005) is applied. A model is needed that incorporates tropospheric chemistry including halogen chemistry in the marine boundary layer as well as in Polar Regions. For the correct computation of iodine compounds, apart from gas phase chemistry, the model should include the most important reactions in the aqueous phase and heterogeneous chemistry. Iodine and its compounds show a relatively large variety of reaction pathways so that a large system of reaction kinetics needs to be taken into account. The required properties are provided by the CAABA/MECCA model.

In the following sections, the model will be introduced and its most important properties and characteristics will be described. After outlining the objective of this modeling study, the specific choice of parameters and model settings is motivated. The model results for the IO concentrations are presented, and model findings are compared with the satellite results. From this, conclusions on the necessary amounts of emitted iodine precursor amounts are obtained.

5.1 Modelling studies of iodine chemistry in the literature

Several studies have assessed the topic of atmospheric iodine chemistry with different specific questions and including different model settings. Depending on the underlying questions asked, the concentrations of some substances are predefined and their influence on other species is investigated. Some of the previously published modelling activities are summarised here.

The role of iodine photochemistry has first been addressed by Chameides and Davis (1980) for the troposphere and by Solomon et al. (1994) also for the stratosphere, with a main focus on the destruction of ozone in the presence of iodine. Chameides and Davis (1980) consider CH_3I as source

of I atoms and calculate the effect on O_3, OH and NO_x levels at a marine location at 30° latitude. They identify several ozone destruction pathways and calculate the abundances of different iodine compounds to lie in the ppt range for given CH_3I concentrations up to 50 ppt. Due to the important tropospheric role of OH, its sources and sinks need to be understood and quantified. Depending on precursor levels between 10 and 50 ppt of CH_3I, the OH concentrations were found to change substantially by 22% and 100%, respectively.

In model calculations by Vogt et al. (1999), emissions of different halocarbons (CH_2I_2, CH_2ClI, and C_3H_7I) in addition to methyl iodide account for atmospheric iodine levels. They considered certain iodine compounds (HI, HOI, INO_2, and $IONO_2$) as reservoirs of temporary nature, which acted as final iodine sinks in previous studies (Chatfield and Crutzen, 1990; Davis et al., 1996). This increases the degree of complexity of the chemical iodine cycling. One important result of their model studies is the realisation, that the photochemical release of Br and Cl atoms from the sea salt phase is facilitated in the presence of iodine. In addition to the impact of iodine itself, the enhanced bromine and chlorine levels lead to an accelerated ozone destruction as compared to the model before including iodine chemistry (Sander and Crutzen, 1996).

In studies conducted by McFiggans et al. (2000), observational constraints of various trace gases, also of IO, have been applied and the impact on the oxidation capacity and several specific compounds has been investigated. One focus of their work lies on the connection of iodine to the aerosols phase, and they calculate high enrichment factors (several orders of magnitude) of iodine in aerosol, in agreement with observations. Additionally, the impact on ozone destruction and denoxification (loss of NO_x) is once again addressed. In their model runs, they use a constant concentration of iodocarbons.

The effect of iodine on the HO_2/OH-ratio has been studied in more detail by Bloss et al. (2005) who find that those studies neglecting the $IO + HO_2 \rightarrow HOI + O_2$ reaction overestimate the HO_2 concentrations as compared to observations. In their model calculation, the present iodine amounts lead to substantial loss of HO_2 and some gain in OH, so that boundary layer chemistry is considerably affected by even small amounts of iodine.

While most model work is adjusted to mid-latitude conditions of the marine boundary layer, recently, Saiz-Lopez et al. (2008) have proposed a mechanism for the release of iodine species in sea-ice covered regions, where emissions from ice algae below the ice sheets play a major role and multi-phase chemistry is employed. They consider the equilibrium reaction

$$HOI + I^- + H^+ \leftrightarrow I_2 + H_2O$$
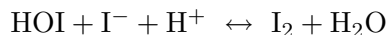
and vertical diffusion of iodine species through brine channels to the sea ice surface, from where I_2 may be released. They conclude from their calculations that the assumed emissions can explain observations of IO in Antarctic spring. The proposed release mechanism is, however, still controversially discussed (Sander, 2008; Carpenter, 2008).

In the following study, the emission rates of organic precursor substances are kept constant within each new model run (similar to the studies by Vogt et al., 1999) instead of the precursor concentrations, and the resulting IO mixing ratios are investigated. First of all, the applied model is now introduced.

5.2 Description of the CAABA/MECCA model

The applied atmospheric chemistry model has an underlying modular structure - the complete code is build up by separate parts, each part covering a certain aspect.

The underlying MESSy structure

The link between the model parts, for example the transfer of parameters and results between the model parts as well as the organisation of the flow of variables is provided by the MESSy (Modular Earth Submodel System) interface (Jöckel et al., 2005). MESSy is a new approach to an Earth System Model (ESM). An ESM is concerned with the entire Earth system and the aim is to combine all parts (such as the atmosphere, biosphere, hydrosphere and others) of the system and to capture not only the subsystems themselves but most importantly the feedback mechanisms and interactions between them. Earth system modelling can be achieved by linking existing domain-specific models to each other. In this domain oriented approach, single models for certain domains such as the whole atmosphere or the entire ocean system are used and an additional program, a so-called coupler, combines all domains by exchanging parameters and values between them.

MESSy is rather process oriented. In this approach, a base model is used to control the model runs and contains for example the central model timer. All important processes are described within individual modules (submodels) which are directly linked to the base model and are not combined into domain specific models first. All submodels can be switch on or off separately and a common interface is used for the transfer of variables between the base model and the submodels.

The MESSy interface structure can also be used if not a complete ESM shall be run but a certain subsystem. In the present case the included system comprises mainly the atmosphere, but also biogenic emissions and surface effects through deposition.

The MECCA module

The atmospheric chemistry is incorporated in the MECCA module (Module Efficiently Calculating the Chemistry of the Atmosphere), and MECCA then acts as a submodel within MESSy. This part contains all relevant chemical reactions and transformations in the gas and aqueous phases and the chemical reaction kinetics (Sander et al., 2005). The involved species and their initial values are defined. For the setup of the reaction schemes, the Kinetic PreProcessor (KPP) software is used, a free software specifically written for the computation of chemical reaction kinetics (Damian et al., 2002; Sandu and Sander, 2006). KPP generates the mathematical program code and performs the integration of the chemical equations.

The chemical reactions are mostly described by a set of stiff ordinary differential equations (ODEs). Differential equations are described as stiff, if slowly varying components need to be considered alongside others which are quickly damped, i.e., in cases when an equilibrium is quickly obtained. In the present case quick and slow reactions participate in the reaction kinetics. For the numerical integration of the differential equations, several integrators are available within KPP. Due to good stability properties, all possible options are suitable for the integration of stiff differential equations (Sandu and Sander, 2006). In the present study, the recommended positive definite Rosenbrock

integrator is applied as default.

The differential equations describe the temporal evolution of the involved chemical species. Species with variable as well as fixed concentrations are considered. The Jacobian matrix $J_f(i,j)$ play an important role in the integration of chemical reactions. It describes how the concentration of the variable species evolves in time depending on the concentrations of all other species (fixed and variable). The functions f_i describe the time derivatives of the concentrations $\mathrm{d}c_i/\mathrm{d}t$ in dependence of the other trace gases. An example equation for a concentration c of trace gas a, which depends on, e.g., 2 other trace gases has the following form:

$$f_a = \frac{\mathrm{d}c_a}{\mathrm{d}t} = -k_1 \cdot c_a \cdot c_b + k_2 \cdot c_c \cdot c_d,$$

where the k_j are the reaction rate coefficients and $c_a...c_d$ are the concentrations of involved species. The first term with negative sign describes a loss reaction while the second summand specifies a production process. The equation for the temporal evolution of concentrations can have in reality a lot more terms, but the general form corresponds to the above equation. Additional loss processes are deposition and photolysis. These do not depend on the concentrations of the other trace gases. The Jacobian matrix contains the partial derivatives of the functions f with respect to the concentrations of all substances.

$$J_f(i,j) = \frac{\partial f_i}{\partial c_j}$$

The MECCA code increases the efficiency of the integration by not using the full Jacobian but saving only the non-zero values and their respective matrix coordinates, i.e. the Jacobian sparsity matrix.

Considering the implemented chemistry, MECCA offers the choice between many different scenarios. The tropospheric as well as stratospheric chemistry are covered and different choices for the included substances are possible. Depending on the individual requirements, the model user may select the appropriate scenario. Gas phase as well as aqueous phase species and reactions can be included. If necessary, the chemical mechanism can also be extended, e.g. if new results from laboratory studies become available. The chemistry involved is based on several previous studies, specifically the halogen chemistry is implemented from Sander and Crutzen (1996) and von Glasow et al. (2002), with partly updated kinetics data. Chemical kinetics data is available, e.g., from Atkinson et al. (2004), Atkinson et al. (2006) and Sander et al. (2006b). A summary of the implemented chemistry and kinetics data is provided (Sander et al., 2005, supplementary material[1]).

The CAABA boxmodel used as base model

MECCA needs to be linked to a base model providing the atmospheric situation for which calculations shall be performed. The base model can be of different degrees of complexity. In the present study, a boxmodel is chosen to provide the basic situation, but also a complete General Circulation Model (GCM) can be applied. For the calculation of the abundances of iodine compounds under

---

[1]http://www.atmos-chem-phys.net/5/445/2005/acp-5-445-2005-supplement.zip

defined conditions, a zero dimensional boxmodel is suitable here. This part is called CAABA - Chemistry as a Boxmodel Application. And the boxmodel in connection with the chemistry provided by MECCA is referred to as the CAABA/MECCA code (Sander et al., 2009). The scheme in Fig. 5.1 shows the general structure of the combined model.

Apart from the atmospheric chemistry which is provided by MECCA, two additional submodules are required. The SAPPHO module provides the photochemistry, i.e. photolysis rates. Emission and deposition reactions and rates are given by the SEMIDEP (Simple Emission and Deposition) module. Within the boxmodel structure parameters for the geolocation and time are chosen, needed for the calculation of photolysis rates. Meteorological settings such as the temperature, pressure and humidity are set which influence the chemical kinetics. Also different properties of the involved aerosols (or the option of excluding aerosols) can be defined.
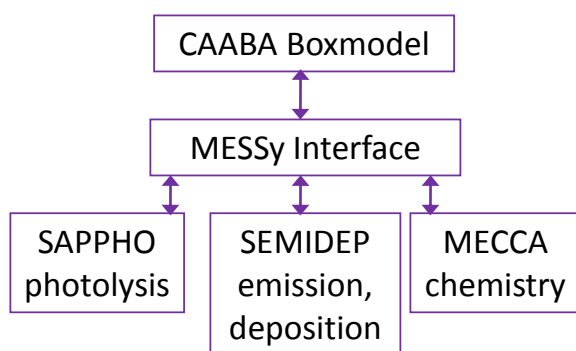

Figure 5.1: Structure of the CAABA/MECCA modeling code. The link between the individual purpose submodels is provided by the MESSy interface. In the present case the boxmodel CAABA serves as base model.

Overview of the implemented iodine chemistry

The complete reaction mechanism incorporated in MECCA contains about 200 gas phase reactions and 60 photolysis reactions, depending on specific choices. The "base run" in this study, for example, has 197 gas phase and 64 photolysis reactions with 112 species involved in total.

The iodine chemistry which is considered in the MECCA code is graphically demonstrated in Fig. 5.2. For this purpose, all reactions and conversions which involve iodine species have been selected from the complete mechanism for an overview of this specific part of the model. The picture does not give information about the relative importance of the single reactions, but shows which species are connected to each other by chemical conversions. The different types of boxes and arrows chosen for the individual cases are explained in the legend. The only species which is not a chemical molecule in this figure is I_{part}, which summarises all particulate iodine substances. The different types of fine particles that can be created by iodine species are not individually treated in this model. Current understanding is that the formation of fine particles from iodine oxides is connected to the OIO molecule, which therefore is the link to particulate iodine in the applied code.

Some existing reactions are not yet incorporated in the model. As laboratory studies progress, the chemical mechanism can be extended and completed. So far, no new reactions have been added.
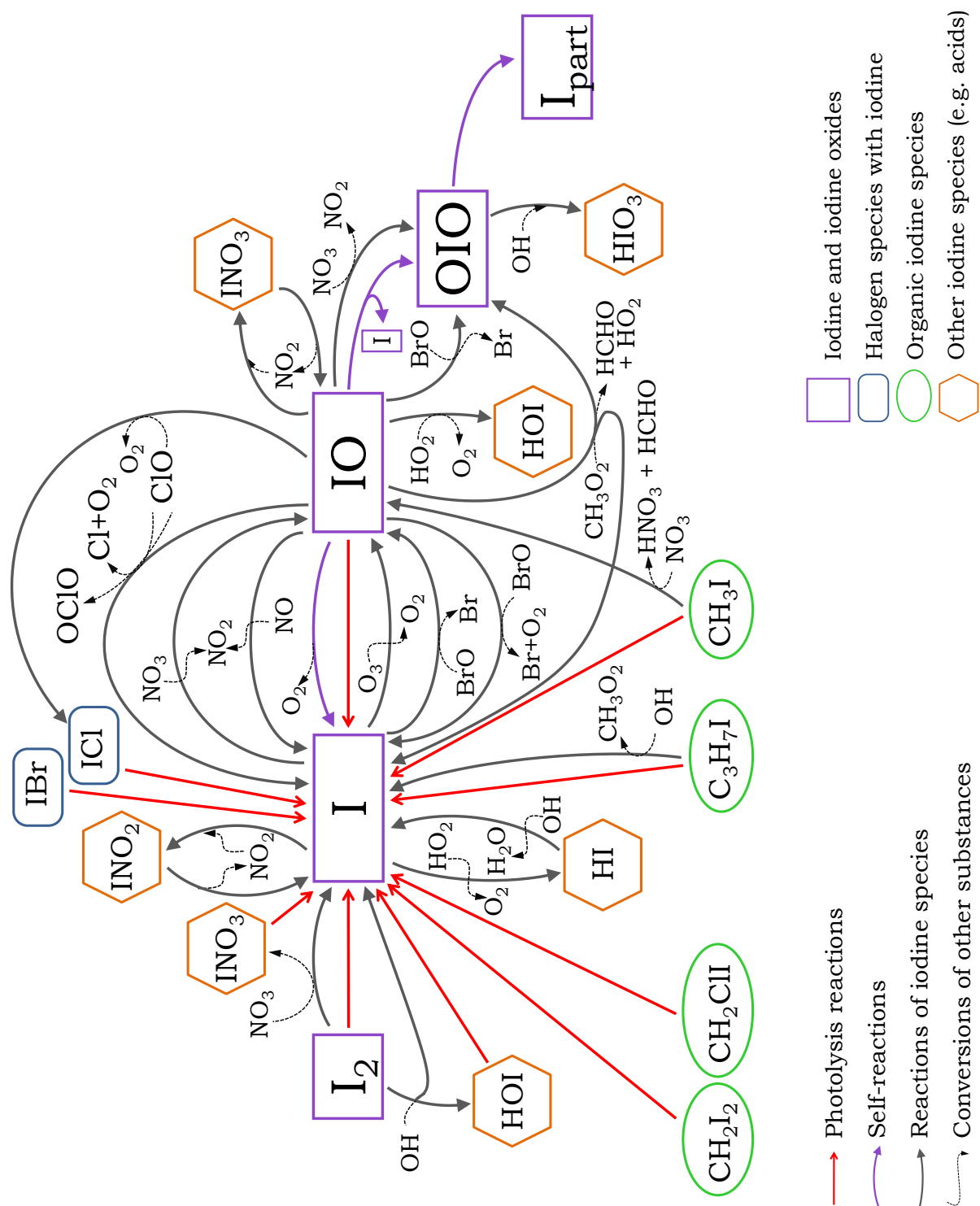
Figure 5.2: Excerpt of the MECCA chemical mechanism showing all reactions and conversions which involve iodine species. Different kinds of species are marked by individual boxes and different classes of reactions by individual arrow types. I$_{\text{part}}$ denotes collectively all particulate iodine substances. As prefactors are omitted for clarity, they have to be added where appropriate to make the stoichiometry correct. Generally present species as O$_2$ may be omitted in some cases.
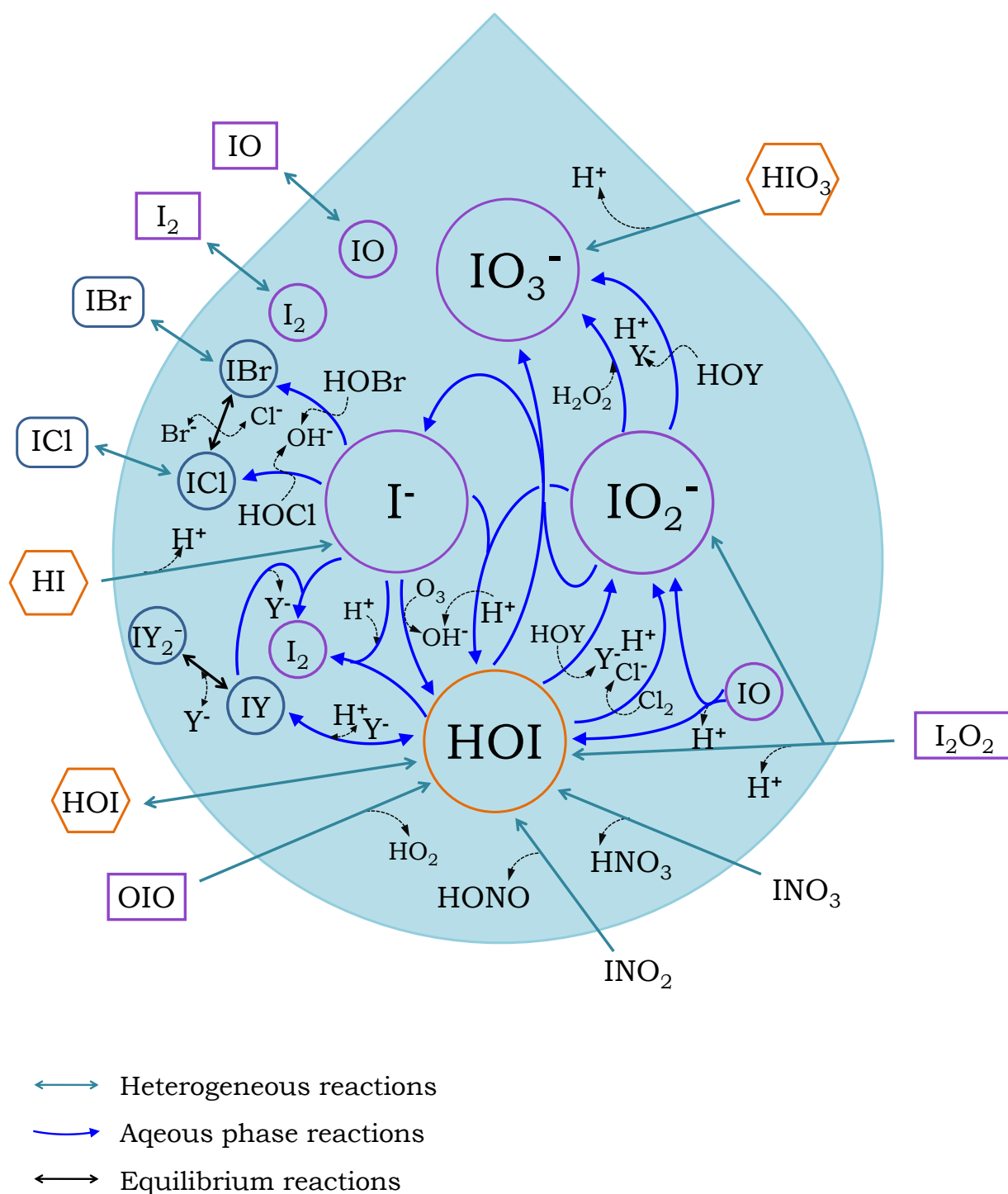
Figure 5.3: Scheme of the aqueous phase reactions related to iodine as considered by the MECCA model. Substances outside the schematic droplet/liquid water containing aerosol belong to the gas phase (cp. Fig. 5.2), all substances inside (surrounded by circles) are dissolved in the liquid phase. The species Y denotes either Cl or Br. The meaning of colours and boxes from Fig. 5.2 is maintained.

5.3 Objectives and model settings

The satellite measurements presented in previous section add new information to the knowledge about amounts and distribution of IO which is important for the picture of iodine chemistry and its relevance for atmospheric composition. Regions with enhanced IO amounts ask for further explanation and interpretation.

In addition to the observed absolute IO columns and distributions as well as upper limits for certain locations, it is of interest to estimate which source strengths of iodine precursors are necessary to produce the observed IO amounts. This needs to be computed taking into account up to date atmospheric chemistry including iodine chemistry as far as it has been assessed by laboratory studies before.

In the conducted model calculations, first of all realistic scenarios of the Antarctic troposphere are set up. The aim is then to compute IO amounts which are in accordance with the satellite observations. As the quantity which is computed and used by the applied model under given conditions is the volume mixing ratio of the trace gases, the column amounts from the satellite retrievals need to be transformed before comparison is possible. As discussed in Sec. 2.4, the conversion from trace gas columns to a concentration at a certain altitude requires the knowledge of the altitude profile. As this is not well known in the case of IO, the VMR inferred from the satellite data shows one order of magnitude difference between a 1 km box profile and a 100 m box profile, for example. Seasonal averages for the slant columns lie in the range of 8×10^{12} molec/cm^2 in the South Polar Region. For an AMF of 4 and the two box profile cases the amounts of the inferred VMR lie between 0.8 and 8 ppt (cp. Chapter 3). In measurements from the ground, several ppt of IO have been reported for some favourable conditions in Antarctica (Saiz-Lopez et al., 2007b), in agreement with above estimations. The open question at this point is, which conditions are needed to produce these concentrations of IO under Antarctic conditions. This shall be investigated in the following by using appropriate settings and varying the emissions of precursors.

The location chosen for the model studies is Halley Station close to the Antarctic coast (75.5°S, 26.5°W). For this location, the typical meteorological conditions (temperature, pressure, humidity) need to be fed into the model code. Due to the vicinity to the ocean from the chosen location, the chemistry of a marine boundary layer is an appropriate choice. Some basic model settings that were kept fixed for all model runs are listed in Table 5.1.
One combination of reasonable parameters and settings is chosen as the "base run" to which subsequent model runs will be compared. A selection of important specific settings is summarised in Tab. 5.2.

Different combinations of settings have been tested in order to gain insight into which parameters are the most influential for the resulting concentration of IO. All properties listed in Tab. 5.2 for the base run have been varied. One focus is on the effect of different emission rates. The chosen cases of emission rates are related to published observations, measurements and other model studies. Usually, emission rates are given either in units of "molecules per cm^2 per second" or in "nmol per m^2 per day". The conversion between the two options is:

$$1 \cdot 10^6 \text{ molec/cm}^2/\text{s} = 1.44 \text{ nmol/m}^2/\text{day}.$$

Parameter	Setting
Location	Halley Station
Latitude	75.5°S
Longitude	26.5°W
Pressure	980 hPa
Humidity	80%
Model Start Time	1st September
Model Duration	15 days
Model Time Step	20 minutes

Table 5.1: Settings for the basic conditions valid for all model runs.

Property	Setting
Temperature	253 K
Aerosols	2 phases: sulphate aerosol, sea salt aerosol
Emissions	CH_3I at $6 \cdot 10^6$ molec/cm^2/s (Vogt et al., 1999)
	CH_2I_2 at $1.32 \cdot 10^6$ molec/cm^2/s (Carpenter et al., 2007)
	cp. Tab. 5.3
Initial amounts	only CH_3I at 2 ppt

Table 5.2: Model parameters and settings as used in the base run.

Whenever the emission rate is given in nmol/m^2/day in the literature, the number is converted to molec/cm^2/s for consistent use and direct comparison throughout this chapter. Table 5.3 lists the definitions of the emission settings applied in some of the test runs. The emissions set in the base run are taken from the only available measurements of organic precursor fluxes conducted in the Antarctic (Carpenter et al., 2007). The time and exact location are not coinciding with highest satellite IO values, so that modeled IO is not expected to be at maximum for the base run. Other observations and studies report higher emission rates, but the knowledge of emission rates are sparse. The base run results in too small IO amounts to explain the satellite observations as shown below.

5.4 Model results

The resulting IO amounts from different model runs are now investigated. Each model run produces time series for each included trace gas and aqueous phase species. Figure 5.4 displays the temporal evolution of the IO concentration calculated by the Base Run. For the first model days, the trace gas amounts change strongly as the situation is mostly not in equilibrium. After stability is achieved, the daily maximum IO amount ranges around 0.012 ppt. This is far below the converted satellite results, about 2 orders of magnitude too small. One interesting finding is that the time of day with maximum IO amounts approximately coincides with the SCIAMACHY overpass time, also for the following model runs. This is a result of the ongoing photochemistry which in first place releases iodine from the photolabile iodocarbons, but also photolytically reduces IO amounts.

Label	Molecule	Settings
Base Run emis2ave		two emitted compounds
	CH_3I	$6 \cdot 10^6$ molec/cm^2/s (Vogt et al., 1999)
	CH_2I_2	$1.3 \cdot 10^6$ molec/cm^2/s (Carpenter et al., 2007)
emis2max		two emitted compounds
	CH_3I	$6 \cdot 10^6$ molec/cm^2/s (Vogt et al., 1999)
	CH_2I_2	$4.2 \cdot 10^6$ molec/cm^2/s (Carpenter et al., 2007)
emis2MH		two emitted compounds only
		according to measurements at Mace Head (Carpenter et al., 2001)
	CH_3I	$6 \cdot 10^6$ molec/cm^2/s (Vogt et al., 1999)
	CH_2I_2	$1.4 \cdot 10^9$ molec/cm^2/s (Carpenter et al., 2001)
emisVogt		all emissions as in (Vogt et al., 1999)
	CH_3I	$6 \cdot 10^6$ molec/cm^2/s
	CH_3H_7I	$1 \cdot 10^7$ molec/cm^2/s
	CH_2I_2	$3 \cdot 10^7$ molec/cm^2/s
	CH_2ClI	$2 \cdot 10^7$ molec/cm^2/s
emisCarpenter		personal communication of model authors with Lucy Carpenter
	CH_3I	$6 \cdot 10^6$ molec/cm^2/s (Vogt et al., 1999)
	CH_3H_7I	$1 \cdot 10^7$ molec/cm^2/s (Vogt et al., 1999)
	CH_2I_2	$3.8 \cdot 10^8$ molec/cm^2/s
	CH_2ClI	$1.3 \cdot 10^9$ molec/cm^2/s

Table 5.3: Model settings for different precursor emission rates, according to different observations and publications.
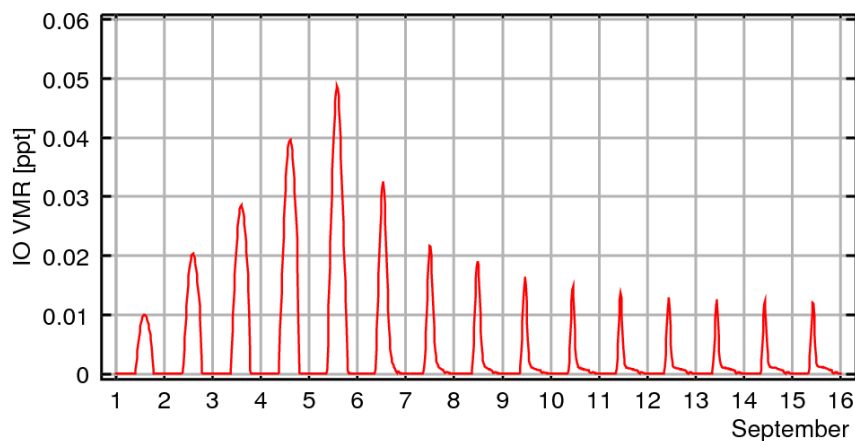

Figure 5.4: Modelled volume mixing ratios of IO for the base run shown for the complete model time period of 15 days.

Results from different emission scenarios

In a next step, the biogenic iodine precursor emissions as reported in the literature are varied as given in Tab. 5.3). The resulting IO volume mixing ratios computed from these five scenarios are compared in Fig. 5.5. For each case, the maximum IO on the last model day is shown. The base run and two other scenarios (emis2max and emisVogt) show values well below 0.8 ppt and consequently cannot explain the IO amounts retrieved from satellite observations. The emissions measured by Carpenter et al. (2001) in Mace Head (emis2MH) and the combination of emissions reported by Vogt et al. (1999) and from personal communication of model authors with L. Carpenter lead to IO VMR amounts between 1 and 3 ppt. For both cases with large IO amounts, the emission of polyhalomethanes (CH_2I_2 and CH_2ICl) are the crucial settings. In the other studies and scenarios, these were either not present or much lower.

Therefore, a comparison of modelled IO concentration in direct dependence of the emission rates has been performed. Figure 5.6 contains input from several model calculations - each point reveals the result from one individual model run. The maximum IO VMR resulting for the last day of the model run time (15th September) is shown versus the appointed emission rate of methyl iodide (red) and diiodomethane (blue). The data points correspond to the model output values, while the solid lines are 4th order polynomial fits included in the graph as a guide to the eye. Very clearly, the achieved IO amounts are much higher for CH_2I_2 emissions than for CH_3I. This difference is not only caused by the two iodine atoms per molecule of CH_2I_2, but mainly by its much larger photolysis rate.

The above findings show that the biogenic emissions observed by Carpenter et al. (2007) in Antarctica during one research cruise are not high enough to account for the IO concentrations observed in the present study at least with the current chemical scheme. The conditions during the research cruise probably did not support the maximum emissions possible, times with higher fluxes are expected. A few point measurements within a few days in the month of December were taken and this cannot suffice to explain observations in all seasons. At other times emissions may well be much higher and biogenic pathways are still considered relevant for iodine release in the Antarctic. In this sense, the model results do not contradict the assumption of biological release.
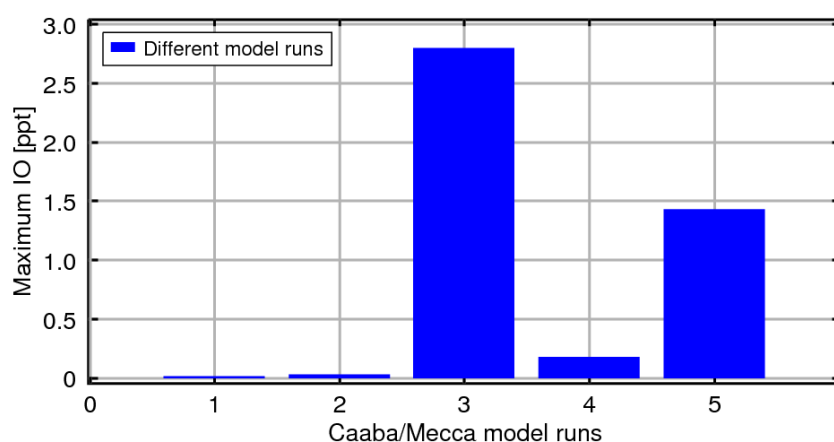

Figure 5.5: Modelled volume mixing ratios of IO (the maximum of the last model day) from five different scenarios with individual emission settings as stated in Tab. 5.3. Model labels: 1) base run, 2) emis2max, 3) emis2MH, 4) emisVogt, 5) emis-Carpenter .
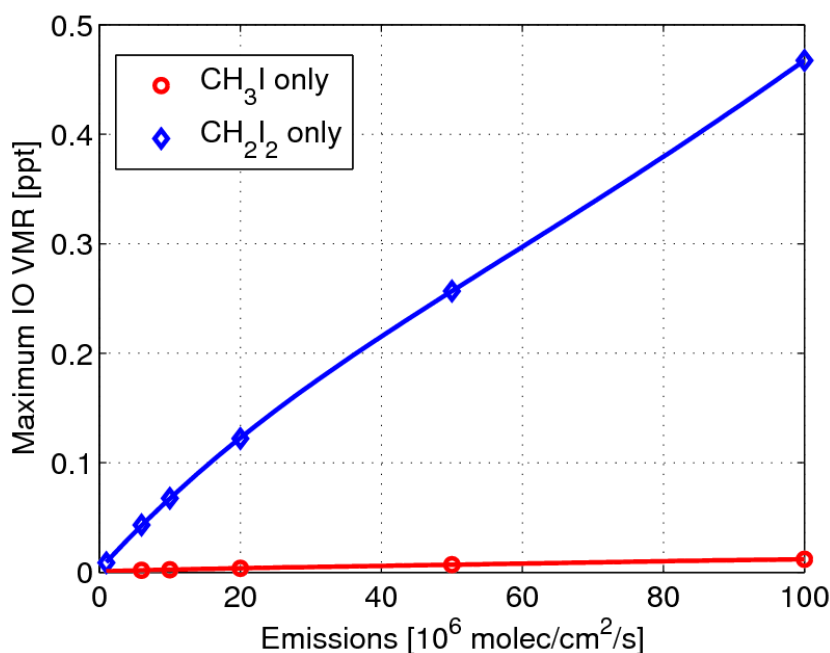
Figure 5.6: Maximum daily IO values on the 15th model day calculated by the CAABA/MECCA code in dependence of the applied emission rates of CH_3I (red) and CH_2I_2 (blue).

Emissions reported at other sites and from other studies, lead to modelled IO amounts in the range calculated from the satellite results in agreement with ground-based measurements. With these emission settings chosen, IO mixing ratios on the order of a few ppt are achieved.

In order to reach the IO amounts seen from satellite, emissions of CH_2I_2 are most important. Observed amounts and emission rates of methyl iodide only lead to an IO mixing ratio on the order of 0.01ppt and cannot explain current satellite observations if IO is confined to the lower atmospheric layers as was reported by Saiz-Lopez et al. (2007c).
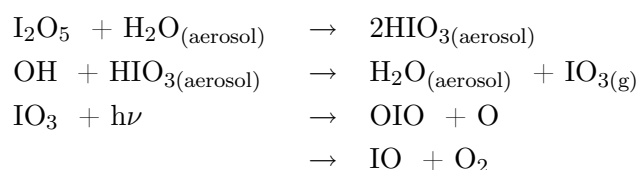
Even if high biogenic emissions are assumed, the resulting IO amounts are rather on the low side. Owing to the low number of available flux measurements, it is possible that higher emission rates occur without having been observed yet. Especially, no measurements were performed within the Antarctic sea ice during the Spring time period. In addition it seems to be likely, that some potentially important processes are not yet considered in the model.

5.5 Proposed model extensions

As mentioned above, applied atmospheric models may be incomplete, possibly in the present case, some reaction pathways are neglected which have a significant influence on the results or new kinetic studies may revise the knowledge on certain reaction rates. The presented calculations result in IO amounts which are clearly on the low side of observations. In regard of potentially missing chemistry or inappropriate kinetics data, candidates for future model changes or extensions need to be identified.

One possibly important reaction has been identified to be neglected in the model, which is the photolysis of the OIO molecule. This reaction has been controversially discussed in the literature. The quantum yield of the respective products is not agreed on. Recent new laboratory work (Gómez Martín et al., 2009) gives new evidence that OIO photolysis with a quantum efficiency of unity, while former laboratory studies had reported a quantum yield 0.05 (Tucceri et al., 2006). Gómez Martín et al. (2009) estimate that iodine emissions need to be five times larger in case the quantum yield takes on the smaller value of 0.05 instead of 1. The fact that one missing reaction which is potentially important may change the modelled IO amount effectively fivefold shows how important the completeness of the chemical mechanisms is to compute values in agreement with real world observations. The effect of including the OIO photolyses with a quantum yield of 1 for iodine atoms will be investigated in future studies.

In addition, several heterogeneous phase reactions, recycling on snow/aerosol surfaces need to be included. Currently, particulate iodine acts as a sink in the model, while sea salt aerosols are modelled to exchange some compounds between aqueous and gas phase. However, the release of gaseous compounds from iodine particles may well be possible. Considering the molecule I_2O_5, which is a compound of particulate iodine and of hygroscopic nature, the following reactions might proceed, where gas phase species react with aqueous phase substances on the aerosol surface:

$$
\begin{aligned}
I_2O_5 \; + \; H_2O_{(aerosol)} \quad &\rightarrow \quad 2HIO_{3(aerosol)} \\
OH \; + \; HIO_{3(aerosol)} \quad &\rightarrow \quad H_2O_{(aerosol)} \; + \; IO_{3(g)} \\
IO_3 \; + \; h\nu \quad &\rightarrow \quad OIO \; + \; O \\
&\rightarrow \quad IO \; + \; O_2
\end{aligned}
$$

In this case, gas phase reactive iodine would be recovered. Presently, it is not known, if these specific reactions occur. Reaction cycles of this type, involving gas phase and aqueous phase species at the same time, deserve further attention and might improve the understanding of iodine recycling from the particulate phase.

6 Analysing ship borne data for the improvement of DOAS retrievals

In April-May 2008, a Bremen MAX-DOAS instrument (Sec.1.9.2) was taken onto a cruise through the Atlantic ocean on the research vessel Polarstern. The instrument is designed for observations in the UV and the visible wavelength regions. In order to investigate the water leaving radiance, data from this cruise is analysed and discussed here. The aim for this study is to extract a correction spectrum for the improvement of satellite retrievals over water bodies.

6.1 Motivation for the following analysis

As discussed in Section 3.1, there are regular artefacts in the satellite retrievals which are common to several of the trace gas products deduced from, e.g., SCIAMACHY observations. One very prominent artefact that has already been examined from different sides are the negative trace gas amounts above the clear ocean regions. It is not clear up to now, why in these wide spread regions some trace gas products show some negative values, e.g. IO (Schönhardt et al., 2008) or CHOCHO (Wittrock, 2006). In other products, no negative values appear, but the pattern of the different ocean regions nevertheless shows up in the global maps. The clear ocean regions contain low chlorophyll concentration and low biological activity.

The problematic effect on the spectroscopic measurements might have different sources. The sunlight travels a larger path length through clear water, where the light path is not obstructed by, e.g., large suspended particles. The water molecules themselves and narrow band spectral features may affect the spectrum of the transmitted light stronger. These influences have their origin in absorption, but also in scattering processes. The absorption by liquid water is broad-band and rather weak at visible wavelengths, but may affect atmospheric measurements nevertheless. Its absorption coefficient has been measured in the laboratory, e.g. by Pope and Fry (1997). Other features are less well known and might have a considerable impact, like the spectrally more structured absorption coefficients by Chlorophyll, certain Phytoplankton types or CDOM (Chromophoric Dissolved Organic Matter). However, the clear water regions contain just little of these substances, which are more prominent in the biologically active areas.

Clear ocean regions often are the calmer regions, leading to a tendency towards a flatter surface. Therefore, polarisation effects will play a larger role here. Another effect is the inelastic scattering of photons at water molecules (and other molecules within the ocean water), i.e. the vibrational Raman scattering. The molecules are excited, e.g., from the ground level to an electronically higher level and relax back to a vibrationally excited state of the electronic ground level. This results in a wavelength shift of the emitted photon as compared to the incident photon and by exactly the same

principle as discussed for the Ring effect (cp. Sec. 1.6.3) causes an in-filling of strong absorption structures, especially of the Fraunhofer lines. Calculating the spectral effect of VRS has already brought some insight into this process and the influence on trace gas retrievals (Vasilkov et al., 2002; Vountas et al., 2003). Nevertheless, some insufficient correction or some additional features in these clear ocean regions are still apparent.

Instead of (or additionally to) calculating the effects that water has on the light spectrum, it should be useful to measure these effects directly. Therefore, the idea developed to use a DOAS system that would specifically observe the water leaving radiance on the Polarstern cruise. For this purpose, some additional viewing directions were added to the usual cycle of measurement scans through the atmosphere. Additional angles at a line-of-sight (LOS) below 0° (below the horizon) were chosen where the instrument is looking downwards - towards the ocean water.

6.2 Instruments and measurement details

The track of the ship cruise during which the DOAS measurements were recorded is shown in Fig. 6.1 and took place from April 18th - May 20th 2008. The usual speed of the research ship was close to 11 kn (i.e. 20 km/h) with daily station periods without ship motion at noon or in the afternoon for around 1 to 2 hours. These calm station periods were quite important for measurements in low viewing angles, as the bow wave or the associated sea spray during usual motion partly obstructed the sight into the ocean water at angles below the horizon.
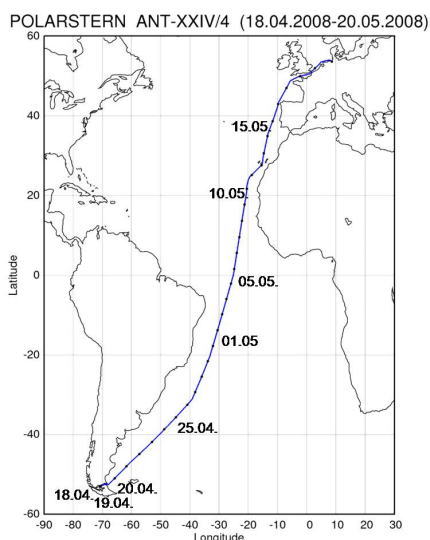

Figure 6.1: The track of the ANT-XXIV/4 Polarstern cruise from Punta Arenas (Chile) to Bremerhaven (Germany).

The DOAS instrument on board comprises two spectrometer units, one measuring in the UV and one in the visible wavelength region, which were both served with light by one mutual telescope. The viewing angle is determined by the position of a mirror mounted within the telescope box. Further basic information on the Bremen MAX-DOAS systems is given in Sec. 1.9.2. Table 6.1 contains some details on the instrument parameters, while Fig. 6.2 shows a schematic of the instrument's viewing geometry on the ship.

Instrument Data	UV instrument	VIS instrument
Spectrometer	Acton 500	Acton 275
Grating	600 lines/mm	300 lines/mm
Wavelength Range	327 - 410 nm	400 - 710 nm

Measurement Information	Usual Value
typical exposure time	0.5 s
integration time (zenith)	120 s
integration time (other directions)	60 s

Table 6.1: Overview of the instruments (top) applied on the Polarstern ship cruise, as well as some relevant measurement settings (bottom).
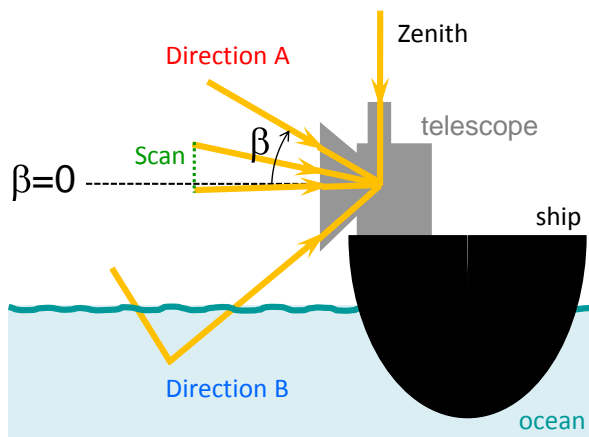
Figure 6.2: Sketch of the viewing geometry of the DOAS telescope onboard the research vessel. The sequence of the viewing angle β, also referred to as line of sight (LOS), was chosen such that viewing into the ocean water was facilitated ($-90° < \beta < 0°$) in addition to the usual scans above the horizon ($\beta > 0°$).

Sequence of viewing angles

The usual measurement sequence comprises viewing towards the zenith, viewing at LOS= $-60°$ (into the water), at LOS= $30°$ (into the atmosphere) and viewing at the scan angles between LOS= $-2°$ and LOS= $14°$ in $2°$ steps. Some additional low angles between $-60°$ and $-48°$ through a lower window in the telescope box and between $-22°$ and $-2°$ through the upper window are included during the occasional station periods of the ship (usually once a day for about 1 to 2 hours).
The integration time is usually 60 s for all slant directions, and 120 s for the zenith observation. A complete sequence therefore takes about 20 minutes. When the sun is too close to the observation direction, the slant viewing directions are interrupted and only zenith observations are performed to avoid too intense illumination and saturation due to direct sun. A typical measurement sequence is depicted in Fig. 6.3, where the LOS is plotted versus universal time here for the 10th of May 2008.

Data correction

Before the Polarstern DOAS measurements could be properly analysed and interpreted, some corrections had to be performed. Owing to the ship motion (especially the pitch and role angles), the viewing direction given by the telescope's mirror angle and determined by the computer control is not the real viewing direction from where photons are collected. The usual integration time is
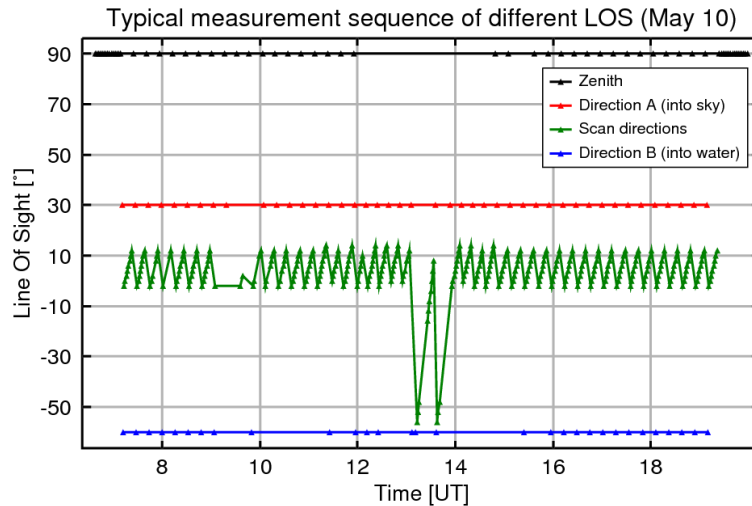
Figure 6.3: Line of sight versus time [UT] for the 10th of May, a typical day of the research campaign.

60 s or 120 s, while the frequency of the ship motion lies on the order of 0.1 Hz, depending on conditions. In any case, the integrated observations then contain measurements in different viewing directions, averaged over a wider range of angles. In order to receive measurements within a smaller interval of angles and to be sure about the real viewing angle, the original spectra (recorded at 2 Hz) were sorted. The sorting routine needs the information on the ship motion as input apart from the original spectra. Information on the pitch and roll angles is available from the ship's navigation platform. The sorting and averaging routine performs the following steps:

- Reading-in of the position information from the ship in high temporal resolution (10 Hz).

- Reading-in of the original spectra (before integration over 60 s or 120 s respectively) with the given measurement time and LOS information in the header.

- The LOS given in each spectrum is corrected by the additional angle from the ship and is assigned to a new class of measurements (in 2° steps).

6.3 Retrieval of the liquid water absorption

First of all one needs to know, if the radiation that was recorded in the water viewing direction has really passed through the ocean water. If this is the case, the spectra should have picked up some liquid water absorption. The absolute absorption coefficient in the visible wavelength region and the differential absorption structure in a smaller spectral interval are shown in Fig. 6.4 from laboratory measurements by Pope and Fry (1997).

For the retrieval of the liquid water absorption, a wavelength region was chosen that still overlaps with the regions of further interest (see below) and where the water absorption has sufficient spectral structures. The following retrievals were performed for the wavelength region from 420 to 540 nm,
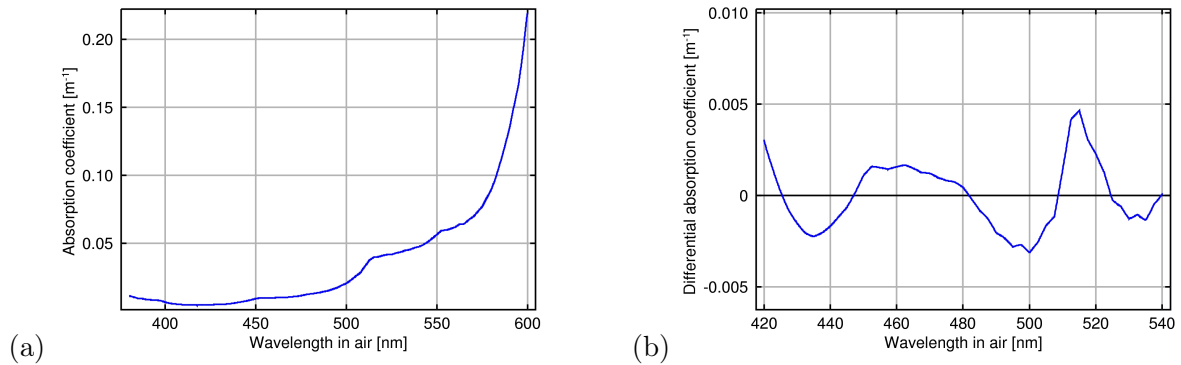
Figure 6.4: (a) Absolute absorption coefficient of pure liquid water as measured by Pope and Fry (1997). (b) Excerpt of this spectrum in differential form, i.e. a polynomial (here of degree 5) has been subtracted to enhance the higher frequency structures.

i.e. the region covered in Fig. 6.4(b). The DOAS fit settings that were applied for the retrieval of the liquid water absorption are listed in Tab. 6.2.

Liquid water retrieval	
Wavelength region	420 - 540 nm
Trace gases	
	$H_2O_{(liq)}$ (Pope and Fry, 1997)
	$H_2O_{(g)}$, 296 K (HITRAN data base)
	O_3, 241 K (Burrows et al., 1999a)
	O_4, 296 K (Greenblatt et al., 1990)
Considered effects	
	5th order polynomial
	Ring effect (SCIATRAN)
	stray light (constant offset)

Table 6.2: DOAS fit settings for the retrieval of liquid water absorption in the visible wavelength region.

The fit factors for the liquid water absorption give the average effective light path through the water, as in this case, not the absorption cross section but the absorption coefficient is applied. A sample fit result for the fitting of the water absorption structures can be inspected in Fig. 6.5. The expectation now is, that for water viewing angles a positive fit factor should result from the fit and a small or negative one for higher viewing angles. The background spectrum is taken from the 30°-direction above the water surface. (This was preferred in comparison the the zenith-sky spectrum to avoid potential additional structures related to the mirror.) It is possible that the 30°-direction also contains a small signature of the water absorption from water leaving radiation scattered into the field of view of the instrument. In case of less water signature in the compared spectrum, the resulting fit factor would be negative. This is observed in some occasions, especially in the fit of the zenith spectra against the 30°-direction. In Fig. 6.6 the water absorption fit factor

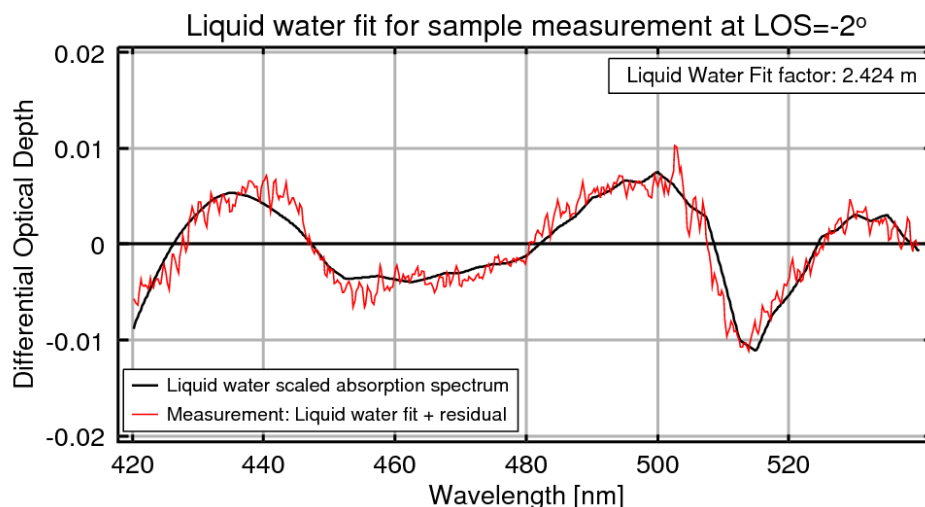(liquid water path) is plotted versus the LOS for two sample days (May 2nd and 12th, 2008).

Figure 6.5: Sample fit result for the water absorption structures showing the differential optical depth vs. wavelength. The scaled reference spectrum (black) originates from Pope and Fry (1997) (cp. Fig. 6.4) and the measurement (red) was taken at a LOS of -2° and shows here the fit result of the water absorption including the residual.

6.4 The mixed water effect

In the following, remaining spectral structures possibly hinting at unconsidered water effects shall be extracted from the measurements. For this purpose, a DOAS fit has been performed. The objective is to remove all known absorption lines and spectral features from the measured spectra and to receive a residual that contains information about all processes that are still unaccounted for. It is important to exclude as many other features from the spectra as possible to reduce the probability of artefacts and remnants of other trace species in the residual. The remainder should be related to the processes affecting the light in the ocean water, which of course needs to be tested. For the extraction of the water effect, suitable DOAS fit settings need to be chosen.

Extraction of the water effect

The wavelength region which is of special interest here, lies around the possible fitting windows of IO, CHOCHO and NO_2. In the spectral interval where these trace species are typically analysed the mentioned problems (cp. Sec. 6.1) occur. The final goal is to improve the satellite retrievals for these atmospheric gases. As it turns out at the end of the following procedures, the discovered spectrum for the mixed water effect does in deed pick up the signal over clear water regions. But unfortunately, the observed effect is not able to eliminate the discussed problems over clear water regions for these trace gases when included in the satellite retrievals.

Considering the spectral region of interest, the presented analysis will concentrate on the observations in the visible wavelength region. The central window that was chosen for the analyses
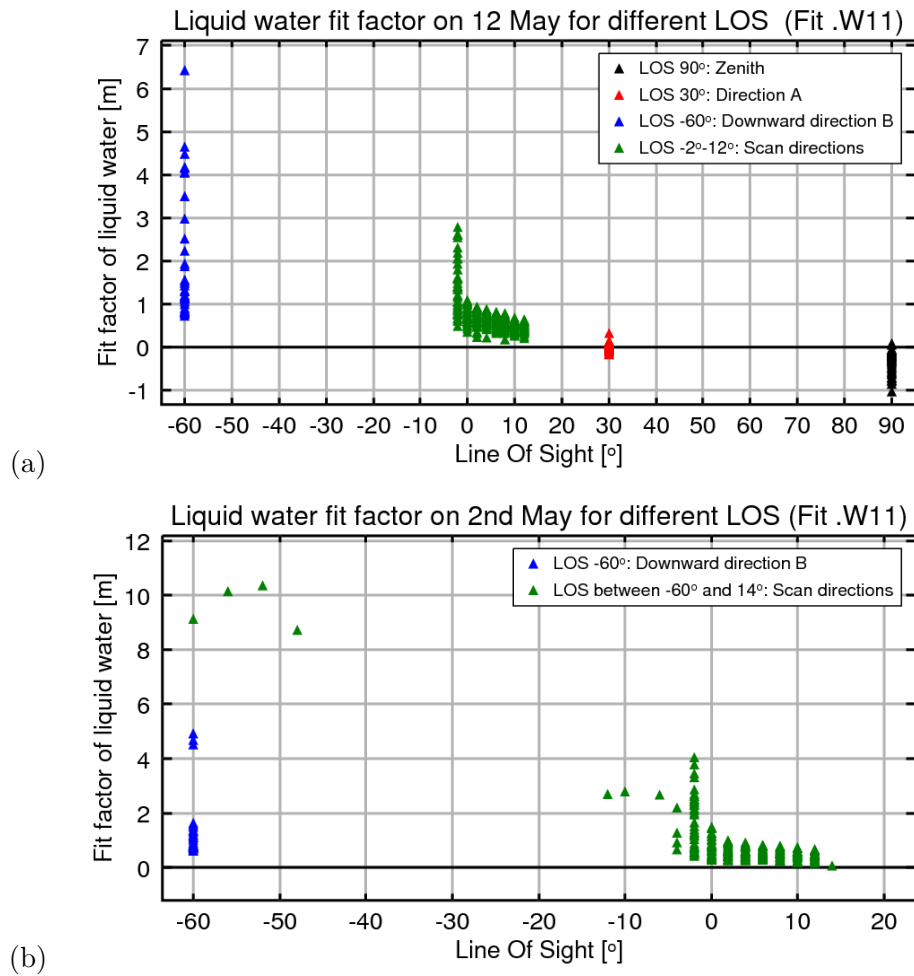
Figure 6.6: Fit factors of the liquid water absorption retrieved from the Polarstern DOAS measurements for two different days, the 12th (a) and the 2nd (b) of May, respectively. For (b) the LOS was restricted to the water viewing directions.

lies between 411 and 455 nm, containing some prominent features of IO, CHOCHO and NO_2. It is necessary that the chosen wavelength window extends a few nm to both wavelength sides beyond the limits of the usual fitting windows of these trace gases because the final product of the present analysis - the residual structure - shall be used in subsequent DOAS retrievals as reference spectrum. Reference spectra always need to be available in a spectrally wider region than the fitting window, as they need to be convolved with the instrument's slit function, also at the borders of the window. Additionally, some shift and squeeze is allowed for the reference spectrum. So a slightly wider window than seemingly necessary is selected.

The applied DOAS retrieval settings for the extraction of the mixed water effect from the remaining residuals are given in Tab. 6.3. The measurements of interest are the spectra recorded at low elevation angles (negative LOS θ) where the light has passed through the ocean water before entering the spectrometer.

DOAS retrieval settings	
wavelength region	411 - 455 nm
background spectrum	direction A (LOS = 30°)
polynomial	5th order
included trace gases	
	NO_2, 221 K (Burrows et al., 1998)
	O_3, 241 K (Burrows et al., 1999a)
	O_4, (Greenblatt et al., 1990)
	$H_2O_{(g)}$, 296 K (HITRAN data base)
considered effects	
	Ring effect (calculated by SCIATRAN)
	stray light (constant)

Table 6.3: Retrieval settings for the DOAS fit from which the residuals are used to extract the mixed water effect.

To make sure, that the fit is reasonably stable, retrievals in shifted or extended surrounding wavelength regions were performed. Only minor changes in the residual within the central range of the wavelength window were obtained, so that the DOAS retrieval can be considered stable for the chosen settings.

For the choice of the polynomial degree, the stability of the residual was tested for an increasing polynomial degree. Finally, the smallest degree was chosen, from which on no large effects were encountered when the degree was increased. For the given measurements and retrieval settings, this was a polynomial of 5th order (six degrees of freedom).

For the extraction of the mixed water effect, only those residuals from measurements during ship station were selected. As discussed and shown in the previous section, for these observations the recorded light really passed through the ocean water before entering the spectrometer and should therefore contain the unaccounted water effects. After the DOAS retrieval with above settings, the fit residuals of the observations during station period were extracted and averaged. For this purpose, only measurements between -60° and -50° were selected. For the individual LOS, different numbers of spectra are available, because observations were not performed for all viewing angles on

every day and not always during station period. Only in B-direction (i.e. at -60° LOS, cp. Sec. 6.2) regular measurements were recorded nearly every day also during the station periods. The analysis is restricted to measurements at station times, because the influence from spray water during ship motion was found to prohibit the clear sight into the ocean water. In total, around 100 spectra could be used for averaging:

- From the low LOS scans (between -58° and -50°):
  3 days for 32°, 13 days for -56°, 3 days for -54°, 13 days for -52°, 1 day for -50° with one or two measurements a day.

- From the lowest LOS, the regular B-direction (at -60°):
  19 days nearly throughout the campaign with a total of 56 single measurements.

In Fig. 6.7, the residual spectra for the different viewing angles are shown. All of the residuals originating from the above mentioned measurements were averaged to yield a weighted mean residual. This is also included in Fig. 6.7 in grey. The plot shows, that the residuals from the different low viewing angles have several structures in common. Some noise on the spectra and individual features in single measurements certainly lead to some differences between the shown residuals. But nevertheless, at several spectral positions, there are clear systematic features. Here, attention should be turned to the structures around 424 - 428 nm, 434 - 438 nm, and 443 - 446 nm. Additionally to the general similarity between the residuals, in these positions persistent structures are most apparent.
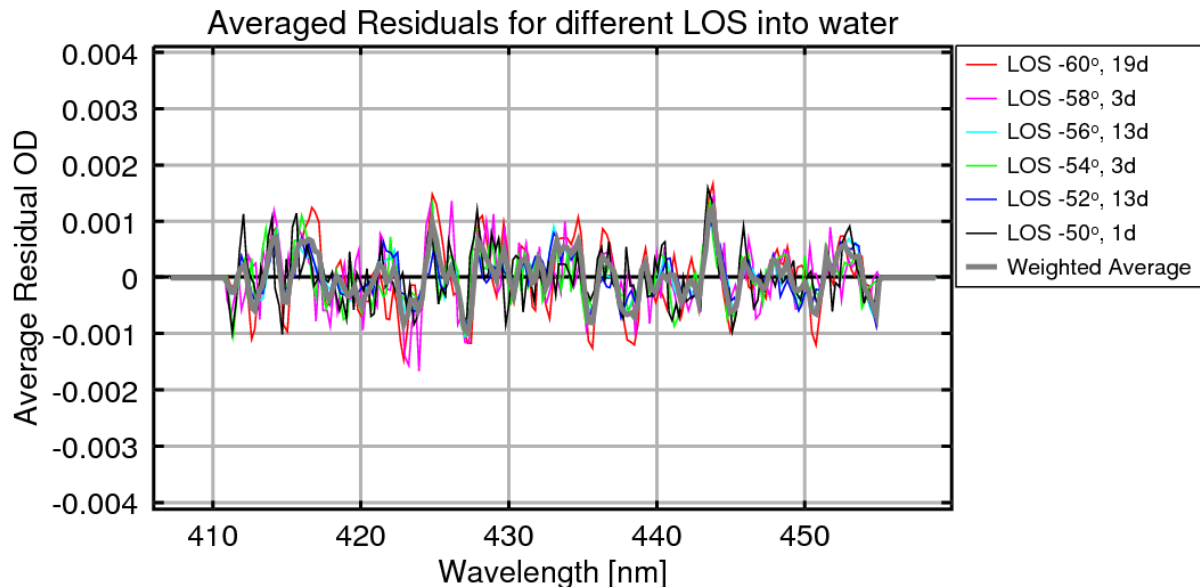

Figure 6.7: Averaged residual spectra for different LOS (shown in different colours) from the measurements taken during ship station. The weighted average over all LOS is shown in grey.

The extracted residual spectrum exhibits fairly high frequent structures. Presently, it is not possible to clearly link these detected systematic structures with a certain physical or other process. Considering the input data (Fig. 6.7), it becomes clear that apart from the systematic features,

which are common to all residual spectra, also other, less specific peaks and structures exist. In these other regions, the differences between the individual measurements are more apparent and certainly, there is some remaining noise in the results. So also the averaged residual spectrum, assigned to the mixed water effect here, contains some yet undefined amount of noise, instrumental effects and retrieval related features, which cannot be removed from a finite set of measurements recorded under varying atmospheric conditions.

It would be interesting and insightful to determine the origin of each of the detected persistent features, but the similarity to known spectral effects like the VRS or the absorption by chlorophyll is not evident. The correlation coefficient in this wavelength region between the VRS spectrum and the retrieved water effect yields a value of $c = 0.05$, i.e. the two spectra are nearly linearly independent. A clear attribution is not possible on the basis of the current knowledge.

Certainly, it is necessary to find out, if a main portion of these extracted structures really is connected to processes happening in the ocean water and are not of, e.g., instrumental origin. This means especially, that the structures should appear only in the water viewing LOS and not in the zenith direction for example. This is investigated in the next section.

Fit factors of the mixed water effect

A confirmation is needed that a substantial part of the extracted average residual is really caused by mixed effects in the ocean water. The extracted water effect can be included in a further DOAS fit to find out how much of these water effect features is found in which of the available viewing angles. The absolute value of the fit factor is expected to be large for angles that view into the water and close to zero for angles viewing into the atmosphere. The extracted residual is now included in a DOAS fit in exactly that spectral form as shown in Fig. 6.7. That means, that absorption lines appear as minima in this reference spectrum. This is exactly contrary to the algebraic sign of absorption cross sections, where absorption lines appear as positive peaks. Therefore, the fit factor will be negative here in case the structures of the declared water effect are detected. Consistently, the same DOAS fit settings are chosen as before in the wavelength region from 411 to 455 nm.

The DOAS retrieval of the mixed water effect is now performed for the measurements of the entire campaign. In Fig. 6.8, an example fit result is shown, with the scaled water effect spectrum (black) and the fit from the actual measurement containing the remaining residual (in red). The (dimensionless) fit factor for this example fit is -1.01±0.10, implying a detection of the water effect, i.e. with correct algebraic sign. The stronger features from the water effect spectrum are well visible in the measurement (Fig. 6.8). Additional noise and unassigned structures are apparent also, as the curve shown in red is an individual measurement.

Now the fit results shall be analysed further by examining how the water effect fit factor depends on the viewing angle. The results of several days of measurements are combined in Fig. 6.9. The respective fit factors for the mixed water effect are plotted versus the line of sight, first of all only for angles towards the water. In the -2°-direction, a large variability can be seen. In this direction, measurements were recorded throughout the day, so that several different conditions are combined here. The average fit factor resulting at -2°-direction is 0.17, but the scatter amounts to ±0.43, which is substantially larger.
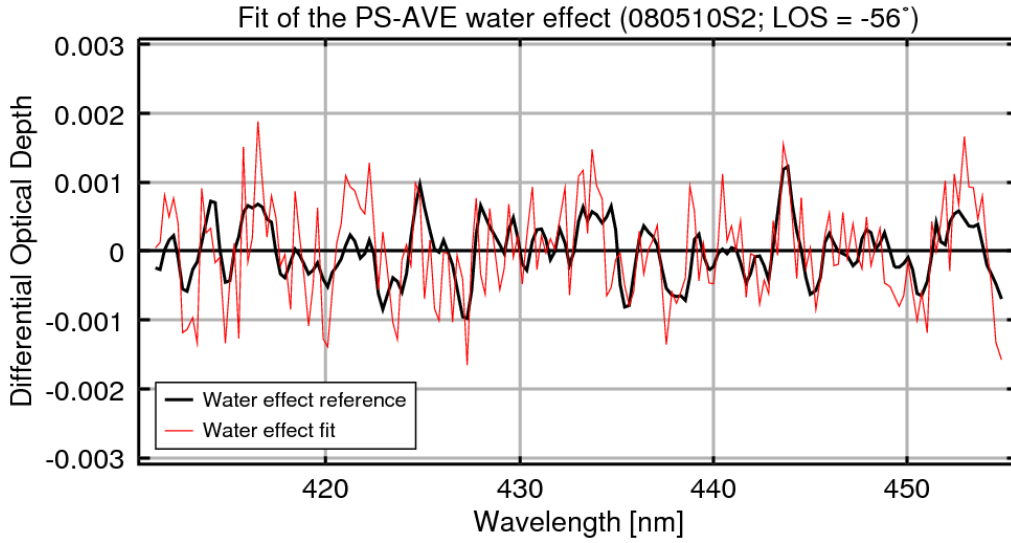
Figure 6.8: Fit result showing an example retrieval of the water effect from one Polarstern measurement on May 10$^{\text{th}}$. The black curve is the scaled water effect as it was extracted from the residuals. The measurement fit result containing the actual residual is plotted in red.

The expected values for positive LOS (above the water) are close to zero, while small deviations from zero can be understood because also at viewing directions above water, parts of the water leaving radiance may be scattered towards the instrument. For May 1st 2008, the retrievals in zenith-sky direction, e.g., yield an average value of the water effect fit factor of -0.30±0.38. This value is still compatible with an average of zero, but also exhibits a large variability. This large variability is mostly due to a substantial noise portion still present in the extracted water effect spectrum. Additionally, the water effect was extracted from spectra recorded at quite different meteorological conditions. It is not possible to further homogenise the evaluation as the data set is already rather restricted. Nevertheless, the retrievals show the correct tendency and behaviour with values around zero at viewing directions above the water and negative fit factors for the low angles.

The fit of a linear function to the water effect fit factor (WEFF) with respect to LOS, based on the data in Fig. 6.9, results in the following dependency:

$$\text{WEFF} \ = \ (0.023 \pm 0.005)/^\circ \ \cdot \ \text{LOS} \ + \ (0.138 \ \pm \ 0.080)$$

Although the data basis is rather small, the expected behaviour is revealed. A strongly negative WEFF would be retrieved for direct downward viewing (i.e. the calculated WEFF at LOS = -90°) as the water path would be long. Considering that the water effect spectrum was retrieved at viewing angles between -60° and -48°, for which the fit factor should be around -1, a fit factor of WEFF(-90°) $= -1.93 \ \pm \ 0.54$ seems reasonable for downward viewing into the water. Calculating from this the intercept with the x-axis LOS$_0$, giving the LOS where the water effect fit factor is zero, a value of LOS$_0$ =-6.0°$^{+3.9°}_{-6.1°}$ is obtained. This interval does not contain the horizon, but is
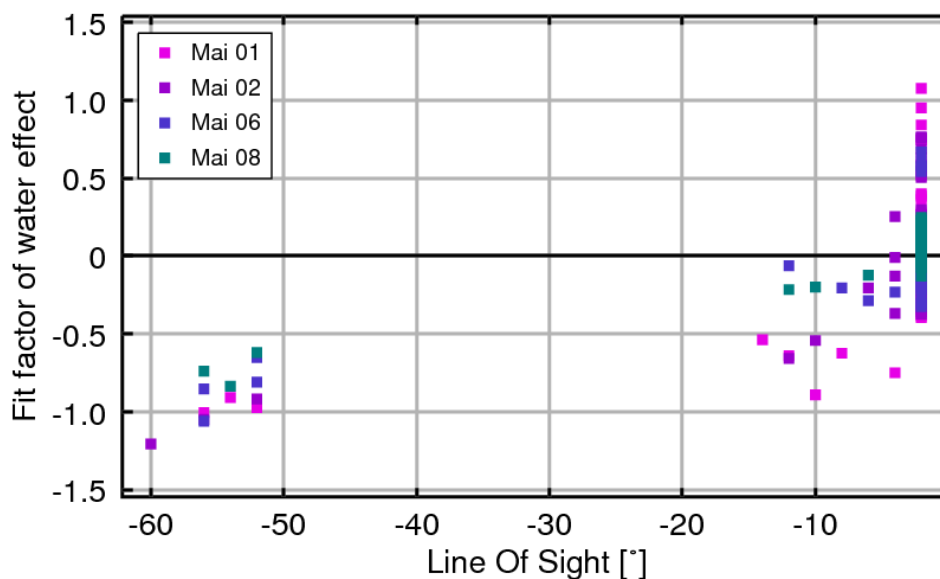
Figure 6.9: Fit factors of the extracted mixed water effect for different lines of sight. For the low angles viewing into water values around -1 are retrieved indicating that the mixed water effect has been detected in these cases. Variabilities of the fit factor, especially for a LOS of -2°, are very large.

very close to the 0° direction, and rather large uncertainty ranges are obtained due to the discussed reasons.

6.5 Retrieval of the water effect in satellite data

The main objective of the analysis of the water effect is the improvement of certain satellite retrievals including the IO retrieval. For this purpose, it needs to be possible to retrieve fit factors for the extracted mixed water effect from satellite data. If the declared water effect actually originates from light passing through ocean water and if the effect is strong enough to be perceivable in the satellite measurements also, it should be possible to distinguish clear ocean regions from turbid areas and land in the satellite observations.

First of all, the water effect is included in the standard IO retrieval for SCIAMACHY observations. All other parameters are kept unaltered, only the new spectrum is considered additionally. The resulting fit factor can then be plotted on a global map. As an example, the retrieval result for a three month period is shown in Fig. 6.11(a).

The same principle can be applied for the detection of the water effect in other satellite observations. In another test, the declared water effect spectrum is included in a fit optimised for the retrieval of NO_2 from the satellite sensor GOME-2 (cp. Sec. 1.9.3). Fig. 6.11(b) contains the resulting fit factor from this analysis, averaged for one month (September 2008).

In both retrievals, the pattern of deep and clear water areas is properly identified. Especially the
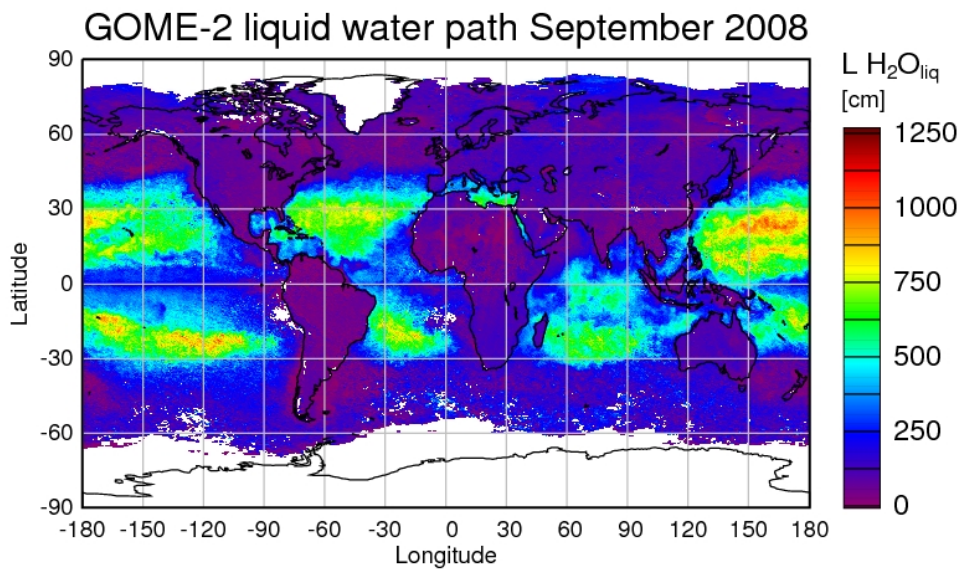
Figure 6.10: Map showing the colour coded fit factor of liquid water absorption as retrieved from GOME-2 observations. The fit factor denotes the effective liquid water path (L H$_2$O$_{liq}$) the photons take on average. The retrieved values are averaged for one month (September 2008). Deep and clear ocean regions (green - red) can be distinguished from turbid waters (e.g. due to biological activity) and land masses (blue and purple). The GOME-2 data for this map have been kindly provided by Andreas Richter, IUP Bremen.

algebraic sign is also correct, as the negative sign (blue colour) implies the detection of the water effect. Fit factors with negative sign are found over the deep and clear ocean regions. When comparing the results of the water effect and the liquid water path from satellite (Fig. 6.10) the agreement of the pattern is well recognizable.

So far, the analysis has been successful. Unfortunately, including the water effect in the satellite retrieval does not improve the trace gas products under investigation. The IO retrieval which suffers from negative trace gas amounts retrieved over the clear ocean regions, still exhibits the same results even after including the correction spectrum in the satellite retrieval.

As the above analysis yields promising results in capturing the water effect in the water viewing directions from the ship measurements as well as the deep ocean pattern from the satellite measurements, the overall concept seems to be suitable for gaining information about the influence of ocean water on the observed light spectra. Nevertheless, the satellite retrievals could not be improved up to now. A larger data set from the ship borne measurements would maybe improve the situation as the quality of the correction spectrum is not very high. Possibly, the remaining scattering and some residual features not related to water influences inhibit a perceptible improvement of satellite retrievals.
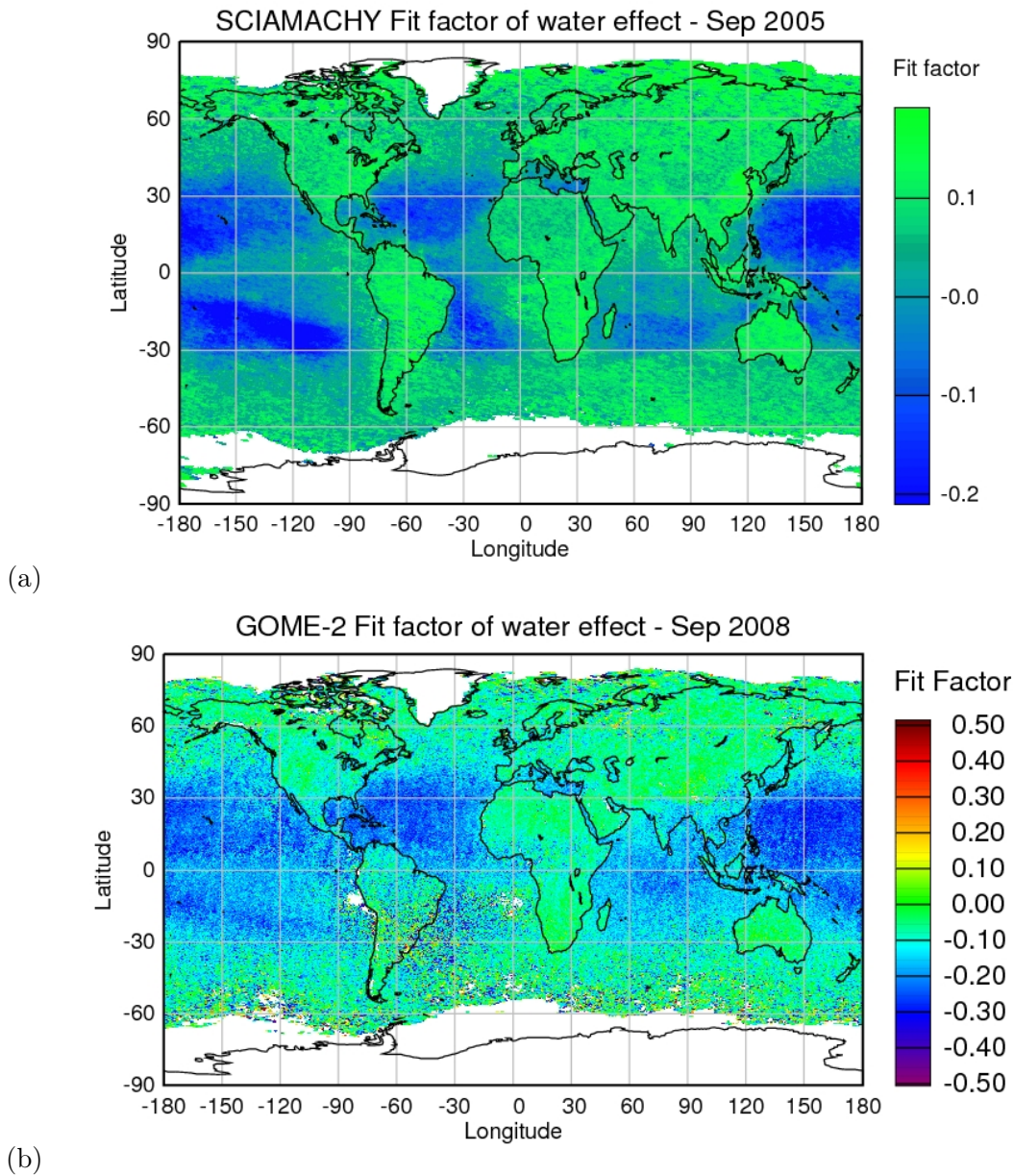
(a)

(b)

Figure 6.11: The fit factor of the water effect as retrieved from SCIAMACHY (a) and from GOME-2 (b) observations. For (a), the values are averaged over three months from September to November 2005, and for (b) the data from September 2008 were used. Negative fit factors denote a detection of the water effect spectrum and therefore imply that the light has passed though ocean water prior to detection. It is important to note the similarity in the pattern as compared to Fig. 6.10. The GOME-2 data for (b) have been kindly provided by Andreas Richter, IUP Bremen.

7 Summary and Conclusions

In the present study, atmospheric columns of iodine monoxide, IO, have been retrieved by absorption spectroscopy on the basis of radiance spectra recorded by the SCIAMACHY sensor. With the successful development of this new scientific trace gas product, the investigation of IO amounts and their spatial and temporal distributions has become possible on a nearly global scale. Through the work presented in this thesis, progress has been achieved in the following aspects:

Enabling the retrieval of IO from SCIAMACHY
The retrieval of IO from the SCIAMACHY sensor has been developed within this study using of the well-established DOAS (Differential Optical Absorption Spectroscopy) technique. Following thorough quality and consistency investigations, the IO standard fit has been defined on the basis of the best results from these tests. The identification of the IO absorption and the determination of column amounts from satellite have thus become possible. Residuals close to the theoretical limits were achieved. An example retrieval, which covers the problematic spectral position of the Fraunhofer G-band and does not fulfill the quality and consistency requirements, demonstrates the generation of some misleading results. The instrument's detection limit for the retrieval of IO has been determined and shows that this limit lies close to the IO amounts previously observed by ground-based instruments. The IO absorption signal may therefore easily be hidden in the instrument noise. The detection limit for a single measurement lies on the order of 7×10^{12} molec/cm^2, however, this limit is considerably reduced by temporal averaging. Seasonal maps exhibit a typical detection limit of 1×10^{12} molec/cm^2. For combined statistical and systematic inaccuracies, an overall error estimate of 3×10^{12} molec/cm^2 is determined. The sensitivity of the measurement method for detection of IO under varying conditions has been assessed through radiative transfer calculations. In comparison to ocean sites, the sensitivity strongly increases for locations over bright surfaces, such as Polar sea ice regions. Over clear ocean regions, the retrieval of IO from SCIAMACHY encounters the same anomaly as some other minor trace gases in that column amounts tend to negative values. A suitable correction procedure still needs to be established.

Global observations of IO columns with a focus on the Antarctic
The newly developed IO product from SCIAMACHY measurements has enabled the investigation of the IO global distribution for the first time. Some regions of special interest have been selected for more detailed analysis and a main focus is set on the Antarctic region.
The Antarctic exhibits the largest widespread IO slant columns globally. In the South Polar region, detailed variations of the IO amounts in space and time have been uncovered. The largest IO amounts in the seasonal averages typically amount to 8×10^{12} molec/cm^2, while some single measurements reach up to 2×10^{13} molec/cm^2. Enhanced IO is found along the Antarctic coast, above

ice shelves and regions covered by sea ice, as well as over parts of the continent. Largest amounts appear mostly in spring time, but the seasonal cycle varies with location. Some similarities are present between the IO results and bromine oxide distributions. BrO also shows highest amounts for Antarctic spring time, however the spatial and temporal details reveal considerable differences. Above sea ice regions around the Antarctic continent, where BrO is enhanced between August and October, IO is found mainly later in the year around November. A second increase in spatial extent of enhanced IO amounts around March is also not reflected in the BrO columns. The revealed differences in the spatial and temporal evolutions of the two trace gases strongly argue for separate release pathways. While an inorganic mechanism is probably dominating for BrO, new evidence is added here for the suggestion of mainly biological sources for IO precursors. Sea ice concentration is reduced in later spring as compared to early spring time, so that emissions of biogenic halogen compounds are facilitated by phytoplankton situated below the sea ice.

From the satellite observations it becomes clear that the Northern and Southern Hemispheres exhibit a considerable difference in IO distributions. No wide spread significant IO amounts are detected in the Arctic Region, especially not in Arctic spring. This constitutes a further differences between atmospheric IO and BrO, as BrO amounts are equally large and widespread over the North Polar spring as in the South. Along some Northern Hemispheric coast lines, enhanced IO columns around 4×10^{12} molec/cm^2 are identified in strongly confined areas. Alignment of the specific coast lines with the satellite ground pixels possibly enhances the detection sensitivity at these locations as compared to other coasts where the geometry is less favourable and potential IO might be concealed. The large difference in IO distribution between the two hemispheres is surprising and so far not fully explained, but different biological conditions on the two hemispheres may be an important aspect.

Enhanced IO has been detected above the Eastern Pacific, where no IO measurements had been reported before. Concentrations of diatoms are increased in this region which stands in connection to the upwelling ocean current there. Diatoms produce and emit iodocarbons, and provide a possible explanation for the formation of IO in that area. Enhanced IO is not observed in other strong upwelling regions, where diatom concentrations are smaller, so the connection to specific types of phytoplankton is probably crucial.

Results from comparison and validation studies

Comparisons with independent measurement data sets of IO have been conducted for validation purposes. Some successful validation studies add confidence to the newly developed IO product. Ground-based LP-DOAS observations in Halley Research Station, Antarctica, reveal a seasonal evolution which is in good agreement with the IO results from satellite extracted above this station. The surface mixing ratios derived from the two different data sets agree well especially when considering the involved uncertainties. A similar conclusion is drawn from a comparison with ground-based data from a Bremen MAX-DOAS instrument at Ny-Ålesund, Spitsbergen, which is promising as an IO concentration in the same order of magnitude of is retrieved from the ground and from satellite. The only independent study of IO from satellite has analysed SCIAMACHY measurements for four individual days above the Southern Hemisphere. The reported IO columns are considerably differ-

ent from the results retrieved in the present work. Using a retrieval version tested within this thesis, their results could be reproduced with smaller amounts but with the same spatial pattern, which in the present case coincides with low fit quality. As a consequence, the differences are respected, but should not result in a loss of confidence in the outcome of the present study.

The dependency of IO amounts on high and low tide at mid-latitude coasts has been investigated from satellite for specific mid-latitude coastal locations. However, neither enhanced IO amounts nor the tidal signal is apparent in the satellite results, most probably due to low IO amounts compared to the instrumental detection limit, strongly localised sources and unfavourable observational conditions.

Results from atmospheric chemistry modelling studies

The CAABA/MECCA chemical box model has been applied for Antarctic case studies. For varying precursor fluxes, the IO surface concentrations have been determined. Using reported emission measurements, IO amounts on the same order of magnitude as observed from satellite can be reproduced, but remain rather on the low side even for the highest reported precursor fluxes. No precursor fluxes are available for those regions with largest satellite IO columns though. In agreement with expectations, the emissions of poly-halogenated carbons are crucial for the production of sufficient IO amounts. In future studies, some additional chemical reaction pathways will be included into the chemical mechanism, e.g., some recycling of gaseous iodine from the particulate phase, and also the photolysis of OIO.

Prospects for future studies

- The time series of the present standard IO product will be further extended for the still ongoing measurements of SCIAMACHY, increasing the IO data base. Further validation and comparison studies using independent data sets shall cover additional locations, e.g., for the Eastern Pacific where recent campaigns reveal enhanced IO amounts from ship-borne instrumentation.

- Further improvements on the satellite data from SCIAMACHY may become possible if the fitting window may be extended beyond the 431 nm region to include more absorption bands of the IO spectrum. For that, better understanding and compensation of the spectral characteristics of atmospheric radiation and of the instrument's response and polarisation sensitivity is required.

- Data from additional satellite instruments may be helpful in adding even more information about the atmospheric IO content. Especially, IO retrievals from GOME-2 would be an interesting product as the spatial coverage is better than for SCIAMACHY. It is not known yet if the signal-to-noise quality of GOME-2 will suffice for the retrieval of such a minor trace gas as IO. For a deeper insight into certain regions and even daily variations, a spectrometer on a geostationary satellite would make an improvement as the data amount per ground location is strongly enhanced. Of course this will not yield global coverage, and is a prospect for the more distant future.

- In order to better quantify the observed IO columns, especially in terms of surface concentrations, detailed information on the IO profile is needed. This information enters the air mass

factor calculation as well as the transformation from a vertical column into a mixing ratio. Currently, however, the uncertainty on the IO altitude profile is large, so that further field measurements are crucial.

- For improved interpretation possibilities of the IO observations, a larger basis of precursor flux measurements in source regions is needed as well as local measurements of IO in specific regions, e.g., within the Antarctic sea ice zone or on the Antarctic continent, in biologically active ocean areas and at coastal sites, preferably over a longer period of time than the typical campaign basis to also assess the seasonal behaviour.

- Some investigated aspects in the present study have remained below the detection limit of the Sciamachy sensor partly due to the comparatively large ground pixel. On the other hand, local ground based measurements are restricted in spatial coverage. This gap may be closed in the future by applying airborne measurements. For specific research tasks, the construction of a new instrument is currently ongoing, which is scheduled for observations from an aircraft platform. The planning and optical testing of a DOAS system based on an imaging spectrometer is proceeding, and the possibility of a custom-built spectrometer using a holographic reflection grating is assessed. The construction with a large opening angle (small F-number) and a reduced number of optical elements is expected to yield good spatial coverage and strong light throughput. With this instrument and the measurement concept of a small and low flying aircraft, a fine ground spatial resolution will be achieved, which provides promising conditions for the measurement of localised IO abundances. More detailed observations of the spatial IO distribution, e.g., along coast lines in the mid-latitudes as well as the detection of localised IO source regions and source strengths will become possible with this instrument.

List of abbreviations

AMSR-E	Advanced Microwave Scanning Radiometer for EOS
ASM	Azimuth Scan Mechanisms/Mirror
CAABA	Chemistry As A Boxmodel Application
CFC	Chloro-Fluoro-Carbons
DOAS	Differential Optical Absorption Spectroscopy
EOS	Earth Observing System
ESA	European Space Agency
ESM	Elevation Scan Mechanisms/Mirror
ESM	Earth System Model (Chapter 5)
GCM	Global Circulation Model
GOME-2	Global Ozone Monitoring Instrument-2
HITRAN	HIgh-resolution TRANsmission molecular absorption database
IVOC	Iodinated Volatile Organic Compound
KPP	Kinetic Pre-Processor
LOS	Line Of Sight
LP-DOAS	Long-Path DOAS
MAX-DOAS	Multi-AXis DOAS
MECCA	Module Efficiently Calculating the Chemistry of the Atmosphere
MBL	Marine Boundary Layer
NASA	National Aeronautics and Space Administration
NRT	Near Real-Time
ODE	Ozone Depletion Event
ODE	Ordinary Differential Equation (Chapter 5)
OMI	Ozone Monitoring Instrument
PET	Pixel Exposure Time
RRS	Rotational Raman Scattering
SCIAMACHY	SCanning Imaging Absorption spectroMeter for Atmospheric CHartographY
SeaWIFS	Sea-viewing WIde Field-Of-view Sensor
SPICS	SCIAMACHY-PMD based Identification and classification of Clouds and Surfaces
SZA	Solar Zenith Angle
VHOC	Volatile Halogenated Organic Compound
VOC	Volatile Organic Compound
VOI	Volatile Organic Iodine
VRS	Vibrational Raman Scattering
VSLS	Very Short-Lived Species

Bibliography

Alicke, B., Hebestreit, K., Stutz, J., and Platt, U.: Iodine oxide in the marine boundary layer, Nature, 397, 572–573, 1999.

Allan, B. J., McFiggans, G., Plane, J. M. C., and Coe, H.: Observations of iodine monoxide in the remote marine boundary layer, J. Geophys. Res., 105, 14 363–14 369, 2000.

Allan, B. J., Plane, J. M. C., and McFiggans, G.: Observations of OIO in the remote marine boundary layer, Geophys. Res. Lett., 28, 1945–1948, 2001.

Alvain, S., Moulin, C., Dandonneau, Y., and Bréon, F.: Remote sensing of phytoplankton groups in case 1 waters from global seawifs imagery, Deep Sea Research, I 52, 1989–2004, 2005.

Amachi, S., Kamagata, Y., Kanagawa, T., and Maramatsu, Y.: Bacteria mediate methylation of iodine in marine and terrestrial environments, Appl. Env. Microbiol., 67, 2718–2722, 2001.

Andreae, M. O., Atlas, E., Harris, G. W., Helas, G., de Kock, A., Koppmann, R., Maenhaut, W., Manø, S., Pollock, W. H., Rudolph, J., Scharffe, D., Schebeske, G., and M., W.: Methyl halide emissions from savanna fires in southern africa, Journal of Geophysical Research, 101, 23 603–23 613, 1996.

Atkinson, R., Baulch, D. L., Cox, R. A., Crowley, J. N., Hampson, R. F., Hynes, R. G., Jenkin, M. E., Rossi, M. J., and Troe, J.: Evaluated kinetic and photochemical data for atmospheric chemistry: Volume I - gas phase reactions of O_x, HO_x, NO_x and SO_x species, Atmospheric Chemistry and Physics, 4, 1461–1738, 2004.

Atkinson, R., Baulch, D. L., Cox, R. A., Crowley, J. N., Hampson, R. F., Hynes, R. G., Jenkin, M. E., Rossi, M. J., Troe, J., and Subcommittee, I.: Evaluated kinetic and photochemical data for atmospheric chemistry: Volume II - gas phase reactions of organic species, Atmospheric Chemistry and Physics, 6, 3625–4055, 2006.

Barrie, L. A., Bottenheim, J. W., Schnell, R. C., Crutzen, P. J., and Rasmussen, R. A.: Ozone destruction and photochemical reactions at polar sunrise in the lower Arctic atmosphere, Nature, 334, 138–141, 1988.

Bates, T. S., Lamb, B. K., Guenther, A., Dignon, J., and Stoiber, R. E.: Sulfur emissions to the atmosphere from natural sources, Journal of Atmospheric Chemistry, 14, 315–337, 1992.

Begoin, M., Richter, A., Kaleschke, L., Tian-Kunze, X., Stohl, A., and Burrows, J. P.: Satellite observations of long range transport of a large BrO cloud in the Arctic, Atmospheric Chemistry and Physics, submitted August, 2009.

Bloss, W. J., Rowley, D. M., Cox, R. A., and Jones, R. L.: Kinetics and products of the IO self-reaction, J. Phys. Chem. A, 105, 7840–7854, 2001.

Bloss, W. J., Lee, J. D., Johnson, G. P., Sommariva, R., Heard, D. E., Saiz-Lopez, A., McFiggans, G., Coe, H., Flynn, M., Williams, P., Rickard, A. R., and Fleming, Z. L.: Impact of halogen monoxide chemistry upon boundary layer OH and HO_2 concentrations at a coastal site, Geophysical Research Letters, 32, L06 814, doi:10.1029/2004GL022084, 2005.

Bobrowski, N., Hönninger, G., Galle, B., and Platt, U.: Detection of bromine monoxide in a volcanic plume, Nature, 423, 273–276, doi:10.1038/nature01625, 2003.

Bogumil, K., Orphal, J., Homann, T., Voigt, S., Spietz, P., Fleischmann, O. C., Vogel, A., Hartmann, M., Bovensmann, H., Frerik, J., and Burrows, J. P.: Measurements of molecular absorption spectra with the sciamachy pre-flight model: Instrument characterization and reference data for atmospheric remote-sensing in the 230-2380 nm region, J. Photochem. Photobiol. A, 157, 2003.

Bovensmann, H., Burrows, J. P., Buchwitz, M., Frerick, J., Noël, S., Rozanov, V. V., Chance, K. V., and Goede, A. P. H.: Sciamachy: Mission objectives and measurement modes, J. Atmos. Sci., 56, 127–150, 1999.

Bracher, A., Vountas, M., Dinter, T., Burrows, J. P., Röttgers, R., and Peeken, I.: Quantitative observation of cyanobacteria and diatoms from space using phytodoas on sciamachy data, Biogeosciences, 6, 751–764, 2009.

Brasseur, G. P., Orlando, J. J., and Tyndall, G. S.: Atmosospheric Chemistry and Global Change, Oxford University Press, 1999.

Brewer, A. W., McElroy, C. T., and Kerr, J. B.: Nitrogen dioxide concentrations in the atmosphere, Nature, 246, 129–133, 1973.

Brinkmann, R.: Rotational raman scattering in planetary atmospheres, Astrophysical Journal, 154, 1087–1093, 1968.

Bösch, H., Camy-Peyret, C., Chipperfield, M. P., Fitzenberger, R., Harder, H., Platt, U., and Pfeilsticker, K.: Upper limits of stratospheric IO and OIO inferred from center-to-limb-darkening-corrected balloon-borne solar occultation visible spectra: Implications for total gaseous iodine and stratospheric ozone, J. Geophys. Res., 108, doi:10.1029/2002JD003078, 2003.

Burrows, J. P., Hölzle, E., Goede, A. P. H., Visser, H., , and Fricke, W.: Sciamachy - scanning imaging absorption spectrometer for atmospheric chartography, Acta Astronautica, 35, 445–451, 1995.

Burrows, J. P., Dehn, A., Deters, B., Himmelmann, S., Richter, A., Voigt, S., and Orphal, J.: Atmospheric remote sensing reference data from gome: Part 1 temperature dependent absorption cross-sections of no2 in the 231-794 nm range, Journal of Quantitative Spectroscopy and Radiative Transfer, 60, 1025–1031, 1998.

Burrows, J. P., Richter, A., Dehn, A., Deters, B., Himmelmann, S., Voigt, S., and Orphal, J.: Atmospheric remote-sensing reference data from gome: Part 2. temperature-dependent absorption cross sections of o3 in the 231-794 nm range, Journal of Quantitative Spectroscopy and Radiative Transfer, 61, 509 – 517, doi:10.1016/S0022-4073(98)00037-5, 1999a.

Burrows, J. P., Weber, M., Buchwitz, M., Rozanov, V. V., Ladstätter-Weißenmayer, A., Richter, A., DeBeek, R., Hoogen, R., Bramstedt, K., and Eichmann, K. U.: The global ozone monitoring experiment (gome): Mission concept and first scientific results, J. Atmos. Sc., 56, 151–175, 1999b.

Butz, A., Bösch, H., Camy-Peyret, C., Chipperfield, M. P., Dorf, M., Kreycy, S., Kritten, L., Prados-Román, C., Schwärzle, J., and Pfeilsticker, K.: Constraints on inorganic gaseous iodine in the tropical upper troposphere and stratosphere inferred from balloon-borne solar occultation observations, Atmospheric Chemistry and Physics Discussions, 9, 14 645–14 681, 2009.

Carpenter, L.: (as editor) Interactive comment on "A mechanism for biologically-induced iodine emissions from sea-ice" by A. Saiz-Lopez and C. S. Boxe, Atmospheric Chemistry and Physics, 8, S1316–S1316, 2008.

Carpenter, L. J., Sturges, W. T., Penkett, S. A., Liss, P. S., Alicke, B., Hebestreit, K., and Platt, U.: Short-lived alkyl iodides and bromides at Mace Head, Ireland: Links to biogenic sources and halogen oxide production, J. Geophys. Res., 104, 1679–1689, 1999.

Carpenter, L. J., Hebestreit, K., Platt, U., , and Liss, P. S.: Coastal zone production of IO precursors: a 2-dimensional study, Atmos. Chem. Phys., 1, 9–18, 2001.

Carpenter, L. J., Hopkins, J. R., Jones, C. E., Lewis, A. C., Parthipan, R., Wevill, D. J., Poissant, L., Pilote, M., and Constant, P.: Abiotic source of reactive organic halogens in the sub-arctic atmosphere?, Environ. Sci. Technol., 39, 8812–8816, 2005.

Carpenter, L. J., Wevill, D. J., Palmer, C. J., and Michels, J.: Depth profiles of volatile iodine and bromine-containing halocarbons in coastal antarctic waters, Marine Chemistry, 103, 227–236, 2007.

Chamberlain, A. C.: Deposition of iodine-131 in northern england in october 1957, Quart. J. Roy. Met. Soc., 85, 350–361, 1960.

Chamberlain, A. C., Eggleton, A. E. J., Megaw, W. J., and Morris, J. B.: Behaviour of iodine vapour in air, Disc. Faraday Soc., 30, 162–169, 1960.

Chameides, W. L. and Davis, D. D.: Iodine: its possible role in tropospheric chemistry, J. Geophys. Res., 85, 7383–7398, 1980.

Chance, K.: Analysis of BrO measurements from the Global Ozone Monitoring Experiment, Geophys. Res. Lett., 25, 3335–3338, 1998.

Chapman, S.: A theory of the upper-atmosphere ozone, Mem. Roy. Meteorol. Soc., 3, 103, 1930.

Charlson, R. J., Lovelock, J. E., Andreae, M. O., and Warren, S. G.: Oceanic phytoplankton, atmospheric sulfur, cloud albedo and climate, Nature, 326, 655–661, 1987.

Chatfield, R. B. and Crutzen, P. J.: Are there interactions of iodine and sulfur species in marine air photochemistry?, J. Geophys. Res., 95, 22 319–22 341, 1990.

Chubachi, S.: Preliminary result of ozone observations at Syowa station from February 1982 to January 1983, Mem. Natl. Inst. Polar Res. [Spec. Issue Jpn. 34], pp. 13–19, 1984.

Cox, R. A. and Coker, G. B.: Absorption cross section and kinetics of io in the photolysis of CH_3I in the presence of ozone, J. Phys. Chem., 87, 4478–4484, 1983.

Cox, R. A., Bloss, W. J., Jones, R. L., and Rowley, D. M.: OIO and the atmospheric cycle of iodine, Geophys. Res. Lett., 26, 1857–1860, 1999.

Damian, V., Sandu, A., Damian, M., Potra, F., and Carmichael, G.: The kinetic preprocessor kpp – a software environment for solving chemical kinetics, Computers and Chemical Engineering, 26, 1567–1579, 2002.

Davis, D., Crawford, J., Liu, S., McKeen, S., Bandy, A., Thornton, D., Rowland, F. S., and Blake, D.: Potential impact of iodine on tropospheric levels of ozone and other critical oxidants, Journal of Geophysical Research, 101D, 2135–2147, 1996.

de Beek, R., Vountas, M., Rozanov, V., Richter, A., and Burrows, J.: The ring effect in the cloudy atmosphere, Geophys. Res. Lett., 28(4), 721–724, 2001.

Demtröder, W.: Experimentalphysik Bd. 3 - Atome, Moleküle und Festkörper, Springer, 2nd edition, 2000.

Dickerson, R. R., Rhoads, K. P., Carsey, T. P., Oltmans, S. J., Crutzen, P. J., and Burrows, J. P.: Ozone in the remote marine boundary layer: a possible role for halogens, J. Geophys. Res, 104, doi:10.1029/1999JD900023, 1999.

Duce, R., Wasson, J. T., Winchester, J. W., and Burns, F.: Atmospheric iodine, bromine and chlorine, J. Geophys. Res, 68, 3943–3947, 1963.

European Parliament: Directive 2002/3/EC of the European Parliament and of the Council of 12 February 2002 relating to ozone in ambient air, Official Journal of the European Communities, 2002.

Farman, J. C., Gardiner, B. G., and Shanklin, J. D.: Large losses of total ozone in Antarctica reveal seasonal ClO_x/NO_x interaction, Nature, 315, 207–210, 1985.

Fleischmann, O. C., Hartmann, M., Burrows, J. P., and Orphal, J.: New ultraviolet absorption cross-sections of BrO at atmospheric temperatures measured by a time-windowing fourier transform spectroscopy, J. Photochem. Photobiol. A., 168, 117–132, 2004.

Francis, P., Burton, M. R., and Oppenheimer, C.: Remote measurements of volcanic gas compositions by solar occultation spectroscopy, Nature, 396, 567–270, doi:10.1038/25115, 1998.

Friess, U., Wagner, T., Pundt, I., Pfeilsticker, K., and Platt, U.: Spectroscopic measurements of tropospheric iodine oxide at neumeyer station, antarctica, Geophys. Res. Lett., 28, doi:10.1029/2003JD004133, 2001.

Giese, B., L. F. A. F. C. and Wiencke, C.: Release of volatile iodinated c1-c4 hydrocarbons by marine macroalgae from various climate zones, Environmental Science and Technology, 33, 2432–2439, 1999.

Gómez Martín, J. C., Spietz, P., and Burrows, J. P.: Spectroscopic studies of the i_2/o_3 photochemistry part 1: Determination of the absolute absorption cross sections of iodine oxides of atmospheric relevance, J. Photochem. Photobiol. A, 176, 15–38, doi:10.1016/j.jphotochem.2005.09.024, 2005.

Gómez Martín, J. C., Spietz, P., and Burrows, J. P.: Kinetic and mechanistic studies of the i_2/o_3 photochemistry, J. Phys. Chem. A., 111, doi:10.1021/jp061186c, 2007.

Gómez Martín, J. C., Ashworth, S. H., Mahajan, A. S., and Plane, J. C. M.: Photochemistry of OIO: Laboratory study and atmospheric implications, Geophys. Res. Lett., 36, L09 802, doi:10.1029/2009GL037642, 2009.

Gottwald, M., Bovensmann, H., Lichtenberg, G., Noel, S., von Bargen, A., Slijkhuis, S., Piters, A., Hoogeveen, R., von Savigny, C., Buchwitz, M., Kokhanovsky, A., Richter, A., Rozanov, A., Holzer-Popp, T., Bramstedt, K., Lambert, J.-C., Skupin, J., Wittrock, F., Schrijver, H., and Burrows, J. P., eds.: SCIA-MACHY, Monitoring the changing Earth's atmosphere, DLR, Institut für Methodik der Fernerkundung (IMF), 2006.

Grainger, J. F. and Ring, J.: Anomalous fraunhofer line profiles, Nature, 193, 762, 1962.

Greenblatt, G. D., Orlando, J. J., Burkholder, J. B., and Ravishankara, A. R.: Absorption measurements of oxygen between 330 and 1140 nm, J. Geophys. Res., 95(D11), 18 577–18 582, 1990.

Hecht, E.: Optik, Oldenbourg Verlag, 3 edn., 2001.

Heckel, A., Richter, A., Tarsu, T., Wittrock, F., Hak, C., Pundt, I., Junkermann, W., and Burrows, J. P.: Max-doas measurements of formaldehyde in the po-valley, Atmospheric Chemistry and Physics, 5, 909–918, 2005.

Hill, V. L. and Manley, S. L.: Release of reactive bromine and iodine from diatoms and its possible role in halogen transfer in polar and tropical oceans, Limnol. Oceanogr., 54, 812–822, 2009.

Hönninger, G., Leser, H., Sebastián, O., and Platt, U.: Ground-based measurements of halogen oxides at the Hudson Bay by active longpath DOAS and passive MAX-DOAS, Geophys. Res. Lett, 31, doi:10.1029/2003GL018982, 2004.

Hooker, S., Esaias, W., Feldman, G., Gregg, W., and McClain, C.: An Overview of SeaWiFS and Ocean Color, NASA Tech. Memo. 104566, Vol. 1, S.B. Hooker and E.R. Firestone, Eds., NASA Goddard Space Flight Center, Greenbelt, Maryland, 24 pp., plus color plates, 1992.

IPCC: Climate Change 2007: The Physical Science Basis. Contribution of Working Group I to the Fourth Assessment Report of the Intergovernmental Panel on Climate Change. Solomon, S., and Qin, D., and Manning, M., and Chen, Z., and Marquis, M., and Averyt, K. B., and Tignor, M., and Miller, H. L. (eds.), Cambridge University Press, 2007.

Jöckel, P., Sander, R., Kerkweg, A., Tost, H., and Lelieveld, J.: Technical note: The modular earth submodel system (messy) - a new approach towards earth system modeling, Atmos. Chem. Phys., 5, 433–444, 2005.

Jimenez, J. L., Bahreini, R., Cocker III, D. R., Zhuang, H., Varutbangkul, V., Flagan, R. C., Seinfeld, J. H., O'Dowd, C. D., and Hoffmann, T.: New particle formation from photooxidation of diiodomethane (CH_2I_2), J. Geophys. Res., 108, 4318, doi:10.1029/2002JD002452, 2003.

Johnston, P. V. and McKenzie, R. L.: NO_2 observations at 45°S during the decreasing phase of solar cycle 21, from 1980 to 1987, Journal Geophysical Research, 94, 3473–3486, 1989.

Joiner, J. and Bhartia, P. K.: The determination of cloud pressures from rotational raman scattering in satellite backscatter ultraviolet measurements, J. Geophys. Res., 100, 23 019–23 026, 1995.

Kaleschke, L., Richter, A., Burrows, J. P., Afe, O., Heygster, G., Notholt, J., Rankin, A. M., Roscoe, H. K., Hollwedel, J., Wagner, T., and Jacobi, H.-W.: Frost flowers on sea ice as a source of sea salt and their influence on tropospheric halogen chemistry, Geophys. Res. Lett., 31, doi:10.1029/2004GL020655, 2004.

Küpper, F., Schweigert, N., Ar Gall, E., Legendre, J.-M., Vilter, H., and Kloareg, B.: Iodine uptake in laminariales involves extracellular, haloperoxidase-mediated oxidation of iodide, Planta, 207, 163–171, 1998.

Küpper, F. C., Carpenter, L. J., McFiggans, G. B., Palmer, C. J., Waite, T. J., Boneberg, E.-M., Woitsch, S., Weiller, M., Abela, R., Grolimund, D., Potin, P., Butler, A., III, G. W. L., Kroneck, P. M. H., Meyer-Klaucke, W., and Feiters, M. C.: Iodide accumulation provides kelp with an inorganic antioxidant impacting atmospheric chemistry, Proceedings of the National Academy of Sciences, 105, 6954–6958, 2008.

Krijger, J. M., Aben, I., and Schrijver, H.: Distinction between clouds and ice/snow covered surfaces in the identification of cloud-free observations using sciamachy pmds, Atmospheric Chemistry and Physics, 5, 2729–2738, 2005.

Kurucz, R., Furenlid, I., Brault, J., and Testerman., L.: Solar Flux Atlas from 296 to 1300 nm, National Solar Observatory, 1984.

Levelt, P. F., Hilsenrath, E., Leppelmeier, G. W., van den Oord, G. H. J., Bhartia, P. K., Tamminen, J., de Haan, J. F., and Veefkind, J. P.: Science objectives of the ozone monitoring instrument, IEEE Transactions on Geoscience and Remote Sensing, 44, doi:10.1109/TGRS.2006.872336., 2006.

Lillian, D., Bir Singh, H., Appleby, A., Lobban, L., Arnts, R., Gumpert, R., Hague, R., Toomey, J., Kazazis, J., Antell, M., Hansen, D., and Scott, B.: Atmospheric fates of halogenated compounds, Environ. Sci. Tech., 9, 1042–1048, 1975.

Lotz, W. A., Vountas, M., Dinter, T., and Burrows, J. P.: Cloud and surface classification using sciamachy polarization measurement devices, Atmos. Chem. Phys. Discuss., 8, 9855–9881, 2008.

Lovelock, J. E.: Hands up for the Gaia hypothesis, Nature, 344, 100–102, 1990.

Lovelock, J. E., Maggs, R. J., and Wade, R. J.: Halogenated hydrocarbons in and over the atlantic, Nature, 241, 194–196, 1973.

Mahaney, W. C., Dohm, J. M., Baker, V. R., Newsom, H. E., Malloch, D., Hancock, R., Campbell, I., Sheppard, D., and Milner, M. W.: Antarctic microbes colonize under mars-like conditions, Tech. rep., http://www.astrobio.net/pdffiles/news_233.pdf, 2002.

Martino, M., Mills, G. P., Woeltjen, J., and Liss, P. S.: A new source of volatile organoiodine compounds in surface seawater, Geophysical Research Letters, 36, doi:10.1029/2008GL036334, 2009.

McFiggans, G., Plane, J. M. C., Allan, B. J., Carpenter, L. J., Coe, H., and O'Dowd, C.: A modeling study of iodine chemistry in the marine boundary layer, J. Geophys. Res., 105, 14 371–14 385, 2000.

McFiggans, G., Coe, H., Burgess, R., Allan, J., Cubison, M., Alfarra, M. R., Saunders, R., Saiz-Lopez, A., Plane, J. M. C., Wevill, D. J., Carpenter, L. J., Rickard, A. R., and Monks, P. S.: Direct evidence for coastal iodine particles from laminaria macroalgae - linkage to emissions of molecular iodine, Atmos. Chem. Phys., 4, 701–713, 2004.

Mäkelä, J. M., Hoffmann, T., Holzke, C., Väkevä, M., Suni, T., Mattila, T., Aalto, P. P., Tapper, U., Kauppinen, E. I., and O'Dowd, C. D.: Biogenic iodine emissions and identification of end-products in coastal ultrafine particles during nucleation bursts, J. Geophys. Res., 107, 8110, doi:10.1029/2001JD000580, 2002.

Molina, M. J. and Rowland, F. S.: Stratospheric sink for chlorofluoromethanes: chlorine atom catalysed destruction of ozone, Nature, 249, 810–814, 1974.

Moore, R. M., Webb, M., Tokarczyk, R., and Wever, R.: Bromoperoxidase and iodoperoxidase enzymes and production of halogenated methanes in marine diatom cultures, J. Geophys. Res., 101, 20 899–20 908, 1996.

Murphy, D. M., Thomson, D. S., and Middlebrook, A. M.: Bromine, iodine, and chlorine in single aerosol particles at cape grim, Geophys. Res. Lett., 24, 3197–3200, 1997.

Noël, S., Bovensmann, H., Burrows, J. P., Frerick, J., Chance, K. V., Goede, A. H. P., and Muller, C.: The sciamachy instrument on envisat-1, sensors, systems, and next-generation satellites ii, Proc. SPIE, 3498, 94–104, 1998.

Noxon, J. F.: Nitrogen dioxide in the stratosphere and troposphere measured by ground-based absorption spectroscopy, Science, 189, 547, 1975.

Noxon, J. F., Whipple, Jr., E. C., and Hyde, R. S.: Stratospheric NO_2, 1. observational method and behavior at mid latitude, J. Geophys. Res., 84, 5047–5065, 1979.

O'Dowd, C. D. and Hoffmann, T.: Coastal new particle formation: A review of the current state-of-the-art, Environ. Chem., 2, doi:10.1071/EN05077, 2005.

O'Dowd, C. D., McFiggans, G., Creasey, D. J., Pirjola, L., Hoell, C., Smith, M. H., Allan, B. J., Plane, J. M. C., Heard, D. E., Lee, J. D., Pilling, M. J., and Kulmala, M.: On the photochemical production of new particles in the coastal boundary layer, Geophys. Res. Lett., 26, 1707–1710, 1999.

O'Dowd, C. D., Hämeri, K., Mäkelä, J. M., Pirjola, L., Kulmala, M., Jennings, S. G., Berresheim, H., Hansson, H.-C., de Leeuw, G., Kunz, G. J., Allen, A. G., Hewitt, C. N., Jackson, A., Viisanen, Y., and Hoffmann, T.: A dedicated study of new particle formation and fate in the coastal environment (PARFORCE): Overview of objectives and achievements, J. Geophys. Res., 107, 8108, doi:10.1029/2001JD000555, 2002a.

O'Dowd, C. D., Jimenez, J. L., Bahreini, R., Flagan, R. C., Seinfeld, J. H., Hameri, K., Pirjola, L., Kulmala, M., Jennings, S. G., and Hoffmann, T.: Marine aerosol formation from biogenic iodine emissions, Nature, 417, 632–636, 2002b.

Oetjen, H.: Measurements of halogen oxides by scattered sunlight differential optical absorption spectroscopy, Ph.D. thesis, University Bremen, 2009.

Pedersén, M., Collén, J., Abrahamsson, K., and Ekdahl, A.: Production of halocarbons by seaweeds: an oxidative stress reaction?, Scientia Marina, 60, 257–263, 1996.

Peters, C., Pechtl, S., Stutz, J., Hebestreit, K., Hönninger, G., Heumann, K. G., Schwarz, A., Winterlik, J., and Platt, U.: Reactive and organic halogen species in three different european coastal environments, Atmos. Chem. Phys., 5, 3357–3375, 2005.

Piot, M. and von Glasow, R.: The potential importance of frost flowers, recycling on snow, and open leads for ozone depletion events, Atmos. Chem. Phys., 8, 2437–2467, 2008.

Platt, U. and Hönninger, G.: The role of halogen species in the troposphere, Chemosphere, 52, 325–338, 2003.

Platt, U. and Perner, D.: Direct measurements of atmospheric CH_2O, HNO_2, O_3, NO_2, SO_2 by differential optical absorption in the near UV,, Journal Geophysical Research, 85, 7453–7458, 1980.

Platt, U. and Stutz, J.: Differential Optical Absorption Spectroscopy - Principles and Applications, Springer-Verlag, 2008.

Platt, U. and von Glasow, R.: Halogens in the troposphere - an international task. science and implementation plan, Geophys. Res. Abstr., 7, White Paper, http://www.igac.noaa.gov/HitT_WhitePaper.pdf, 2005.

Pope, R. M. and Fry, E.: Absorption spectrum (380-700nm) of pure water. ii. integrating cavity measurements, Applied Optics, 36, 1997.

Rasmussen, R. A., Khalil, M. A. K., Gunawardena, R., and Hoyt, D.: Atmospheric methyl iodide (CH_3I), Journal of Geophysical Research, 87, 2086–3090, 1982.

Ravishankara, A. R., Solomon, S., Turnipseed, A. A., and Warren, R. F.: Atmospheric lifetimes of long-lived halogenated species, Science, 259, 1993.

Read, K. A., Mahajan, A. S., Carpenter, L. J., Evans, M. J., Faria, B. V. E., Heard, D. E., Hopkins, J. R., Lee, J. D., Moller, S. J., Lewis, A. C., Mendes, L., McQuaid, J. B., Oetjen, H., Saiz-Lopez, A., Pilling, M. J., and Plane, J. M. C.: Extensive halogen-mediated ozone destruction over the tropical atlantic ocean, Nature, 453, 1232–1235, doi:10.1038/nature07035, 2008.

Reifenhäuser, W. and Heuman, K. G.: Determination of methyl iodide in the antarctic atmosphere and the south polar sea, Atmos. Environ., 26A, 2905–2912, 1992.

Richter, A.: Absorptionsspektrospokische Messungen stratosphärischer Spurengase über Bremen, 53°N, Ph.D. thesis, University Bremen, 1997.

Richter, A., Wittrock, F., Eisinger, M., and Burrows, J. P.: GOME observations of tropospheric BrO in Northern Hemispheric spring and summer 1997, Geophys. Res. Lett, 25, 2683–2686, 1998.

Richter, A., Eyring, V., Burrows, J. P., Bovensmann, H., Lauer, A., Sierk, B., and Crutzen, P. J.: Satellite measurements of NO_2 from international shipping emissions, Geophys. Res. Lett., 31, doi:10.1029/2004GL020822, 2004.

Richter, A., Burrows, J. P., Nüß, H., Granier, C., and Niemeier, U.: Increase in tropospheric nitrogen dioxide over china observed from space, Nature, 437, doi:10.1038/nature04092, 2005.

Robertson, H. A. and Falconer, I. R.: Accumulation of radioactive iodine in thyroid glands subsequent to nuclear weapon tests and the accident at windscale, Nature, 184, 1699–1702, 1959.

Rozanov, A., Bovensmann, H., Bracher, A., Hrechanyy, S., Rozanov, V., Sinnhuber, M., Stroh, F., and Burrows, J. P.: NO_2 and BrO vertical profile retrieval from SCIAMACHY limb measurements: Sensitivity studies, Advances in Space Research, 36, 846–854, Atmospheric Remote Sensing: Earth's Surface, Troposphere, Stratosphere and Mesosphere-I, 2005a.

Rozanov, A., Rozanov, V.-V., Buchwitz, M., Kokhanovsky, A., and Burrows, J. P.: SCIATRAN 2.0. A new radiative transfer model for geophysical applications in the 175-2400 nm spectral region, Adv. Space Res., 36, 1015–1019, doi:10.1016/j.asr.2005.03.012, 2005b.

Rozanov, V. V., Diebel, D., Spurr, R. J. D., and Burrows, J. P.: Gometran: A radiative transfer model for the satellite project GOME, the plane-parallel version, J. Geophys. Res., 102, 16 683–16 695, 1997.

Saiz-Lopez, A. and Plane, J. M. C.: Novel iodine chemistry in the marine boundary layer, Geophysical Rsearch Letters, 31, L04 112, doi:10.1029/2003GL019215, 2004.

Saiz-Lopez, A., Shillito, J. A., Coe, H., and Plane, J. M. C.: Measurements and modelling of i_2, io, oio, bro and no_3 in the mid-latitude marine boundary layer, Atmos. Chem. Phys., 6, 1513–1528, 2006.

Saiz-Lopez, A., Chance, K., Liu, X., Kurosu, T. P., and Sander, S. P.: First observations of iodine oxide from space, Geophys. Res. Lett., 34, doi:doi:10.1029/2007GL030111, 2007a.

Saiz-Lopez, A., Mahajan, A. S., Salmon, R. A., Bauguitte, S. J.-B., , Jones, A. E., Roscoe, H. K., and Plane, J. M. C.: Boundary layer halogens in coastal antarctica, Science, 317, 348, doi:10.1126/science.1141408, 2007b.

Saiz-Lopez, A., Plane, J. M. C., Mahajan, A. S., Anderson, P. S., Bauguitte, S. J.-B., Jones, A. E., Roscoe, H. K., Salmon, R. A., Bloss, W. J., Lee, J. D., and Heard, D. E.: On the vertical distribution of boundary layer halogens over coastal antarctica: implications for O_3, HO_x, NO_x and the Hg lifetime, Atmos. Chem. Phys. Discuss., 7, 9385–9417, 2007c.

Saiz-Lopez, A., Plane, J. M. C., Mahajan, A. S., Anderson, P. S., Bauguitte, S. J.-B., Jones, A. E., Roscoe, H. K., Salmon, R. A., Bloss, W. J., Lee, J. D., and Heard, D. E.: On the vertical distribution of boundary layer halogens over coastal antarctica: implications for O_3, HO_x, NO_x and the Hg lifetime, Atmospheric Chemistry and Physics, 8, 887–900, 2008.

Sander, R.: (as referee) Interactive comment on "A mechanism for biologically-induced iodine emissions from sea-ice" by A. Saiz-Lopez and C. S. Boxe, Atmospheric Chemistry and Physics, 8, S602–S603, 2008.

Sander, R. and Crutzen, P. J.: Model study indicating halogen activation and ozone destruction in polluted air masses transported to the sea, J. Geophys. Res., 101, 9121–9138, 1996.

Sander, R., Kerkweg, A., Jöckel, P., and Lelieveld, J.: Technical note: The new comprehensive atmospheric chemistry module MECCA, Atmos. Chem. Phys., 5, 445–450, 2005.

Sander, R., Burrows, J., and Kaleschke, L.: Carbonate precipitation in brine - a potential trigger for tropospheric ozone depletion events, Atmospheric Chemistry and Physics, 6, 4653–4658, 2006a.

Sander, R., Gromov, S., Harder, H., Jöckel, P., Kerkweg, A., Kubistin, D., Riede, H., Taraborrelli, D., and Xie, Z.-Q.: The atmospheric chemistry box model CAABA/MECCA-3.0, Geoscientific Model Development Discussions, 2009.

Sander, S. P., Finlayson-Pitts, B. J., Friedl, R. R., Golden, D. M., Huie, R. E., Keller-Rudek, H., Kolb, C. E., Kurylo, M. J., Molina, M. J., Moortgat, G. K., Orkin, V. L., Ravishankara, A. R., and Wine, P. H.: Chemical Kinetics and Photochemical Data for Use in Atmospheric Studies, JPL Publication 06-2, Evaluation Number 15, Jet Propulsion Laboratory, Pasadena, 2006b.

Sandu, A. and Sander, R.: Technical note: Simulating chemical systems in fortran90 and matlab with the kinetic preprocessor KPP-2.1, Atmospheric Chemistry and Physics, 6, 187–195, 2006.

Schall, C., Laturnus, F., and Heumann, K. G.: Biogenic volatile organoiodine and organobromine compounds released from polar macroalgae, Chemosphere, 28, 1315–1324, 1994.

Schönhardt, A., Richter, A., Wittrock, F., Kirk, H., and Burrows, J. P.: First observations of atmospheric iodine oxide columns from satellite, Geophys. Res. Abstr., 9, 2007.

Schönhardt, A., Richter, A., Wittrock, F., Kirk, H., H., O., Roscoe, H. K., and Burrows, J. P.: Observations of iodine monoxide columns from satellite, Atmos. Chem. Phys., 8, 637–653, 2008.

Schröter, W., Lautenschläger, K.-H., and Bibrack, H.: Taschenbuch der Chemie, Verlag Harri Deutsch, 13 edn., 1988.

Shefov, N. N.: Spectroscopic, photoelectric, and radar investigations of aurorae and the nightglow, Izd. Akad. Nauk, 1, 1959.

Simpson, W. R., Carlson, D., Hönninger, G., Douglas, T. A., Sturm, M., Perovich, D., and Platt, U.: First-year sea-ice contact predicts bromine monoxide (BrO) levels at barrow, alaska better than potential frost flower contact, Atmospheric Chemistry and Physics, 7, 621–627, 2007a.

Simpson, W. R., von Glasow, R., Riedel, K., Anderson, P., Ariya, P., Bottenheim, J., Burrows, J., Carpenter, L. J., Frieß, U., Goodsite, M. E., Heard, D., Hutterli, M., Jacobi, H.-W., Kaleschke, L., Neff, B., Plane, J., Platt, U., Richter, A., Roscoe, H., Sander, R., Shepson, P., Sodeau, J., Steffen, A., Wagner, T., and Wolff, E.: Halogens and their role in polar boundary-layer ozone depletion, Atmospheric Chemistry and Physics, 7, 4375–4418, 2007b.

Sinnhuber, B.-M., Rozanov, A., Sheode, N., Afe, O. T., Richter, A., Sinnhuber, M., Wittrock, F., and Burrows, J. P.: Global observations of stratospheric bromine monoxide from SCIAMACHY, Geophysical Research Letters, 32, doi:10.1029/2005GL023839, 2005.

Solomon, S., Schmeltekopf, A. L., and Sanders, R. W.: On the interpretation of zenith sky absorption measurements, Journal of Geophysical Research, 92, 8311–8319, 1987.

Solomon, S., Garcia, R. R., and Ravishankara, A. R.: On the role of iodine in ozone depletion, J. Geophys. Res., 99, 20 491–20 499, 1994.

Spietz, P., Gómez Martín, J. C., and Burrows, J. P.: Spectroscopic studies of the i_2/o_3 photochemistry, Part 2: Improved spectra of iodine oxides and analysis of the IO absorption spectrum, J. Photochem. Photobiol. A, 176, 50–67, doi:10.1016/j.jphotochem.2005.08.023, 2005.

Spreen, G., Kaleschke, L., and Heygster, G.: Sea ice remote sensing using amsr-e 89 ghz channels, J. Geophys. Res., 113, doi:10.1029/2005JC003384, 2008.

Stöcker, H.: Taschenbuch der Physik, Verlag Harri Deutsch, 2nd edn., 1995.

Stolarski, R. S. and Cicerone, R. J.: Stratospheric chlorine: a possible sink for ozone, Can. J. Chem., 52, 1610–1615, 1974.

Stutz, J., Pikelnaya, O., Hurlock, S. C., Trick, S., Pechtl, S., and von Glasow, R.: Daytime OIO in the Gulf of Maine, Geophys. Res. Lett., 34, L22 816, doi:10.1029/2007GL031332, 2007.

Thomas, D. N. and Diekmann, G. S., eds.: Sea Ice: An introduction to its physics, chemistry, biology and geology, Blackwell Publishing Company, 2003.

Tokarczyk, R. and Moore, R. M.: Production of volatile organohalogens by phytoplankton cultures, Geophysical Research Letters, 21, 285–288, 1994.

Truesdale, V. W., Canosa-Mas, C. E., and W., L. G.: Disproportionation and reduction of molecular iodine added to seawater, Marine Chemistry, 51, 55–60, 1995.

Tucceri, M. E., Hölscher, D., Rodriguez, A., Dillon, T. J., and Crowley, J. N.: Absorption cross section and photolysis of OIO, Physical Chemistry Chemical Physics, 8, 834–846, 2006.

Vasilkov, A. P., Joiner, J., Gleason, J., and Bhartia, P.: Ocean Raman scattering in satellite backscatter UV measurements, Geophys. Res. Let., 10, 10, 2002.

Vogt, R., Sander, R., von Glasow, R., and Crutzen, P. J.: Iodine chemistry and its role in halogen activation and ozone loss in the marine boundary layer: A model study., J. Atmos. Chem., 32, 375–395, 1999.

Volkamer, R., Spietz, P., Burrows, J., and Platt, U.: High-resolution absorption cross-section of glyoxal in the uv/vis and ir spectral ranges, J. Photochem. Photobiol., 172, 2005.

von Glasow, R., Sander, R., Bott, A., and Crutzen, P. J.: Modeling halogen chemistry in the marine boundary layer. 1. Cloud-free MBL, J. Geophys. Res., 107, 4341, doi:10.1029/2001JD000942, 2002.

Vountas, M., Rozanov, V. V., and Burrows, J. P.: Ring effect: Impact of rotational raman scattering on radiative transfer in earth's atmosphere, J. Quant. Spectrosc. Radiat. Transfer, 60, 943–961, 1998.

Vountas, M., Richter, A., Wittrock, F., and Burrows, J. P.: Inelastic scattering in ocean water and its impact on trace gas retrievals from satellite data, Atmospheric Chemistry and Physics, 3, 1365–1375, 2003.

Vrekoussis, M., Wittrock, F., Richter, A., and Burrows, J. P.: Temporal and spatial variability of glyoxal as observed from space, Atmospheric Chemistry and Physics, 9, 4485–4504, 2009.

Wada, R., Beames, J. M., and Orr-Ewing, A. J.: Measurement of IO radical concentrations in the marine boundary layer using a cavity ring-down spectrometer, Journal of Atmospheric Chemistry, 58, 69–87, doi:10.1007/s10874-007-9080-z, 2007.

Wagner, T. and Platt, U.: Satellite mapping of enhanced bro concentration in the troposphere, Nature, 395, 486–490, 1998.

Wayne, R. P.: Chemistry of Atmospheres, Oxford University Press, 3rd edition, 2000.

Wennberg, P. O., Brault, J. W., Hanisco, T. F., Salawitch, R. J., and Mount, G. H.: The atmospheric column abundance of IO: implications for stratospheric ozone, J. Geophys. Res., 102, 8887–8898, 1997.

Whalley, L. K., Furneaux, K. L., Gravestock, T., Atkinson, H. M., Bale, C., Ingham, T., Bloss, W. J., and Heard, D.: Detection of iodine monoxide radicals in the marine boundary layer using laser induced fluorescence spectroscopy, J. Atmos. Chem., 58, 19–39, doi:10.1007/s10874-007-9075-9, 2007.

WHO: Iodine Deficiency in Europe: A continuing public health problem. Andersson, M., and de Benoist, B., and Darnton-Hill, I., and Delange, F. (eds.), World Health Organization, ISBN 978-92-4-159396-0, 2007.

Wittrock, F.: The retrieval of oxygenated volatile organic compounds by remote sensing techniques, Ph.D. thesis, University Bremen, 2006.

Wittrock, F., Müller, R., Richter, A., Bovensmann, H., and Burrows, J. P.: Measurements of iodine monoxide (IO) above Spitsbergen, Geophys. Res. Lett., 27, 1471–1474, 2000.

Wittrock, F., Oetjen, H., Richter, A., Fietkau, S., Medeke, T., Rozanov, A., and Burrows, J. P.: MAX-DOAS measurements of atmospheric trace gases in Ny-Ålesund - Radiative transfer studies and their application, Atmos. Chem. Phys., 4, 2004.

WMO, 2006: Scientific Assessment of Ozone Depletion: 2006, Global Ozone Research and Monitoring Project-Report No. 50, World Meteorological Organization, final release published Febuary 2007.

Zingler, J. and Platt, U.: Iodine oxide in the dead sea valley: Evidence for inorganic sources of boundary layer IO, J. Geophys. Res., 110, doi:10.1029/2004JD004993, 2005.

Erklärung

Hiermit erkläre ich, dass ich die Arbeit ohne unerlaubte fremde Hilfe angefertigt habe, dass ich weiterhin keine anderen als die angegebenen Quellen und Hilfsmittel benutzt und die den benutzten Werken wörtlich oder inhaltlich entnommenen Stellen als solche kenntlich gemacht habe.

Bremen, 03.September 2009

Anja Schönhardt

Acknowledgements